

**Colloidally Dispersed Upconversion Nanoparticles: How Surface
Composition Affects Brightness, Stability, and Cytotoxicity**

Dissertation

zur Erlangung des
DOKTORGRADES DER NATURWISSENSCHAFTEN
(Dr. rer. nat.)
an der
Naturwissenschaftlichen Fakultät IV
- Chemie und Pharmazie -
der Universität Regensburg



vorgelegt von
Susanne Märkl
aus Regensburg
im Oktober 2022

Die vorliegende Dissertation entstand in der Zeit von Dezember 2018 bis Oktober 2022 am Institut für Analytische Chemie, Chemo- und Biosensorik der Universität Regensburg.

Die Arbeit wurde angeleitet von Prof. Dr. Joachim Wegener und Dr. Thomas Hirsch.

Promotionsgesuch eingereicht am:

Prüfungsausschuss

Vorsitzender: PD Dr. Max Keller

Erstgutachter: Prof. Dr. Joachim Wegener

Zweitgutachter: Prof. Dr. Achim Göpferich

Drittprüferin: Prof. Dr. Miriam Breuning

„Da steh ich nun ich armer Tor und bin so klug als wie zuvor.“

— Dr. Faust

Für meine Familie

Danksagung

Ich möchte mich zunächst herzlichst bei **Prof. Dr. Joachim Wegener** und **Dr. Thomas Hirsch** für die Möglichkeit bedanken, dieses spannende Promotionsthema als Mitglied zweier Arbeitsgruppen behandeln zu dürfen. Außerdem möchte mich für die immer hilfreichen Diskussionen bedanken.

Für die Übernahme des Zweitgutachtens und des Amts der Drittprüferin möchte ich mich bei **Prof. Dr. Achim Göpferich** und **Prof. Dr. Miriam Breunig** bedanken. Mein Dank gilt ebenso **PD Dr. Max Keller** für die Ausübung der Funktion des Prüfungsvorsitzenden.

Bei **Dr. Frédéric Przybilla** und **Prof. Dr. Yves Mely** möchte ich mich für die Betreuung während des Forschungsaufenthalts an der Universität Straßburg bedanken.

Dr. Max Keller danke ich für die Ermöglichung des GPCR Projekts und die hilfreichen Diskussionen. Mein Dank gilt auch **Jakob Gleixner** und **Lisa Schindler**, die mir die hierfür benötigte Substanzen zur Verfügung gestellt und die Radioligandbindungsstudien durchgeführt haben.

Prof. Dr. Reinhard Rachel und **Prof. Dr. Ralph Witzgall** danke ich für die Ermöglichung der elektronenmikroskopischen Analyse von Zellen und **Helga Othmen** für die Probenvorbereitung und Aufnahmen.

Mein besonderer Dank gilt **Alexandra Schroter** für ihr immer offenes Ohr bei arbeits(un-)relevanten Fragestellungen und für die tolle Zeit um und an der Uni in den letzten neun Jahren.

Besonders danken möchte ich auch **Dr. Michael Skiba** für die unermüdlichen Diskussionen über GPCRs und die Korrektur dieser Arbeit, aber vor allem dafür, dass er mich überzeugt hat, dass jedes noch so unerwartete Ergebnis ein gutes Ergebnis ist.

Bedanken möchte ich mich bei **Dr. Markus Buchner** und **Dr. Sandy Franziska Himmelstoß** sowie bei **Dr. Lisa Pütz**, dass sie mich in die Welt der UCNPs bzw. der Zellen eingeführt haben und meine Begeisterung für diese Themen geweckt haben.

Ich möchte mich bei **Lisa Tetek** und **Jannik Feiler** bedanken, die im Rahmen ihrer Bachelorarbeit und Forschungspraktikum an zwei Studien dieser Arbeit beteiligt waren.

Danke auch an **Joachim Rewitzer** für die Unterstützung bei den ICP-OES und ICP-MS Messungen sowie für den leckeren Kaffee. Bei **Rosi Walter**, **Barbara Goricnik** und **Nadja Hinterreiter** möchte ich mich für die stets verfügbare Unterstützung bedanken.

Mein Dank gilt auch **Ulrike Schießl** und **Dr. Marc Schlosser** für die TGA und XRD Messungen. Weiterhin danke ich **Svenja Berit Seiffert** und **Dr. Sabine Kröger** von der BASF für die Durchführung der LA-ICP-MS Messungen.

Last but not least danke ich meinen vielen lieben aktuellen und ehemaligen Kollegen aus dem **1. und 4. Stock** für die stets äußerst angenehme Arbeitsatmosphäre, die hilfreichen Motivationsschübe bei morgendlichen Schwimmrunden, bei einem Nachmittagskaffee oder bei einem Feierabendbier und besonders auch für die tolle außeruniversitäre Zeit!

Table of Contents

1	Introduction.....	1
1.1	<i>Nanomedicine.....</i>	<i>1</i>
1.2	<i>Characteristics of Upconversion Nanoparticles.....</i>	<i>4</i>
1.3	<i>The Bioidentity of Nanoparticles</i>	<i>8</i>
1.4	<i>Cellular Phenotypes Determining Particle Internalization</i>	<i>12</i>
1.5	<i>Interactions of Nanoparticles with Cells: From Extracellular Attraction to Internalization and Toxicity.....</i>	<i>14</i>
1.6	<i>G Protein-Coupled Receptors: Structure, Function, and Signal Transduction</i>	<i>21</i>
2	Objectives	25
3	Material and Methods.....	27
3.1	<i>Particle Preparation and Characterization.....</i>	<i>27</i>
3.1.1	<i>Particle Syntheses.....</i>	<i>27</i>
3.1.2	<i>Surface Modifications.....</i>	<i>30</i>
3.1.3	<i>Surface Functionalization</i>	<i>33</i>
3.1.4	<i>Particle Characterization</i>	<i>39</i>
3.2	<i>Cell Culture and Techniques</i>	<i>43</i>
3.2.1	<i>Cell Lines.....</i>	<i>43</i>
3.2.2	<i>Subcultivation.....</i>	<i>44</i>
3.2.3	<i>Cryopreservation and Recultivation</i>	<i>45</i>
3.2.4	<i>General Experimental Procedures and Considerations</i>	<i>46</i>
3.2.5	<i>Impedance-Based Cell Analysis.....</i>	<i>46</i>
3.2.6	<i>Inductively Coupled Plasma - Mass Spectrometry.....</i>	<i>52</i>
3.2.7	<i>Laser Ablation - Inductively Coupled Plasma - Mass Spectrometry.....</i>	<i>53</i>
3.2.8	<i>Microscopic Techniques.....</i>	<i>54</i>
3.2.9	<i>Cell Viability Assay PrestoBlue™</i>	<i>59</i>
3.2.10	<i>Detection of Reactive Oxygen Species</i>	<i>60</i>
3.2.11	<i>Radioligand Competition Binding Assay.....</i>	<i>61</i>
4	Small and Bright Water-Protected Upconversion Nanoparticles with Long-Time Stability in Complex, Aqueous Media	63
4.1	<i>Preface</i>	<i>63</i>
4.2	<i>Introduction</i>	<i>64</i>

4.3	<i>Particle Preparation and Characterization</i>	66
4.4	<i>Surface Modification of Upconversion Nanoparticles with Phospholipid Membrane Coating</i>	68
4.5	<i>Colloidal Stability of Upconversion Nanoparticles in Water</i>	71
4.6	<i>Brightness of Upconversion Nanoparticles in Aqueous Media</i>	73
4.7	<i>Colloidal Stability of Upconversion Nanoparticles in Ionic Solutions</i>	75
4.8	<i>Colloidal Stability of Upconversion Nanoparticles in Isotonic Buffer and Media</i>	78
4.9	<i>Microscopic Imaging of Small Phospholipid Membrane Coated Nanoparticles</i>	81
4.10	<i>Conclusion</i>	86
5	Time-Resolved Analysis of Upconversion Nanoparticle Uptake and Cytotoxicity in Non-Cancerous Epithelial Cells	89
5.1	<i>Preface</i>	89
5.2	<i>Introduction</i>	90
5.3	<i>Particle Preparation and Characterization</i>	93
5.4	<i>Toxicity of Upconversion Nanoparticles with Amphiphilic Polymer and Phospholipid Membrane Coating</i>	97
5.5	<i>Internalization of Upconversion Nanoparticles with Amphiphilic Polymer or Phospholipid Membrane Coating</i>	102
5.6	<i>Stability of Upconversion Nanoparticles with Amphiphilic Polymer and Phospholipid Membrane Coating</i>	104
5.7	<i>Toxicity Evaluation of Released Ions</i>	107
5.8	<i>Possible Uptake Pathways of Non-Toxic Upconversion Nanoparticles</i>	108
5.9	<i>Conclusion</i>	114
6	Toxicity Profile of Poorly Surface-Protected Upconversion Nanoparticles in Contact to Epithelial Cells	117
6.1	<i>Preface</i>	117
6.2	<i>Introduction</i>	117
6.3	<i>Particle Preparation and Characterization</i>	119
6.4	<i>Analysis of Nanoparticle Internalization</i>	121
6.5	<i>End-Point Cell Viability Assay</i>	123
6.6	<i>Impedance-Based Cell Analysis</i>	125
6.6.1	<i>Toxicity</i>	126
6.6.2	<i>Cell Migration</i>	135

6.6.3	Cell Adhesion	138
6.7	Toxicity Profile and Summary	141
7	Upconversion Nanoparticles for Photodynamic Therapy	145
7.1	Preface.....	145
7.2	Introduction	145
7.3	Particle Functionalization and Characterization	148
7.4	Rose Bengal Uptake by Cells.....	154
7.5	Toxicity of Rose Bengal Functionalized Nanoparticles	158
7.6	Rose Bengal and Upconversion Nanoparticle Uptake by Cells.....	162
7.7	Production of Reactive Oxygen Species upon Irradiation of Rose Bengal.....	169
7.7.1	Fluorometric Detection of Cellular Levels of Reactive Oxygen Species	170
7.7.2	Detection of Cell Death upon Production of Reactive Oxygen Species.....	174
7.8	Conclusion and Outlook.....	176
8	Upconversion Nanoparticles to Study G Protein-Coupled Receptors	179
8.1	Preface	179
8.2	Introduction	179
8.3	Particle Functionalization with an Agonist	181
8.4	Characterization of Cell Stimulation by Free Agonist	185
8.5	Characterization of Cell Stimulation and Receptor Binding by Agonist-Functionalized Nanoparticles.....	189
8.6	Particle Functionalization for Reduced Non-Specific Binding	196
8.7	Characterization of Cell Stimulation by Agonist-Functionalized Nanoparticles with a Second Cell Model.....	202
8.8	Characterization of Cell Stimulation by Agonist-Functionalized Nanoparticles in the Antagonism Assay	206
8.9	Characterization of Cell Stimulation by Agonist-Functionalized Nanoparticles in the Presence of Serum Proteins	210
8.10	Conclusion and Outlook	215
9	Summary	219
10	Zusammenfassung.....	223
	References	227
11	Appendix	255

11.1	<i>Supporting Figures and Tables</i>	255
11.2	<i>List of Materials</i>	261
12	Curriculum Vitae	265
	Eidesstattliche Erklärung	269

1 Introduction

1.1 Nanomedicine

Nanomedicine is the interdisciplinary field at the interface of nanoengineering, nanotechnology, life science, and medicine. It aims to enhance the patients' quality of life by developing better and more patient-oriented drugs and devices for early diagnostics, prevention, and therapy of a wide range of diseases with high specificity, efficacy, and personalization (Pelaz et al., 2017). Nanomaterials have diameters between 1 nm and 100 nm in at least one dimension and are characterized by a high surface to volume ratio. They have unique size-dependent properties and are attractive by their large surface area for flexible functionalization with various drugs and targeting moieties (Jeevanandam et al., 2018; Kopac, 2021). There is a wide variety of nanomaterials with different features (optical, electronic, and magnetic) available for various applications of nanomedicine. This includes lipid- or protein-based nanoparticles, polymeric nanomaterials, metal or metal oxide particles, and many other inorganic nanocrystals as semiconducting quantum dots or lanthanide doped nanoparticles. The nanomaterials can be applied as biosensors for high-throughput diagnostics in biological fluids for the rapid detection of biomarkers and molecular alterations. This is also feasible for the direct analysis of diseases in the body (Pelaz et al., 2017). Their main feature is their utilization as smart transport systems for pharmaceutical agents across biological barriers to a certain target site. As drug delivery vehicles they can enhance the drug solubility, availability, accumulation, stability, and half-life of the drugs. Moreover, they can release the drugs with temporal and spatial control in the desired tissue by adding targeting or stimuli-responsive moieties (Zhang et al., 2020a; Pelaz et al., 2017; Sun et al., 2020). This systematical drug administration can improve drug efficacy by reducing toxic side effects (Shi et al., 2017). Many of these features can be combined to design multimodal nanoparticles with the ability to simultaneously diagnose as well as treat diseases and monitor the therapeutic success (Chow et al., 2013). Well-functioning nanomaterials are suitable to establish a generic platform, which enables a rapid adaption of the medical nanodevice to evolving needs and new applications without the necessity to start always with the design from the beginning. This is

achieved by the replacement, fine-tuning, or alignment of only a few features of the surface ligands by keeping the rest of the nanodevice constant (Germain et al., 2020).

The very promising field of nanomedicine with many well-known particle syntheses and functionalization methods has already entered preclinical trials 15 years ago (Lammers et al., 2020). However, a review of the literature on preclinical research demonstrated that only 0.7% (median) of the intravenously injected nanoparticles accumulated in the desired (tumor) tissue on average (Wilhelm et al., 2016). It was claimed that the preclinical research over one decade did not come up with working strategies for their main objective of improving drug delivery. In addition, mostly disappointing clinical trial results were reported. These worrying circumstances triggered statements as the “beginning of the end of nanomedicine” and funding of the U.S. National Cancer Institute (NCI) was terminated (Park, 2019; Lammers et al., 2020).

Nanomedicine must face many challenges before revolutionizing the theranostics tools. Their size makes them capable of passing and processing of intrinsic biological messages (Lara et al., 2017). Although nanoformulations can have improved clinical outcomes compared to conventional drugs, they are foreign for human cells. They likely react with cells and cellular components by controlling cellular processes (Augustine et al., 2020; Zhang et al., 2020a). They can travel through an organism, enter, and accumulate in various organs to activate inflammatory and immunological responses. Even materials, which are inert in bulk phase, such as gold, silver, or iron, can be harmful on a nanoscale (Umair et al., 2016). Thus, the size of the nanomaterials results in I) unknown and difficult to predict side effects, which need to be analyzed and understood in detail. The II) non-standardized characterization methods enable only poor data comparison or even misinterpretation, decelerating the process. The list of challenges is extended by III) the difficult translation of their efficacy from *in vitro* to *in vivo* applications, IV) difficulties in large-scale production, and V) incomplete understanding of long-term effects (Latreille et al., 2022; Sharma et al., 2021; Mahmoudi, 2021). Even if the progress of nanomedicine is not as fast as desired and many challenges need to be overcome, one has to consider the great success for a relatively young field. There are > 400 ongoing clinical trials on nanomedicine formulations to improve the therapies for widely common diseases as cancer, diabetes, cardiovascular disease, inflammatory bowel disease, or rheumatoid arthritis. More than 50 nanoparticle-based drug products have made their way

into FDA-approved clinical use, mostly based on liposomes, protein-based NPs, and iron as well as metal oxide nanocrystals (Lammers et al., 2020; Germain et al., 2020). The approvals include formulations for the simultaneous delivery of two drugs at a synergic ratio against leukemia (Vyxeos, 2017), the encapsulation of siRNA (Onpattro, 2018) or of mRNA (BNT162b2, 2020 and mRNA-1273, 2020) into lipid nanoparticles as drug against amyloidosis or vaccines against COVID-19, respectively. These three examples demonstrate the rising importance and the huge potential of next generations of nanomedicine, satisfying the current needs on specific and well-controlled drug delivery formulations, and expanding the scope to a broader range of diseases (Germain et al., 2020; Sharma et al., 2021).

Standardization of studies, characterization methods, and parameters can help to analyze and interpret the continuously growing data pool (Faria et al., 2018). For example, the often-used mass concentration implies the administration and delivery of equal particle concentrations for dissimilar materials and neglects the agglomeration of the particles. However, the actual particle number and active surface area can vary by orders of magnitude for different nanomaterials, giving rise to non-substantiated data comparison and misinterpretation (Teeguarden et al., 2007; Cohen et al., 2014). A detailed knowledge on nanoparticle internalization and fate on a cellular scale, within tissue organoids, and within the addressed tissue is deeply required before applying them *in vivo*. Interdisciplinary, systematic, and coordinated studies may help to solve challenges, to improve the nanoparticle efficacy and safety in biological systems, and to move nanomedicine further from a promising to a powerful tool for theranostic applications.

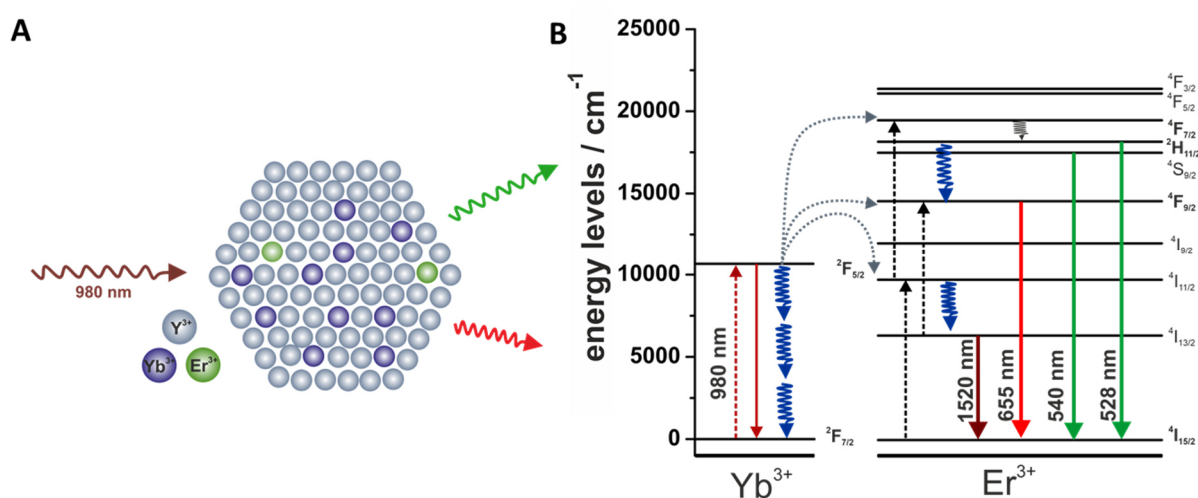
1.2 Characteristics of Upconversion Nanoparticles

The upconversion process has attracted the interest of many researchers since the 1960s and has made its way into nanoparticles (Auzel, 2004). The so-called upconversion nanoparticles (UCNPs) have been predicted to find applications across different fields of research, *e.g.* in solar cells and theranostics (Haase et al., 2011; Chen et al., 2014; He et al., 2016). The UCNPs show the unique ability to emit light in the visible range of the spectrum upon excitation with light of the biological window in the near infrared (NIR). The NIR excitation is accompanied by many advantages as I) its reduced phototoxicity, II) reduced autofluorescence of biological material, and III) a deeper tissue penetration (up to 10 cm, (Weissleder, 2001)). The high photostability results in a IV) high signal to noise ratio and V) a high sensitivity (Yang, 2014). Among these, VI) their sharp emission bands in the VIS and NIR are characterized by VII) large (anti-) Stokes shifts and VIII) long lifetimes (ms) IX) without photobleaching. Moreover, the UCNPs have X) multiple emission bands, which are XI) tunable by changing the dopant ions (Yang, 2014).

The upconversion process of converting two or more low-energy photons into a higher energy photon is incorporated into nanoparticles by doping sensitizer and activator ions with matching energy levels into suitable host materials. The choice of the host lattice contributes to the efficiency of the multiphoton process as it determines the distance between the dopants and, thereby, tailors the probability of energy transfers to occur. Moreover, the host material should have low phonon energies to reduce non-radiative decays and to enable long lifetimes of the excited ion states (Haase et al., 2011). This is facilitated by fluoride based materials with optically active phonon modes of around 350 cm^{-1} (Suyver et al., 2006). One of the most efficient UCNP designs consists of the lanthanide ions Yb^{3+} as sensitizer and Er^{3+} as activator ions, which are embedded in the hexagonal NaYF_4 host lattice (**Scheme 1.1A**, (Homann C. et al., 2018)). However, the upconversion efficiency is rather low in the particles with minimized non-radiative decay due to the small absorption coefficient of Yb^{3+} ($10\text{ M}^{-1}\cdot\text{cm}^{-1}$), competing Stokes emission, and the forbidden nature of electronic f-f transitions between the lanthanide ions.

The upconversion process can occur in particles by many mechanisms with the highest probability for energy transfer upconversion (ETU, 10^{-3}), excited state absorption (ESA, 10^{-5}),

and photon avalanche (10^{-6}) (Auzel, 2004). The most probable upconversion process ETU is shown in **Scheme 1.1B** for the $\text{Yb}^{3+}/\text{Er}^{3+}$ UCNPs. The activator ion Yb^{3+} absorbs a 980 nm photon and reaches the next higher energy level. The excited Yb^{3+} transfers its energy to a Er^{3+} ion in proximity, which is promoted from ground state to a higher energy state. This process happens twice so that Er^{3+} populates a higher energy level. After the transfer of the photons, the Er^{3+} ions can either relax directly to the ground state, emitting a green photon (528 nm, 540 nm), or undergo phonon relaxation before emitting a red or NIR photon (655 nm, 1550 nm) (Auzel, 2004).



Scheme 1.1. (A) UCNPs with hexagonal NaYF_4 host lattice doped with sensitizer ions Yb^{3+} and activator ions Er^{3+} , which is excitable by 980 nm for luminescence in the green and red range of the electromagnetic spectrum. (B) Energy level diagram of the energy transfer upconversion (ETU) of Yb^{3+} to Er^{3+} in $\text{NaYF}_4(\text{Yb},\text{Er})$ adapted from (Arppe R. et al., 2015). Dashed arrows represent absorption (red, black), curved and dashed arrows energy transfer (grey), solid arrows emission (red, green) and curly arrows non-radiative relaxation processes (black, blue).

The efficiency of upconversion in UCNPs is influenced by the particle design (host lattice, dopant ions) and the competing photophysical processes. Moreover, it changes with the particle size as those with a high surface to volume ratio have a higher probability for surface defects and surface quenching by ligand and solvent molecules (Wen et al., 2018). Especially when it comes to applications in water, the excited states of Yb^{3+} and Er^{3+} are highly quenched as the energy of O-H vibrations fits the energy distance between several states (**Scheme 1.1B** blue curly arrows (Arppe R. et al., 2015)). So far, several strategies have been pursued to maintain the brightness of the particles by *e.g.*, I) energy harvesting *via* organic ligands, II) adjusting the particle composition, or III) changing the particle architecture (Homann C. et al.,

2018; Wiesholler et al., 2018). However, the strategies I) and III) lead to particles, which are highly saturated with mainly hydrophobic ligands resulting in poor colloidal stability in water and limited space for functional ligands, or to large particles, which are not useful for *in vitro* or *in vivo* applications. To date, the synthesis of UCNPs with perfect characteristics for *in vitro* applications in terms of size, chemical and colloidal stability, and brightness remains challenging and is part of ongoing research.

UCNPs have been already introduced to the field of nanomedicine in various proof of concept studies on bioimaging, diagnosis, and light-activated therapy (Li et al., 2020). Due to the low background and their multiple emission maxima, UCNPs are an ideal luminescent reporter for biosensing with a potential self-referencing feature. Many analytes are accessible in biosensing approaches with UCNPs in “turn-off” or “turn-on” designs. Analytes with absorbance bands overlapping with the upconversion luminescence bands can “turn-off” the upconversion luminescence by the inner-filter effect. Non-overlapping analytes are accessible by attaching analyte sensitive molecules (LRET acceptor), which undergo luminescence resonance energy transfer (LRET) with the UCNPs (LRET donor). In the presence of the analyte, the LRET acceptor alters its optical properties so that no LRET occurs and the upconversion luminescence is “turned-on” (Li et al., 2020). These two sensing mechanisms were adapted for lateral flow assays with biological fluids to detect, *e.g.* myoglobin, hepatitis B, or influenza viruses (Ji et al., 2019; Kim et al., 2018; Martiskainen et al., 2021) and the *in vitro* and *in vivo* detection of disease biomarkers (*e.g.* DNA, thrombin, ATP) or metal ions (Huang et al., 2014; Yang et al., 2018; Li et al., 2020).

The NIR excitation of UCNPs allows for the remote, controllable drug release in deep tissues, which are not accessible by common luminescent drug transporters. In general, the *in vivo* drug release makes use of UV-mediated photochemical reactions as photoactivation or photocleavage of organic bonds at the desired location. This established machinery for UV-mediated drug release can be easily adapted to the UCNPs for a NIR-to-UV-mediated process. For example, the cancer drug 5-fluorouracil (5-FU) was conjugated to the UCNPs by a photocleavable derivative of o-phosphoryl ethanolamine and could be cleaved completely by the UCNPs emission upon NIR excitation within 14 min *in vitro* (Diao et al., 2015). Another idea was the attachment of photoswitchable polymers to the particles with cavities large enough

for biomolecules. The cages can be (re-)opened by UCNP emissions for spatiotemporally cargo release. This approach was utilized to promote the neural differentiation of human-induced pluripotent stem cells (hiPSC-NSCs) *via* UCNPs, which were modified with spiropyran cages to hold the neurogenic differentiation factor retinoic acid (Zhang et al., 2020b).

The deep tissue accessibility with UCNP is also advantageous for light-activated therapy to kill tumor cells by generating toxic reactive-oxygen species (ROS) by means of photosensitizers (PS) in a very local manner. The photodynamic therapy (PDT) is a promising strategy to treat cancer and dermatological disorders with reduced side-effects and precise targeting of the diseased tissue. The common UV/VIS irradiation restricts the application of PDT only to surface tissue. However, an UCNP-based therapy method provides access to deeper tissues using UCNP as nanotransformers to excite the PS by upconversion luminescence and shift the excitation into the biological window (Qiu et al., 2018). So far, UCNP have been loaded with several PS alone or in combination as dual-photosensitizer probe to enhance ROS production, for example with chlorin e6, merocyanine 540, or rose bengal (Fedoryshin et al., 2014). Moreover, this NIR-induced PDT was combined with chemotherapy at a multimodal particle with imaging capability. The multifunctional UCNP were designed with multiple emission bands to I) trigger the release of the anticancer drug (AB3) by photocleaving a polymer using UV emissions, II) activate the photosensitizer rose bengal to generate ROS by 540 nm emissions, and III) keep the red emission for imaging. The targeting ligand KE108 was anchored for a specific tumoral uptake of these “jack of all trades” (Chen et al., 2017).

UCNP can be applied for long-time bioimaging in living cells or in tissues since they overcome the issues of common organic fluorophores or other fluorescent probes such as strong background fluorescence and poor photostability. The particles can additionally contain Gd^{3+} as dopant ions for multimodal bioimaging with magnetic resonance imaging capability to enhance the spatial resolution and sensitivity (Liang et al., 2020). Very recently, the design of upconversion particles was modified and the UCNP were applied in a revolutionizing approach for bioimaging. NP with Tm^{3+} dopants, having slow intermediate-state decay rates, in doping amounts of $\geq 8\%$ were prepared without sensitizer ions. They were irradiated with 1,450 nm light, provided by a strong pump-laser with $20 \text{ kW}\cdot\text{cm}^{-2}$. With this setup, photon-avalanche nanoparticles (ANP) were obtained for giant non-linear optical response. These

nanoparticles can be applied in super-resolution imaging in the NIR with sub-70-nm imaging resolution (Lee et al., 2021).

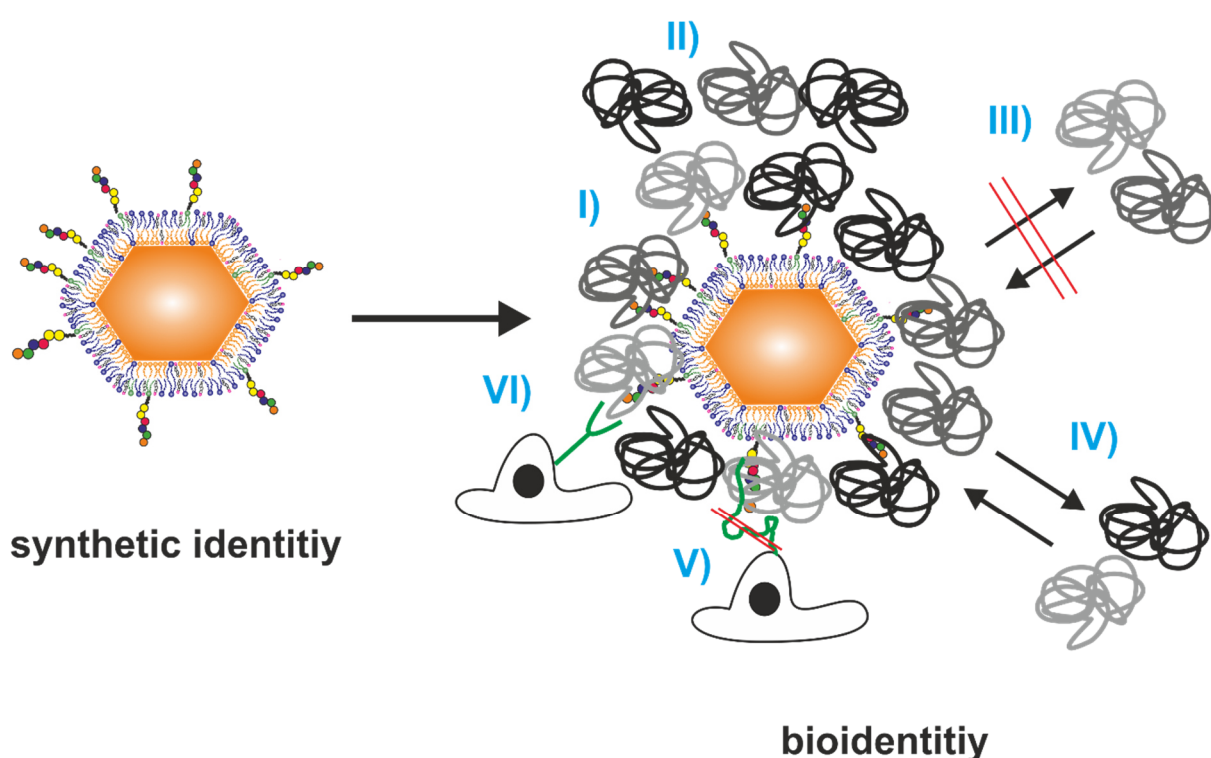
1.3 The Bioidentity of Nanoparticles

There is a variety of engineered (in-)organic nanoparticles for bioapplications with different physical (optical, electronic, and magnetic) and physiochemical properties (composition, size, shape, and surface chemistry). Considering applications in biological cells or organisms, the nanoparticle itself gets less important, but the nature of the surface coating is of paramount importance as it determines the fate of the particle. The surface ligands prevent the particles from aggregation, precipitation, and ensure colloidal stability. The chemical stability of inorganic particles with a non-negligible tendency to dissolve can be enhanced by suitable ligands to slow down or even prevent dissolution. It is rather the particle surface than the particle material the cell recognizes and deals with (Walczyk et al., 2010). Thus, there are many studies on particle internalization and cell viability with focus on the surface ligands of identical particle cores. For example cell viability rises in contact to UCNPs with following surface modifications: bare < polyacrylic acid, polyethylene imine < citrate < polyethylene glycol (Gnach et al., 2015; Tian et al., 2015).

However, it may be not the pristine particle surface dictating the fate of the nanoparticle but the protein corona (Walczyk et al., 2010). The protein corona (PC) is the coating layer around a particle, which is inevitably formed by biomolecules within minutes when the particle comes in contact to biological fluids (Tenzer et al., 2013). As the composition of the coating is not limited to proteins but includes also other biomolecules attaching to the particle, the term biomolecular corona is sometimes used instead (Hadjidemetriou et al., 2017). The unpredictable biotransformation alters the synthetic identity of the particle into its *bioidentity* (**Scheme 1.2**) and can change the functional properties, the pharmacological, and toxicity profile of the particle (Cai et al., 2019). Thus, a deep understanding of the PC is considered as one of the most important keys to minimize the gap between ambitious nanomaterial design and physiological reality to push nanomedicine to clinical translation (Cai et al., 2019).

The PC surrounding a nanoparticle can be described as soft or hard. The hard corona is related to an irreversibly adsorbed protein layer, whereas the soft corona describes a loosely attached

protein layer. The soft corona is highly dynamic and the proteins can be exchanged continuously by other molecules (Latreille et al., 2022). It is also possible that a quickly formed soft corona is converted to an irreversible hard corona after a certain time due to orientational and conformational changes of the attached proteins. Moreover, protein multilayers can be formed around the particle, consisting of an inner hard protein layer and additionally adsorbed protein layers with weaker affinity (Milani et al., 2012). The proteins in the outer layers attach in an organized way and can potentially change their secondary structures (Marichal et al., 2019; Fleischer et al., 2014).



Scheme 1.2. Change of synthetic identity of a nanoparticle with targeting moiety (colored circles) to its bioidentity in biological environment with biomolecule and protein (black, grey) adsorption in (I) monolayers or (II) multilayers of (III) static or (IV) dynamic nature. The protein corona (V) hides the pristine receptor binding moieties of the nanoparticle and (VI) enables recognition by different receptors of various cell types.

Even if the PC dictates the affinity of the particle to the plasma membrane, cell recognition, and internalization kinetics, the composition and characteristics of the PC can be tailored by nanoparticle design. Thus, the fate of the nanoparticles is still somewhat defined by their pristine features since these determine the nature and amount of attaching biomolecules and

proteins. Hydrophobic particles interact with more hydrophobic proteins *via* van der Waals interactions (Saha et al., 2016). The hydrophilic particles will interact with charged proteins by stronger electrostatic attraction. The charge density of the particles tailors the PC thickness as more densely charged NPs have a thicker PC than less charged NPs. Highly positively charged nanoparticles interact strongly with proteins having an isoelectric point at $\text{pH} < 5.5$, whereas highly negatively charged ones prefers interactions with proteins of an isoelectric point at $\text{pH} > 5.5$ (Partikel et al., 2019; Rampado et al., 2020). However, these are just rough trends and proteins have regions of positive and negative charge, enabling loose/strong interactions with different NPs. For example, serum albumin with an isoelectric point of $\text{pH} 4.7$ has 60 lysine groups for attraction to negative charged particles as well (Fleischer et al., 2014; Carter et al., 1994).

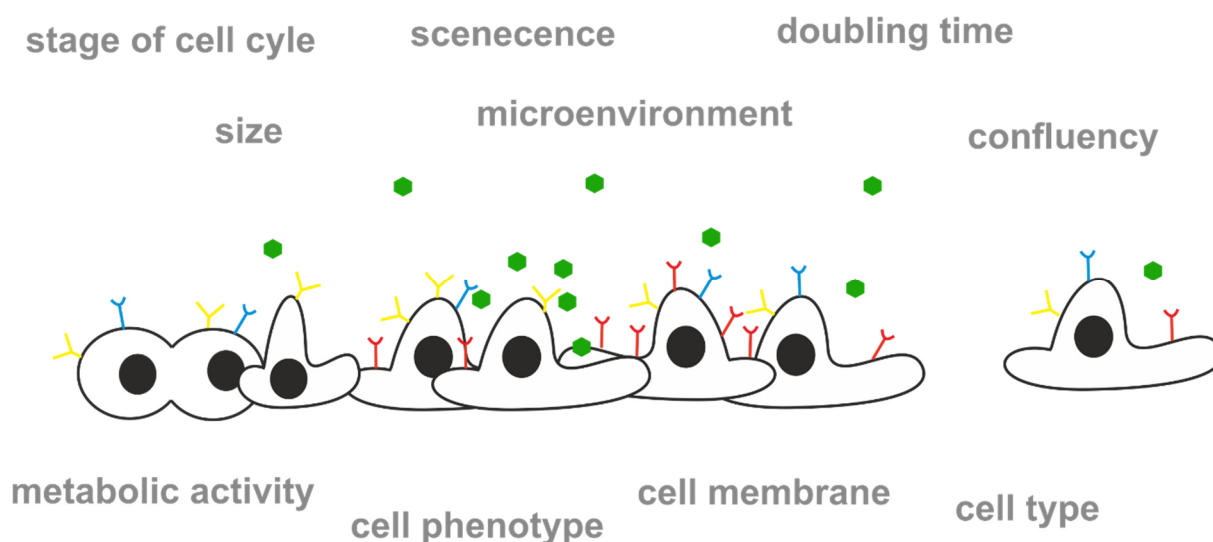
Moreover, the adsorbed protein layers can hide the original targeting moiety of the particle, potentially impairing its targeting capability (Cai et al., 2019). The attached proteins may interact with other surface receptors, which may lead to misinterpretation of the intended, molecularly specific interaction (Shang et al., 2014). This can also lead to fast nanoparticle internalization by phagocytic cells *in vivo* and, hence, to a rapid clearance from the bloodstream before the nanoparticle could become bioactive. Depending on the nanoparticle to protein ratio and the types of attached proteins, the protein corona can increase nanoparticle aggregation. The nanoparticles may tend to aggregate more strongly at low protein concentrations, while high protein concentrations may stabilize the nanoparticles. Inherently sticky proteins as immunoglobulins and fibrinogens, capable of binding to foreign materials, may facilitate particle aggregation. Additionally, these proteins are large and may interact with several particles. Small proteins like serum albumin can cover more efficiently individual particles and, thereby, prevent inter-particle interactions (Rampado et al., 2020).

The understanding of the PC and the hardly predictable impact on the nanoparticle bioidentity has evoked the interest in the design of so-called stealth nanoparticles with a reduced protein corona. The most popular surface modification for the formation of stealth nanoparticles is poly(ethylene glycol) (PEG), which can attract large amounts of water molecules to form a water barrier against attaching proteins (Pombo García et al., 2014). PEG is well-known to limit the formation of PC and uncontrolled internalization to prolong the blood circulation time (Banerjee et al., 2011). The PEG coating has already found its way into clinical studies for

surface modifications of nanoparticles (Yang et al., 2021). However, PEG-coated nanoparticles tend to aggregate under conditions with high-ionic strength and substantially increase the hydrodynamic diameter of the particles, which is adverse for clearance (Pombo García et al., 2014). The optimal number of PEG groups and therefore its chain length has to be identified for each application individually to reduce protein adsorption on the particle and not to hinder their cellular uptake. PEGylated nanoparticles may induce hypersensitivity reactions in humans and trigger an immune response by the formation of anti-PEG antibodies (Ingen-Housz-Oro et al., 2017; Mohamed et al., 2019; Pombo García et al., 2014). These adverse reactivities may cause potential concerns. New promising surface concepts are zwitterionic molecules or polymers, containing positively and negatively charged groups with an overall neutral charge. They have anti-fouling properties due to the highly hydrophilic surface as the water molecules form a well-structured layer. Prominent examples are (poly-)sulfobetaine derivatives or phospholipids like phosphatidylcholine derivatives to imitate cellular membranes (Pombo García et al., 2014; Debayle et al., 2019). There are also approaches to coat particles with entire cell membranes to give the particle the same identity as the membrane-donating cells, hinder their undesired uptake, and elongate blood circulation times. The demand for synthetic and biomimetic strategies remains high to prepare nanoparticles with predictable and controllable biological identity in terms of particle stability, biocompatibility, cellular uptake, and circular lifetime for an improved nanomedicine safety and efficiency (Cai et al., 2019; Hu et al., 2017; Kopac, 2021).

1.4 Cellular Phenotypes Determining Particle Internalization

The evaluation of nanoparticle toxicity requires the detailed analysis of cell-particle interactions. Besides the characteristics of the nanoparticles themselves, the interactions of cells and nanoparticles highly depends on several cellular phenotypes. These define their ability to internalize the particles, to deal with them intracellularly, and whether or not the cell can induce their dissolution (Laurent et al., 2012). The first encounter between the nanomaterial and the cells occurs at the cellular plasma membrane, which is built up by several types of phospholipids, surface proteins, and sugar moieties in a cell type specific composition. The membrane composition affects the available binding sites for nanomaterials, including nature and number of receptors, the membrane properties (surface charge, tension, elasticity, thickness), the cell size, and the direct microenvironment. Together with the metabolic activity of the cells, the cellular response towards the nanomaterial and, hence, the internalization mechanism and kinetics are regulated (Rodríguez-Hernández et al., 2020; Kettler et al., 2014; Behzadi et al., 2017). Large variations of these phenotypes can be found for different cell types (*e.g.*, phagocytic vs non-phagocytic cells, non-transformed vs cancer cells and monocytes vs macrophages (Unfried et al., 2007)), cell lines (Kim et al., 2015), and even in cells of the same origin (Snijder et al., 2009). Additionally, the cell senescence, confluency, doubling time, and stage of cell cycle with particle internalization highest for $G_2/M > S > G_0/G_1$ can affect the internalization capability (Kim et al., 2011). All these parameters regulate the intracellular particle dose the cell has to deal with and contribute eventually to the fate of the nanoparticle (Kim et al., 2011; Foroozandeh et al., 2019; Nehls et al., 2019). Therefore, a comprehensive evaluation of nanomaterial toxicity requires the analysis of many processes influencing the outcome of toxicity assays (**Scheme 1.3**). It is important to communicate these parameters and experimental conditions in publications to enable the correlation of data from various studies using the same cell line and particle design (Faria et al., 2018).

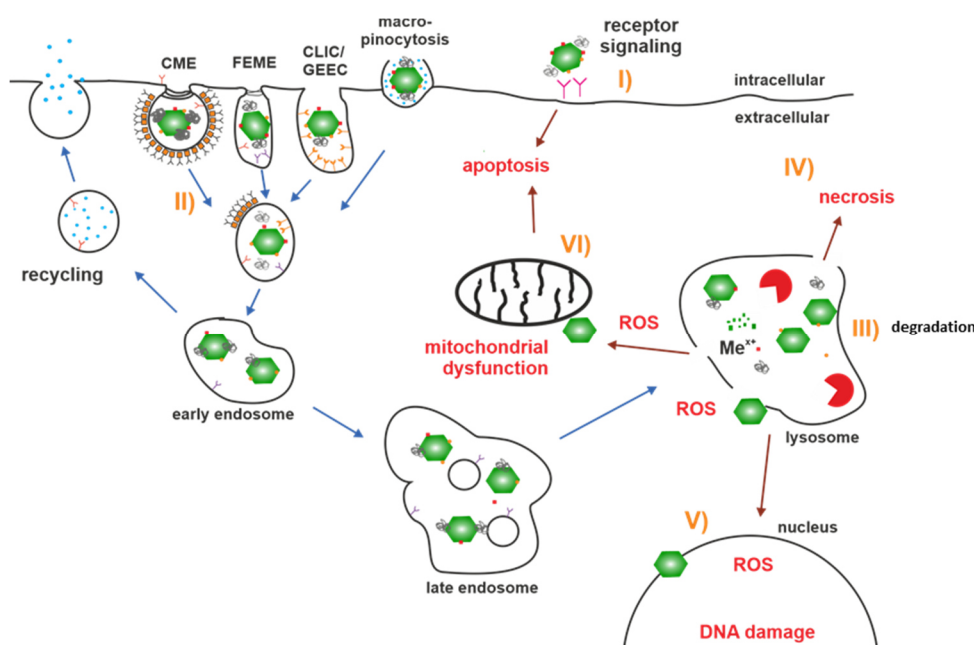


Scheme 1.3. Overview of cell parameters influencing the internalization of the nanoparticles and the experimental outcome.

Among all the tissues in the human body, cancer tissues belong to the most targeted ones in nanomedicine. However, toxicity measurements on cancer cell lines alone are not sufficient to evaluate the toxicity of a given nanomaterial for *in vivo* applications. The results obtained from the transformed cell lines cannot be transferred necessarily to normal cells. The cancer cells may express different amounts of receptors on the cell surface, have an upregulated metabolic activity with short doubling times, and are known to be resilient to cytotoxic effects (Guller et al., 2015; Chang et al., 2007). It is rather required to expand the analysis of internalization, therapeutic performance, and particle procession to cell lines, which are similar to the target cell types *in vivo* and to those, which are in contact to the particles after their administration and involved in particle clearance or biodistribution. For example, after intravenous injection the accumulation of nanoparticles has been reported in liver, spleen, kidney, heart, lung, bone marrow, and brain. Thus, cells from these organs are of interest, which the nanoparticles have to overcome to enter the organs such as the barrier forming and organ lining endothelial and epithelial cells (Bourquin et al., 2018). To date, most experiments on cellular toxicity of upconversion nanoparticles are limited to cancer cell lines (Guller et al., 2015; Gnach et al., 2015) but need to be expanded to normal cell lines of interest to assess their impact on regular cell physiology.

1.5 Interactions of Nanoparticles with Cells: From Extracellular Attraction to Internalization and Toxicity

Nanomedicine has the potential to improve the treatment of many diseases (cf. **Chapter 1.1**). In order to do so, a comprehensive understanding of the cellular uptake mechanisms and the onward processing of the particles within the cells are necessary to estimate their therapeutic activity, delivery efficiency, and get a judgment on their potential translation into *in vivo* studies (Rennick et al., 2021). In this chapter, the nanoparticles and their possible interactions with cells are summarized in the order of occurrence from extracellular attraction to cell death. They are schematically depicted in **Scheme 1.4**.



Scheme 1.4. Overview of nanoparticle-cell-interaction: I) binding to transmembrane receptor with activation of signaling cascades; II) particle internalization by endocytosis pathways (e.g. clathrin-mediated endocytosis (CME), fast endophilin-mediated endocytosis (FEME), clathrin-independent carrier (CLIC) endocytosis /glycosylphosphatidylinositol-anchored protein enriched early endocytic compartment endocytosis (GEEC), or macropinocytosis) and vesicle maturation to early endosomes, late endosomes, and lysosomes or recycling (blue arrows); III) intracellular particle degradation and dissolution in lysosomes to metal ions (Me^{2+}), leading to ROS formation, lysosomal rupture or lysosomal breakdown; released vesicle loading inducing IV) necrosis or V)/VI) stress-dependent signaling pathways including DNA damage, mitochondrial dysfunction, and apoptosis. Scheme drawn according to (Rennick et al., 2021; Shang et al., 2014).

Extracellular Interactions

Interactions of cells with nanomaterials start at the extracellular side of the plasma membrane. These are strongly dependent on the physiochemical properties of the nanomaterials, including size, shape and surface characteristics, and on cell-specific factors as cell type or stage of the cell cycle (Mahmoudi et al., 2012). At first, the nanoparticle gets in contact with the cellular membrane, according to its surface properties (ligand, ligand density, charge) after the formation of a protein corona (cf. **Chapter 1.3**). Mostly, the particles are wrapped by the cellular plasma membrane, internalized *via* different pathways, and induce intracellular interactions. However, the particles can activate also cellular pathways without crossing the cell membrane.

Nanoparticles can initiate indirect toxic responses across cell barriers in cells, that are protected from direct particle encounter by biological barriers like epithelial cell layers. The indirect response is mediated by intercellular communication. For example, DNA damage was induced by 30 nm cobalt-chromium nanoparticles in primary human fibroblast cells, which were cultured below trophoblast or corneal cell barriers. The cell response, leading to the production of oxygen radicals in mitochondria, occurred without translocation of the particles but *via* purine nucleotide second messengers (cAMP, cGMP) and intercellular signaling (Sood et al., 2011).

Nanoparticles interact with membrane receptors and modulate signal transduction pathways. For example, 14 nm carbon nanoparticle activated the epidermal growth factor receptor (EGFR) and β 1-integrins in lung epithelial cells, inducing cell proliferation (Marano et al., 2011). Cell proliferation as response to EGFR stimulation was also observed in Ras-transformed breast epithelial cells with exposure to 9 nm superparamagnetic iron oxide NPs (Rauch et al., 2012).

Internalization

Understanding the internalization routes of particles into cells is required to design particles, capable of mediating the uptake by target pathways of the cells of interest in predefined numbers. Nanoparticle internalization is highly dependent on the cell type and on the physiochemical properties of the particles. Especially the particle size, composition, and mass can tailor the particle attachment to the cellular membrane and their uptake efficiency due to

some contrary factors: I) particle diffusion to cell membrane is slower for larger particles, but II) particle sedimentation is more pronounced for larger particles with a higher mass as demonstrated for AuNPs and SNPs (Cho et al., 2011; Yazdimamaghani et al., 2018); III) membrane-wrapping and ligand-to receptor interactions may be favored for larger particles (Shang et al., 2014); IV) some endocytosis pathways are limited in size of the carrier vesicle (Sousa de Almeida et al., 2021).

The size-dependent endocytosis pathways are still part of ongoing research to correct outdated understandings. All activated pathways have in common that the internalized cargo is guided to early endosomes, from which they are either recycled back to the extracellular side of the cell membrane or they remain in the endosomes and mature to late endosomes and lysosomes. An overview of the main endocytosis pathways is depicted in **Scheme 1.4**. The principal pathways of nanoparticle uptake are the six cell type dependent uptake mechanisms: clathrin-mediated endocytoses (CME, clathrin- and dynamin-dependent), fast endophilin-mediated endocytosis (FEME, clathrin-independent but dynamin-dependent), clathrin-independent carrier (CLIC)/glycosylphosphatidylinositol-anchored protein enriched early endocytic compartment (GEEC) endocytosis (clathrin and dynamin independent), macropinocytosis, and phagocytosis.

The clathrin-mediated pathway occurs in all mammalian cells. Depending on the cell type, the clathrin-coated pits can occupy 1 – 2% of the plasma membrane surface to internalize nutrients as cholesterol in form of low-density lipoproteins (Brown et al., 1999). The clathrin-coated pits have a distinct morphology, which can be easily recognized by electron microscopy. The upper size limit for the cargo of this pathway is the average size of clathrin-coated vesicle of around 100 nm (Ehrlich et al., 2004). However, the clathrin-coated pits may be elongated by actin recruitment for the uptake of larger cargoes (Li et al., 2016).

FEME is known for the extremely rapid internalization (10 s) of transmembrane receptors. Thus, the internalization of the cargo is induced into the tubular shaped carriers upon receptor binding. The maximal size for the cargo is limited to the endocytic carrier size of 80 nm times several hundred nm. The abundance of this pathway is still unknown as it is only recently discovered and not many cell lines have been studied yet (Rennick et al., 2021).

CLIC/GEEC is a constitutive endocytic pathway, identified in many cultured cell lines. It is involved in the uptake of abundant surface proteins, fluids, and membranes. The CLICs mature

into tubular GEECs with dimensions of 100 nm times several hundred nm, which is a similar size as observed for the FEME endocytosis.

Several cell lines use macropinocytosis to internalize soluble molecules and nutrients. It is characterized by the actin-driven membrane ruffles, which enclose large volumes of extracellular medium (Condon et al., 2018). Those membrane ruffles are recycled from the macropinosome to the membrane while the large vesicles shrink. The maximal cargo size depends on the cell type and is >200 nm. Macropinocytosis can be constitutive or induced in many mammalian cells (Lin et al., 2020). Constitutive macropinocytosis levels are often upregulated in cultured cells and can also be stimulated by growth factors in culture medium, making it difficult to translate the cell studies in culture to the target cells *in vivo* (Palm, 2019). Phagocytosis is not discussed here as this uptake mechanism for cargo larger than 500 nm is limited to professional phagocytes (Niedergang et al., 2018), which are not part of this thesis. Caveolae-mediated endocytosis (CVME) must be treated with caution for nanoparticle uptake. CVME has been seen as ubiquitous and molecularly well-defined endocytosis pathway similar to CME. However, the colocalization of overexpressed caveolin was attributed falsely to CVME. Moreover, the role of CVME in nanoparticle uptake is controversial as it shares components with the CLIC/GEEC pathway, which has been discovered only lately. Thus, the repeated assignment of an uptake mechanism as CVME in the past might have been not correctly and has to be reconsidered (Rennick et al., 2021; Rewatkar et al., 2015).

The clear assignment of the uptake route to one mechanism is not always possible as for example, dynamin is involved in different pathways or CLIC/GEEC share components of macropinocytosis. It is also possible that cross talk between pathways occurs or the inhibition of one route can lead to the enhancement of another for compensation. Moreover, the inhibitors used to block one specific uptake pathway may also restrict other ones and need to be chosen carefully. Thus, studies on nanoparticle internalization, which were carried out prior to the understanding of FEME and CLIC/GEEC, need to be treated with caution (Rennick et al., 2021).

The analysis of nanoparticle uptake *in vitro* and its translation to *in vivo* conditions in terms of particle surface properties are rather difficult as the bioidentity of a nanoparticle is not easy to determine or predict. The biomolecular corona around the particle can hide the initial target moiety and the attached biomolecules as folic acid, transferrin, or hyaluronic acid can

stimulate different receptor-mediated pathways (Zhang et al., 2020a). Size-dependent predictions may also be difficult and may lead to misinterpretation as the biological media can cause particle aggregation so that the effective particle size is significantly larger than the one determined in simple buffer solutions. However, the size is less important for particles <100 nm as those may be possibly internalized by all available pathways (Rennick et al., 2021). Even if it seems difficult to analyze nanoparticle internalization correctly, to predict internalization behavior in advance, and to translate the results to other cell lines *in vitro* or *in vivo*, the detailed analysis of internalization pathways and particle numbers with reliable protocols can support the interpretation of potential toxicities and reveal the fate of the biotransformed particles.

Intracellular Interactions

Once the particle crossed the barrier into the cell, it is likely that the particles are decomposed, including adsorbed biomolecules, surface ligands, and particle material (Shang et al., 2014). Especially the acidic conditions in lysosomes can be challenging for many nanomaterials and may alter the characteristics of the particles, which have been determined before their addition to cells. Besides the formation of a protein corona, the particle disintegration process contributes to the term “biotransformation” as well.

It is challenging to predict the biotransformation of the particles from solubility constants as these do not consider the surface and edge effects of differently sized nanoparticles or even large particle agglomerates. The influence of surface modifications is not accessible as well. Moreover, the physiological fluid composition and the potential presence of chelating ions and molecules may also alter saturation concentration and dissolution tendency (Misra et al., 2012; Utembe et al., 2015). However, one can roughly estimate the dissolution tendency of certain nanoparticles even without solubility constants. Metal oxide as well as metal alloy-based particles have a lower degree of stability and tend to dissolve faster in aqueous solution, under acidic conditions, and in biological media than the corresponding metal nanoparticles (Manuja et al., 2021). For example, copper oxide particles dissolved completely at pH 5.5 within three days, while copper nanoparticles of similar size dissolved only by 20% (Studer et al., 2010). However, the complete dissolution of metallic particles, considered as inert for a long time, was also observed during long-term experiments. Degradation of the aggregated

nanoparticles in the lysosomes was reported for example for lipoic acid coated 8 nm silver nanoparticles within 48 h, releasing Ag^+ in the lysosomes of osteogenic cells (RAW 264.7 and Saos-2) and forming secondary nanoparticle structures (Porter et al., 2021). Such a biotransformation was similar for gold nanoparticles. Citrate capped (4 – 22) nm gold nanoparticles were degraded in primary human skin fibroblast cells and recrystallized into biologically stable nanostructures within two weeks (Balfourier et al., 2020). The dissolution of the NaYF_4 -based nanocrystals, typically considered as being very stable, has been observed as well when highly diluted in water and buffers (Lahtinen et al., 2017; Dukhno et al., 2018).

The toxicity of nanomaterials is assessable from the particles themselves or from their degraded products such as released ions (Xia et al., 2008). The released ions may not necessarily indicate toxicity if the former particles are non-toxic or degradation takes place with slow kinetics so that the ions do not accumulate significantly. The detailed toxicity pathway may be dependent on the nature of the particle, but many metal and metal oxide particles have been known to produce reactive oxygen species (ROS) within the cell, triggering various cell responses (Yang et al., 2021). These may include alterations in metabolic activity, morphology and structural changes of the cells (loss of membrane integrity, cell shrinkage/swelling, alteration on cortical F-actin), alterations of critical cell functions (division, differentiation, signal transduction, scavenging ability to ROS, low ATP levels), and disturbance of organelle functioning (mitochondrial dysfunction, uncontrolled Ca^{2+} ion release due to stress to the endoplasmic reticulum, inflammation due to lysosomal rupture) (Liu et al., 2020). If the cells cannot recover from these challenges, the nanoparticles induce cell death as apoptosis, autophagy, or necrosis. The cell death mechanism depends on the chemical nature of the nanoparticles, their concentration, exposure time, and the cell type (Rauch et al., 2013).

Cellular Interactions with UCNPs

The data on the toxicity of NaYF_4 -based UCNPs is not extensive so far and long-time interactions with this nanomaterial have not been under detailed analysis yet. It is possible that UCNPs themselves initiate similar pathways in the cells as other nanomaterials. Up to now, there are already a few studies focusing the cell viability of cells exposed to NaYF_4 -based UCNPs, summarized by Gnach and coworker in a review article (Gnach et al., 2015). These

studies focus mainly on the acute toxicity and the results were not put into context with other cell indices or with the biotransformation of those particles (Oliveira et al., 2019). Moreover, cancer cells were often the cell type of interest so that the obtained information cannot be easily adapted to normal cells. The studies claim little to no toxicity of UCNPs *in vitro* and also in some *in vivo* experiments. However, a few studies already exist, claiming their toxic effect on cells is due to their degradation behavior in cell-free experiments (Mendez-Gonzalez et al., 2022; Lisjak et al., 2021; Saleh et al., 2020; Lahtinen et al., 2017). Single studies give first hints that NaYF₄-based UCNPs are indeed toxic to cells, which is assigned to the biotransformation of the particles in human endothelial cells (EA.hy926), epithelial cancer cells (Hep G2), or human myeloid cell line (THP-1) (Lisjak et al., 2021; Li et al., 2015; Wang et al., 2020). Disruption of mitochondrial homeostasis with ROS formation, inducing apoptosis, was observed and for poly(acrylic acid) or poly(ethylene imine) coated 35 nm NaYF₄(Yb,Er) in HepG2 cells (Wang et al., 2020). ATP deprivation was correlated to apoptosis for 30 nm bare NaYF₄(Yb,Er) in epithelial cancer cells (HeLa, (Tian et al., 2015)). Oleate capped NaYF₄(Yb,Er) induced an inflammation response in THP-1 cells upon biotransformation (Li et al., 2015). These data give a first idea on possible cellular toxicity pathways but do not allow to comment on the general toxicity of UCNPs at present stage.

1.6 G Protein-Coupled Receptors: Structure, Function, and Signal Transduction

The G protein-coupled receptors (GPCRs) are the largest family of cell-surface receptors and regulate many cellular functions and cell-specific responses in diverse signaling mechanisms to maintain cellular homeostasis and to ensure coordinated cellular activity. Their dysfunction contributes to several diseases as allergies, diabetes, asthma, some forms of cancer, or cardiac malfunctions, among others. Hence, they have become a very attractive target for therapy. Already 15% of the around 800 human GPCRs are targeted so far by around 35% of all FDA-approved drugs. The potential for drug discovery is enormous (Insel et al., 2019).

Despite the variety of ligands for GPCRs (ions, peptides, proteins, lipids, photons, and biogenic amines), GPCRs share the same structural properties for a classical way of functioning, including agonist binding, activation of G-proteins, and the modulation of downstream effector proteins. GPCRs have seven hydrophobic transmembrane segments (TM1-TM7) with high homology, which are connected by alternating extracellular (ECL1-ECL3) and intracellular loops (ICL1-ICL3). The N-terminus and the ECLs modulate the access of the ligand to the binding site. The TM regions are responsible for ligand binding and the transduction of the information to the ICLs by conformational changes. Upon the extracellular signal, the ICLs can interact with the intracellular signaling proteins. The interconnecting hydrophilic loop regions are divergent for the detection of a wide spectrum of extracellular signals and individual combinations of signal transduction activities (Koivula et al., 1975; Rosenbaum et al., 2009; Venkatakrishnan et al., 2013).

The G proteins are heterotrimeric proteins with an α , β , and γ subunit. The α subunit has a GTPase activity with a binding site for GDP/GTP. It has 16 different isoforms, making up four subfamilies, and defines the primary effector protein, which is targeted and (de-)activated for the onward signaling cascade. The subfamily $G\alpha_s$ activates canonically the adenylate cyclase (AC), generating cyclic AMP (cAMP), while $G\alpha_i$ inhibits the adenylate cyclase. $G\alpha_q$ activates phospholipase C, converting phosphatidylinositol to inositol-triphosphate (IP_3) and triggering the release of Ca^{2+} ions into the cytoplasm. $G\alpha_{12/13}$ stimulates the RhoA protein, which is involved in cytoskeletal regulations and cell cycle progression. The β subunit forms a complex with the γ subunit and modulates as $\beta\gamma$ heterodimer the activity of some effectors. The five different $G\beta$ homologs are responsible for the effector binding, while the eleven different $G\gamma$

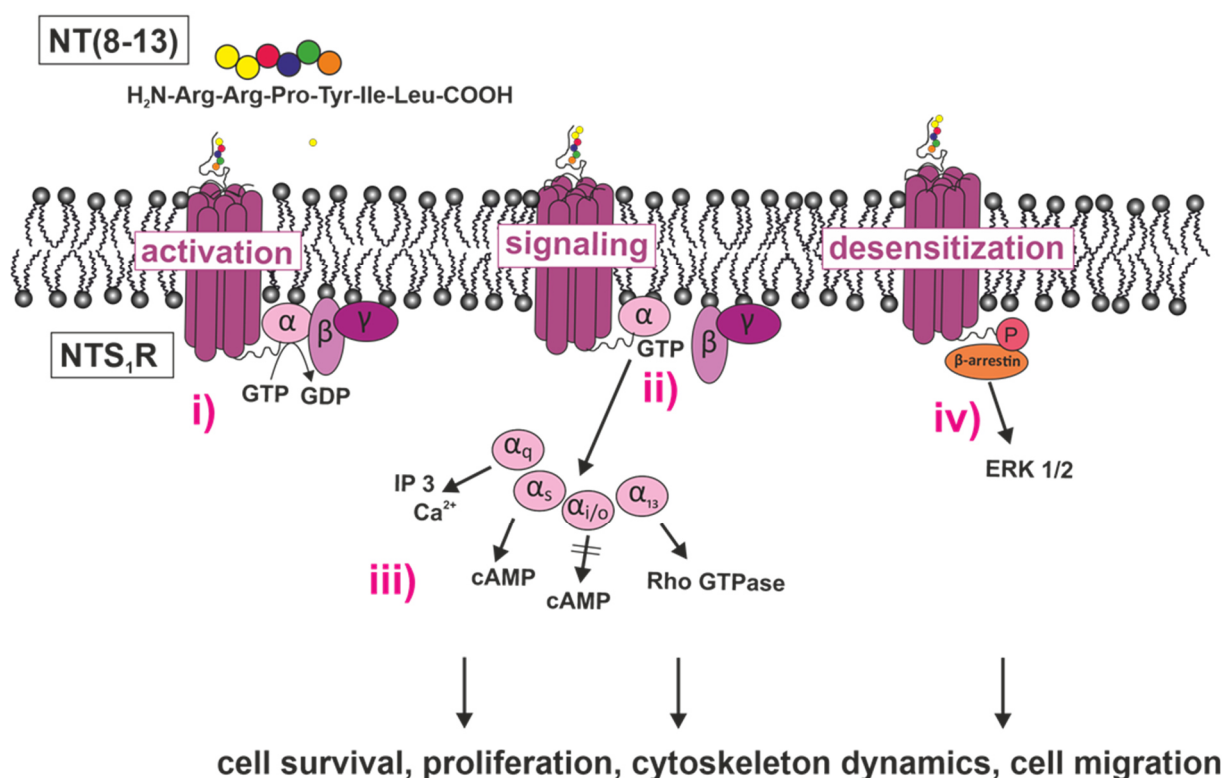
homologs interact with the receptors *via* their C-terminus (Downes et al., 1999). Thus, dependent on the isoform of the G-protein coupled to the GPCR, the extracellular signal triggers a specific intracellular signaling cascade as cellular response.

The activation of a GPCR can also lead to its phosphorylation by a GPCR-coupled kinase (GRK), which triggers the dissociation of the G-protein and the binding of the inhibitory protein β -arrestin 1/2. These proteins are signaling and regulator proteins, which activate extracellular signal-regulated kinases (ERK) and promote the internalization of the receptor by clathrin-mediated endocytosis. They are involved in the receptor desensitization and recycling process (Freedman et al., 1996).

The interactions of all these proteins in the signal transduction of G protein-coupled receptors is demonstrated with the main signaling pathways of the model GPCR used in this thesis, the human neurotensin 1 receptor (hNTS₁R). hNTS₁R is endogenously activated by the peptides neuromedin N (NN) and neurotensin (NT) with its minimal bioactive fragment NT(8-13) (Besserer-Offroy et al., 2017; Furuta et al., 1984). The neurotensin and the hNTS₁R regulate several physiological processes as blood pressure, hypothermia, or functions of the gastrointestinal tract and are linked to the development and progression of digestive cancer and other cancer types (Ouyang et al., 2017). Their signaling pathways have been well-studied for different cell types as HT-29, N1E-115, or NTS₁R-transfected cell models.

The stimulation of the signaling cascade upon activation of the hNTS₁ receptor by NT(8-13) is shown in **Scheme 1.5**. The activation of the hNTS₁R by the binding of an agonist i) enables the exchange of GDP by GTP at the α subunit of the G protein, which is followed by the ii) dissociation of the G protein from the receptor and its separation into the $G\alpha$ and $G\beta\gamma$ subunits. The hNTS₁R is coupled to $G\alpha_s$, $G\alpha_{q/11}$, $G\alpha_{i/o}$ and $G\alpha_{13}$ and, hence, iii) stimulates the corresponding signaling pathways. The receptor is preferentially coupled to $G\alpha_s$ over $G\alpha_{i/o}$ to hNTS₁R, promoting the activation of AC and the production of cAMP. The engagement of $G\alpha_q$ is associated with the production of IP₃ by the phospholipase C and the release of Ca²⁺ into the cytoplasm. NTS₁R is also reported to bind $G\alpha_{13}$ -containing G proteins, which contribute to the activation of Rho GTPases and, thereby, cytoskeletal rearrangements as well as formations of stress fibers. iv) Activated hNTS₁R may be phosphorylated by GRKs and recruit β -arrestin 1/2. This leads to desensitization and/or ERK1/2 activation, which is finally followed by the agonist-stimulated NTS₁R internalization in a clathrin- and dynamin-dependent pathway. Each

of these activated pathways further stimulates downstream effector proteins and transcription factors, participating in gene transcription for cell survival, proliferation, cytoskeleton dynamics, and cell migration (Turner et al., 1990; Besserer-Offroy et al., 2017; Christou et al., 2020; Wu et al., 2012; Pierce et al., 2001; Yin et al., 2019).



Scheme 1.5. Canonical signaling pathways of the model GPCR hNTS₁R upon stimulation with the peptidyl agonist NT(8-13): i) binding of the ligand activates the receptor by the exchange of GDP by GTP; ii) dissociation of Gα and Gβγ subunits; iii) activation of Gα_{q/11}, Gα_s, Gα_{i/o} and Gα₁₃-coupled signaling pathways and the downstream effectors and second messengers inositol-triphosphate (IP₃), intracellular Ca²⁺ levels, cyclic AMP (cAMP) and the Rho GTPases; iv) phosphorylation of the hNTS₁R and the recruitment of β-arrestin 1/2 for desensitization and activation of extracellular signal-regulated kinases (ERK 1/2) with receptor regeneration. The stimulation of these pathways is correlated to cell survival, proliferation, cytoskeleton dynamics, and cell migration.

The simultaneous stimulation of many pathways by a ligand or drug often comes with many side effects. These can be reduced by creating biased ligands, which selectively trigger one GPCR pathway rather than a mixture. Thus, the GPCR research focuses on the discovery of drugs with functional selectivity. An example for this is the molecule ML314, a β-arrestin-biased NTS₁R agonist (Barak et al., 2016; Rankovic et al., 2016).

(Ant-)agonists against GPCRs, which are recycled *via* internalization, can be used as entrance for precisely controlled receptor-mediated particle internalization into specific cell models. As the GPCR ligands are available in a high number on the nanoparticle surface, multiple binding of the nanoparticle to the cell is possible. This principle of multivalency, the dramatically enhanced interaction due to multiple binding events, is well-known from the interactions of a virus with its host cell and is highly attractive for the development of new drug concepts with reduced required doses. Multivalent architecture is obtained by attaching ligands in a defined distance to polymers (synthetic or biological) or by functionalizing nanocarriers as dendrimers, micelles, or inorganic nanoparticles with many ligands. Especially the inorganic nanoparticles convince as multivalent ligand carriers since they can be prepared precisely in a desired size and the additional properties of the particles core (fluorescence or magnetism) can be used to design multimodal tools for theranostics or the analysis of binding events and receptor stimulation (Fedoryshin et al., 2014; Bakshi et al., 2022). For example, membrane mimetic lipid nanodiscs were shown to be a suitable platform to study structural and biophysical characteristics of GPCRs in lipid environments (Lavington et al., 2020). Quantum dots turned out to be an effective bioimaging tool to analyze the role of endosomal trafficking in serotonin-signaling pathways (Fichter et al., 2010). Evidence on the endosomal signaling of an opioid receptor could be given by nanoparticles with an encapsulated agonist (Jimenez-Vargas et al., 2020).

Especially when applying multivalent nanocarriers in drug development, there is a high need of establishing a well-functioning multivalent nanodevice platform with particles, which are easy-to-functionalize, well-dispersed, biocompatible, and which can be easily adapted to various ligand-receptor-systems. To do so, it is important to be aware of possibly changing binding events or stimulation and the particle fate after binding when going from native ligands to modified or to particle-attached ligands. It remains challenging to identify the optimal multivalent particle design, maintaining the intrinsic affinity and stimulation of the monovalent ligand, in terms of particle properties (size and shape), linker properties (molecular structure, functional groups, size, flexibility, ligand density, ligand mobility), and ligand properties (Bakshi et al., 2022).

2 Objectives

In recent years the lanthanide doped upconversion nanoparticles (UCNPs) have attracted many researchers across scientific disciplines due to their unique ability to convert near-infrared light into higher energy visible light. A lot of effort was dedicated to the improvement of synthesis protocols to obtain reproducibly monodisperse particles with well-defined size, emissions, and brightness. The substantiated synthesis knowhow paved the way for UCNPs into various *in vivo* studies. However, critical voices have raised concerns in the last years, claiming the degradation of the nanoparticles, which had been considered as chemically stable for a long time. So far, only little is known about the impact of this relatively new class of nanomaterials and the their degradation products on cells and organisms (Liang et al., 2020; Gnach et al., 2015; Wen et al., 2018; Torresan et al., 2021; Haase et al., 2011).

It was the aim of this thesis to go one step back and evaluate the interactions of cells and UCNPs in detail to be able to produce safer nanoparticles for nanomedicine. Studies were focused on the importance of the surface characteristics for safe UCNPs. This should be examined under different aspects in the five main chapters of this thesis:

- I) the design of surface protected UCNPs;
- II) the influence of surface protections on the toxicity of UCNPs;
- III) the evaluation of a comprehensive toxicity profile of poorly shielded UCNPs;
- IV) their capability as drug carrier for photodynamic therapy;
- V) their suitability as tool for the study of G protein-coupled receptors.

Therefore, the nanoparticles should be modified with a primary ligand layer, protecting the particles against colloidal instability and poor brightness in biological media. The surface ligands should be suitable for functionalization with biomolecules while maintaining the particle stability. After characterizing the UCNPs in detail, the impact of the surface properties on their overall biocompatibility should be analyzed *in vitro*. For this purpose, normal epithelial cells should be chosen as model cell line. Several techniques, monitoring cell physiology from different perspectives, should be applied to figure out the fate of these nanoparticles in contact to cells. Another objective was to examine the potential of UCNP-

attached ligands to efficiently transport molecules of interest into the cells. Finally, safer UCNPs functionalized with agonistic ligands for GPCRs should be prepared to study binding of the particle to the target receptor, its agonistic potency, stimulating efficiency, and receptor-mediated internalization of UCNPs.

3 Material and Methods

A detailed list of the chemicals and consumables used in this work is given in the Appendix.

3.1 Particle Preparation and Characterization

Small and medium sized upconversion particles (UCNPs) of core or core-shell architecture were synthesized with a NaYF₄ host lattice, Yb³⁺ as sensitizer ion, and activator ions Tm³⁺ or Er³⁺. The particles were further coated with polyacrylic acid (PAA), lysine (Lys), amphiphilic polymer (AP), or phospholipid membrane (PLM) and functionalized with rose bengal (RB) or a neurotensin derivative (NT(8-13)) for their application in different studies. An overview of all particles is given in Table 3.1 and described in the following section.

Table 3.1. Overview of upconversion nanoparticles including diameter, particle architecture, composition, surface modification and functionalization, and the chapter in which these particles have been discussed and described in detail.

diameter	architecture	composition	surface coating	chapter
12 nm	core-shell	NaYF ₄ (20%Yb,2%Er)@NaYF ₄	PAA, AP, PLM	4
12 nm	core-shell	NaYF ₄ (25%Yb,0.3%Tm)@NaYF ₄	PAA, AP, PLM	4
15 nm	core-shell	NaYF ₄ (20%Yb,2%Er)@NaYF ₄	PLM, AP-RB	4, 5, 7
25 nm	core	NaYF ₄ (20%Yb,2%Er)	AP	6
24 nm	core-shell ^(AS)	NaYbF ₄ (20%Er)@NaYF ₄	AP, AP-RB, PLM-RB, Lys-RB	7
33 nm	core-shell	NaYF ₄ (20%Yb,2%Er)@NaYF ₄	AP, PLM, PLM-NT(8-13)	5, 8

^(AS) particles were obtained from Alexandra Schroter (Schroter et al., 2022)

3.1.1 Particle Syntheses

Precursor Rare Earth Oleates

Rare earth oleates (RE-OA) were used as precursor in some UCNPs syntheses. They were prepared from the RE chlorides in the desired RE ratio for the particles according to a protocol by Park *et al.* (Park et al., 2004). The RE chlorides RECl₃·H₂O (30 mmol) were dissolved in H₂O (39 mL) before EtOH (60 mL) and hexane (105 mL) were added to dissolve sodium oleate (Na-OA, 30 mmol). After refluxing under rigorous stirring at 60 °C overnight, the reaction mixture was cooled to room temperature. The upper phase was evaporated under vacuum to obtain the RE OA. The waxy product was stored at -20 °C.

The following RE chloride were used to prepare the RE OA: Y-OA ($\text{YCl}_3 \cdot \text{H}_2\text{O}$ (100%)), Y/Yb/Er-OA ($\text{YCl}_3 \cdot \text{H}_2\text{O}$ (78%), $\text{YbCl}_3 \cdot \text{H}_2\text{O}$ (20%) and $\text{ErCl}_3 \cdot \text{H}_2\text{O}$ (2%)), and Y/Yb/Tm-OA ($\text{YCl}_3 \cdot \text{H}_2\text{O}$ (74.7%), $\text{YbCl}_3 \cdot \text{H}_2\text{O}$ (25%) and $\text{TmCl}_3 \cdot \text{H}_2\text{O}$ (0.3%)).

Shell Precursor Particles $\alpha\text{-NaYF}_4$

Cubic shell precursor particles $\alpha\text{-NaYF}_4$ were prepared from the yttrium oleate. Y-OA (20 mmol) and sodium oleate (40 mmol) were dissolved in oleic acid (200 mL) and octadecene (200 mL). The reaction mixture was heated under nitrogen atmosphere to 100 °C and degassed under vacuum at 100 °C for 1 h. After the addition of NH_4F (100 mmol) under N_2 atmosphere, it was heated to 200 °C for 1 h. Cooled to room temperature, the nanoparticles were precipitated with ethanol (cyclohexane/EtOH ~1:5, v/v) and collected by centrifugation (3,000 g, 5 min). After two washing steps with cyclohexane/ethanol (~1:10, v/v), the pure shell material $\alpha\text{-NaYF}_4$ was dispersed in cyclohexane.

Small Core Particles $\beta\text{-NaYF}_4(20\%\text{Yb}, 2\%\text{Er})$

Hexagonal upconversion nanoparticles $\beta\text{-NaYF}_4(20\%\text{Yb}, 2\%\text{Er})$ with small diameters were synthesized from the RE-OA in high boiling solvents oleic acid and octadecene (1:1). Therefore, a high Na-OA to RE-OA ratio was used according to a protocol by Haase *et al.* (Rinkel et al., 2014). Y/Yb/Er-OA (10 mmol, 78% Y^{3+} , 20% Yb^{3+} and 2% Er^{3+}) and sodium oleate (80 mmol) were dissolved in octadecene (120 mL) and oleic acid (120 mL). After heating the reaction mixture to 100 °C under N_2 atmosphere, it was evaporated for 1 h and a clear solution was obtained. NH_4F (110 mmol) was added before degassing the mixture three times. It was heated to 300 – 325 °C ($16\text{ }^\circ\text{C} \cdot \text{min}^{-1}$) for 30 min before cooling to room temperature. The suspension was centrifuged (1,000 g, 3 min). The obtained pellet was washed with cyclohexane and centrifuged again. The nanoparticles precipitated from the supernatant by adding ethanol (cyclohexane/EtOH ~1:5, v/v) and were collected by centrifugation (3000 g, 5 min). Two washing steps were performed with cyclohexane/ethanol (~1:10, v/v). Finally, the pure $\beta\text{-NaYF}_4(20\%\text{Yb}, 2\%\text{Er})$ were redispersed in cyclohexane and aggregates were removed by centrifugation (3,000 g, 5 min).

Small Core Particles β -NaYF₄(25%Yb,0.3%Tm)

Hexagonal β -NaYF₄(25%Yb,0.3%Tm) were synthesized according to the procedure for NaYF₄(Yb,Er) from the Y/Yb/Tm-OA (74.7% Y³⁺, 25% Yb³⁺ and 0.3% Tm³⁺).

Medium Core Particles β -NaYF₄(20%Yb,2%Er)

Hexagonal β -NaYF₄ nanoparticles doped with 20% Yb³⁺ and 2% Er³⁺ were synthesized with the RE chlorides according to literature (Li et al., 2008). The salts of YCl₃·6H₂O (0.78 mmol), YbCl₃·6H₂O (0.2 mmol) and ErCl₃·6H₂O (0.02 mmol) were dissolved in methanol (3 mL) and oleic acid (8 mL) as well as 1-octadecene (15 mL) was added under N₂ flow. The mixture was heated to 160 °C and vacuum was applied for 30 min. Afterwards, the reaction mixture was cooled to room temperature to add NH₄F (4 mmol) and NaOH (2.5 mmol) in methanol (5 mL). The suspension was kept at 120 °C under N₂ flow for 30 min and heated to reflux (320 °C) with a heat rate of 16 °C·min⁻¹ for 25 min. When the solution was cooled to room temperature, ethanol was added (cyclohexane/EtOH ~1:10, v/v) to precipitate the UCNPs. They were collected *via* centrifugation (2,000 g, 5 min) and the obtained pellet was redispersed in cyclohexane. The upconversion nanoparticles were washed three times with cyclohexane/ethanol (~1:10, v/v) until a clear supernatant was obtained. After the final redispersion of UCNPs in cyclohexane (10 mL), aggregates were removed by centrifugation (3,000 g, 5 min).

Small Core-Shell Nanoparticles

Hexagonal core-shell nanoparticles β -NaYF₄(Yb,Er)@NaYF₄ or β -NaYF₄(Yb,Tm)@NaYF₄ with 1 nm thick shell were synthesized using 8.4 nm hexagonal core β -NaYF₄(Yb,Er) or β -NaYF₄(Yb,Tm) and α -cubic shell precursor NaYF₄ in a ratio of 5:4. Core particles (2 mmol) and shell precursor particles (1.6 mmol) were dissolved separately in 1-octadecene and oleic acid (each 5 mL per 1 mmol particles). Both solutions were heated to 125 °C under nitrogen, followed by evaporation at 125 °C for 15 min. The β -UCNPs were combined with 2 mL of shell precursor material under nitrogen atmosphere and heated to 325 °C (heat rate 16 °C·min⁻¹) while the residual α -UCNPs were kept at 125 °C. α -UCNPs were injected to the β -UCNPs in small portions every 5 min so that the temperature did not fall below 300 °C. After the final addition the solution was refluxed for 5 min before cooling to room temperature. The

purification of the oleate coated core-shell particles UCNPs@OA was done in the same way as described in the synthesis of small core particles.

Core-shell particles UCNPs@OA with 10 nm cores and 2.5 nm thick shell were obtained with this procedure using core particles NaYF₄(Yb,Er) and cubic precursor particles NaYF₄ in a ratio of 1:1.6.

Medium Core-Shell Nanoparticles

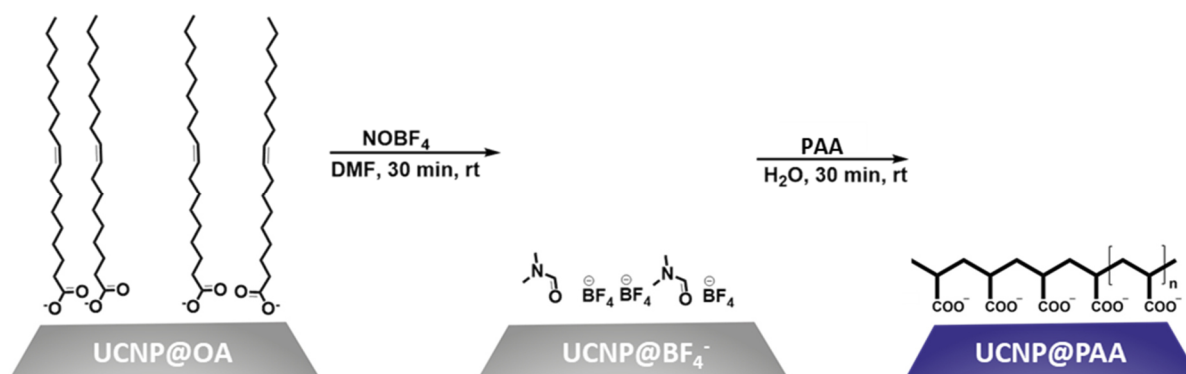
The core-shell synthesis for medium UCNPs@OA was carried out with ~25 nm cores β -NaYF₄(Yb,Er) according to the protocol above, except that the ratio of precursor NaYF₄/ core NaYF₄ (Yb,Er) for a 3 nm shell was 1:0.75 and the time between the stepwise injections of precursor NaYF₄ to core UCNPs was 10 min.

3.1.2 Surface Modifications

Surface Modification with Poly(Acrylic Acid)

The 12 nm UCNPs@PAA were prepared by ligand exchange in a two-step process from the UCNPs@OA with poly(acrylic acid) (PAA) using nitrosyl tetrafluoroborate (NOBF₄) (**Scheme 3.1**, (Dong et al., 2011)). At first, dimethylformamid (DMF, 3 mL) and oleate coated UCNPs NaYF₄:Yb,Er@NaYF₄ (200 mg in 3 mL cyclohexane) were mixed and stirred at 30 °C. After 10 min NOBF₄ was added in excess (500 mg) and stirred for another 20 min. The oleate free particles in the DMF phase were precipitated by the addition of chloroform (DMF/CHCl₃ ~1:10, v/v) and collected *via* centrifugation (1,000 g, 5 min). The nanoparticles were washed once by dispersing in DMF and precipitating with CHCl₃. After centrifugation (1,000 g, 5 min) the BF₄⁻ and DMF stabilized UCNPs were finally dispersed in DMF and aggregates were removed by centrifugation (1,000 g, 5 min).

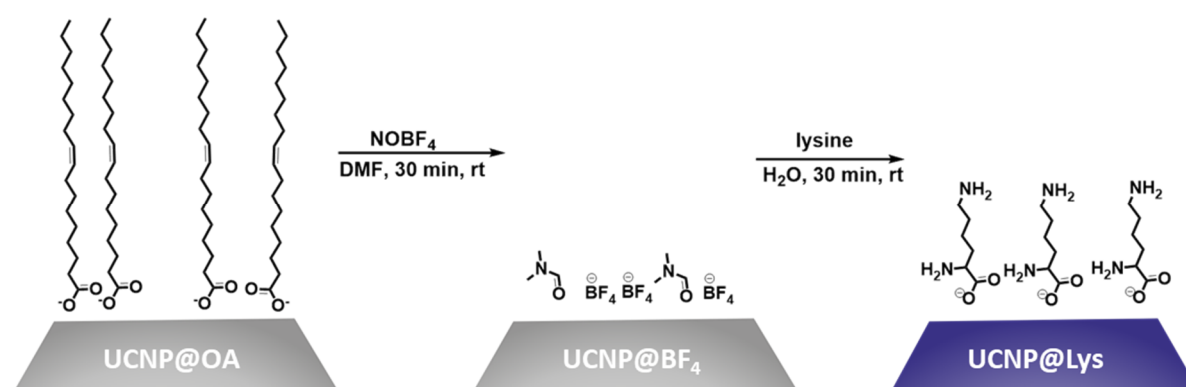
The BF₄⁻ was substituted with the ligand PAA. Thus, PAA (20 mg, M_w~2,100 kDa) was dissolved (10 mL, HEPES (10 mM, pH 7.4)) and stirred at room temperature (rt) for 10 min. UCNPs@BF₄ (100 mg in DMF) were added slowly and the clear mixture was stirred at rt for 20 min. The UCNPs were collected by repeated centrifugation steps (21,000 g, at least 2 h). The UCNPs pellet was purified twice by dispersing in water or HEPES, followed by centrifugation (21,000 g, 2 h). Finally, the UCNPs@PAA were dispersed in water or HEPES and aggregates were removed (5,000 g, 5 min).



Scheme 3.1. Monolayer surface modification of UCNPs@OA to prepare UCNPs@PAA in a two-step approach *via* ligand exchange with 1) NOBF_4 in DMF and 2) the poly(acrylic acid) in H_2O .

Surface Modification with Lysine

Lysine (Lys) coated nanoparticles UCNPs@Lys were prepared analogously to the PAA coating in a two-step approach from UCNPs@OA *via* UCNPs@ BF_4 (**Scheme 3.2**), using 1 mg lysine per 10 mg 24 nm UCNPs.



Scheme 3.2. Monolayer surface modification of UCNPs@OA to prepare UCNPs@Lys in a two-step approach *via* ligand exchange with 1) NOBF_4 in DMF and 2) the lysine in H_2O .

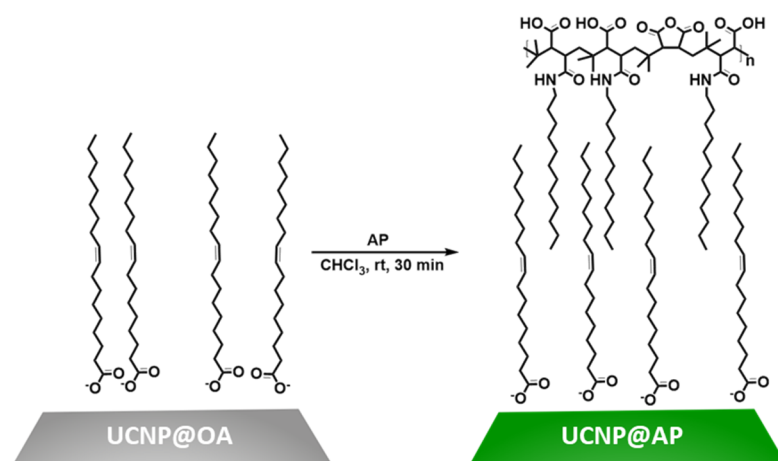
Surface Modification with an Amphiphilic Polymer

The 12 nm UCNPs@OA were coated with an amphiphilic polymer (AP) to form a bilayer with oleate as inner leaflet according to **Scheme 3.3** (Lin et al., 2008). Firstly, the amphiphilic polymer was prepared by attaching dodecylamine side chains (15 mmol) to 75% of the anhydride groups of poly(isobutyl-maleic anhydride) (PIBMAD, $\sim 6,000 \text{ g}\cdot\text{mol}^{-1}$, 20 mmol). Both reactants were dissolved in tetrahydrofuran (100 mL) and heated to 60°C for 2 h before the reaction mixture was concentrated to 25 mL and heated under reflux conditions at 75°C for 15 h. After

solvent evaporation the amphiphilic polymer was dissolved in CHCl_3 (40 mL), yielding in a monomer concentration of 0.5 M.

The UCNPs@OA (200 mg) were dried and dispersed in CHCl_3 (3 mL) before AP (0.5 M in CHCl_3 , 16 mL) was added. The dispersion was stirred at rt for 30 min and the solvent was removed under vacuum. The particles were dispersed in NaOH (0.2 M, 20 mL) and sonicated for 30 min. The UCNPs were washed by repeated centrifugation (21,000 g, 2 h) and redispersion in double distilled water. After three washing steps the UCNPs@AP were finally dispersed in double distilled water and centrifuged to remove aggregates (5,000 g, 5 min).

The 25 nm and 33 nm UCNPs@AP were prepared analogously using 0.75 mL AP (0.5 M, CHCl_3) to coat 25 mg UCNPs@OA.

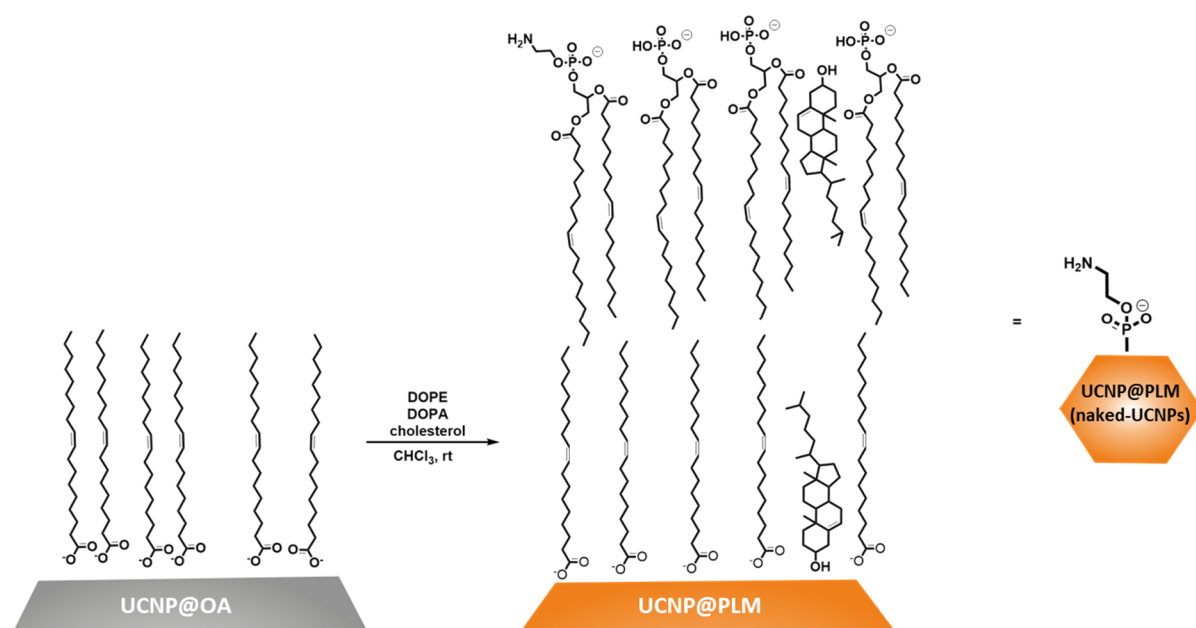


Scheme 3.3. Bilayer surface modification of UCNPs@OA with an amphiphilic polymer (AP) to obtain UCNPs@AP. One repeat unit n is shown.

Surface Modification with a Phospholipid Membrane

12 – 33 nm UCNPs were incubated with a phospholipid mixture to form a bilayer together with the oleate, which had been already attached to the particle (**Scheme 3.4**, (Rojas-Gutierrez et al., 2016)). The oleate coated UCNPs (2 mg) dissolved in cyclohexane were dried and dispersed in CHCl_3 (1.5 mL). The lipid mixture (29 μmol , 64% DOPA, 7% DOPE, 29% cholesterol, in 1.5 mL CHCl_3) was added and the clear solution was sonicated for 10 min. Afterwards the solution was kept under vacuum for 10 min to obtain a nanoparticle-lipid film at the surface of the reaction vassel. The film was dispersed in CHCl_3 (1.5 mL), sonicated, and evaporated two more times. After the final evaporating step, the lipid film was further dried under vacuum for 12 h to remove residual solvent traces. The film was hydrated in HEPES buffer (10 mM, pH 7.4)

under rigorous stirring at 70 °C for 1 h and sonicated heavily for 20 min. The precipitated unmodified UCNPs were separated from UCNPs@PLM by centrifugation (3,000 g, 5 min). The modified UCNPs from the supernatant were filtered with a 220 nm poly(ether sulfone) (PES)-filter and purified by several centrifugation/redispersion steps in water (21,000 g, 2 h). Finally, particles were redispersed in water and aggregates removed by centrifugation (3,000 g, 5 min).



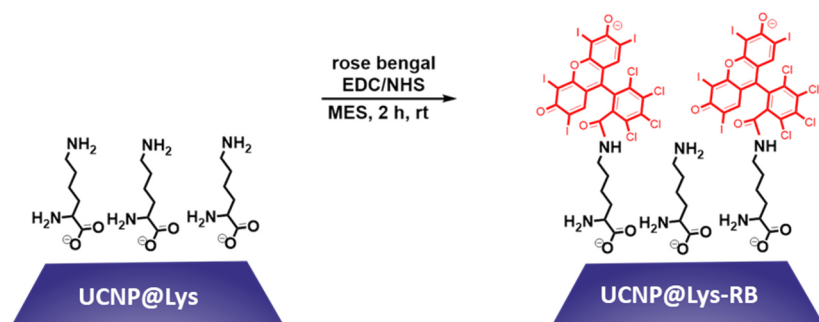
Scheme 3.4. Bilayer surface modification of UCNPs@OA with the lipids DOPA, DOPE and cholesterol for particles with a phospholipid membrane coating (UCNPs@PLM). The UCNPs@PLM served as starting particles for surface functionalization with a neurotensin derivative and are referred as naked-UCNPs in this chapter and in Chapter 8.

3.1.3 Surface Functionalization

Surface Functionalization of UCNPs@Lys with Rose Bengal

24 nm $\text{NaYF}_4(20\%\text{Yb}, 2\%\text{Er})@\text{NaYF}_4@\text{Lys}$ were used to attach the photosensitizer rose bengal directly on the free amine groups of lysine to the particles *via* 1-ethyl-3-(3-dimethylaminopropyl)carbodiimide and N-hydroxysuccinimide (EDC/NHS) chemistry (**Scheme 3.5**). The carboxy group of rose bengal (0.45 μmol) was activated with EDC (4 μmol) and NHS (5.5 μmol) in MES buffer (0.3 mL, 50 mM, pH 5.5) by stirring at rt for 2 h. UCNPs@Lys (0.5 mg, H_2O) were added and stirred at rt for 2 h. The UCNPs@Lys-RB in the supernatant were purified by several centrifugation/redispersing steps in water at 21,000 g for 1–2 h until the

supernatant was clear. Finally, the pink UCNPs@Lys-RB pellet was redispersed in water (0.5 mL) and centrifuged at 3,000 g for 5 min to remove aggregated particles.



Scheme 3.5. Surface functionalization of UCNPs@Lys with the photosensitizer rose bengal *via* EDC/NHS activation to UCNPs@Lys-RB.

Surface Functionalization of UCNPs@AP with Rose-Bengal

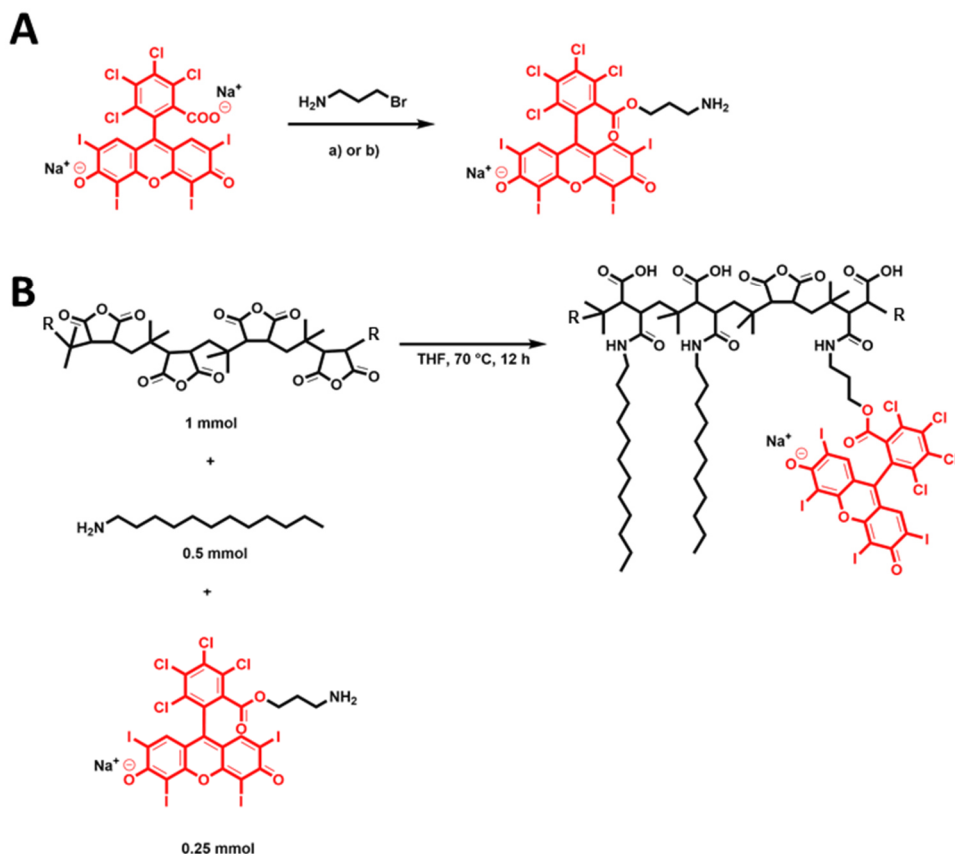
Rose bengal was attached to the amphiphilic polymer (AP) prior to particle decoration to obtain a rose bengal functionalized amphiphilic polymer (AP-RB) for directly coating of the 24 nm NaYbF₄(20%Er)@NaYF₄@OA or 15 nm NaYF₄(20%Yb,2%Er)@NaYF₄@OA.

To prepare AP-RB an aminated rose bengal was required. This was obtained *via* a substitution reaction of the bromide of 3-bromopropylamine by carboxy-oxygen of rose bengal (**Scheme 3.6A**), according to a modified protocol of Callan *et al.* (Nomikou *et al.*, 2012). Rose bengal (0.98 mmol) was dissolved with 3-bromopropylamine hydrobromide (2.94 mmol) in DMF (10 mL, anhydrous). After refluxing at 80 °C for 7 h, the solvent was evaporated. The aminated rose bengal was purified by stirring in diethyl ether at rt for 18 h, filtration and stirring in water at rt for 18 h. The product was dried at rt and lyophilized.

¹H-NMR (300 MHz, DMSO-d₆): 1.65 (qu, CH₂, 2H), 2.64 (s, CH₂, 2H), 4.01 (t, OCH₂, 2H), 7.5 (s, ArH, 2h), 7.63 (s, NH₂, 2H) (**Figure A 7**).

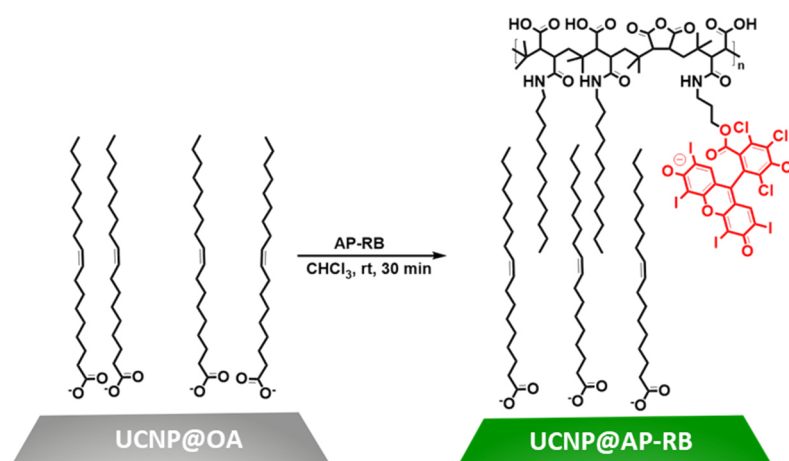
HR-MS (ESI+) (m/z): calculated for C₂₃H₁₁Cl₄I₄NO₅ is 1029.5643, found 1029.5654.

The rose bengal functionalized amphiphilic polymer (AP-RB) was prepared by dissolving poly(isobutyl-maleic anhydride) (PIBMAD, 2 mmol), dodecyl amine (1 mmol) and aminated rose bengal (0.5 mmol) in THF (6 mL) (**Scheme 3.6B**). The reaction mixture was heated to 60 °C for 2 h, concentrated to 2 mL and heated under reflux conditions at 70 °C for 12 h. The solvent was removed by rotary evaporation. Finally, AP-RB was dissolved in CHCl₃ (0.5 M monomers).



Scheme 3.6. Synthesis of rose bengal functionalized amphiphilic polymer (AP-RB). A) Amination of rose bengal with 3-bromopropylamin and B) attachment of aminated rose bengal (25%) with dodecyl amine (50%) to PIBMAD.

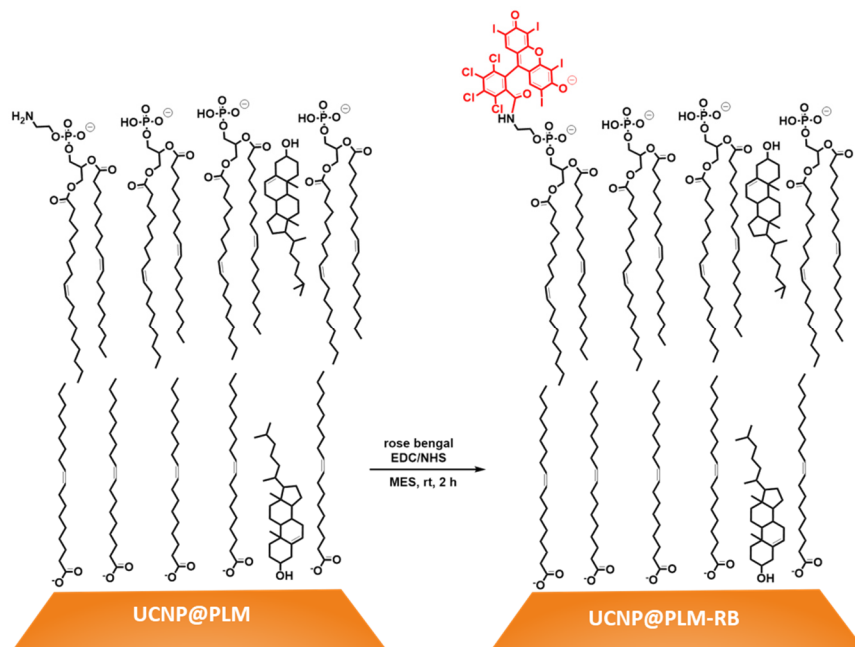
The UCNPs@AP-RB were prepared from UCNPs@OA with AP-RB (0.5 M monomer concentration) as described for UCNPs@AP (Scheme 3.7).



Scheme 3.7. Surface functionalization of UCNPs@OA with the amphiphilic polymer AP-RB to UCNPs@AP-RB.

Surface Functionalization of UCNPs@PLM with Rose-Bengal

Rose bengal was covalently bound to the amine groups of 24 nm NaYF₄(20%Yb,2%Er)@NaYF₄@PLM *via* EDC/NHS chemistry, according to the protocol described for UCNPs@Lys-RB (**Scheme 3.8**).



Scheme 3.8. Surface functionalization of UCNPs@PLM with rose bengal *via* EDC/NHS activation of rose bengal to obtain UCNPs@PLM-RB.

Surface Functionalization of UCNPs@PLM with NT(8-13)

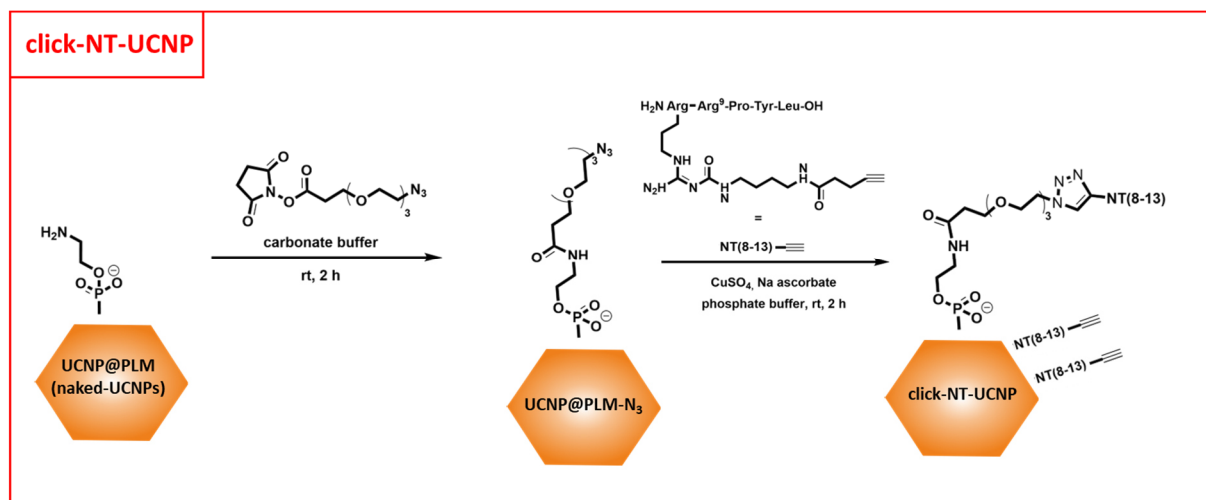
UCNPs@PLM (naked-UCNPs) were functionalized with i) an azido-PEG₃-NHS ester and the neurotensin (NT) derivative alkyne-NT(8-13) to obtain click-NT-UCNPs with covalently attached alkyne-NT(8-13). Control Particles without covalent binding of the agonist were prepared by treating the naked-UCNPs ii) with a non-reactive PEG₃-NHS ester and the alkyne-NT(8-13) for dummy-NT-UCNPs or iii) with alkyne-NT(8-13) for naked-NT-UCNPs.

Click-NT-UCNPs

Click-NT-UCNPs were prepared in a two-step reaction by i) attaching an azido linker at the UCNPs@PLM and 2) a click-reaction with the neurotensin (NT) derivative alkyne-NT(8-13) (**Scheme 3.9**). The linker azido-PEG₃-NHS ester was bound to the amine groups (DOPE) of UCNPs@PLM (33 nm NaYF₄(20%Yb,2%Er)@NaYF₄). The UCNPs@PLM (2 mg·mL⁻¹, 47 μM DOPE) were stirred with the linker (300 μM) in carbonate buffer (300 μL, 5 mM, pH 9) at 350 rpm, 37 °C for 1 h. To increase the efficiency of the reaction, the linker attachment

reaction was repeated. The reaction dispersion was centrifuged (10,000 g, 60 min) and the collected particles were redispersed in carbonate buffer with azido linker (300 μM) and stirred at 350 rpm and 37 °C for 1 h. The particle dispersion was diluted (0.2 $\text{mg}\cdot\text{mL}^{-1}$), centrifuged (10,000 g, 60 min) and the pellet was dispersed in H_2O (2 mL). The washing steps were repeated twice to remove unbound linker. Finally, UCNPs@PLM- N_3 were dispersed in H_2O (0.5 mL) and concentrated with ultra-centrifugal filter (molecular weight cut-off 3 kDa, 5,000 g) for 25 min. The particle dispersion (0.1 – 0.2 mL) was put from the eluent compartment into the reaction tube (2 mL) at 1,000 g (1 min), while aggregates remained in the filter.

The alkyne-NT(8-13) (300 μM) was clicked to the UCNPs@PLM- N_3 (2 $\text{mg}\cdot\text{mL}^{-2}$) in phosphate buffer (0.2 μL , 8.2 mM, pH 7.4), supplemented with CuSO_4 (60 μM) and sodium ascorbate (180 μM), by stirring at 300 rpm, 37 °C for 30 min. The click-NT-UCNPs are diluted (0.8 $\text{mg}\cdot\text{mL}^{-1}$) and purified by dialysis in a dialysis tube (molecular weight cut-off 12 – 14 kDa) against H_2O (0.5 L). The dialysate was exchanged after 2 – 4 h, 6 – 8 h, 10 – 14 h, and 3 – 5 h. Aggregates were removed by centrifugation (1,000 g, 5 min).



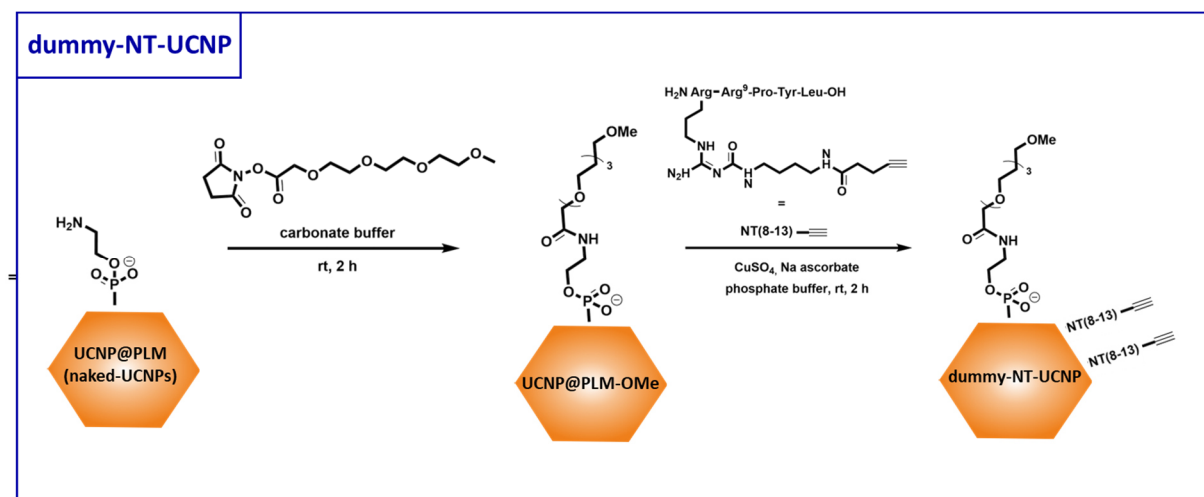
Scheme 3.9. Two step surface functionalization to prepare click-NT-UCNPs from naked UCNPs@PLM by attaching the i) azido linker for the ii) click-reaction with alkyne-NT(8-13).

This procedure was iteratively adapted during the thesis to improve the removal of electrostatically attached NT(8-13) by I) increasing the number of dialysis steps to five; II) pre-saturating PA groups with guanidinium chloride (GdmCl, 3 mM) 30 min prior to the addition of alkyne-NT(8-13) (300 μM); III) pre-saturation with less active derivative N(Me)-Leu-NT(8-13) (200 μM) 30 min prior to addition of alkyne-NT(8-13) (100 μM); IV) dialysis in PBS with

stepwise decrease of phosphate concentration (0.5 L, from 8.2 mM (step 1) to 0.8 mM (step 4)).

Dummy-NT-UCNPs

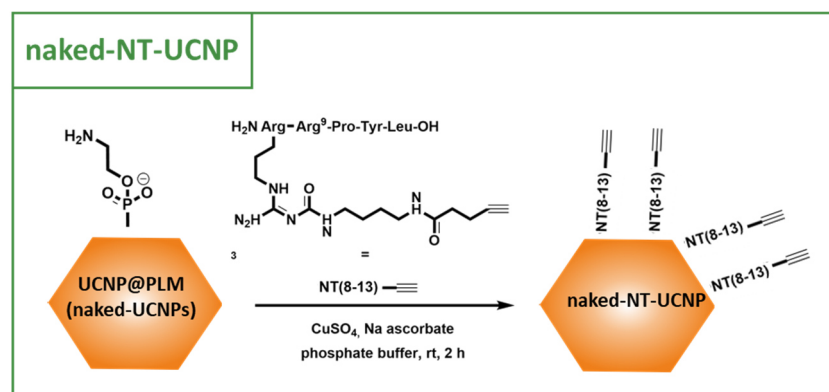
Dummy-NT-UCNPs were prepared analogously to click-NT-UCNPs using the dummy linker methyl-ether-PEG₃-NHS ester with a non-reactive ether group instead of a reacting azido group (Scheme 3.10).



Scheme 3.10. Surface functionalization of naked UCNPs@PLM by the attachment of the dummy linker and following incubation with the reagents for the click-reaction for dummy-NT-UCNPs.

Naked-NT-UCNPs

Naked-NT-UCNPs were prepared by incubation of UCNPs@PLM with the click-reagents, according to the procedure described for the synthesis of click-NT-UCNPs (Scheme 3.11).



Scheme 3.11. Surface functionalization of naked UCNPs@PLM by incubation with the reagents of the click reaction, resulting in naked-NT-UCNPs.

3.1.4 Particle Characterization

Inductively Coupled Plasma- Optical Emission Spectroscopy

The composition of the UCNPs and their mass concentrations were determined by optical emission spectroscopy combined with inductive coupled plasma excitation (ICP-OES) Spectroblue FMX36 (Spectro, Kleve, Germany). Calibrations of the RE ions were performed using a multielement standard with the emission bands at 313 nm (Tm), 329 nm (Yb), 337 nm (Er), and 371 nm (Y). The UCNPs were dried, dissolved in sulfuric acid (500 μ L, \geq 95%, w/w) and diluted with H₂O (9.5 mL) for analysis. The amount of rare earth ions are given as mean \pm standard deviation obtained by repeated measurements (N = 3).

Transmission Electron Microscopy

Transmission electron microscopy (TEM) was performed with the 120 kV CM12 microscope (Phillips, Amsterdam, Netherlands). The particle dispersions (\sim 1.5 mg·mL⁻¹ in cyclohexane or H₂O) were dropped on copper grids (coated with carbon, 400 mesh). The samples for the negative staining were prepared as follows: The carbon coated copper grids were made hydrophilic with 15 standard cubic centimeters per minute (sccm) O₂ for 1 min by the PlasmaFlecto 10 (Plasma Technology, Herrenberg-Gültstein, Germany). After the particle dispersion (\sim 1.5 mg·mL⁻¹) was dropped on the hydrophilized grid and dried with a filter paper from below, the UCNPs@PLM were negatively stained with phosphotungstic acid (1% in H₂O, w/v, pH 7.25) for 90 s. The excess solution was removed with a filter paper.

All obtained micrographs were used to measure the diameter of the particles with the software ImageJ (Wayne Rasband, National Institute of Health, Bethesda, USA). The diameters were plotted in a histogram with bin size 0.5 nm and the distribution was approximated with a normal distribution curve providing the mean diameter with standard deviation.

Dynamic Light Scattering

Dynamic light scattering measurements of the particles were performed in different solvents at rt with the Malvern Zetasizer Nano ZS (Malvern, Herrenberg, Germany). Intensity-weighted particle-size distribution was chosen to detect sensitively aggregated particles. One representative distribution is shown. The mean solvodynamic diameter with the standard deviations was determined from three measurements.

Surface Zeta Potential

The surface zeta potential of the particles in water (10 mM NaCl) or in various ion solutions and buffers was determined with the Malvern Zetasizer Nano ZS. The average zeta potential with standard deviation was determined from three measurements. The conductivity was set around $1 \text{ mS}\cdot\text{cm}^{-1}$ with NaCl (final concentration 10 mM) for particles stored in H_2O . It was between 0.2 and $5 \text{ mS}\cdot\text{cm}^{-1}$ for the stability study with different ionic conditions and $> 5 \text{ mS}\cdot\text{cm}^{-1}$ for the 138 mM NaCl solution.

Luminescence Spectroscopy

Luminescence spectra were recorded with a home-built set-up, consisting of a spectrometer (225 – 1000 nm, RGB photonics, Regensburg, Germany), mounts, filters, lenses, optical fibers (Thorlabs, Bergkirchen, Germany; Ocean Optics, Duiven, Netherlands; Spindler and Hoyer, Göttingen, Germany), an adjustable stage (Edmund Optics, New Jersey, USA) and a 980 nm laser (cw, $144 \text{ W}\cdot\text{cm}^{-2}$, Picotronic, Koblenz, Germany). The spectrometer was controlled with the software Waves (RGB photonics).

Measurements in aqueous media were performed at $144 \text{ W}\cdot\text{cm}^{-2}$ resulting in $85 \text{ W}\cdot\text{cm}^{-2}$ due to H_2O absorption in a 1 cm light path. The laser power density for measurements in cyclohexane and D_2O was adjusted to $85 \text{ W}\cdot\text{cm}^{-2}$ with ND filters for comparable measurements in solvents without H_2O absorption.

Photometry

Absorbance spectra of rose bengal ($5 \mu\text{M}$, H_2O) and rose bengal-functionalized UCNPs ($50 \mu\text{g}\cdot\text{mL}^{-1}$, H_2O) were recorded with a Cary 50 UV-VIS spectrophotometer (Agilent Technologies, Santa Clara, USA).

The maximal absorbance values of the UCNPs-attached rose bengal together with the particle concentration, determined by ICP-OES, are used to determine the number of rose bengal per particle and the iodine (four iodine per RB) to yttrium ratio. The extinction coefficient of rose bengal in DMSO ($\epsilon_{567\text{nm}}(\text{DMSO}) = 89,000 \text{ dm}^3\cdot\text{mol}^{-1}\text{cm}^{-1}$) with a similar absorbance maximum was used for the calculations (Ludvíková et al., 2016).

Wide-field Upconversion Microscopy

Wide-field upconversion micrographs of 33 nm UCNPs@AP/PLM were taken to determine the time-resolved luminescence of individual particles.

Setup

The inverted microscope IX71 (Olympus, Japan) capable of recording optical z-sections was equipped with a 974 nm laser (cw, 350 mW, 8 kW·cm⁻², Qphotonics, USA) for epi-illumination *via* a single mode fiber. The long-pass excitation filter ($\lambda = 780$ nm, Chroma, Kreuzau, Germany), a dichroic mirror ($\lambda = 875$ nm, Chroma), and a short-pass filter ($\lambda = 700$ nm, Chroma) were used to collect the green and red emission of the UCNPs. Images were taken using a 100× objective (NA ~ 1.49) upon 100 ms exposure time with an electron multiplying CCD camera (ImageEM X2 C9100-23B, Hamamatsu, Hamilton Township, USA). The setup was controlled by scripts within the MicroManager. The microscopy setup and procedure has been described in detail by F. Przybilla (University of Strasbourg, France, (Dukhno et al., 2018)).

Sample Preparation

The negatively charged UCNPs@AP/PLM in H₂O or in DPBS (5% FCS (v/v), 1 mg·mL⁻¹ glucose) were immobilized on a polyethyleneimine (PEI) coated 8 well chambered cover glass for 30 min (0.2 µg·mL⁻¹, 0.6 mL per well). The particle suspension was supplemented with NaF (1 mM) for the imaging of the first data point at rt or 37 °C to prevent possible particle dissolution. After imaging of the first data point, the adsorbed UCNPs were washed three times and kept under H₂O at rt or 37 °C for the following measurements. It was controlled by microscopy that UCNPs did not detach during the washing procedure.

Data Processing

All images were obtained from an averaged stack of 100 images (100 ms exposure time). The images were further drift-corrected before the spot intensity was determined (ImageJ, grid/collection stitching plugin and scripts written by Przybilla (Dukhno et al., 2018)). The UCNP spot intensities of 100 images with ROIs of 40 µm x 40 µm were plotted in a histogram and fitted with a gaussian model to compare the central intensity (x_c) of the particles with mean and corresponding standard deviation. Values with $3 \times S/N \leq 350$ were removed from analysis. The total intensity of all integrated luminescence spots was determined for each time point and normalized to the starting values to monitor luminescence losses. Luminescence losses were fitted with an exponential decay function.

X-Ray Diffractometry

X-Ray diffraction patterns (XRD) of the UCNPs were recorded by Dr. Marc Schlosser (working group of Prof. Pfitzner, university of Regensburg) with a STOE STADI P (Darmstadt, Germany)

diffractometer with a Dectris Mythen 1K detector using monochromatic $\text{Cu}_{K\alpha}$ radiation ($\lambda = 1.54056 \text{ \AA}$) and a step size of 0.005° .

Thermogravimetric Analysis

Thermogravimetric analysis of UCNP@OA was carried out by Ulrike Schiebl (working group of Prof. Pfitzner, university of Regensburg) with the thermogravimeter TG 50 (Mettler Toledo, Greifensee, Switzerland) under nitrogen atmosphere from $25 - 700^\circ\text{C}$ with a heating rate of $10^\circ\text{C}/\text{min}$. A rough estimation of the surface coverage of the UCNP with OA was determined by the following equations.

The relative mass loss was assumed to be only due to surface ligands, thus the absolute mass (m_{total}) was the sum of the mass of plain UCNP ($m_{\text{plain UCNP}}$) and the mass of OA ligands (m_{OA}):

$$m_{\text{total}} = m_{\text{plain UCNP}} + m_{\text{OA}}$$

The number of UCNP (N_{UCNP}) was determined from the mass of plain UCNP and the mass of one single UCNP (m_{UCNP}):

$$N_{\text{UCNP}} = \frac{m_{\text{plain UCNP}}}{m_{\text{UCNP}}}$$

The mass of one UCNP was calculated by the density of NaYF_4 (ρ_{NaYF_4} , $4.23 \text{ g}\cdot\text{cm}^{-3}$) (Tan et al., 2011) and the volume of one UCNP (V_{UCNP}), obtained from TEM analysis and the hexagonal geometry of the UCNP with edge length (a), height (h) and particle diameter ($2a = d = h$):

$$m_{\text{UCNP}} = \frac{\rho_{\text{NaYF}_4}}{V_{\text{UCNP}}} = \frac{\rho_{\text{NaYF}_4}}{6 \cdot a^2 \cdot \frac{\sqrt{3}}{4} \cdot h} = \frac{\rho_{\text{NaYF}_4}}{\frac{3\sqrt{3}}{8} \cdot d^3}$$

The total number of OA molecules (N_{OA}) was determined with the Avogadro constant (N_A):

$$N_{\text{OA}} = \frac{m_{\text{OA}}}{M_{\text{OA}}} \cdot N_A$$

The amount of OA ligands per one single particle was obtained by

$$N_{\text{OA/UCNP}} = \frac{N_{\text{OA}}}{N_{\text{UCNP}}}$$

The total surface coverage of the UCNP by OA ligands was obtained by calculating the surface area of one hexagonal UCNP (A_{UCNP}) and considering the surface of the carboxylic group of OA (A_{OA} , 0.2 nm^2) (Tong et al., 2015; Zhang et al., 2006):

$$\text{surface coverage} = \frac{N_{\text{OA/UCNP}} \cdot A_{\text{OA}}}{A_{\text{UCNP}}}$$

3.2 Cell Culture and Techniques

All cell culture work was performed under sterile conditions in a laminar flow hood (HERAsafe, Thermo Fischer Scientific, Waltham, USA). The media and liquid reagents were delivered sterile or sterilized by passing through a sterile filter (0.2 μm pore size, poly(ether sulfone)). The consumables and substrates were autoclaved (120 °C, 20 min, Autoclave DX-45, Systec, Linden, Germany), sterilized in an Ar-Plasma (Argon Plasma Cleaner PDC 32G-2, Harrick Plasma, Ithaca, USA) or incubated with ethanol. All cells were grown in polystyrene culture flasks with a growth area of 25 cm² or 75 cm² using 4 mL or 10 mL of culture medium. They were cultivated in an incubator (Thermo Fischer Scientific, Waltham, USA) at 37 °C under 5% CO₂ (v/v) and 95% relative humidity. All reagents, buffers and media were pre-warmed in a 37 °C water bath before use. Substrates were preincubated with cell culture medium prior to cell seeding for at least 30 min. The cells were counted with a Bürker hemacytometer for the experiments (Bürker, LO-Laboroptik GmbH, Friedrichsdorf, Germany).

3.2.1 Cell Lines

Three adherent cell lines were cultured for the projects of this thesis. The renal normal rat kidney cells (NRK) were the model cell line to test the toxicity and internalization behavior of various UCNPs. The epithelial-like cells (NRK-52E) grow as monolayers with cobblestone morphology (**Figure 3.1A**). The cells were obtained from the *Deutsche Sammlung von Mikroorganismen und Zellkulturen* (DSMZ). The NRK cells were cultivated in Dulbecco's Modified Eagle's Medium (DMEM) with 3.7 g·L⁻¹ NaHCO₃ and 4.5 g·L⁻¹ D-glucose, supplemented with fetal bovine serum (FBS, 5% (v/v)), L-glutamine (1 mM) and penicillin/streptomycin (each 100 $\mu\text{g}\cdot\text{mL}^{-1}$). The NRK-52E cell line was used for the experiments in passage number numbers 17 – 36.

The human HT-29 colon adenocarcinoma cell line as well as the Chinese hamster ovary (CHO) cell line CHO-hNTS₁R were the test cell lines to analyze the stimulation properties of NT(8-13), coupled to UCNPS. The HT-29 cells are epithelial-like and grow in large colonies to a confluent monolayer (**Figure 3.1B, C**). They express the human neurotensin 1 receptor (hNTS₁R) endogenously with approximately 45,000 receptors/cell (Keller et al., 2016). The cell line was kindly provided by PD Dr. Max Keller (University of Regensburg, Germany). The HT-29 cells

were cultivated in Roswell Park Memorial Institute medium (RPMI1640) supplemented with FBS (10% (v/v)), L-glutamine (2 mM) and penicillin/streptomycin (each 100 $\mu\text{g}\cdot\text{mL}^{-1}$). The HT-29 cell line was used in passage numbers 173 - 186.

The CHO-hNTS₁R cell line is a derivative of CHO-FRT cell line, which was stably transfected with the hNTS₁ receptor gene *via* the pcDNA5/FRT vector, expressing approximately 300,000 hNTS₁R per cell (Keller et al., 2016). The epithelial cells with a long-stretched morphology grow in a monolayer (**Figure 3.1D**). The cell line was kindly provided by PD Dr. Max Keller (University of Regensburg, Germany). The CHO-hNTS₁R cells were cultivated in Dulbecco's Modified Eagle's Medium / Ham's Nutrient Mixture F12 (DMEM/HAM12, 1:1 mixture) supplemented with FBS (10% (v/v)), L-glutamine (2 mM), penicillin/streptomycin (each 100 $\mu\text{g}\cdot\text{mL}^{-1}$) and the selection antibiotics hygromycin B gold (125 $\mu\text{g}\cdot\text{mL}^{-1}$). The CHO-hNTS₁R cell line was used in passage numbers 8 – 12.

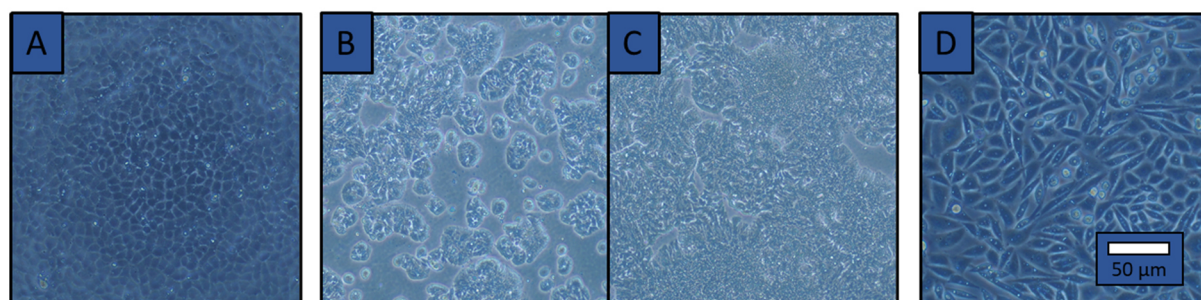


Figure 3.1. Phase-contrast microscopy images of the cell lines, used in this thesis: (A) NRK, (B,C) HT-29 in colonies and in ~95% confluence and (D) CHO-hNTS₁R. Scale bar 50 μm .

3.2.2 Subcultivation

The cells were subcultivated, when 95% confluence was reached, once (NRK, HT-29) or twice a week (CHO-hNT₁sR). The cell media of NRK and HT-29 cells were additionally exchanged after 3 – 4 days.

The subcultivation process of the three cell lines, grown on a T25 flask, was started by washing with Dulbecco's Phosphate Buffered Saline without Ca^{2+} and Mg^{2+} (DPBS⁻) to remove dead cells as well as divalent ions, required for cell-cell and cell-matrix contacts. If required, the cells were washed or incubated with ethylenediaminetetraacetic acid (EDTA, 1 mM in DPBS⁻, 4 mL) for 10 min at 37 °C to chelate residue divalent ions. After removal of the EDTA solution, the cells were trypsinized (0.05% (w/v) with 1 mM EDTA in DPBS⁻, 1 mL) for 2 – 10 min at 37 °C. The incubation with the digesting enzyme trypsin, a serin protease cleaving after lysine and

arginine, was necessary to separate the cells from each other and detach them from the substrate. By adding the culture medium without selection antibiotics (10 mL) the enzyme was inactivated and the digestion process was stopped. The cell suspension was centrifuged (110 g, 5 – 10 min, rt) and the cell pellet resuspended in fresh medium without selection antibiotics (4 mL). The cells were seeded on new culture flasks in a ratio of 1:10 (CHO-hNTS₁R, HT29) or 1:20 (NRK) in the culture medium with selection antibiotics, if required.

Table 3.2. Subculture protocols for the cell lines NRK, HT-29 and CHO-hNTS₁R.

	NRK	HT-29	CHO-hNTS ₁ R
washing with DPBS⁻	2x	1x	1x
treatment with EDTA (1 mM)	10 min incubation	1x washing	-
incubation with trypsin (0.05%)	10 min	7 min	5 min
centrifugation time @110 g	10 min	5 min	10 min

3.2.3 Cryopreservation and Recultivation

Cryopreservation was performed with cells at 80% confluency. Cells were detached from the substrate as described in **Chapter 3.3.2**. After centrifugation the cell pellet of one T25 flask was resuspended in freezing media (1.8 mL). The freezing media for NRK was 10% (v/v) dimethyl sulfoxide (DMSO) in FBS and for HT-29 and CHO-hNTS₁R 10% DMSO (v/v) in culture medium. The cryoprotective DMSO works as frost protection agent to prevent the formation of intracellular ice crystals, which may lead to cell membrane damage and necrosis. The aliquots were cooled down to -80 °C in an isopropyl alcohol bath at 1 °C·min⁻¹. After 24 h the aliquots were transferred to liquid nitrogen (-178 °C) for long term storage.

Recultivation of the cells was started by pre-warming the aliquot in a freezer (-20 °C, 2 h) and warming up in a water bath (37 °C). After transferring the cell suspension into a centrifuge tube, pre-warmed culture medium (16 mL) was added dropwise to minimize osmotic stress and cells were centrifuged (100 g, 10 min, RT). The supernatant was discarded and the cell pellet was resuspended in full culture medium without selection antibiotics (4 mL). The

resuspended cells were seeded in four culture flasks T25 in culture medium without selection antibiotics (1:2, 1:4, 1:8). After 24 h the culture medium was exchanged and the cells were subcultivated after reaching 95% confluency with the protocol described in the previous chapter. Selection medium was added to the cells earliest after the following subcultivation.

3.2.4 General Experimental Procedures and Considerations

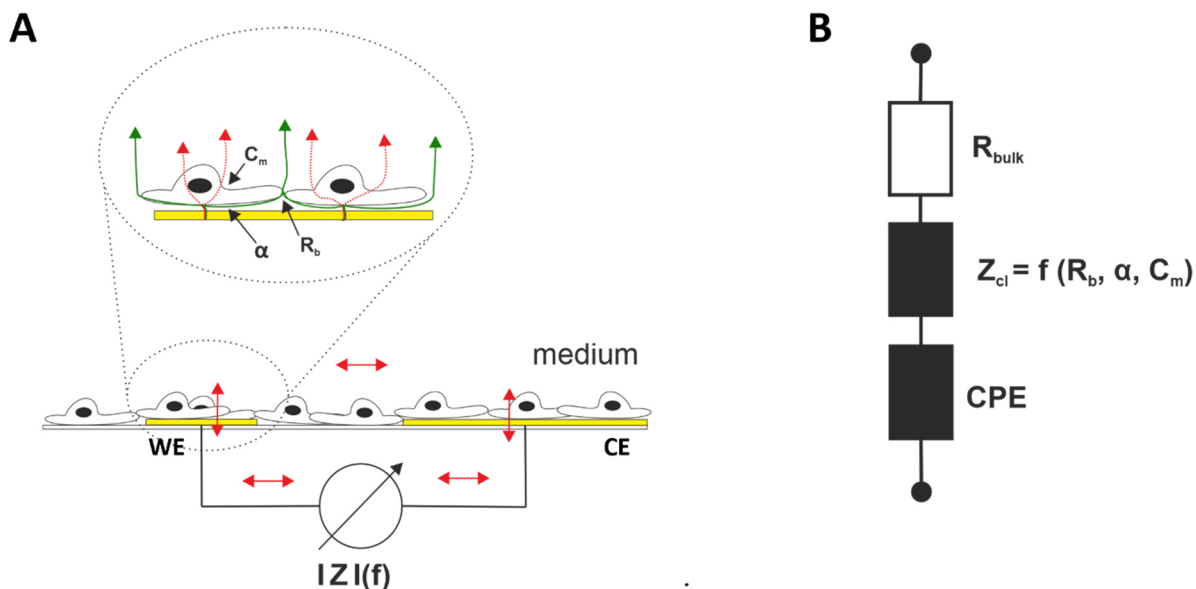
For all experiments, cells were seeded to confluence in cell culture medium two days before the experiments were started. The cells were seeded in the following densities: NRK cells $250,000 \text{ cells}\cdot\text{cm}^{-2}$, HT-29 cells $500,000 \text{ cells}\cdot\text{cm}^{-2}$ and CHO-hNTS₁R cells $150,000 \text{ cells}\cdot\text{cm}^{-2}$. They were cultivated at 37 °C and 5% CO₂ for 48 h with a fresh medium supply after 24 h. On the day of the experiment, particle suspension in the desired medium or buffer were prepared by dilution. As particle stock dispersions in water were used for dilution, the osmolarity of the final dispersion with the highest concentration had to be aligned before lower concentrated particle suspensions were prepared from this. The alignment of osmolarity was done by adding NaCl solution (final 150 mM) proportional to the volume of particle stock solution in water. The adequate osmolarity and the colloidal stability of the particle dispersion were verified prior to the experiments.

3.2.5 Impedance-Based Cell Analysis

The impedance-based cell analysis is a non-invasive technique to monitor morphology changes of (living) cells online and in real-time. The method was developed 1984 by Giaever and Keese, named electrical cell-substrate impedance sensing (ECIS), and is based on recording the impedance (alternating current (AC) resistance) of cell-covered gold electrodes (Giaever et al., 1984). The cells are grown as monolayer on a small working electrode (WE) and the co-planar, much larger counter electrode (CE) (**Scheme 3.12A**). The two electrodes are electrically connected by the surrounding culture medium. Due to the electrode configuration, the measured impedance is mostly assigned to the impedance of the WE and the cells grown on it, acting as insulating particles at low frequencies. This system can be described by an equivalent circuit with similar frequency-dependent electrical properties (Wegener et al., 1999) (**Scheme 3.12B**). The gold electrodes and, especially, the electrode/electrolyte interface are represented by the constant phase element (CPE), which

is a non-ideal capacitor. The interface-related impedance of the CPE is described by the two parameters n_{CPE} and A_{CPE} , reflecting the topology of the electrodes in terms of surface roughness and chemical inhomogeneities and hence the deviations from an ideal capacitor. The resistance of the bulk medium is represented by R_{bulk} . The cell layer has capacitive (cell membrane) and resistive properties (cell-cell and cell-substrate contacts) and is described by the impedance of the cell layer (Z_{cl}). The electrical circuit elements describing the electrode (n_{CPE} and A_{CPE}), the cell layer (Z_{cl}), and R_{bulk} are connected in series as shown in (**Scheme 3.12B**). The total impedance of this system is calculated according to Ohm's and Kirchhoff's law. The current always takes the pathway with the lowest impedance. Thus, depending on the frequency, the applied alternating current flows underneath and between the cells (paracellular pathway) or through the cells (transcellular pathway). The paracellular pathway dominates at low frequencies and the current passes the cleft between electrode surface and cell, followed by the paracellular cleft so that changes on the intercellular cleft as well as on the cell substrate contacts are detected (green arrow, **Scheme 3.12A**). The transcellular pathway predominates at high frequencies and the current couples capacitively through the cell membranes (red arrow, **Scheme 3.12A**). Thus, the impedance at high frequencies is sensitive towards changes of the cell membrane and electrode coverage. By choosing the right frequency, detailed information on the cellular conditions in response to external stimuli are accessible, *e.g.* swelling/shrinking, the formation or break-down of cell-cell or cell-substrate contacts or membrane pores, rounding, and detaching from the electrode.

Beneath the information, which are directly accessible by the impedance, Z_{cl} can be translated by the transfer function of the ECIS model into three cell-related parameters, which are interpretable in a physiological manner: the specific resistance of cell-cell contacts (R_b), the specific resistance of cell-substrate contacts (α), and the membrane capacitance as serial combination of apical and basolateral cell membrane (C_m) (Giaever et al., 1991). C_m is found to be around $1 \mu\text{F}\cdot\text{cm}^{-2}$ for most of the cell lines without membrane foldings, while the other two parameters are cell type-specific (Reiss et al., 2015).



Scheme 3.12. (A) Principle of the impedance-based cell analysis. A small AC current of $1 \mu\text{A}$ is applied between a small working electrode (WE) and a larger counter electrode (CE) to monitor the impedance $|Z|(f)$ of the system, dominated by the impedance of the WE and the cells grown on the WE. Depending on the frequency, the current takes the paracellular (green, line) or the transcellular pathways (red, dashed). The cell-related parameters target the cleft between electrode surface and cell (α), the intercellular cleft (R_b), and the cell membrane capacitance (C_m). (B) The equivalent circuit consists of the constant phase element (CPE, electrode/electrolyte interface), the impedance of the cell layer (Z_{cl}), and the resistance of the bulk medium (R_{bulk}).

Fit of Impedance Courses

The impedance spectra were analyzed *via* the ECIS transfer function using an in-house fit software from Dr. M. Skiba and Prof. J. Wegener (University of Regensburg, Germany) to derive the three cell-related parameters R_b , α and C_m . Details of the model and the ECIS transfer function have been described by Dr. C. Götz (Götz, 2018). The modeling process demands values for R_{bulk} and the electrode parameters n_{CPE} and A_{CPE} . R_{bulk} is accessible by the impedance value at the high-frequency end of the impedance spectrum (**Figure 3.2**). Here, it was kept constant during the fitting process. The electrode parameters were adjusted continuously during the fitting processes to account for drifting of the electrode/electrolyte interface. They were obtained from each impedance spectrum by linearly fitting the four lowest frequency data points, which were dominated just by the CPE. The logarithmic form of this impedance magnitude provides a linear equation with the slope $-n_{CPE}$ and the intercept as

$-\log(A_{CPE})$ (**Figure 3.2**). The analysis was validated with an independent algorithm from Ivar Giaever, written in the program language APL.

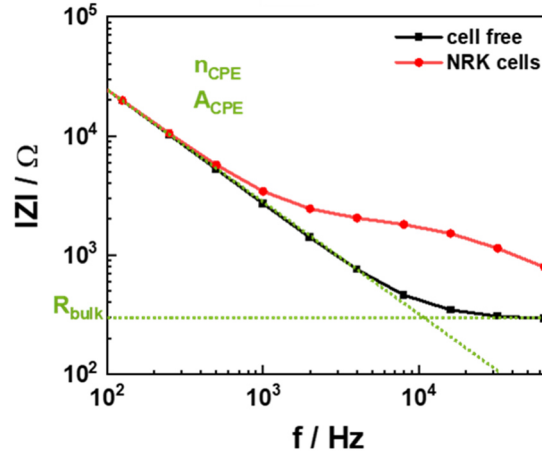


Figure 3.2. Frequency-dependent impedance spectra of a cell-free and a NRK cell-covered electrode. The electrode parameters are obtained by a linear fit of the first four parameter at the low frequency end with the slope $-n_{CPE}$ and the intercept $-\log(A_{CPE})$. The impedance at the highest frequency of the cell-free electrode is assumed to be equal to R_{bulk} .

Setup

In this thesis, the ECIS approach was used to analyze the cytotoxicity of different UCNP on epithelial cells and their impact on the cellular adhesion and migration capability. Experiments have been performed with the ECIS ZΘ device (Applied BioPhysics Inc., Troy, USA) or with a homebuilt device. GPCR activation by their respective agonist, freely available or attached to UCNP, was monitored on cells expressing the GPCR with the ECIS ZΘ device. The experiments on both devices were referred to as impedance-based cell assays.

The experiments were performed in 8-well or 96-well arrays, which were mounted in an array holder within a humidified incubator at 37 °C. Parts of the electronics of the ECIS ZΘ device were placed inside the incubator. The commercial ECIS ZΘ device was controlled by the ECIS software (Applied BioPhysics Inc.). A sinusoidal AC current of 1 μA was applied to monitor the impedance at different frequencies (100 – 64,000 Hz) of individual wells in 8-well or 96-well format.

Measurements with the self-made device was carried out in 8-well format. A standard ECIS-array holder (Applied BioPhysics Inc.) connected the arrays to a relay, which was linked to the

impedance analyzer (SI1260, Solartron Instruments, Farnborough, UK) and a computer to control the setup with a LabVIEW (National Instruments, Austin, USA) software, written by J. Wegener (University of Regensburg, Germany). A sinusoidal AC voltage of 50 mV was applied to record the impedance at different frequencies (1 – 10⁶ Hz).

Cytotoxicity

The cytotoxicity of UCNPs on NRK cells was monitored *via* the impedance-based cell assay and described by the impedance magnitude (4 kHz, 32 kHz) and capacitance (32 kHz). The cells, confluent grown on 8W10E arrays (Applied Biophysics Inc., ten electrodes per well with a total electrode area of 0.49 mm²), were allowed to adapt to the measurement medium (200 µL) for > 3 h until a stable baseline was reached before various UCNPs in different media were added (double-concentrated, 200 µL) according to **Table 3.3**.

Table 3.3. UCNPs and media applied in the cytotoxicity measurements using NRK cells as model organisms and the ECIS technique for monitoring.

UCNPs	medium	passage numbers	chapter
25 nm UCNPs@AP	L-15, 5% FCS, 100 µg·mL ⁻¹ Pen/Strep	14 – 37	6
33 nm UCNPs@AP	L-15, 5% FCS, 100 µg·mL ⁻¹ Pen/Strep	24 – 27	5
33 nm UCNPs@AP	DPBS ⁺⁺ , 5% FCS, 1 mg·mL ⁻¹ glucose, 100 µg·mL ⁻¹ Pen/Strep	24 – 27	5
15 nm UCNPs@AP-RB	L-15, 5% FCS, 100 µg·mL ⁻¹ Pen/Strep	22 - 24	7
24 nm UCNPs@AP-RB	L-15, 5% FCS, 100 µg·mL ⁻¹ Pen/Strep	22 - 25	7
33 nm UCNPs@PLM	NRK cell culture medium	29, 30	5
33 nm UCNPs@PLM	DPBS ⁺⁺ , 5% FCS, 1 mg·mL ⁻¹ glucose, 100 µg·mL ⁻¹ Pen/Strep	24 – 27	5
24 nm UCNPs@PLM-RB	NRK cell culture medium	24, 25	7
24 nm UCNPs@Lys-RB	L-15 + 5%FCS + 100 µg·mL ⁻¹ Pen/Strep	24, 25	7

The impedance and capacitance changes were monitored for at least 72 h. The resulting time courses of impedance or capacitance were normalized to the time point before particle addition ($|Z| = |Z|_t / |Z|_{0h}$, time point 0 h). The mean normalized impedance after 72 h with

the corresponding standard error of the mean (mean \pm SEM, $N \geq 4(2)$) was used to determine the potencies. Sigmoidal concentration response relations were approximated by a logistic model (4 parameters).

Migration

The migration ability of NRK cells (passage number 33 – 36) exposed to 25 nm UCNPs@AP (L-15, 5% FCS, 100 $\mu\text{g}\cdot\text{mL}^{-1}$ penicillin/streptomycin) was analyzed with confluent grown NRK cells on commercially available 8W1E arrays (Applied BioPhysics Inc., one electrode per well with a size of 0.049 mm^2). As soon as cells adapted to the new media (200 μL), the UCNPs were added double-concentrated (200 μL) at time point 0 h. The cells were electrically wounded (2400 μA , 32 kHz, 30 s) after exposure to particles for 4 – 24 h and the recovery to the baseline impedance values of cell-covered electrodes was monitored for at least 15 h. The resulting impedance time course was normalized to the time point of the wounding pulse ($|Z|_{\text{norm.}} = |Z|_t / |Z|_{0\text{ h}}$, time point 0 h).

Data evaluation was carried out using the normalized area under the time-dependent impedance curve (norm. AUC, 0 – 15 h, normalized to the AUC of cells in absence of UCNPs) to determine EC_{50} values (potencies) for each incubation time with a 4-parametric logistic model.

Adhesion

Adhesion of NRK cells (passage number 33 – 36) from suspension (450 000 $\text{cells}\cdot\text{cm}^{-2}$) in presence of UCNPs@AP was monitored *via* the ECIS technique using commercially available 8W10E arrays (Applied BioPhysics Inc., ten electrodes per well with a total electrode area of 0.49 mm^2). The NRK cells were added to the particle suspensions in the wells of an ECIS electrode array and the impedance changes reported for 24 h. The time courses of impedance and capacitance were normalized to the time point of the particle addition. The normalized area under the curve (norm. AUC, 0 – 24 h, normalized to the AUC of cells in absence of UCNPs) was determined (mean \pm SEM, $N \geq 3(3)$) and plotted in a concentration-dependent manner to determine the potency (EC_{50}) with a 4-parametric logistic model.

Stimulation of NTS₁R Expressing Cells

CHO-hNTS₁R cells (passage number 10 – 12) or HT-29 cells (passage number 173 – 179) were seeded to confluence in culture medium on commercially available 96W1E+ arrays (Applied

BioPhysics Inc., two electrodes per well with a total electrode area of 0.256 mm²). The measurement was started after 48 h, when the culture medium was removed and BSA (100 μ L, 0.5% (w/v))-supplemented DPBS⁺ (DPBS⁻, 0.18 mM CaCl₂, 1 mg·mL⁻¹ glucose)) was added to reduce unspecific binding of particles to the cells. After 20 min BSA-containing DPBS⁺ was exchanged with BSA-free DPBS⁺ (37.5 μ L) until a stable baseline was reached (~20 min). NT(8-13) or particles were added in forthfold concentration (12.5 μ L) and the impedance was monitored for at least 60 min.

Inhibition experiments were performed with the CHO-hNTS₁R cell line and SR142948, an antagonist for the hNTS₁R. After 20 min incubation in 0.5% BSA (v/v, DPBS⁺) and 15 min adaption to DPBS⁺, the antagonist (12.5 μ L, 4 μ M for NT(8-13) and 10 μ M for particles) was added 5 min prior to the NT(8-13) or particle solution. 12.5 μ L of the supernatant was removed carefully and the NT(8-13) (12.5 μ L, 10 nM) or particle solution (12.5 μ L, 2 μ g·mL⁻¹), equipped with SR142948 (4 μ M or 10 μ M), was added.

The impedance change was determined with the time point before substance addition ($\Delta|Z| = |Z_t| - |Z|_{0h}$). The maximal impedance change $\Delta|Z|_{max}$ after around 2 min (HT-29) or around 15 min (CHO-hNTS₁R) was plotted against the log(c). Sigmoidal concentration response relations were approximated with a logistic function (4 parameter) to determine the potencies (EC₅₀).

3.2.6 Inductively Coupled Plasma - Mass Spectrometry

NRK cells, seeded to confluence in 96W cell culture plates (Greiner Bio-One, Frickenhausen, Germany), were incubated with UCNPs@AP (Leibovitz L-15, 5% FCS (v/v)) for 24 h before the measurement. The cells were washed twice with DPBS⁻ and treated with trypsin (30 min, 0.05% (w/v), 1 mM EDTA in DPBS⁻, 0.1 mL). Detached cells were collected *via* centrifugation (110 g, 10 min, rt). The cell pellet was dried at 70 °C before lysis in H₂SO₄ (500 μ L, \geq 95%). The samples were diluted with H₂O (9.5 mL) and supplemented with the internal standard Rh (10,000 ppb, 4 μ L) to determine the mass of RE ions (⁸⁹Y, ¹⁶⁶Er, ¹⁷⁴Yb) using a ICP mass spectrometer ELAN 9000 (PerkinElmer, Waltham, USA). With the UCNPs diameter, determined by electron microscopy, and the particle density ($\rho = 4.23$ g·cm⁻³ for NaYF₄ (Tan et al., 2011)), the number of UCNPs per well was obtained. The values were corrected by the

number of UCNPs binding non-specifically to the polystyrene 96W plate, which was determined by performing the same procedure in cell-free wells.

To determine the number of UCNPs per cell, the average number of cells per well was counted after cell removal from the surface as $(350 \pm 30) \cdot 10^3 \text{ cells} \cdot \text{cm}^{-2}$ and $(1.1 \pm 0.1) \cdot 10^5 \text{ c/well}$ (four times in four wells of two independent cell subcultures). This number was in good agreement to the mean number of NRK cells confluent grown in a cell culture T25 flask with around $(330 - 380) \cdot 10^3 \text{ cells} \cdot \text{cm}^{-2}$.

The volume fraction, which was necessary to host the UCNPs in one cell, was estimated, assuming a cylindric cell shape with a diameter of $15 \mu\text{m}$ (obtained by phase contrast microscopy) and a height of $3.5 \mu\text{m}$ (determined *via* electron microscopy).

3.2.7 Laser Ablation - Inductively Coupled Plasma - Mass Spectrometry

Prior to the cell analysis the iodine to yttrium (I/Y) ratio of the particles in suspension were determined by ICP-MS. UCNPs were diluted in NH_4OH (3%) for the determination of iodine, and in HNO_3 (2%) for quantifying yttrium. The standards for LA-ICP-MS were prepared in gelatine (10%, w/w) according to the determined I/Y ratios of the particles.

Sample Preparation

NRK cells (passage number 18 and 19) were seeded to confluence in 8 well inserts (Applied BioPhysics Inc.), glued at microscopic slides. They were cultivated at 37°C and 5% CO_2 for two days with a fresh medium supply after 24 h. After 48 h the culture medium was replaced by the UCNPs suspensions ($50 \mu\text{g} \cdot \text{mL}^{-1}$ UCNPs@PLM-RB, UCNPs@AP-RB or UCNPs@Lys-RB in DMEM, 5% FCS) and incubated for 5 h or 10 h at 37°C and 5% CO_2 . They were rinsed twice with DPBS, fixed in paraformaldehyde (4%, w/v, DPBS⁺⁺) for 10 min and rinsed three times with water before drying at 40°C .

Setup and Procedure

For LA-ICP-MS analysis, a 193 nm ArF Excimer Laser (NWR193 Excimer Laser Ablation System, Elemental Scientific Lasers, Bozeman, USA) was coupled to an ICP-MS Triple Quadrupole (8900 ICP-MS Triple Quad, Agilent Technologies, Santa Clara, USA). For the single cell analysis, each ablated cell was transported in an Ar carrier gas flow ($900 \text{ mL} \cdot \text{min}^{-1}$) and introduced to the ICP-MS. For imaging, a He carrier gas flow was applied ($900 \text{ mL} \cdot \text{min}^{-1}$). An additional gas flow (Ar, $1 \text{ L} \cdot \text{min}^{-1}$) was added in a Dual Concentric Injector (DCI, Elemental Scientific Lasers,

Bozeman, USA) and the sample transferred *via* a quartz injector pipe (inner diameter: 3.5 mm) into the plasma. The ICP-MS was equipped with platinum sampler and skimmer.

The cell membrane, cytoplasm, and especially the cell nuclei contain phosphorus, which was monitored in imaging mode to display the cell morphology. As $^{31}\text{P}^+$ suffers from polyatomic interferences (*e.g.* $^{14}\text{N}^{16}\text{O}^{1}\text{H}^+$, $^{13}\text{C}^{18}\text{O}^+$), it was operated in triple quadrupole modus with O_2 as reaction gas. The set-up was tuned daily for maximum signal intensity and an oxide ratio (m/z 232/248) below 1.5% with a NIST Glass standard (NIST SRM 612, National Institute of Standards and Technology, Gaithersburg, USA). Each cell and the gelatin standards were ablated with 5 bursts and a spot size of 25 μm . A laser pulse frequency of 100 Hz and a laser energy density of $0.5 \text{ J}\cdot\text{cm}^{-2}$ ensured a fully ablation but avoided ablation of the glass slide. For the single cell analysis, the isotopes $^{127}\text{I}^+$ and $^{89}\text{Y}^+$ were monitored with a dwell time of 40 μs . For imaging purpose, the isotopes $^{31}\text{P}^{16}\text{O}^+$, $^{89}\text{Y}^{16}\text{O}^+$, $^{166}\text{Er}^{16}\text{O}^+$, $^{174}\text{Yb}^+$ were monitored each with a dwell time of 50 ms. A laser scan speed of $16 \mu\text{m}\cdot\text{s}^{-1}$ and a spot size of 4 μm was applied. The energy and frequency were the same as for the single cell analysis.

To determine the beginning of a cell injection, a threshold was determined according to the 3σ criterion of the intensities ($\text{IBKG}^{(89}\text{Y}^+)$). For an identified cell, the rose bengal to UCNPs ratio was calculated by dividing the total signal intensities of $^{127}\text{I}^+$ by the total $^{89}\text{Y}^+$ signal intensities. For the evaluation, a RStudio and a home-made script developed by Svenja Seiffert and Felix Riewald were used. The intensities and ratios were plotted as box plot, showing the mean \pm SD, the median and 10 – 90% of the data points in the boxes.

These experiments were performed in cooperation with Svenja Berit Seiffert and Dr. Sabine Kröger from BASF (Ludwigshafen am Rhein, Germany). The samples were prepared by the author and the LA-ICP-MS measurements as well as the analysis was made by Svenja Berit Seiffert.

3.2.8 Microscopic Techniques

Phase Contrast Microscopy

An inverse phase contrast microscope (Nikon Diaphot, Nikon, Düsseldorf, Germany) was used to check and document the cell status. Micrographs were taken with a 10 \times objective (E10 25, Nikon) by a digicam D500 (Nikon) upon 0.3 s exposure time with or without blue filter. The acquired images were processed by the software ImageJ.

Two-Photon Laser Scanning Microscopy

Setup

The epi-fluorescence laser scanning microscope LSM710 (Zeiss, Oberkochen, Germany) was equipped with a multiphoton laser (1,100 mW at 980 nm) for irradiating the UCNPs. Images were taken with 40× magnification (NA ~ 1.1, LD C-apochromat, Zeiss) upon irradiation with 405 nm and 980 nm (6.3 μs/pixel) in the laser scanning mode controlled via the software ZEN 1.3 SP1 (Zeiss) and processed by the software ImageJ.

Sample Preparation

NRK cells (passage number 18) were seeded to confluence in 8 well inserts (Applied BioPhysics Inc.), glued upon microscopic slides. They were exposed to 12 nm UCNPs@PLM (50 μg·mL⁻¹) in DMEM (5% FCS, (v/v)) at 37 °C for different exposure times. After incubation the cells were rinsed twice with DPBS⁺⁺, fixed in paraformaldehyde (4%, w/v, DPBS⁺⁺) for 10 min and treated with Triton X-100 (0.5%, (v/v), DPBS⁺⁺) for 10 min to permeabilize the cell membrane for the nuclei stain 4',6-diamidino-2-phenylindole (DAPI, 100 ng·mL⁻¹, DPBS⁺⁺) to enter (2 min). Finally, the fixed and stained cell samples were washed three times with DPBS⁺⁺.

Wide-Field Upconversion Microscopy with 640 W·cm⁻² Irradiation

Setup

The inverted wide-field epi-fluorescence microscope Eclipse Ti-E (Nikon) with z-section capability was equipped with a 980 nm laser diode (cw, 4 W, 640 W·cm⁻², Wavespectrum, Beijing, China) *via* a multimodal optical fiber (105 μm fiber core, 0.22 NA, Wavespectrum) and a filter cube for the detection of Er³⁺ doped UCNPs. The filter cube contained a long-pass excitation filter (λ = 830 nm, Schott, Germany), a dichroic mirror (λ = 875 nm, AHF Analysetechnik, Germany), and a band-pass filter (λ = 535 ± 70 nm, OD₉₈₀ ~ 6, Chroma, USA). Images were taken with a 100× objective (NA ~ 1.49, CFI HP apochromat TIRF, Nikon) by a sCMOS camera (5.5 megapixel, Neo, Andor Technology, UK) controlled *via* the software NIS Elements 4.5 (Nikon) and processed by the software ImageJ.

Sample Preparation

NRK cells (passage number 16 – 37) were seeded to confluence in white microplates with F-bottom or in 8 well inserts (Applied BioPhysics Inc.), glued upon microscopic slides. They were exposed to 12 nm UCNPs@PLM (50 μg·mL⁻¹) in different media at 4 °C or 37 °C for

different exposure times. After incubation the cell samples were prepared as described for the two-photon scanning microscope.

Wide-Field Upconversion Microscopy with $8 \text{ kW}\cdot\text{cm}^{-2}$ Irradiation

Setup

The inverted microscope IX71 (Olympus, Japan) with z-section capability was equipped with a 633 nm HeLa laser and a 974 nm laser (974 nm, cw, 350 mW, $8 \text{ kW}\cdot\text{cm}^{-2}$, Qphotonics, USA) for epi-illumination *via* a single mode fiber and a filter system to excite DiR or the Er^{3+} doped UCNPs. The long-pass excitation filter ($\lambda = 780 \text{ nm}$, Chroma, Kreuzau, Germany), a dichroic mirror ($\lambda = 875 \text{ nm}$, Chroma), and a short-pass filter ($\lambda = 700 \text{ nm}$, Chroma) were used to collect the green and red emission of the UCNPs. The filter system for the collection of the DiR emission consisted of a dichroic mirror ($\lambda = 635 \text{ nm}$, Semrock, New York, USA), a notch filter (633 nm, Semrock) and a long pass filter ($\lambda = 647 \text{ nm}$, Chroma). Images were taken with a 100 \times objective (NA ~ 1.49) upon 100 ms illumination time with an electron multiplying CCD camera (ImageEM X2 C9100-23B, Hamamatsu, Hamilton Township, USA). The setup was controlled by scripts within the MicroManager. The microscopy setup and procedure has been described in detail by F. Przybilla (University of Strasbourg, France, (Dukhno et al., 2018)).

Sample Preparation

NRK cells (passage numbers 16 – 23), CHO-hNTS₁Rs cells (passage numbers 7 – 9) or HT-29 cells (183 – 186) were seeded to confluence in cell culture medium in glass rings (d = 6 mm), glued in μ -dishes with glass bottom (ibidi GmbH, Gräfelfing, Germany) two days prior to the experiment. After 48 h the cells were treated with the dye 1,1-dioctadecyl-3,3,3,3-tetramethylindotricarbocyanine iodide (DiR, 2.5 μM in DPBS + 5% FBS (v/v), 1 $\text{mg}\cdot\text{mL}^{-1}$ glucose) at 37 °C and 0% CO_2 to visualize cell bodies and the nucleus. The DiR solution for co-staining was removed after 20 min and the cells were washed twice with the experimental buffer before particle suspensions were added for a certain time according to **Table 3.4**.

For the inhibition study NRK or CHO-hNTS₁R cells were preincubated with the inhibitors (200 μM dynasore, 0.45 M sucrose or 10 μM SR142948) 5 min prior to particle addition.

After incubation the cells were rinsed twice with pre-warmed DPBS and incubated with prewarmed paraformaldehyde (4% (w/v) in DPBS⁺⁺) at rt for 10 min. Finally, the cells were

washed three times with DPBS⁺⁺. Microscopic stacks were taken with 974 nm (8 kW·cm⁻²) illumination for UCNPs and 633 nm illumination for DiR staining.

Data Analysis

The focal plane providing a maximum of upconversion intensity and DiR stain was chosen for further data evaluation of internalization studies by ImageJ. The upconversion luminescence intensity per region of interest (ROI) of at least 25 ROIs (40 µm x 40 µm with 3 - 4 cells, > 25 ROIs from two independent cell passage numbers) was determined for every condition with ImageJ. The intensity per ROI was plotted in a box plot, showing the mean ± SEM, the median and 25 - 75% of the data points in the boxes.

Table 3.4. Overview of cell lines, applied particles, incubation media and incubation conditions for wide field upconversion microscopy studies.

cell line	UCNPs	incubation media	conditions
NRK Chapter 5	33 nm UCNPs@AP 33 nm UCNPs@PLM 15 nm UCNPs@PLM	DPBS ⁺⁺ (5% FCS, 1 mg·mL ⁻¹ glucose) L-15/DMEM (5 % FCS)	1 h, 6 h 37 °C, 0% CO ₂
	33 nm UCNPs@PLM + 0.45 M sucrose + 200 µM dynasore	DPBS ⁺⁺ (5% FCS, 1 mg·mL ⁻¹ glucose)	1 h 4 °C or 37 °C, 0% CO ₂
HT-29 Chapter 8	functionalized 33 nm UCNPs@PLM: naked-UCNPs naked-NT-UCNPs (der, PBS) click-NT-UCNPs (der, PBS)	DPBS ⁺⁻ (DPBS ⁻ , 0.18 mM CaCl ₂ , 1 mg·mL ⁻¹ glucose)	40 min, 2 h 37 °C, 0% CO ₂
	functionalized 33 nm UCNPs@PLM: naked-UCNPs naked-NT-UCNPs (der, PBS) click-NT-UCNPs (der, PBS)	DPBS ⁺⁻ (DPBS ⁻ , 0.18 mM CaCl ₂ , 1 mg·mL ⁻¹ glucose)	20 min 37 °C, 0% CO ₂
CHO-HNTS₁R Chapter 8	naked-UCNPs (der, PBS) click-NT-UCNPs (der, PBS)		20 min
	naked-UCNPs (der, PBS) click-NT-UCNPs (der, PBS) + 4 µM SR 142948		37 °C, 0% CO ₂

Fluorescence Confocal Laser Scanning Microscopy

Setup

The confocal laser-scanning microscope (CLSM) Eclipse 90i microscope (Nikon, Japan) was equipped with a C1 scanning unit, excitation lasers with 405 nm (for DAPI) and with 543 nm (for rose bengal) (Melles Griot, USA), and a fluorescence detector with a band pass filter

($\lambda = 435 \pm 50$ nm) and a longpass filter ($\lambda_{\text{cut-on}} = 650$ nm). Images were taken with a 60 \times objective (NA ~ 1.00) by the software EZ-C1 (Nikon) and processed by the software ImageJ.

Sample Preparation

NRK cells were seeded to confluence in glass rings (d = 6 mm), glued in petridishes. They were exposed to 15 nm or 24 nm UCNPs@AP/PLM/Lys-Rb ($50 \mu\text{g}\cdot\text{mL}^{-1}$) in different media at 37 °C for 3 – 24 h. After incubation the cell samples were prepared as described for the two-photon scanning microscope.

Electron Microscopy

NRK cells (passage number 18 and 29) were seeded to confluence on 12 mm coverslips in 24 well arrays (37 °C, 5% CO₂). After 48 h the culture medium was replaced by the 12 nm or 33 nm UCNPs@PLM suspension ($600 \mu\text{L}$, $50 \mu\text{g}\cdot\text{mL}^{-1}$ of 12 nm UCNPs@PLM or $200 \mu\text{g}\cdot\text{mL}^{-1}$ of 33 nm UCNPs@PLM in culture medium). The cells were incubated with the particles for 10 min, 1 h or 24 h at 37 °C and 5% CO₂. After a particular incubation time the cells were washed twice with prewarmed DPBS and fixed with prewarmed glutaraldehyde (2%, w/v, 0.1 M cacodylate buffer, pH 7.4) for at least 3 min. Cells were washed 3 \times 2 min with cacodylate buffer (0.1 M, pH 7.4) and 3 \times 2 min with water prior to the incubation with uranyl acetate (1%, w/v, H₂O) on ice for 60 min. Afterwards the samples were washed 5 \times 2 min with H₂O and dehydrated with ethanol (stepwise rising ethanol concentration 30 – 100%, each 2 \times 2 min) as well as acetone (2 \times 2 min). The samples were kept in a mixture of epon and acetone (1:1) for 5 min before the final hardening in epon at 30 °C for 1 h and at 60 °C for 2 – 3 h. The cover slips were flushed with liquid nitrogen. 70 nm thin cell sections were trimmed and cut with a diamond knife set on the microtome UC6 (Leica). Micrographs of the cell sections were taken with a transmission electron microscope (Zeiss 902) at 80 kV. All samples were prepared twice. These experiments were performed in cooperation with Prof. Witzgall's group. The first steps of the procedure were carried out by the author and continued by Helga Othmen after the fixation step. Images were taken by Helga Othmen. The results have been discussed with Prof. R. Witzgall and Prof. R. Rachel.

3.2.9 Cell Viability Assay PrestoBlue™

The PrestoBlue™ assay was used to determine the intrinsic toxicity of particles UCNPs@AP and UCNPs@PLM (**Chapter 5 and 6**) and to determine the cell death initiated by ROS production with UCNPs@AP-RB in the photodynamic therapy study (**Chapter 8**).

The cell viability assay PrestoBlue™ targets the cell metabolism with the dye resazurin. As far as the cells are viable and have an intact metabolism, they produce enough NADH to reduce irreversibly blue resazurin to red resorufin, which is detected fluorometrically ($\lambda_{\text{exc}} = 572\text{nm}$, $\lambda_{\text{em}} = 586\text{ nm}$) irreversibly.

NRK cells were seeded on 96W plates. After two days of cultivation, the UCNPs were added to the cells in different concentrations (100 μL , L-15, 5% FCS (v/v), 100 $\mu\text{g}\cdot\text{mL}^{-1}$ penicillin and 100 $\mu\text{g}\cdot\text{mL}^{-1}$ streptomycin) and incubated at 37 °C and 0% CO₂ for 14 – 72 h.

For the photodynamic therapy study, UCNPs@AP-RB were removed after 14 h, the cells washed three times with DPBS⁺⁺ before cells were kept in DPBS⁺⁺ (1 $\text{mg}\cdot\text{mL}^{-1}$ glucose) for the illumination with 528 nm (LED array, unknown power density) for 0 – 10 min. The cells were allowed to recover 2 h before their viability was examined.

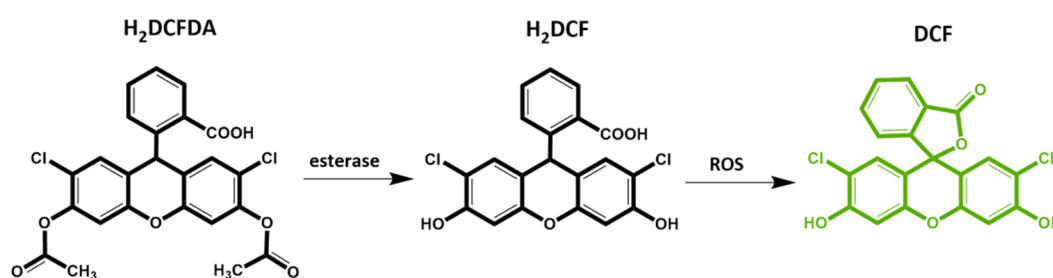
After aspiration of the particle solutions, the cells were incubated with the resazurin solution (100 μL , 10 $\mu\text{g}\cdot\text{mL}^{-1}$, DPBS⁺⁺, 1 $\text{mg}\cdot\text{mL}^{-1}$ glucose) at 37 °C and 0% CO₂ for 60 min. The fluorescence intensity was measured at $\lambda_{\text{em}} = 600\text{ nm}$ ($\lambda_{\text{exc}} = 532\text{ nm}$) with the microplate reader GENios (Tecan, Männedorf, Switzerland). A positive control (zero cell viability) was provided by treating cells with Triton X-100 (0.5%, v/v). A conversion of resazurin by UCNPs was excluded in cell-free experiments.

The PrestoBlue® assay was performed in three individual experiments with a three-fold replication for every condition. The blank corrected intensities of UCNPs treated (I_x) and non-treated (I_0) cells were determined for each of the three individual experiments to calculate the mean cell viability ($I_x/I_0\cdot 100\%$) with the corresponding error from the gaussian error propagation. The mean cell viabilities with error were used to determine the instrumental weighted mean \pm error from all data.

3.2.10 Detection of Reactive Oxygen Species

The DCF reactive oxygen species (ROS) assay is used to quantify the ROS production within the cells after UCNPS@AP-RB treatment and excitation of rose bengal (**Chapter 8**).

The fluorescence-based DCF assay, detecting reactive oxygen species, was performed with the ROS-sensitive dye 2',7'-dichlorofluorescein (DCF). The dye is applied to the cells in its lipophilic derivative H₂DCFDA to diffuse across the cell membrane but is turned intracellularly into its hydrophilic derivative H₂DCF by cellular esterases so that it cannot escape the cells anymore. It is oxidized to fluorescent DCF ($\lambda_{\text{exc}} = 498 \text{ nm}$, $\lambda_{\text{em}} = 522 \text{ nm}$) by ROS (**Scheme 3.13**).



Scheme 3.13. Principle of the DCF assay, including ester bond cleavage of H₂DCFDA by (cellular) esterases, oxidation of H₂DCF by ROS to fluorescent DCF.

NRK cells (passage number 18 – 23) were seeded to confluence in black 96 well plates to guarantee the excitation of individual wells in this assay and avoid light scattering from adjacent wells within the same well plate. Two days after seeding, cells were incubated with 15 nm UCNPs NaYbF₄(20%Er)@NaYF₄ or 24 nm NaYF₄(20%Yb,2%Er)@NaYF₄ (L-15, 5% FCS (v/v), 100 $\mu\text{g}\cdot\text{mL}^{-1}$ penicillin/streptomycin) at 37 °C and 0% CO₂ for 14 h. The particle solutions were removed and the cells were washed twice with DPBS⁺⁺ before exposure to H₂DCFDA (15 μM , DPBS⁺⁺, 1 $\text{mg}\cdot\text{mL}^{-1}$ glucose) for 30 min. Non-internalized H₂DCFDA was removed by gently washing the cells three times with DPBS⁺⁺ before cells were kept in DPBS⁺⁺ (1 $\text{mg}\cdot\text{mL}^{-1}$ glucose) for the irradiation with 528 nm (96 LED array, unknown power density) for 0 – 10 min. Non-irradiated wells were covered with aluminium foil during irradiation. The fluorescence intensity of DCF was measured ($\lambda_{\text{exc}} = 485 \text{ nm}$, $\lambda_{\text{em}} = 528 \text{ nm}$, bottom) before/after irradiation and after irradiation every 30 min for 3 h. In between, cells were incubated at 37 °C, 0% CO₂. Positive control for cellular ROS production was tert-butyl hydroperoxide (100 μM , DPBS⁺⁺, 1 $\text{mg}\cdot\text{mL}^{-1}$ glucose) without irradiation. The potential conversion of H₂DCFDA (15 μM , H₂O) by

irradiated or non-irradiated UCNPs ($100 \mu\text{g}\cdot\text{mL}^{-1}$, H_2O) was excluded in cell-free experiments. Cell-free and UCNPs-free but irradiated H_2DCFDA samples were used as blank to correct all obtained values.

The blank-corrected DCF intensities of UCNPs treated (I_x) and non-treated (I_0) cells was determined and the mean ratio of I_x/I_0 with corresponding error from gaussian error propagation was calculated for each independent experiments with three replicates. Three independent experiments were performed to determine the instrumental weighted mean with the corresponding error.

3.2.11 Radioligand Competition Binding Assay

HT-29 cells (passage number 176 – 180) were seeded to confluence in culture medium on white 96W plates with clear bottom (Corning Incorporated Life Science, Corning, USA). The radioligand competition binding assay was carried out by Lisa Schindler (PD Dr. Keller's working group). On the day of the experiment, the culture medium was removed and the cells were incubated with BSA (0.5% (w/v), DPBS^{+-} , $1 \text{ mg}\cdot\text{mL}^{-1}$ glucose, $100 \mu\text{L}$) for 20 min to reduce unspecific binding of particles to the cells. After removal of BSA-supplemented DPBS^{+-} , DPBS^{+-} ($80 \mu\text{L}$), the protease inhibitor bacitracin ($100 \mu\text{g}\cdot\text{mL}^{-1}$), the radioligand $[^3\text{H}]27$ ($10 \mu\text{L}$, 1 mM) and the competitor particles ($10 \mu\text{L}$) for the competition binding experiment were added to the cells. Unspecific binding was determined by DPBS^{+-} ($80 \mu\text{L}$) with $[^3\text{H}]27$ ($10 \mu\text{L}$, 1 mM) and NT(8-13) ($10 \mu\text{L}$, 500 mM) in excess. The cells were incubated with the competitor particles under gently shaking at 37°C and $0\% \text{ CO}_2$ for 2 h. After incubation, the supernatant was removed and the cells were washed twice with ice-cold PBS. Lysis solution was added ($25 \mu\text{L}$, H_2O , 8 M urea, 3 M acetic acid, 1% (w/v) Triton-X-100) to the cells and the plates were shaken for 30 min at rt. Liquid scintillator ($200 \mu\text{L}$) was added before the plates were sealed with a transparent sealing tape (permanent seal for microplates) and turned up-side down for a complete mixing of lysis solution and cells. After 1 h in the dark, the radioactivity (unspecific or total binding) was measured with a MicroBeta2 plate counter (PerkinElmer, Waltham, USA). Displacement of $[^3\text{H}]27$ or specific binding of $[^3\text{H}]27$ was determined out of unspecific binding-corrected total binding values of competitor particles (total binding(X)) or control (without particles, total binding (0)).

$$\text{displacement [\%]} = \frac{1}{\text{specific binding [\%]}} = \frac{\text{total binding}(0) - \text{unspecific binding}}{\text{total binding}(X) - \text{unspecific binding}}$$

All overview experiments were performed once with three replicates and the mean \pm SD was determined.

4 Small and Bright Water-Protected Upconversion Nanoparticles with Long-Time Stability in Complex, Aqueous Media

4.1 Preface

This paragraph summarizes collaborative research work in accordance with § 8 Abs. 1 Satz 2 Punkt 7 of the “Ordnung zum Erwerb des akademischen Grades eines Doktors der Naturwissenschaften (Dr. rer. nat.) an der Universität Regensburg vom 18. Juni 2009“.

The sections 4.2. – 4.7. of the following chapter were mainly adapted from:

“Small and Bright Water-Protected Upconversion Nanoparticles with Long-Time Stability in Complex, Aqueous Media”

Susanne Märkl, Alexandra Schroter, Thomas Hirsch, Nano Letters, 2020.

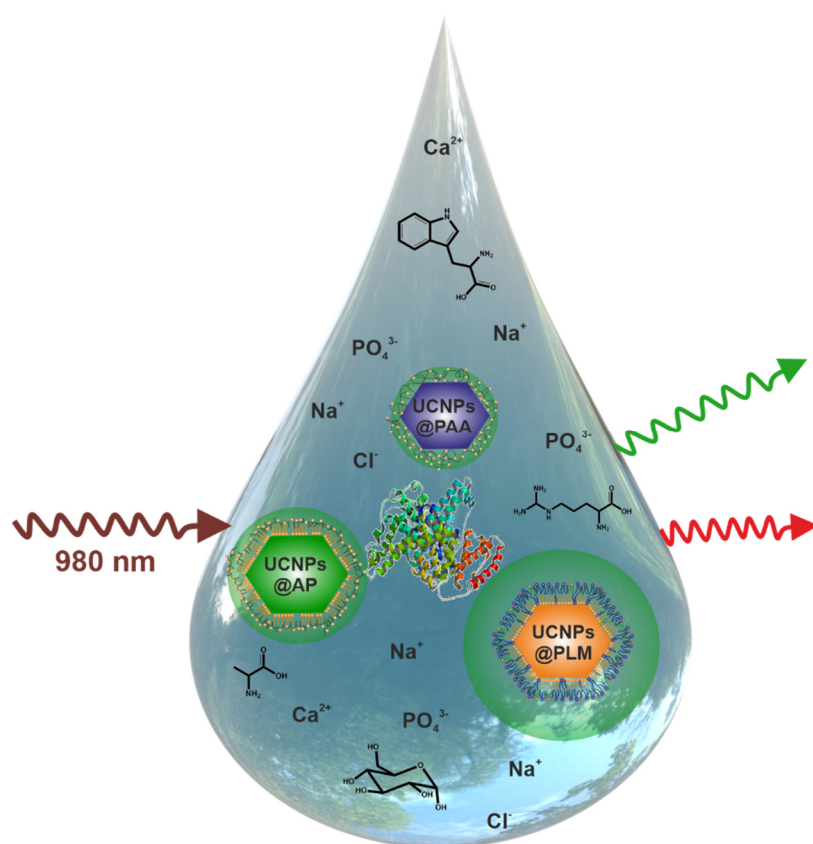
DOI: 10.1021/acs.nanolett.0c03327

Chapter 4.2. was adapted to the style of this thesis. Some results were discussed in more detail in **Chapter 4.3. – 4.7.** Additional sequences were added or adapted in the text. The **Figures 4.1. – 4.8.** were adapted from the publication. Most of the experimental and theoretical work presented in this chapter was carried out solely by the author. Synthesis strategies were discussed with Alexandra Schroter. The concept and structure of the publication was planned together with Dr. Thomas Hirsch. The author wrote the manuscript. Dr. Thomas Hirsch revised the manuscript and is corresponding author.

4.2 Introduction

Due to their unique ability to emit visible light upon excitation in the near-infrared (NIR) the upconversion nanoparticles (UCNPs) have attracted the interest of many researches promoting these luminescent probes in life science (DaCosta et al., 2014). Especially small nanoparticles are desired for bio applications, which has guided research in the direction to extend the established synthesis protocols for the preparation of monodisperse < 10 nm UCNPs (Wen et al., 2018). However, the reduction of the nanoparticle size increases the surface to volume ratio relative to the number of particles and, hence, a high luminescence quenching is reported (Muhr et al., 2017). If small UCNPs are dispersed in aqueous media, the upconversion efficiency will become critically low as the excited states of the rare earth ions can be quenched by water (Wilhelm et al., 2015). Different approaches have been considered to enhance the upconversion luminescence efficiency, *e.g.* by variations in the particle architecture and composition, or by decorating the particle surface with organic ligands for energy harvesting (Wiesholler et al., 2018; Schroter et al., 2022). So far, only little attention has been attributed to the ligands to protect the particle surface against quenching. Besides quenching water molecules at the particle surface are also known to trigger particle degradation and the release of rare earth ions, possibly undergoing undesired interactions with biomaterials (Li et al., 2015). Moreover, poor colloidal stability of particles has been reported in buffers, at acidic or basic pH, and in high ionic strength media, leading to precipitation and aggregation (Mandl et al., 2019; S. Wilhelm, 2017; Plohl et al., 2017a). Thus, surface protection of the nanoparticles is highly desired and needs to be ensured when it comes to *in vitro* or *in vivo* applications (Saw et al., 2020). Most synthesis protocols for UCNPs end up with a hydrophobic coating so that further modification is required anyway to render them dispersible in aqueous solution. Different surface strategies are well-known to stabilize UCNPs in water (V. Muhr et al., 2014). The most versatile modification, the ligand exchange strategy, suffers from a low surface coverage, independently how strong the interaction between particle and ligand area (Himmelstoß et al., 2019). Motivated by this, the shielding properties of various coatings on small ~10 nm UCNPs are compared to identify a suitable particle system for biomedical applications. The surface coatings in focus of this study are hydrophobic barrier forming amphiphilic bilayers. The representative for ligand exchange is

poly(acrylic acid) (PAA), which is known for its colloidal stability in some applications (Rafique et al., 2018; Liu et al., 2015). The amphiphilic bilayers consist of oleate with either an amphiphilic polymer (AP) or with lipids to form a phospholipid membrane mimicking bilayer (PLM). So far, the self-assembling phospholipid bilayers have been applied to disperse large Tm^{3+} doped UCNPs in water (Rojas-Gutierrez et al., 2016; Meijer et al., 2019). In this work, small Er^{3+} -doped particles demonstrate for the first time the outstanding protection of small UCNPs by PLM coatings against disintegration and agglomeration in water, phosphate buffer, in a wide pH range, in high ionic solutions, and in complex cell media with minimized loss of the brightness of the upconversion luminescence due to water quenching (**Scheme 4.1**).



Scheme 4.1. Surface modified particles UCNPs@PAA, UCNPs@AP and UCNPs@PLM tackle the challenges upon dispersion in biological media differently: I) water quenching of upconversion luminescence (green and red) upon irradiation with 980 nm light, II) colloidal destabilization due to high ionic strength, III) destabilizing Ca^{2+} and phosphate ions, IV) and attachment/ligand substitution with (de-) stabilizing sugars, vitamins, amino acids, and serum proteins.

4.3 Particle Preparation and Characterization

Small and hexagonally shaped predominantly green emitting upconversion nanoparticles with NaYF₄ as host lattice and the dopants Yb³⁺ and Er³⁺ were prepared by a modified protocol developed by Haase *et al* (Rinkel et al., 2014). The core particles had a diameter of 8.4 ± 0.8 nm and an elemental composition of $(21.6 \pm 0.3)\%$ Yb³⁺ and $(2.34 \pm 0.04)\%$ Er³⁺, analyzed by inductively coupled plasma atomic emission spectroscopy (ICP-OES, **Table 4.1**). They were protected by a ~ 1.5 nm inert shell of NaYF₄ which leads to a 50-fold increase of the green luminescence (**Figure 4.1D**). The average diameter of this oleate (OA) coated core-shell nanoparticles NaYF₄(Yb,Er)@NaYF₄ is (11.7 ± 0.9) nm according to statistical transmission electron micrograph (TEM) analysis (**Figure 4.1A,B**). The low polydispersity index of (0.10 ± 0.02) obtained from dynamic light scattering ($1 \text{ mg}\cdot\text{mL}^{-1}$ in cyclohexane) proved that the particles are monodisperse in solution (**Figure 4.1C**). The comparison of the X-ray powder diffraction pattern of the core-shell particles with the standard pattern of cubic and core phase NaYF₄ confirmed the hexagonal crystal lattice (**Figure 4.1**).

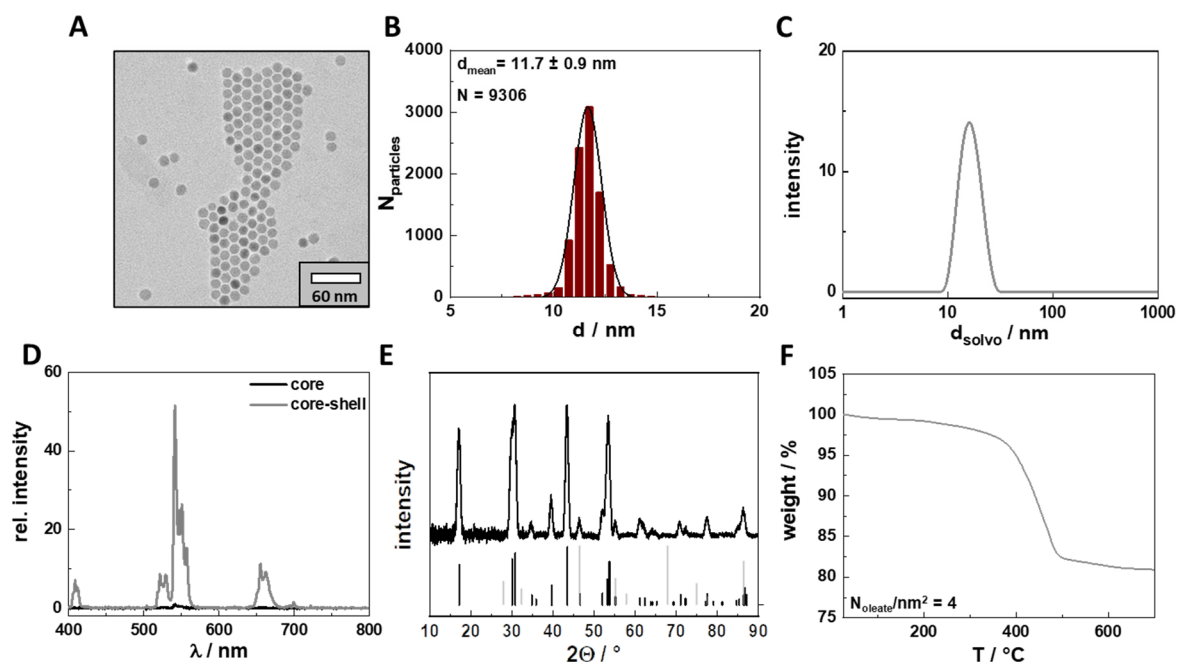


Figure 4.1. Characterization of oleate coated core-shell nanoparticles $\text{NaYF}_4(\text{Yb,Er})@\text{NaYF}_4$: (A) Transmission electron micrograph (scale bar 60 nm) and (B) corresponding particle size distribution (mean \pm SD) of (11.7 ± 0.9) nm, (C) representative intensity weighted particle size distribution in cyclohexane ($1 \text{ mg} \cdot \text{mL}^{-1}$) measured by dynamic light scattering ($N = 3$) at rt, (D) luminescence spectra in comparison to core particles in cyclohexane ($1 \text{ mg} \cdot \text{mL}^{-1}$, normalized to N_{UCNPs}) upon NIR excitation at rt, (E) X-Ray powder diffraction pattern (above) with standard pattern (below) of hexagonal (black, ICDD PDF #16-0334) and cubic (grey, ICDD PDF #39-0724) phase NaYF_4 and (F) thermogravimetric analysis with calculated amount of oleate ligands per nm^2 nanoparticle surface: $N_{\text{oleate}}/\text{UCNPs} = 400$, 77% surface coverage.

An analogous particle with blue emission based on Tm^{3+} activator ions was prepared and characterized in a similar way. 8.8 nm $\text{NaYF}_4(\text{Yb,Tm})$ core particles with an elemental composition of $\sim 75.8\% \text{ Y}^{3+}$, $\sim 23.7\% \text{ Yb}^{3+}$ and $\sim 0.576\% \text{ Tm}^{3+}$ (**Table 4.1**) were coated with an ~ 1.5 nm inert shell to obtain (11.4 ± 1.5) nm oleate coated core-shell particles $\text{NaYF}_4(\text{Yb,Tm})@\text{NaYF}_4@\text{OA}$ (**Figure 4.2A,B**). Their crystal lattice is hexagonal and they are monodisperse in solution according to X-ray diffraction and DLS measurements (**Figure 4.2C,D**). Their similar characteristics in size, crystal lattice, and monodispersity make the Tm^{3+} doped particles ideal for comparative studies with the Er^{3+} doped ones.

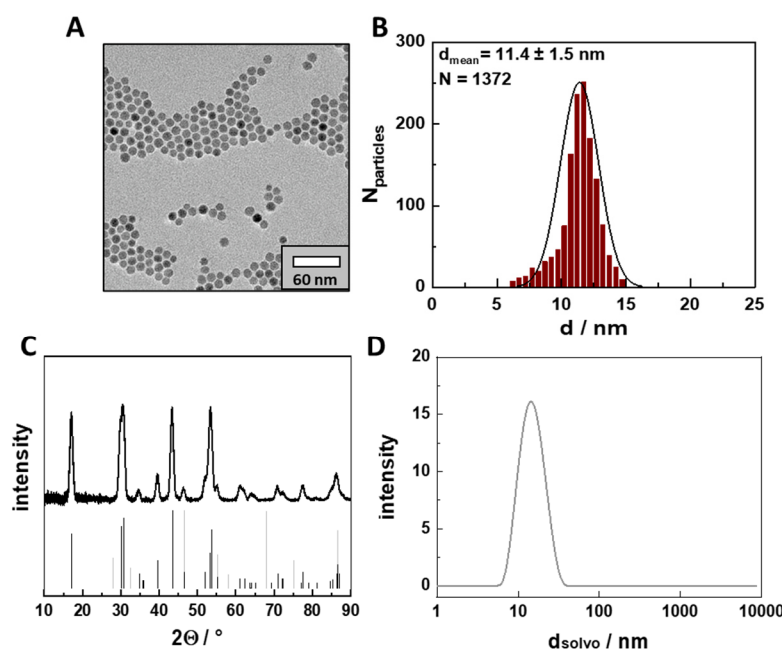


Figure 4.2. TEM images and corresponding particle size distributions (mean \pm SD) of oleate coated (11.4 ± 1.5) nm core-shell particles $\text{NaYF}_4(24\%\text{Yb}, 0.5\%\text{Tm})@\text{NaYF}_4$ (with (8.8 ± 0.9) nm core particles). X-ray powder diffraction pattern (above) of these particles with standard pattern (below) of hexagonal (black, ICDD PDF #16-0334) and cubic (grey, ICDD PDF #39-0724) phase NaYF_4 . (D) Representative intensity weighted particle size distribution in cyclohexane ($1 \text{ mg}\cdot\text{mL}^{-1}$) measured by dynamic light scattering at rt ($N = 3$).

Table 4.1. Composition of Er^{3+} and Tm^{3+} doped core and core-shell UCNP determined by ICP-OES.

	$[\text{Y}^{3+}] / \%$	$[\text{Yb}^{3+}] / \%$	$[\text{Er}^{3+}] / \%$	$[\text{Tm}^{3+}] / \%$
$\text{NaYF}_4(\text{Yb}, \text{Er})$	76.2 ± 0.2	21.6 ± 0.3	2.34 ± 0.04	-
$\text{NaYF}_4(\text{Yb}, \text{Er})@\text{NaYF}_4$	79.5 ± 0.5	18.6 ± 0.1	1.92 ± 0.01	-
$\text{NaYF}_4(\text{Yb}, \text{Tm})$	75.8 ± 0.5	23.7 ± 0.2	-	0.576 ± 0.001
$\text{NaYF}_4(\text{Yb}, \text{Tm})@\text{NaYF}_4$	88.7 ± 0.6	10.94 ± 0.04	-	0.359 ± 0.001

4.4 Surface Modification of Upconversion Nanoparticles with Phospholipid Membrane Coating

The oleate molecules, stabilizing the Er^{3+} doped UCNP with 77% surface coverage (4 OA molecules per nm^2 , TGA, **Figure 4.1**), serve as basis for the development of a surface

modification with a reduced permeability for water and ions. However, since the inverted cone-shaped oleate molecules do not cover the whole surface of the nanoparticle, cone-shaped phospholipids and cholesterol can fill the remaining places to form, together with OA, a planar inner leaflet at the surface in accordance with the geometric packing theory (Israelachvili et al., 1976; Cullis et al., 1986; Mouritsen, 2011; McMahon et al., 2015; Klose et al., 2013). It is assumed, that the lipids also attach to the edges of the hexagonal UCNP since these molecules have the tendency for negative curvature aggregates (cf. **Figure 4.3A**) (Zegarlińska et al., 2018). Building up an outer leaflet as well, a lipid mixture was used to form together with the attached oleate (OA) a dense biological membrane mimicking a phospholipid membrane (PLM) (P. A. Rojas-Gutierrez et al., 2016). Here, the lipid 1,2-dioleoyl-sn-glycero-3-phosphate (DOPA, 64%) was the main component and 1,2-dioleoyl-sn-glycero-3-phosphoethanolamine (DOPE, 7%) was added to minimize ionic repulsion and to stabilize the membrane by hydrogen bonding (May et al., 2008; Kooijman et al., 2007). Cholesterol (29%) integrates into the bilayer between OA and the phospholipids to increase the hydrophobicity of the membrane.

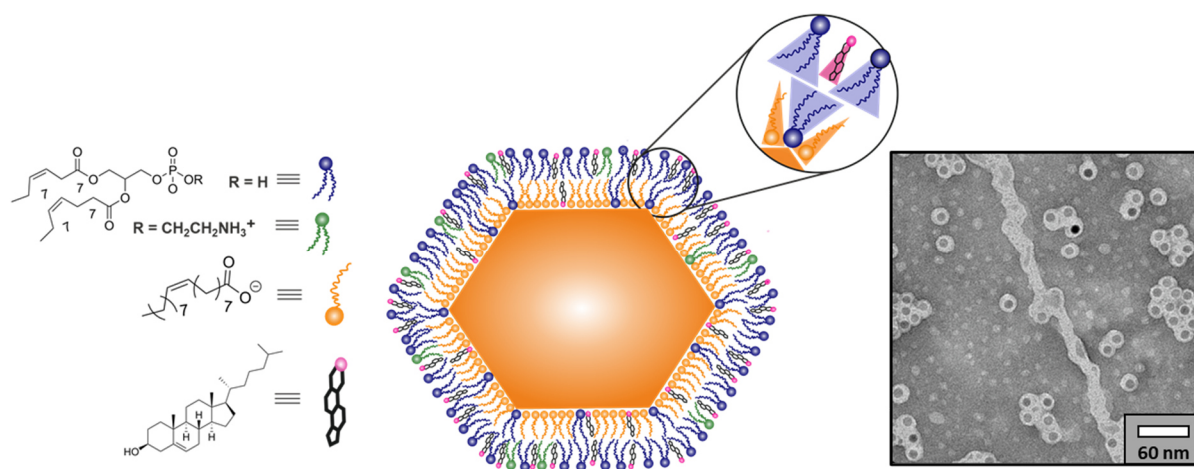


Figure 4.3. Schematic overview of the phospholipid membrane attaching to the particle and negative staining TEM image of phospholipid membrane wrapped UCNP NaYF₄(Yb,Er)@NaYF₄@PLM with 1% phosphotungstic acid.

A study of various amounts of cholesterol showed that higher contents than 29% cannot further improve the upconversion luminescence of the particle (**Figure 4.4**), which implies that no denser lipid packing can be achieved with this approach around the ~12 nm UCNP.

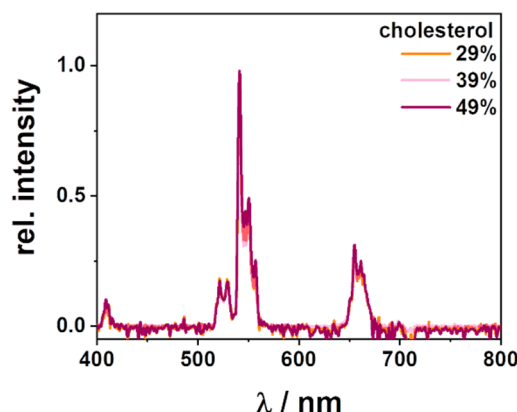
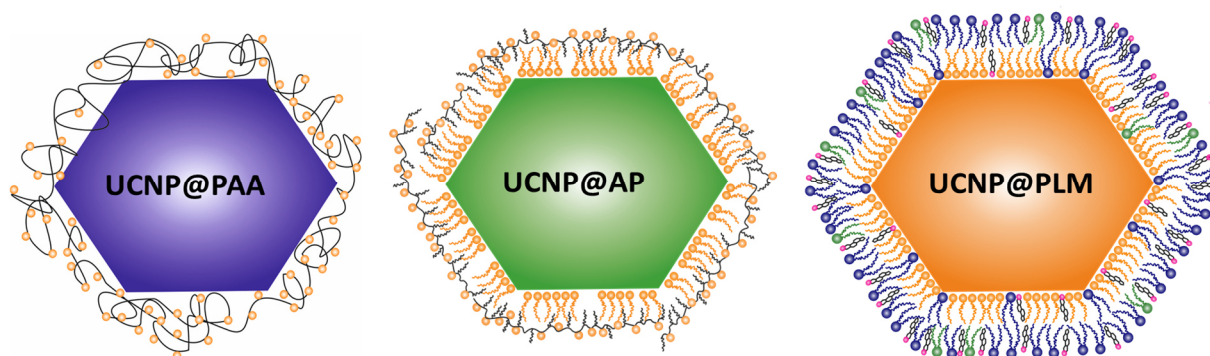


Figure 4.4. Luminescence spectra of PLM coated UCNP prepared with a lipid mixture containing 29%, 39% or 49% in H₂O upon irradiation with 980 nm at $\sim 85 \text{ W}\cdot\text{cm}^{-2}$ at rt ($1 \text{ mg}\cdot\text{mL}^{-1}$, normalized to N_{UCNPs}).

Due to the high surface-to-volume ratio enveloping small hexagonal shaped UCNP by a PLM requires special care. It is important to assure a homogeneously mixed and well dried film of lipids and UCNP before hydrating since micelle formation is favored in organic - aqueous solvent mixtures (Nagarajan, 2002). Electrostatic repulsion of the ionic surfactant DOPA at the surface of the nanoparticle is further reduced by adding a salt as sodium chloride to the hydration medium. The hydration process in the formation of PLM coated UCNP demands high temperatures of $\sim 70^\circ\text{C}$ to minimize steric repulsion of the unsaturated fatty acids (Nagarajan, 2002). Paying attention to these parameters during the hydration step enhances the total yield of PLM functionalized UCNP (lipid mixture: 64% DOPA, 7% DOPE and 29% cholesterol) after all purification steps to $\sim 60\%$. The negative stained TEM images visualize the phospholipid membrane enveloped UCNP and reveal well-separated UCNP@PLM (**Figure 4.3B**).

The PLM coating was compared in terms of brightness and stability to the poly(acrylic acid) (PAA) ligand and to an amphiphilic polymer (AP) bilayer coating consisting of poly(isobutyl-maleic anhydride) with 75% dodecylamine side chains (**Scheme 4.2**).



Scheme 4.2. Overview of modified particles for this study: poly(acrylic acid) (PAA), amphiphilic polymer (AP), and phospholipid membrane (PLM) coated particles UCNPs@PAA, UCNPs@AP, and UCNPs@PLM.

4.5 Colloidal Stability of Upconversion Nanoparticles in Water

The colloidal stability of the particles was examined by DLS measurements, zeta potential measurements and TEM analysis (**Figure 4.5, Table 4.2**). Particles modified with PAA, AP, or PLM showed one peak with a low polydispersity index ~ 0.2 in the DLS measurements in H_2O . TEM micrographs of the Er doped UCNPs in H_2O indicated single particles, adjoined each other but did not stick together. These two analyses together with zeta potentials < -30 mV confirmed the colloidal stability of the particles in water. Long-time DLS measurements showed only slight d_{hydro} fluctuations of 0.4% for UCNPs@PLM and higher d_{hydro} fluctuations of 18% and 33% for polymer coated particles UCNPs@AP and UCNPs@PAA. These demonstrates the excellent colloidal stability of the UCNPs@PLM for at least 2.5 months at 6 °C.

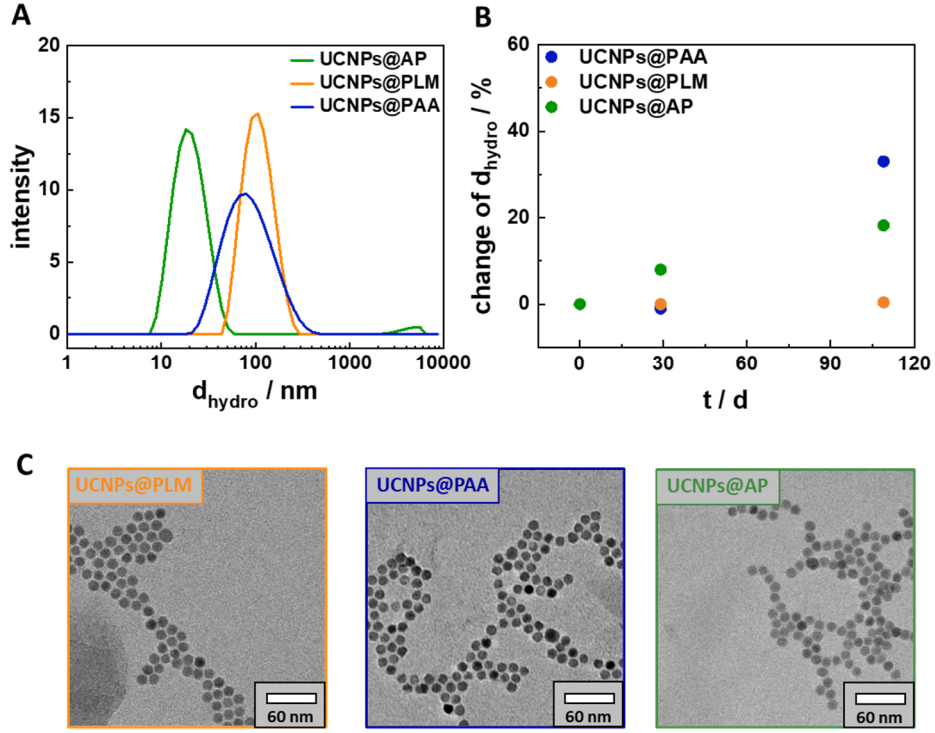


Figure 4.5. (A) Representative DLS measurement at rt ($t = 0$ d, $N = 3$), (B) time dependent change of hydrodynamic diameter (d_{hydro} , mean \pm SD, note that SD are small) and (C) TEM images of Er doped UCNPs modified with AP, PLM or PAA in H_2O ($t = 109$ d, stored at 6°).

Table 4.2. Solvodynamic diameter (d_{solv} , mean \pm SD) with corresponding polydispersity index (Pdl, mean \pm SD) and zeta potential (ζ , mean \pm SD) of OA and surface modified UCNPs^{Er} NaYF₄(Yb,Er)@NaYF₄ and UCNPsTm NaYF₄(Yb,Tm)@NaYF₄ with phospholipid bilayer (PLM), poly(aycrylic acid) (PAA) and amphiphilic polymer AP measured at rt.

particle system	d_{solv} / nm	Pdl	ζ / mV
UCNPs ^{Er} @OA	16.15 ± 0.08	0.10 ± 0.02	-
UCNPs ^{Er} @PLM	100 ± 1	0.11 ± 0.02	-36.9 ± 0.3
UCNPs ^{Er*} @PAA	73.1 ± 0.5	0.184 ± 0.005	-37 ± 1
UCNPs ^{Er} @AP	17.34 ± 0.04	0.221 ± 0.002	-39 ± 1
UCNPs Tm @OA	14.1 ± 0.3	0.11 ± 0.05	-
UCNPs Tm @PLM	101.2 ± 0.2	0.19 ± 0.01	-
UCNPs Tm @PAA	55 ± 1	0.18 ± 0.01	-
UCNPs Tm @AP	20.09 ± 0.09	0.19 ± 0.01	-

4.6 Brightness of Upconversion Nanoparticles in Aqueous Media

In water, the Er^{3+} emissions are prone to non-radiative deactivation by O-H-vibrations, which perfectly match the gaps of higher energy levels of the Er^{3+} ion (**Figure 4.6A**). The extent of the quenching gets obvious by comparing the small PLM wrapped particles in H_2O to those prepared in D_2O . Without any presence of O-H vibrations, the green luminescence is 13-times more intense (**Figure 4.6B**). These PLM coated UCNPs in D_2O are considered as the particles with the highest brightness. Even more critically is the fact that water molecules do not only negatively affect the luminescence properties but also trigger particles' disintegration when highly diluted (Dukhno et al., 2018; S. Wilhelm, 2017). Therefore, an excellent protection by the ligands is needed to maintain brightness and stability of small UCNPs in aqueous media. When the UCNPs were modified *via* ligand exchange by PAA, the intensity of the green upconversion luminescence in water is reduced by a factor of ~ 20 compared to the aforementioned brightest UCNPs@PLM dispersed in D_2O ($85 \text{ W}\cdot\text{cm}^{-2}$, **Figure 4.6B**). The total upconversion luminescence of particles with AP bilayer increases in intensity in water by $\sim 70\%$, while those with PLM coating are $> 700\%$ brighter than PAA coated ones (**Figure 4.6C**). Ligand exchange coatings as PAA render the particles water-dispersible, but they do not serve as a hydrophobic barrier. Consequently, water can easily get access to the surface of the nanoparticles, which was also revealed by DLS. The UCNPs@PAA have a hydrodynamic diameter of $73.1 \pm 0.5 \text{ nm}$ suggesting the PAA coating as a very loose and disordered one (**Table 4.2**). Differently to that, an AP can be directly attached to OA coated UCNPs to form a hydrophobic bilayer, which is pretty compact as the smaller hydrodynamic diameter compared to UCNPs@PAA suggests ($17.34 \pm 0.04 \text{ nm}$, **Table 4.2**). The protection by the amphiphilic bilayer is already visible in the brightness increase of UCNPs@AP compared to UCNPs@PAA (**Figure 4.6C**). Nevertheless, an amphiphilic polymer cannot develop a highly ordered bilayer with the OA as self-assembling lipids do. The barrier function of the phospholipid membrane is actually bigger as the green Er^{3+} emission is enhanced by $> 700\%$, compared to the PAA coated UCNPs. An image of the differently modified UCNPs in cuvette upon irradiation depicts the different brightness and hence the barrier function of the particles (**Figure 4.6D**).

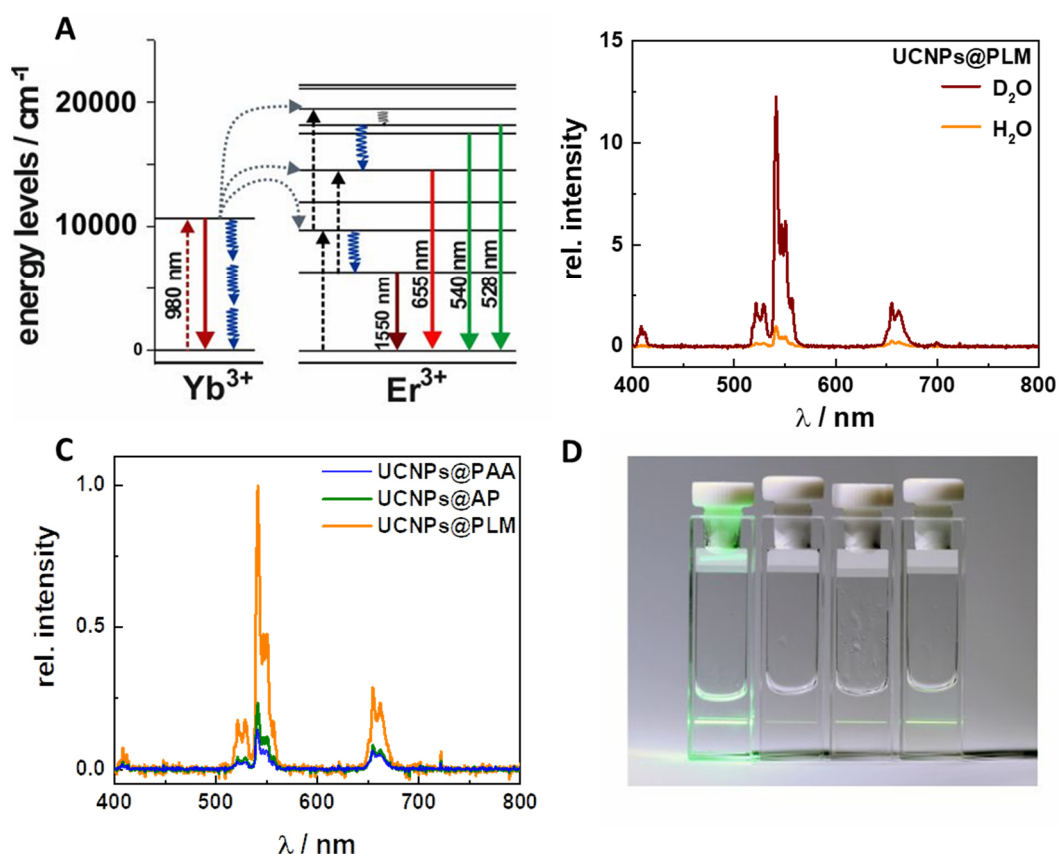


Figure 4.6. (A) Energy level diagram of UCNPs consisting of the activator/sensitizer pair $\text{Yb}^{3+}/\text{Er}^{3+}$ with dashed and solid arrows representing photon absorption and emission and blue zigzag arrows representing non-radiative deactivation by O-H vibrations. (B) Luminescence spectra of PLM modified 11.6 nm UCNPs $\text{NaYF}_4(\text{Yb},\text{Er})@\text{NaYF}_4$ ($1 \text{ mg}\cdot\text{mL}^{-1}$) at rt in H_2O and D_2O upon irradiation with 980 nm ($85 \text{ W}\cdot\text{cm}^{-2}$, power densities were corrected by the absorption of the solvent, spectra normalized to N_{UCNPs}). (C) Luminescence spectra of PAA, AP, or PLM modified 11.6 nm UCNPs $\text{NaYF}_4(\text{Yb},\text{Er})@\text{NaYF}_4$ ($1 \text{ mg}\cdot\text{mL}^{-1}$) at rt in H_2O . (D) Images of cuvettes containing OA, PAA, AP, or PLM coated 11.6 nm UCNPs $\text{NaYF}_4(\text{Yb},\text{Er})@\text{NaYF}_4$ ($1 \text{ mg}\cdot\text{mL}^{-1}$) in cyclohexane or H_2O upon irradiation with 980 nm at $85 \text{ W}\cdot\text{cm}^{-2}$ (spectra normalized to N_{UCNPs}).

Assuming that the increasing brightness reflects the protection of the particles against water, Tm^{3+} doped UCNP systems were analyzed to prove this hypothesis. Unlike for Er^{3+} energy levels, O-H vibrations do not deactivate higher-state energy levels of Tm^{3+} and, hence, the Tm^{3+} emissions should not be affected by water (**Figure 4.7A**). **Figure 4.7B** depicts the luminescence spectra of PAA, AP and PLM coated Tm^{3+} -doped UCNPs in water upon irradiation with 980 nm. Here, almost identical luminescence intensities for all particle systems in water are observed indicating that water protection does not have any influence on the Tm^{3+} emissions. In contrast to the Er^{3+} emissions, none of the Tm^{3+} emissions are

quenched by water. The differences in the luminescence intensities of various modified Er^{3+} doped UCNPs can be clearly assigned to a varying amount of water molecules penetrating the coating of the nanoparticles.

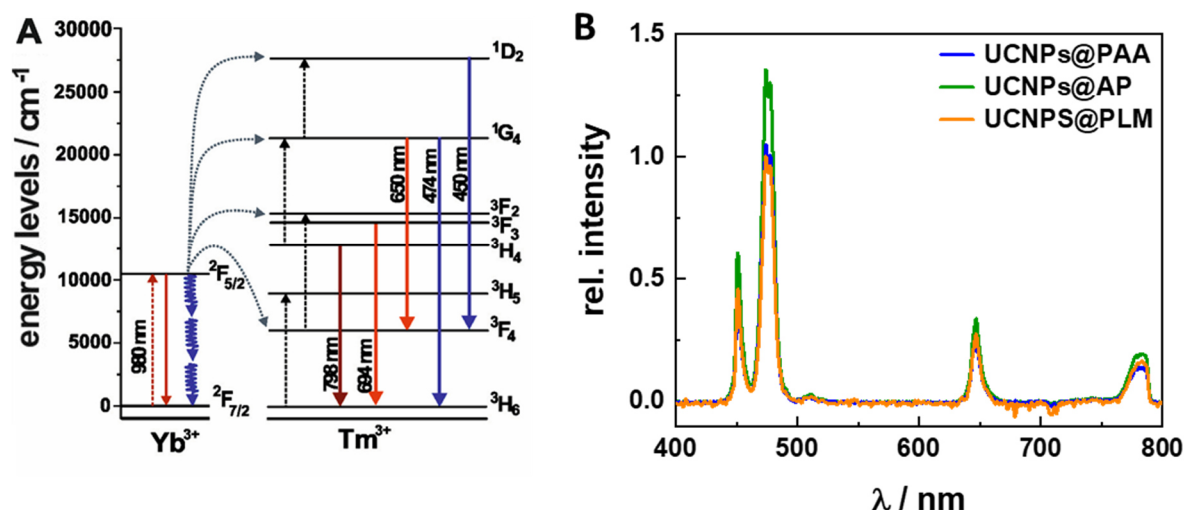


Figure 4.7. (A) Energy level diagram of UCNPs consisting of the activator/sensitizer pair $\text{Yb}^{3+}/\text{Tm}^{3+}$. (B) Luminescence spectra of AP, PLM, or PAA coated 11.4 nm UCNPs $\text{NaYF}_4(\text{Yb,Tm})@\text{NaYF}_4$ ($1 \text{ mg} \cdot \text{mL}^{-1}$) at rt in H_2O upon irradiation with 980 nm at $\sim 85 \text{ W} \cdot \text{cm}^{-2}$ (spectra normalized to N_{UCNPs}).

Differently modified UCNPs with Er^{3+} or Tm^{3+} doping demonstrated that the best protection with the lowest water permeability was achieved by a hydrophobic barrier of closely packed phospholipids with OA and cholesterol. It is suggested that the nanoparticles wrapped with a phospholipid bilayer, independently of the dopant ions, have an increased long-time stability in highly diluted aqueous media. A detailed study on the chemical stability of modified particles is shown in **Chapter 5**.

4.7 Colloidal Stability of Upconversion Nanoparticles in Ionic Solutions

For using such probes in *in vitro* or even *in vivo* applications, it is important to get colloidal stability over a wide range of pH, ionic strength, and in presence of complex media such as cell culture media. Here, the influence of various ions and buffers in physiological concentrations on the stability of the particle system with the lowest water permeability, UCNPs@PLM ($0.2 \text{ mg} \cdot \text{mL}^{-1}$) are examined individually by monitoring the green emission (area

under the curve from 510 to 570 nm, $AUC_{510-570\text{ nm}}$), hydrodynamic diameter (d_{hydro}), and zeta potential (**Figure 4.8**).

To analyze the colloidal stability of UCNPs@PLM at various pH values the buffers phosphate (1.8 mM, pH 7.4), carbonate (44.0 mM, pH 9.2), both in physiological concentrations, and acetate (10.0 mM, pH 4) were picked. The zeta potential of the UCNPs stays around -50 mV and -55 mV in almost neutral (phosphate buffer, pH 7.4) and basic (carbonate pH 9.2) conditions within 96 h and is just constantly a little bit higher with -36 mV at pH 4 (acetate buffer). The particles do neither show big changes of d_{hydro} and $AUC_{510-570\text{ nm}}$ when they were diluted in acetate or carbonate buffer nor in the critical phosphate buffer (**Figure 4.8A-C**). Small changes of both values are due to attaching ions to the PLM in the first hours and due to laser fluctuations within the 96 h.

The high ionic strength solution of the monovalent salt NaCl (138 mM) does not affect the stability of the particles as constant hydrodynamic diameters and green emissions show (**Figure 4.8D-F**). UCNPs@PLM are also not destabilized by Cl^- with the counter ion K^+ (5.3 mM KCl) and by Na^+ with counter ion SO_4^{2-} (0.8 mM Na_2SO_4). Zeta potentials of UCNPs in the salt solutions remain constant during the measurement time. The potentials range from -36 mV and -55 mV in monovalent salt solutions but are lower at around -16 mV when divalent cations coordinate to the PLM. Mg^{2+} (1 mM MgCl_2) does not disturb the particles as there is just a small increase of the d_{hydro} , which might be due to headgroup swelling (Binder et al., 2002; Alsop et al., 2016) However, coordinating Ca^{2+} (1.8 mM CaCl_2) changes the lipophilic coating around the particles, which can be observed by increasing d_{hydro} and decreasing $AUC_{510-570\text{ nm}}$ until a stable signal is obtained 48 h after dissolution in CaCl_2 solution.

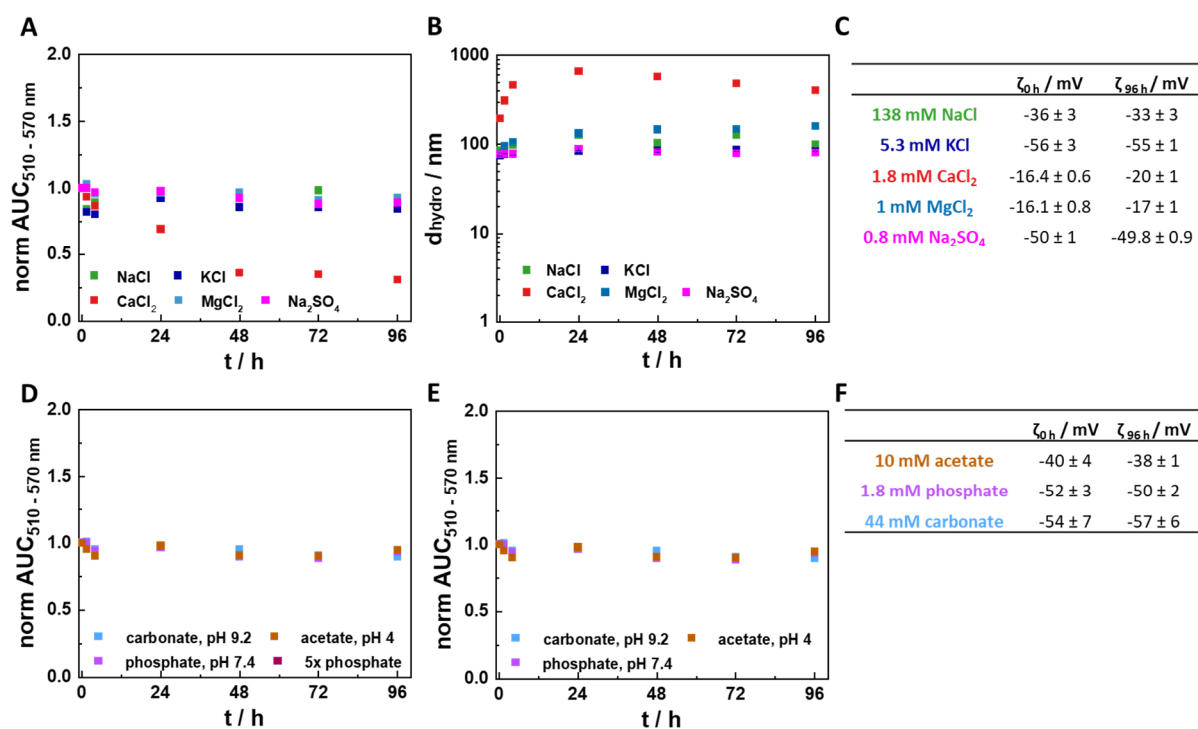


Figure 4.8. Influence of (A, B, C) various ions (138 mM NaCl, 5.3 mM KCl, 1 mM MgCl_2 , 1.8 mM CaCl_2 , 0.8 mM Na_2SO_4), (D, E, F) pH values (1.8 mM phosphate at pH 7.4, 44 mM carbonate at pH 9.2) at physiological concentrations, and acetate buffer (10 mM at pH 4) on the stability of the particles UCNPs@PLM ($0.2 \text{ mg} \cdot \text{mL}^{-1}$) measured by the area under the green curve ($\text{AUC}_{510-570 \text{ nm}}$) upon irradiation with 980 nm (cw, $85 \text{ W} \cdot \text{cm}^{-2}$, normalized to N_{UCNPs}), the hydrodynamic diameter (d_{hydro} , mean \pm SD, $N = 3$), and the zeta potential (ζ , mean \pm SD, $N = 3$) for 96 h at rt.

It is recommended to start luminescence measurements in salty media or in complex cell media after a few hours when the signal is constant as there are also small fluctuations of $\text{AUC}_{510-570 \text{ nm}}$ of UCNPs@PLM in the other ionic solutions in the first few hours. Special attention must be paid to UCNPs in Ca^{2+} containing media, especially when there are no additives with stabilizing effects as in cell medium without fetal calf serum (FCS) as the signal changes a lot in pure Ca^{2+} solution within the first 48 h. From all particle hydration and storage media it turned out that storage of the UCNPs in HEPES buffer (10 mM, pH 7.4) is most suited for applications in physiological fluids compared to H_2O and NaCl (15 mM).

4.8 Colloidal Stability of Upconversion Nanoparticles in Isotonic Buffer and Media

Stability in Serum-Supplemented Media

In general, most of the *in vitro* studies are performed as pre-check for future *in vivo* applications and should be carried out in an environment imitating the future biological matrix as good as possible since biotransformation of nanomaterials may occur, potentially changing their nanotoxicity, pharmacological profile, and applicability. Therefore, serum protein-supplemented cell culture medium is often the medium of choice and it is required that the desired particles are colloidal stable under these conditions.

The colloidal stability of UCNPs with Er^{3+} ions with basic PAA, AP, or PLM coating was tested in different FCS-supplemented media *via* DLS. **Figure 4.9** shows the comparison of hydrodynamic diameters of the particles in H_2O and DMEM (5% FCS). UCNPs@PAA aggregate upon dilution in DMEM (5% FCS), while UCNPs@AP and UCNPs@PLM remain stable. The d_{hydro} of UCNPs@AP increased from $(18.7 \pm 0.2 \text{ nm})$ in H_2O to $(93 \pm 3) \text{ nm}$ in DMEM (5% FCS). The increase of d_{hydro} can be attributed to the formation of a protein corona around the UCNPs (Latreille et al., 2022; Casals et al., 2010). In contrast, an increase is not observed for the UCNPs@PLM with d_{hydro} of $(102 \pm 1) \text{ nm}$ in H_2O and of $(97 \pm 2) \text{ nm}$ in DMEM (5% FCS). However, as the UCNPs@PLM are not stable in DMEM without FCS, the formation of a stabilizing protein corona around the UCNPs could be assumed in DMEM, supplemented with FCS (data not shown here). The hydrodynamic diameters of UCNPs@PLM are already relatively high in H_2O , compared to other surface coatings and the actual diameter of the bare crystals. Large d_{hydro} of UCNPs@PLM has also been observed by other work groups (Meijer et al., 2019). This may be due the formation of large hydrate shells around phosphate groups decorating the main part of the UCNPs@PLM surface. These shells may be masked when the particles are further coated with proteins due to two effects, cancelling out each other. (I) The proteins hide the phosphate groups, potentially leading to a less thick hydrate shell and hence a reduction of d_{hydro} . (II) The protein corona itself may also contribute to the ligands and increase d_{hydro} . Thus, the final d_{hydro} of UCNPs@PLM with protein corona in DMEM (5% FCS) might almost remain the same as in H_2O .

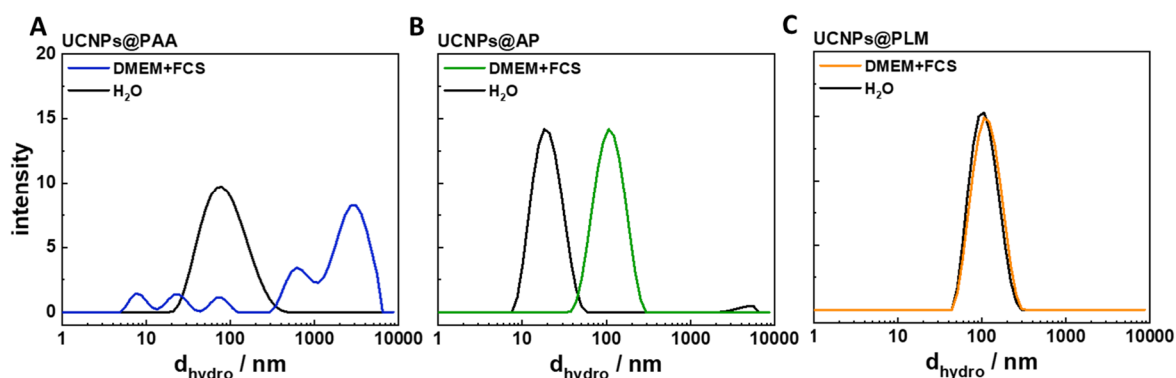


Figure 4.9. Representative intensity weighted hydrodynamic diameters (d_{hydro}) of 12 nm $\text{NaYF}_4(\text{Yb,Er})@ \text{NaYF}_4$ core-shell particles ($0.4 \text{ mg} \cdot \text{mL}^{-1}$) (A) UCNPs@PAA, (B) UCNPs@AP, and (C) UCNPs@AP at rt in H_2O or DMEM (5% FCS). Y-axes have the same scale.

UCNPs@PAA were not stable in DMEM (5% FCS) and L-15 (5% FCS), while UCNPs@AP and UCNPs@PLM are stable for at least 4 days, confirming their applicability in these media (**Figure 4.10**). However, some batches of UCNPs@PLM were not stable in L-15 (5% FCS) but in DMEM (5% FCS) (data not shown here). It was assumed, that the four times higher number of amino acids in L-15 than in DMEM led to destabilization of the particles when the PLM coating was not formed as tight as within other batches. Especially amino acid with sulfhydryl-moiety are known to intercalate into the hydrophobic lipid bilayer, destabilizing the particles, and hence initiating aggregation (Iyer et al., 2019; J. C. Mathai et al., 2008; Wang et al., 2015; Iyer et al., 2019). Therefore, UCNPs@PLM were applied in DMEM (5 % FCS) to the cells in the following projects.

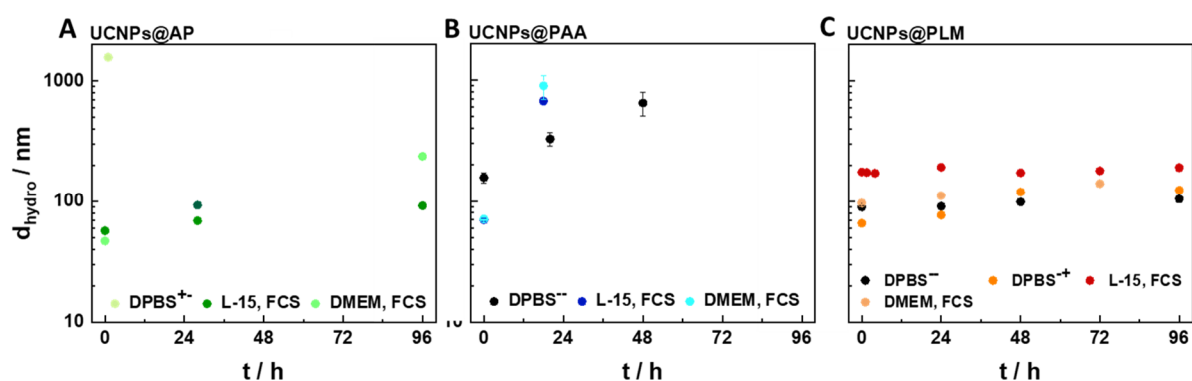


Figure 4.10. Time-dependent change of hydrodynamic diameters (d_{hydro}) of 12 nm $\text{NaYF}_4(\text{Yb,Er})@ \text{NaYF}_4$ core-shell particles ($0.4 \text{ mg} \cdot \text{mL}^{-1}$) (A) UCNPs@PAA, (B) UCNPs@AP, and (C) UCNPs@PLM at rt in DPBS^- , DPBS^+ (DPBS^- , 0.18 mM CaCl_2), L-15 (5% FCS, (v/v)) and DMEM (5% FCS, (v/v)). Y-axes have the same scale.

Stability in Serum-Free Isotonic Buffer

Before applying UCNPs, functionalized with targeting or stimulating moieties, in complex biological media, it is useful to verify the functioning of those UCNPs in serum-free medium so that the particle surface remains uncovered and the functional biomolecules are not hidden under a protein corona. In addition, for *in vitro* short-time applications of UCNPs *e.g.*, as labels, it is also not required to use complex cell culture medium but rather isotonic buffers. Thus, the stability of UCNPs in isotonic buffers suitable for cellular experiments had to be verified for these applications as well.

Often used balanced salt solutions are Dulbecco's phosphate-buffered saline (DPBS), Earle's balanced salt solution (EBSS), or Hank's balanced salt solution (HBSS), consisting of monovalent and divalent ions, phosphates and/or carbonates to stabilize the pH value, and glucose as energy supply for the cells. Divalent ions are required for the formation of cell-cell and cell-substrate contacts, for cellular communication, and the proper functioning of membrane proteins (Gonzalez-Mariscal et al., 1990; Wegener et al., 2000; Yang et al., 1993). Impedance-based analysis of the cells under study in this thesis revealed that the HT-29 cells and NRK cells in DPBS⁻ without divalent ions lose the contacts to each other and to the substrate immediately or within hours, respectively (**Figure A 1**). Thus, DPBS⁻ is not suitable for cell studies even if it might be suitable for the UCNPs.

However, high Ca²⁺ concentrations (1.8 mM) led to the destabilization of the UCNPs@PLM (**Figure 4.8**). When applied in DPBS⁻ without divalent ions or in DPBS⁺ with low Ca²⁺ levels (DPBS⁻, 0.18 mM), the UCNPs@PLM were stable for at least 4 d (**Figure 4.10**). In contrast, UCNPs@AP and UCNPs@PAA were neither stable in DPBS⁻ nor in DPBS⁺ and aggregated immediately or within hours.

As UCNPs@PAA were not stable in isotonic solutions with or without serum, their scope of applications is limited to non-cellular applications. UCNPs@AP is suitable for applications in serum-containing media. UCNPs@PLM can be applied under serum-supplemented conditions but also in isotonic buffer with low Ca²⁺ content as DPBS⁺. In terms of colloidal stability they are the most suitable particle modification for cellular studies among the three tested ones. The cell-cell contacts and the cell morphology can be maintained in DPBS⁺ for short-time experiments, demonstrated by a stable impedance signal for epithelial NRK cells for at least

15 h and HT-29 cells for at least 2 h (**Figure A 1**). Thus, DPBS⁺ is the buffer of choice for serum-free UCNPs@PLM experiments.

4.9 Microscopic Imaging of Small Phospholipid Membrane Coated Nanoparticles

Suitability for microscopic imaging of these small UCNPs with PLM coating in cells was tested by a two-photon laser scanning microscopy and by wide-field upconversion microscopy with z-section capability upon excitation with 980 nm.

Two-Photon Laser Scanning Microscopy

Presence of 12 nm UCNPs@PLM ($10 \mu\text{g}\cdot\text{mL}^{-1}$, DMEM, 5% FCS) in the cells are documented with the two-photon laser scanning microscopy (**Figure 4.11**). After 8 h incubation time, only a few luminescence spots around the nuclei are imaged in some cells, while after 20 h incubation, most of the cells have luminescent areas of upconversion around the nuclei. However, the upconversion intensity is captured blurry with this microscopy setup, enabling only a rough estimation of the location of UCNPs, while DAPI stained nuclei are captured clearly.

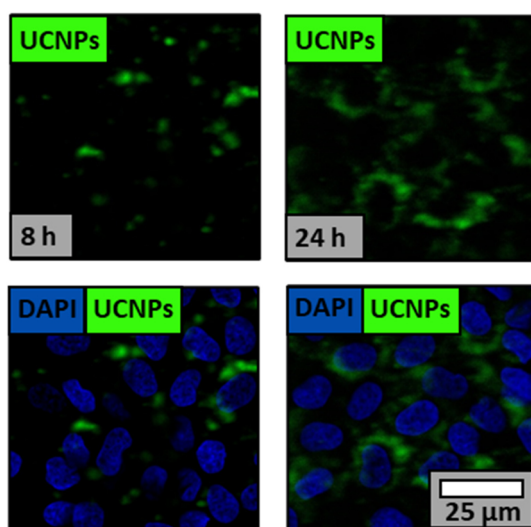


Figure 4.11. Two-photon laser scanning micrographs of NRK cells (passage number 19) incubated with 12 nm UCNPs@PLM ($50 \mu\text{g}\cdot\text{mL}^{-1}$, DMEM + 5% FCS) at 37 °C for 8 h or 24 h and stained with the nuclear dye DAPI. Upconversion intensity is captured upon irradiation with 980 nm (1.1 W) and depicted in green and with an overlay with DAPI-stained nuclei in blue.

The poor resolution of the upconversion luminescence obtained by this microscope may be found in the photo-physical characteristics of UCNPs. The upconversion process in NaYF₄(Yb,Er) is based on the absorption of 980 nm light of sensitizer ions Yb³⁺, followed by the

energy transfer of two photons from Yb^{3+} to the activator ions Er^{3+} . Compared to organic dyes with lifetimes of nanoseconds, the Laporte-forbidden excited Er^{3+} ions have rather long lifetimes in the millisecond range before they emit light in the green and red (Auzel, 2004; Berezin et al., 2010). When commercial microscopes are applied for imaging of UCNPs in the scanning mode, the scan rate must be slowed down strongly to hinder crosstalk between neighboring pixels and hence the smearing of the captured intensity. Thus, either the scan speed must be slowed down strongly (from $\mu\text{s}/\text{pixel}$ to ms/pixel), which may be not practical for experiments requiring high time-resolution (Pichaandi et al., 2011; Peng et al., 2019), or pinholes have to be applied, which only collect the light of a small area (down to one pixel). Due to the low quantum yield of UCNPs and the small size of the pinhole, lasers with very high power densities $10^5 \text{ W}\cdot\text{cm}^{-2}$ and long pixel dwell times of several milliseconds are needed to detect upconversion (Yu et al., 2009). Another idea is to process images later on *via* deconvolution techniques, enabling the application of short pixel dwell times and low power densities (Gainer et al., 2012). However, the most promising method for imaging UCNPs in scanning microscopes is to prepare UCNPs, which are highly doped with sensitizer and activator ions. Luminescence intensities could be enhanced drastically in these highly doped inert core–active shell UCNPs $\text{NaYF}_4@\text{NaYbF}_4(10\%\text{Tm}^{3+})$, enabling pixel dwell time of $10 \mu\text{s}$ (Peng et al., 2019). Highly doped UCNPs $\text{NaYF}_4(8\text{--}100\%\text{Tm}^{3+})@\text{NaYF}_4(20\%\text{Gd}^{3+})$ can be also optimized to trigger upconversion photon avalanche processes upon $1,064 \text{ nm}$ illumination for super resolution microscopy (Lee et al., 2021). Nevertheless, these improvement strategies were not feasible with the available equipment in the scope of this project, making this microscope less attractive for imaging of the UCNPs@PLM.

Wide-Field Upconversion Microscopy ($640 \text{ W}\cdot\text{cm}^{-2}$)

As different method, the non-scanning wide-field upconversion microscopy was applied to image the particle internalization by NRK cells. The sample was illuminated by a collimated 980 nm laser (cw, $640 \text{ W}\cdot\text{cm}^{-2}$) with this epi-fluorescence setup. The micrographs of the 12 nm UCNPs@PLM ($50 \mu\text{g}\cdot\text{mL}^{-1}$, DMEM, 5% FCS)-treated NRK cells shows upconversion intensity already after 4 h in some single cells (**Figure 4.12**). DAPI-stained nuclei have a reduced resolution compared to the laser scanning micrographs (cf. **Figure 4.11**). After 8 h more

upconversion spots around a few cells are identified. However, most of the cell nuclei are surrounded by upconversion spots in lower or higher intensity after 24 h of incubation time.

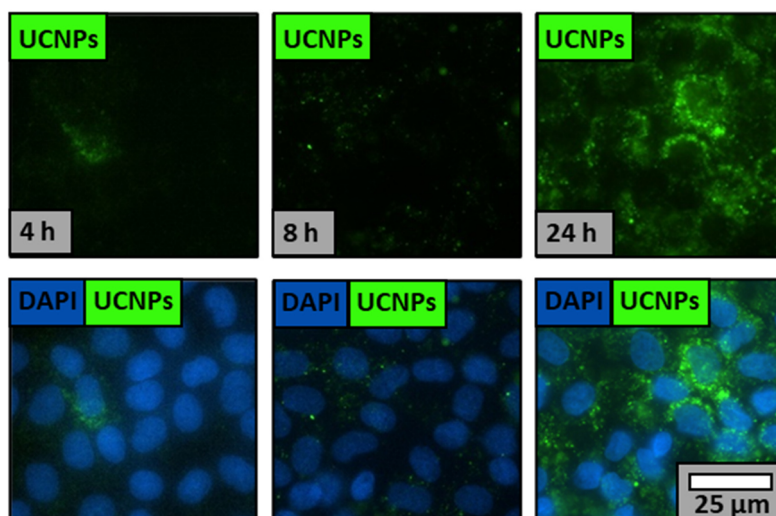


Figure 4.12. Wide-field upconversion micrographs of NRK cells (passage number 19) exposed to 12 nm UCNPs@PLM ($50 \mu\text{g}\cdot\text{mL}^{-1}$, DMEM + 5% FCS) at 37°C for 4 h, 8 h, or 24 h, showing upconversion intensity (green) upon irradiation with 980 nm (cw, $640 \text{ W}\cdot\text{cm}^{-2}$) and DAPI-stained nuclei (blue) in the overlay.

Dyes as DAPI cannot be localized in high resolution with the wide-field mode due to the out-of-focus background fluorescence. Thus, confocal scanning microscopy is often the preferred method in (three dimensional) cellular imaging with dyes. In contrast, the upconversion nanoparticles were imaged blurry with the scanning mode but can be imaged in a non-smearing manner with the wide-field imaging mode (cf. **Figure 4.11** and **Figure 4.12**). Individual spots can be clearly distinguished. They might belong to individual particles (Park et al., 2015), neighboring particles, or particle aggregates (Dukhno et al., 2018). Moreover, a three-dimensional impression of UCNPs-treated cells or tissue was obtained with the wide-field microscopy. This is feasible by adjusting the focal plane of the objective and imaging stepwise over the z-axis as the autofluorescence of cells and, thereby, the out-of-focus background is reduced (Park et al., 2015).

Here, the wide-field upconversion micrographs indicate that UCNPs@PLM internalization takes several hours as only a few upconversion spots were imaged after 4 h and 8 h. However, it has been reported that UCNPs@PLM can be found within the cells already after 0.5 h, which is contrary to the results of the two microscopy studies here (Rojas-Gutierrez et al., 2019).

To examine this contradiction, the particle internalization was tracked by transmission electron microscopy (TEM), sensitive to individual nanoparticles of high contrast. Uptake events of NRK cells, treated with 12 nm UCNPs@PLM ($20 \mu\text{g}\cdot\text{mL}^{-1}$, DMEM, 5% FCS), were visualized after 1 h and 24 h by means of 70 nm thick cell cross sections. After 1 h individual UCNPs and UCNP clusters are found within the cells in vesicles. After 24 h mostly highly aggregated and only a few single UCNPs@PLM are found within matured vesicles (**Figure 4.13B**, cf. **Chapter 5** for a detailed analysis).

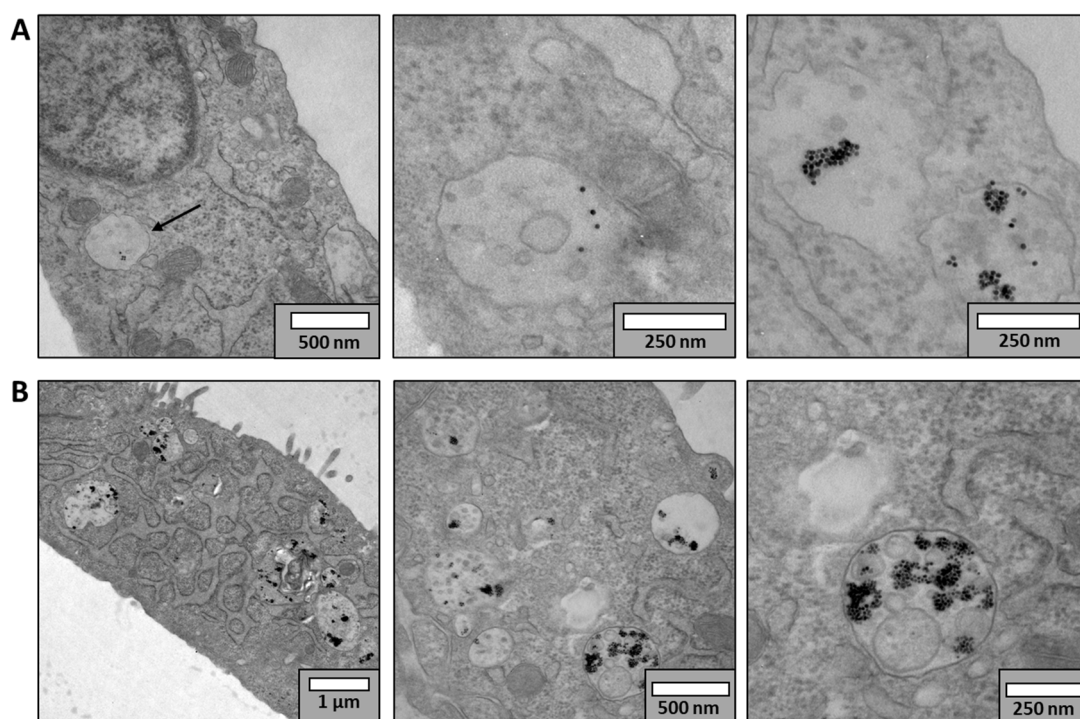


Figure 4.13. Electron microscopy images of 70 nm thick cross sections of NRK cells (passage number 18) exposed to 12 nm UCNPs@PLM ($20 \mu\text{g}\cdot\text{mL}^{-1}$, DMEM, 5% FCS) at 37 °C for (A) 1 h or (B) 24 h. Detailed analysis of some images is given in **Figure 5.14**.

The high number of aggregates within one vesicle might have led to a locally increased upconversion intensity due to many UCNPs in very close proximity. Thus, after a certain time, when UCNPs are stored in high numbers in the vesicles, they may get imageable with the laser scanning microscope and the wide-field upconversion microscope equipped with the $640 \text{ W}\cdot\text{cm}^{-2}$ laser. The sensitivity of these two microscopes is not enough to localize individual UCNPs, leading to a wrong time scale of internalization.

Wide-Field Upconversion Microscopy ($8 \text{ kW}\cdot\text{cm}^{-2}$)

Equipping an epi-fluorescence wide-field upconversion microscope with a laser of higher power density ($8 \text{ kW}\cdot\text{cm}^{-2}$, cw) and different optics improved the imaging capability of the UCNPs further. Here, the dye 1,1-dioctadecyl-3,3,3,3-tetramethylindotricarbocyanine iodide (DiR), incorporating into external and internal membranes and binding to hydrophobic molecules, was used to visualize the cell bodies and nuclei. UCNPs@PLM ($10 \mu\text{g}\cdot\text{mL}^{-1}$, DMEM, 5% FCS) are already detected sharply as individual spots around the nuclei after 1 h (**Figure 4.14**). The intensity and number of upconversion spots increase highly when imaging took place after 6 h and 24 h of incubation time so that the intensity had to be adjusted to provide distinguishable spots after 24 h. The very small upconversion spots after 1 h are assigned to individual UCNPs, whereas bigger spots are assigned to small particle assemblies or particles in very close proximity (Dukhno et al., 2018). The spots with highly increased intensity may belong to bigger aggregates. In accordance with the electron micrographs, the wide-field upconversion micrographs, taken with a higher power density, confirmed that UCNP internalization takes place much faster as indicated by the other two microscopes.

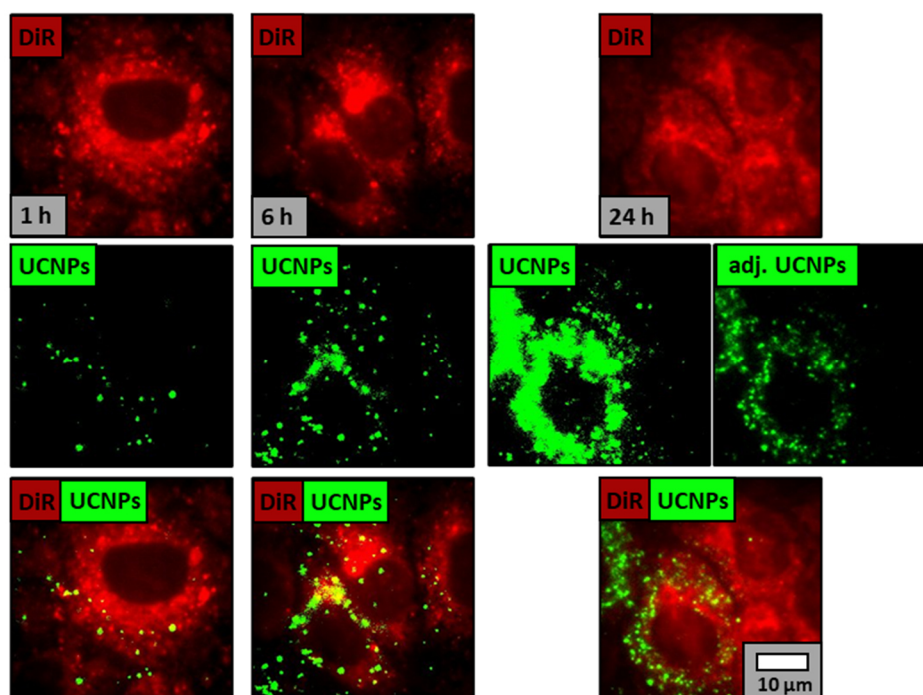


Figure 4.14. Wide-field upconversion micrographs of NRK cells (passage number 19) treated with 15 nm UCNPs@PLM ($10 \mu\text{g}\cdot\text{mL}^{-1}$, DMEM + 5% FCS) at 37°C for 1 h, 6 h or 24 h. Cell bodies were visualized by DiR staining (red). Upconversion intensity (green) was collected upon irradiation with 980 nm (cw, $8 \text{ kW}\cdot\text{cm}^{-2}$).

The small UCNPs@PLM could be imaged by scanning and wide-field microscopes although with different resolution. In comparison, the wide-field upconversion microscope technique is preferred over the scanning microscope due to the higher spatial resolution of the imaged upconversion spots. However, if the laser power is too low, only large aggregates within matured endosomes are visible, which may lead to misinterpretation.

4.10 Conclusion

In conclusion, monodisperse <12 nm core-shell particles doped with either Yb³⁺/Er³⁺ or Yb³⁺/Tm³⁺ were used to study the impact of various surface modifications on their protection ability in aqueous solutions. Er³⁺ doped UCNPs with the self-assembling membrane PLM turned out to have a 700% and 500% higher brightness compared to PAA and AP capped particles, suggesting that PLM minimizes the amount of water molecules attaching to the surface of the nanoparticles and thus, reducing the non-radiative phonon deactivation. This hypothesis was verified as the control particles with Tm³⁺ dopants did not show this brightness enhancement by applying a bilayer around the UCNPs. Moreover, the PLM enveloped UCNPs show excellent colloidal stability under acidic, basic, and at physiological conditions for at least 96 h. These particles were also not affected in high ionic strength environments (~140 mM NaCl) and in various pure mono- and divalent ion solutions at physiological concentrations. The only ion which requires special attention and further investigation is Ca²⁺. Nevertheless, the UCNPs show also in Ca²⁺ containing solution continuous luminescence within the 96 h after a stable signal was reached. In complex matrices as cell media with 5% FCS the UCNPs remain stable within at least 96 h. Thus, the hydrophobic phospholipid bilayer transforms the UCNPs to brighter and more sensitive probes and provides them not only with a higher protection against water degradation but provides also a high colloidal stability in buffer, in high ionic strength solutions, and in complex cell media. Further improvements in terms of stability can be obtained by evolving this concept and increase the hydrophobicity and tightness of the bilayer coating *e.g.*, via variations of lipid composition, crosslinking of the bilayer molecules, or by excluding water during the PLM preparation. As the small PLM coated UCNPs are bright enough for imaging with high spatial resolution using wide-field upconversion microscopes, they are suggested as model system for studying cellular interactions. The large variability of

modified lipids and the possibility to insert hydrophobic molecules provide a toolbox to construct small luminescent vehicles for applications on a cellular level.

5 Time-Resolved Analysis of Upconversion Nanoparticle Uptake and Cytotoxicity in Non-Cancerous Epithelial Cells

5.1 Preface

This paragraph summarizes collaborative research work in accordance with § 8 Abs. 1 Satz 2 Punkt 7 of the “Ordnung zum Erwerb des akademischen Grades eines Doktors der Naturwissenschaften (Dr. rer. nat.) an der Universität Regensburg vom 18. Juni 2009“.

The sections 5.2 – 5.6, 5.8 and 5.9 of the following chapter were mainly adapted from:

“Time-Resolved Analysis of Upconversion Nanoparticle Uptake and Cytotoxicity in Non-Cancerous Epithelial Cells”

Susanne Märkl, Frederic Przybilla, Reinhard Rachel, Thomas Hirsch, Max Keller, Ralph Witzgall, Yves Mely, Joachim Wegener

submitted to the journal *Journal of Materials Chemistry B* (July 2022)

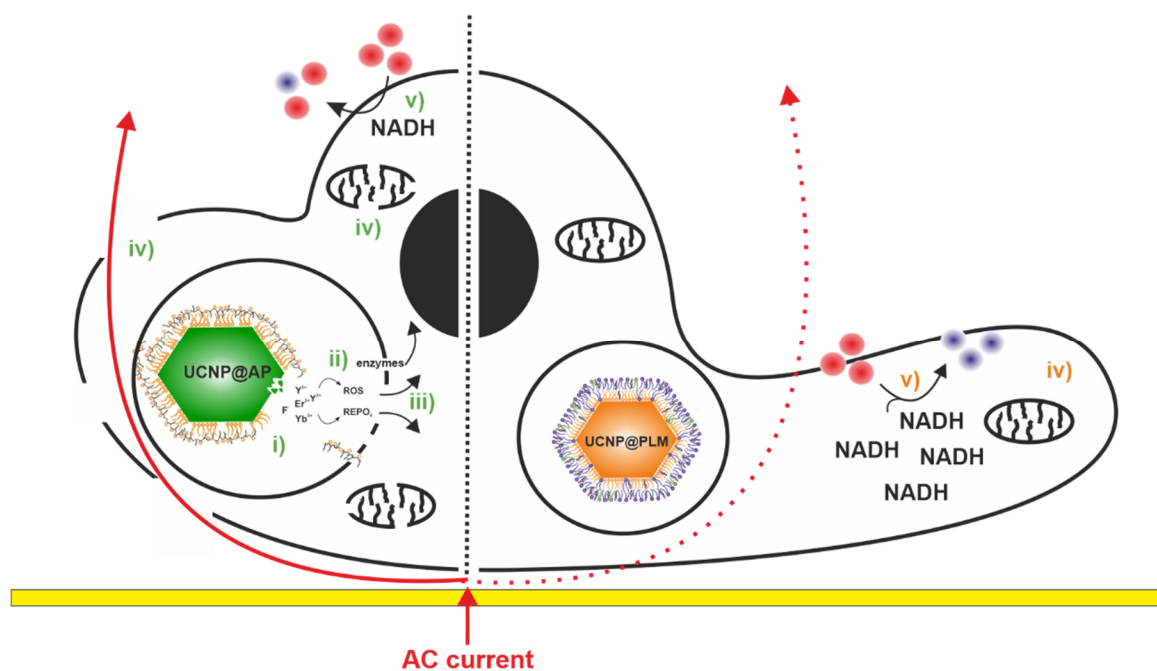
Chapter 5.2, Chapter 5.4, Chapter 5.8, and Chapter 5.9 was adapted to the style of this thesis. Some results were discussed in more detail in **Chapter 5.3** according to the supporting information of the paper. **Chapter 5.7** was added. The **Figures 5.1. – 5.9., Figure 5.11, Figure 5.13** and **Figure 5.14** were adapted from the publication and the supporting information. **Figure 5.10, Figure 5.12, Figure A 3 and Figure A 4** were added.

Most of the experimental and theoretical work presented in this chapter was carried out solely by the author. Particle modification strategies were discussed together with Dr. Thomas Hirsch and PD Dr. Max Keller. The upconversion microscopy studies were carried out by the author in cooperation with Dr. Frédéric Przybilla and Prof. Yves Mely at the University of Strasbourg. Helga Othmen prepared the ultrathin sections of the cells and took the electron micrographs. The electron microscopy results were discussed together with Prof. Ralph Witzgall and Prof. Reinhard Rachel. The concept and structure of the publication was planned together with Prof. Joachim Wegener and Dr. Thomas Hirsch. The author wrote the manuscript. All authors revised the manuscript. Prof. Joachim Wegener is corresponding author.

5.2 Introduction

The rare earth doped upconversion particles (UCNPs) have become a promising class of luminescent probes in the biomedical field. They attract attention due to their unique ability to convert near-infrared (NIR) light into higher energy light of the visible (VIS) range of the spectrum (Haase et al., 2011). The scope of applications range from imaging and targeting over drug delivery and sensing applications or even a combination of these features to multifunctional or multimodal probes (Li et al., 2014; Wang et al., 2020; Fan et al., 2016). However, in a biological environment using biocompatible concentrations, particle brightness is limited as the luminescence efficiency of the UCNPs suffers from water quenching and particle disintegration comes into play ((Li et al., 2014; Dukhno et al., 2018; Lahtinen et al., 2017; Märkl et al., 2020), cf. **Chapter 4**). Especially the particle dissolution inside living cells may lead to unknown interactions and trigger toxic responses. The released ions of metallic and metalorganic nanoparticles have been reported as primary source of nanotoxicity (Yang et al., 2021) and need to be considered also for NaYF₄-based UCNPs (Torresan et al., 2021). So far, most studies assessing the cytotoxicity of UCNPs report on low toxicity. However, these data were mainly obtained by end-point assays within a limited concentration range and short exposure times for a few different cell types only, mostly cancer cells (Guller et al., 2015; Gnach et al., 2015; Wang et al., 2020). Studying the cell fate upon UCNP exposure by just one endpoint readout can easily produce a false-negative outcome and is oversimplified, in particular if potential biotransformation of the particles and the biological impact of the disintegration products are left aside (Wang et al., 2020; Gnach et al., 2015). The dissolution of NaYF₄-based UCNPs in living systems was demonstrated to induce the formation of rare earth phosphates in lysosomes, and inflammatory responses (Li et al., 2015). This study has motivated researchers to improve the design of the UCNPs surface by hydrophobic bilayers, inorganic shells, or strongly complexing ligands for a better control of the particle/liquid interface and a reduced particle disintegration (Mendez-Gonzalez et al., 2022; Lisjak et al., 2021; Vozlič et al., 2021; Plohl et al., 2017b; Kembuan et al., 2021; Estebanez et al., 2019; Saleh et al., 2020; Bastos et al., 2022). Nevertheless, most of these studies on UCNPs dissolution have been only performed in steady-state conditions in the cuvette and need to be correlated to nanoparticle toxicity *in vitro*. When going from *in vitro* to *in vivo* applications, detailed

studies on UCNPs cytotoxicity need to be performed on more than just a single cell phenotype and must consider long term exposures. In this context, a suitable technique for more detailed in vitro studies is non-invasive electrical cell-substrate impedance sensing (ECIS) (Giaever et al., 1984). In such an assay, the cells are adherently grown on gold-film electrodes. The cell bodies block current flow as long as they are spread on the electrode surface and their membranes are intact. Once the cells shrink (apoptosis) or their membranes become permeable (necrosis), the electrical impedance drops, indicating cytotoxic effects (Giaever et al., 1984; Zinkl et al., 2019). In parallel to such wholistic assays, a special focus should be directed to the potential interactions of the nanoparticles or their disintegration products with cellular organelles and enzymes. Importantly, studies should be extended to normal cells to avoid a biased perspective on the interactions of particles with tumor cells and their peculiar behaviors with respect to particle clearance and biodistribution (Oliveira et al., 2019). Especially the cell lines, which come in contact to the nanoparticles during *in vivo* injection, clearance, and accumulation, are of interest such as epithelial, endothelial, or phagocytic cells. This work reveals the time-resolved impact of different surface coatings on nanoparticle uptake, stability, and long-time cytotoxicity in contact to non-cancerous epithelial-like cells. The surface coatings provide an individually efficient shielding from the aqueous environment. Upconversion nanoparticles of the type $\text{NaYF}_4(\text{Yb,Er})@\text{NaYF}_4$ have been selected as model systems as they show only very low dissolution tendency but a high optical sensitivity for changes that occur on the particle surface. These particles were coated with the bilayer forming and intrinsically non-toxic amphiphilic polymer (AP) or a phospholipid membrane (PLM), both providing the UCNPs with a thin organic coating for sufficient colloidal stability and brightness in biological media. An overview of the proposed fate of the nanoparticles and experimental means to study the associated phenomena is depicted in **Scheme 5.1**.



Scheme 5.1. Overview of the fate of differently shielded UCNPs@AP and UCNPs@PLM in NRK cells. Dissolution of UCNPs@AP as observed in absence of living organisms may be adapted to lysosomal particle degradation, resulting in REPO₄ as well as ROS formation, vesicle damage, and the release of vesicle loading into the cytoplasm. The induced stress on cells has been reported by cell metabolism and cell morphology alterations. The cell metabolism was accessible by sensing NADH with the PrestoBlue™ assay. Cell morphology changes as cell swelling, membrane rupture and detaching were monitored by the (un-)hindered current flow through the cell *via* the impedance-based cell analysis. Red lines represent the unhindered current flow and dashed lines the hindered one. The vertical black dashed line serves for distinction.

5.3 Particle Preparation and Characterization

Oleate (OA) coated UCNP_s with core-shell architecture NaYF₄(20%Yb,2%Er)@NaYF₄ were synthesized in two different sizes. The statistical analysis of transmission electron microscopy (TEM) images reveals average diameters of (12 ± 1) nm (**Figure 5.1A**) and (33 ± 1) nm (**Figure 5.1B**) for the core-shell UCNP_s@OA, made from (8 ± 2) nm or (26.3 ± 0.7) nm core particles. Using the diameters from the TEM analysis, the number of particles in suspension was determined to enable quantitative comparisons to other particles. A $100 \mu\text{g}\cdot\text{mL}^{-1}$ particle suspension consists of $2\cdot 10^{13}/\text{mL}$ of 12 nm UCNP_s (35 nM) or $1\cdot 10^{12}/\text{mL}$ of 33 nm UCNP_s (2 nM).

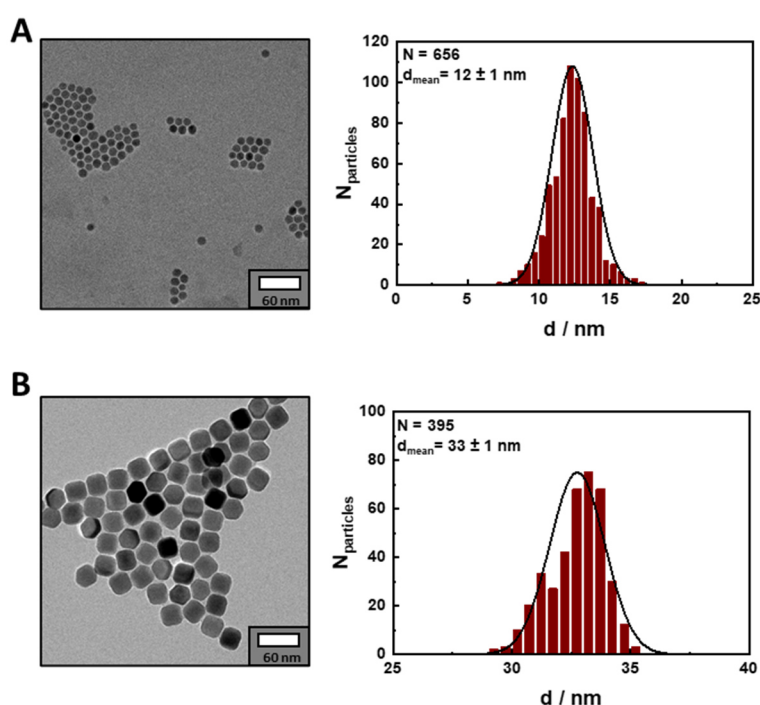


Figure 5.1. Transmission electron micrographs (scale bar 60 nm) and corresponding particle size distribution (mean \pm SD) of (A) (12 ± 1) nm and (B) (33 ± 1) nm oleate coated core-shell UCNP_s NaYF₄(Yb,Er)@NaYF₄ in cyclohexane.

Both particles were modified with bilayer coatings consisting either of an amphiphilic polymer (AP) poly(isobutyl-maleic anhydride) with 75% dodecylamine side chains or a phospholipid membrane (PLM) made of 1,2-dioleoyl-sn-glycero-3-phosphate (DOPA, 64%), 1,2-dioleoyl-sn-glycero-3-phosphoethanolamine (DOPE, 7%) and cholesterol (29%) (cf. **Scheme 3.3**, **Scheme 3.4**).

The colloidal stability of the UCNPs@AP and UCNPs@PLM in H₂O as well as in media for cell experiments was verified by intensity-weighted dynamic light scattering (DLS) measurements with a narrow distribution and their negative zeta potentials in H₂O (10 mM NaCl) (**Figure 5.2**, cf. **Table A 1** for exact values).

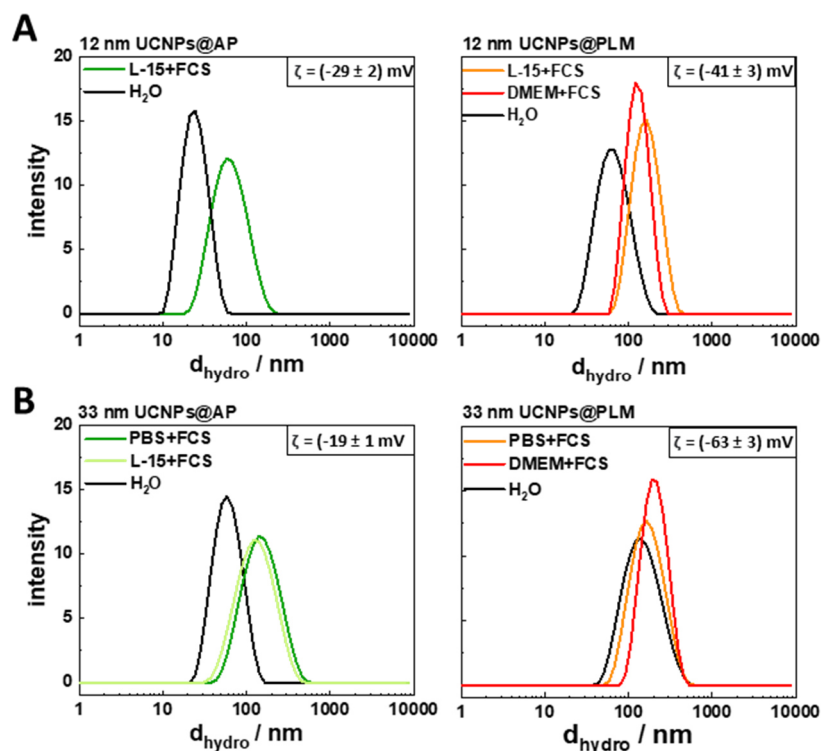


Figure 5.2. Representative intensity weighted hydrodynamic diameters (d_{hydro} , mean \pm SD, $N = 3$) of the (A) 12 nm and (B) 33 nm UCNPs@AP and PLM@UCNPs in water, DPBS (DPBS⁺⁺, 5% FCS, 1 mg·mL⁻¹ glucose) or Leibovitz L-15 (5% FCS) measured by dynamic light scattering (400 $\mu\text{g}\cdot\text{mL}^{-1}$). Zeta potentials (ζ , mean \pm SD, $N = 3$) were measured in saline (10 mM NaCl in H₂O). Y-axes have the same scale.

Luminescence spectra were recorded of all particles in H₂O upon 980 nm irradiation (cw, 85 W·cm⁻²) (**Figure 5.3**). The 12 nm UCNPs have a more pronounced green luminescence with a ratio of green to red luminescence $I_{\text{g/r}} \sim 2$. Despite the 2 nm thick shell NaYF₄, the 12 nm UCNPs are still sensitive towards water quenching and the protecting ability as well as the tightness of the particle coatings are visible in the luminescence spectra (cf. **Chapter 4** for detailed discussion). The 12 nm UCNPs@PLM are twice as bright as the UCNPs@AP, indicating a better shielding of UCNPs from water by the phospholipid membrane. In contrast, the 33 nm UCNPs with 3 nm thick shell NaYF₄ have an inverse ratio of green and red fluorescence with $I_{\text{g/r}} \sim 0.6$. This indicates that water quenching, especially of the green emission, is reduced.

Moreover, 33 nm UCNPs@AP are almost as bright as the UCNPs@PLM as they show 80% of the luminescence intensity of the UCNPs@PLM.

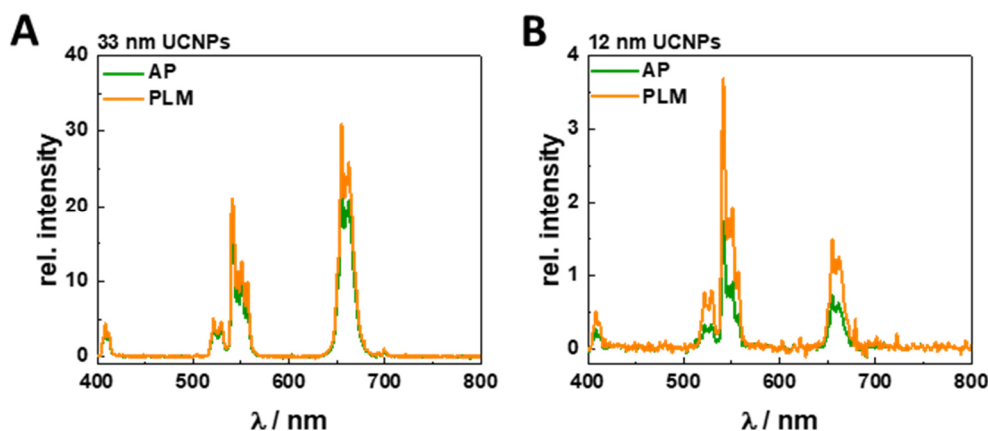


Figure 5.3. Luminescence spectra of 12 nm and 33 nm UCNPs@AP and UCNPs@PLM at rt in H₂O (400 $\mu\text{g}\cdot\text{mL}^{-1}$) upon 980 nm irradiation (cw, 85 W $\cdot\text{cm}^{-2}$, normalized to N_{UCNPs}).

The homogeneity in luminescence intensities on a single particle level was proven for the 33 nm UCNPs by wide-field upconversion microscopy, showing distinguishable luminescent spots of individual UCNPs and some particle assemblies (**Figure 5.4**). The central upconversion intensities (X_c) of UCNPs@AP is $2,530 \pm 30$ cts ($N = 894$) and of UCNPs@PLM $3,220 \pm 400$ cts ($N = 1,509$). On average, a single 33 nm UCNPs@AP is almost as bright as a 33 nm UCNPs@PLM, matching the ensemble results in solution. The intensity of single 12 nm UCNPs@AP was too low for robust measurements of luminescence on a single particle level as they are only detectable when forming aggregates, making them so far unsuitable as probe for microscopic detection in cells and tissues. Throughout this study, UCNPs of either 12 nm or 33 nm diameter were used. The larger UCNPs were used for optical studies to take advantage of their better signal to noise ratio. Surface coatings were only compared for particles of the same size.

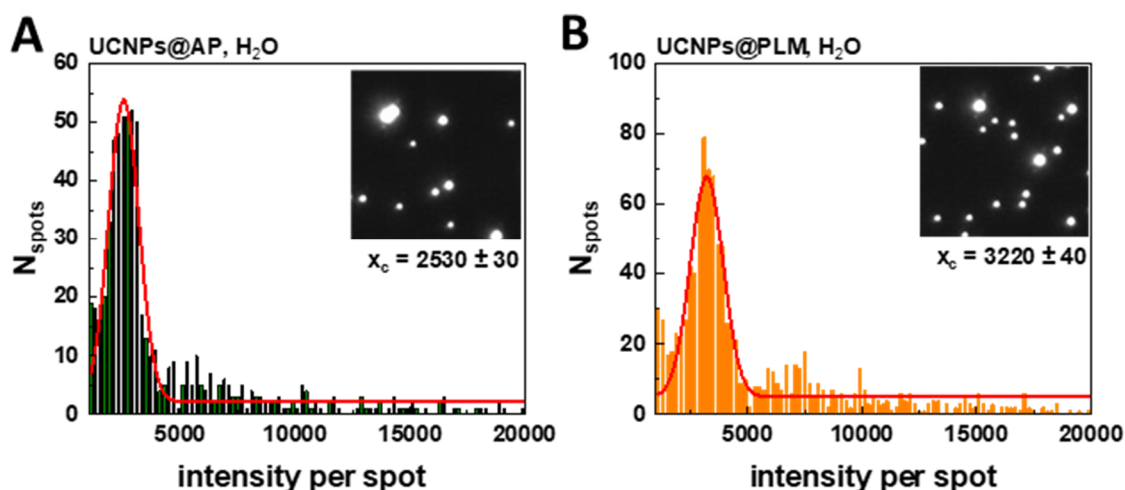


Figure 5.4. Luminescence intensity distribution with central upconversion intensity (x_c) of individual 33 nm UCNPs@AP and UCNPs@PLM at rt in an aqueous solution (1 mM NaF) with representative wide-field upconversion micrographs ($\lambda_{\text{exc}} = 974 \text{ nm}$, $8 \text{ kW}\cdot\text{cm}^{-2}$, cw).

An intrinsic toxicity of the PLM coating can be ruled out since the PLM bilayer consists of endogenous components of the mammalian cell membrane. The toxicity of the amphiphilic polymer was examined for NRK cells. AP forms aggregates with a hydrodynamic diameter of $\sim 10 \text{ nm}$ in water and $\sim 30 \text{ nm}$ in fetal calf serum (FCS) containing buffers (**Figure 5.5A**). NRK cells were exposed to the AP aggregates in a dilution that was similar to that of the coated UCNPs@AP (15 mM monomer concentration) and the cell response was monitored by ECIS (**Figure 5.5B**). The impedance of the NRK cells does not decrease for at least 60 h upon exposure to AP agglomerates, indicating that cells remain unaffected by the presence of AP and show no sign of toxicity in this concentration range.

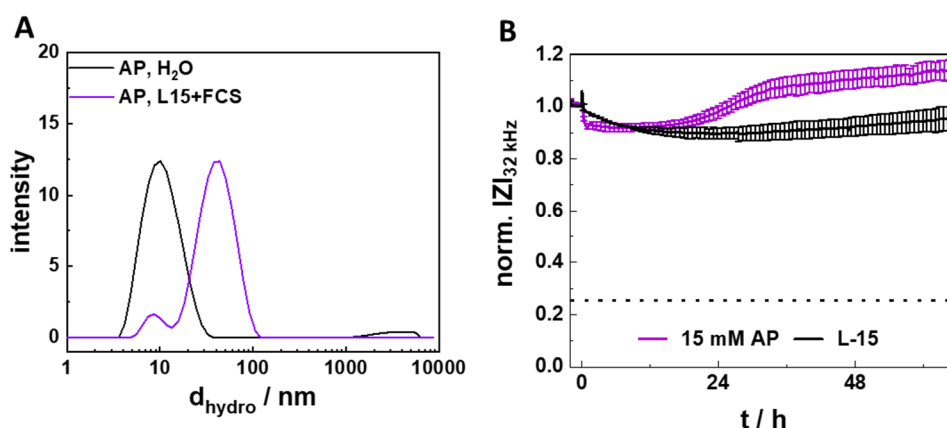


Figure 5.5. (A) Representative DLS of AP without UCNPs (15 mM) at rt in H₂O and L-15 (5% FCS). (B) Averaged and normalized impedance time courses of NRK cells (recorded at 32 kHz), incubated with AP w/o UCNPs (15 mM, L-15, 5% FCS) at 37 °C (mean \pm SEM, three independent experiments). AP was added at time point 0 h. Dashed lines represent the impedance level of cell-free electrodes. Average baseline impedance magnitude was (1.084 ± 0.007) k Ω before compound addition ($N = 33$).

5.4 Toxicity of Upconversion Nanoparticles with Amphiphilic Polymer and Phospholipid Membrane Coating

Both, the AP and PLM coating, ensure UCNPs with sufficient brightness and colloidal stability for bioanalytical applications, but this may change when applied to cells. In order to evaluate the biocompatibility of the UCNPs, non-transformed NRK cells were selected as epithelial-like model cell line from a major organ involved in particle clearance and biodistribution (Du et al., 2018). The UCNPs@AP and UCNPs@PLM were tested for their cytotoxicity in a resazurin-based PrestoBlue™ assay, probing cellular redox metabolism and, thus, cell viability by the cellular content of reduced redox coenzymes. The exposure time was set to the often-used incubation time of 24 h to enable a comparison to data already reported in the literature (**Figure 5.6A**). Cells incubated with the highest concentration of UCNPs@PLM ($200 \mu\text{g}\cdot\text{mL}^{-1}$) are still capable of reducing the non-fluorescent resazurin to fluorescent resorufin indicating an intact redox metabolism. In contrast, cells exposed to UCNPs@AP at concentrations $> 5 \mu\text{g}\cdot\text{mL}^{-1}$ show a concentration-dependent loss of viability with a $\sim 20\%$ drop for the highest concentration ($200 \mu\text{g}\cdot\text{mL}^{-1}$). Low concentrations of UCNPs@AP ($0.5 - 1 \mu\text{g}\cdot\text{mL}^{-1}$) increase cell metabolism, resulting in cell viabilities that are formally higher than observed for controls but may indicate the onset of cellular defense mechanisms. This effect, often observed for

potentially toxic substances, is defined as *hormesis* and has been already reported for nanoparticles (Iavicoli et al., 2010; Jiao et al., 2014; Stebbing, 1982). Phase contrast light microscopy images of cells (**Figure 5.6B**) exposed to UCNPs@PLM are indistinguishable from those of untreated cells. In contrast, micrographs of cell layers treated with UCNPs@AP reveal partly spherical and detached cells as well as cell debris. Thus, after 24 h of incubation UCNPs@PLM did not significantly affect NRK cells, whereas a concentration-dependent effect of UCNPs@AP on cell viability and morphology was observed.

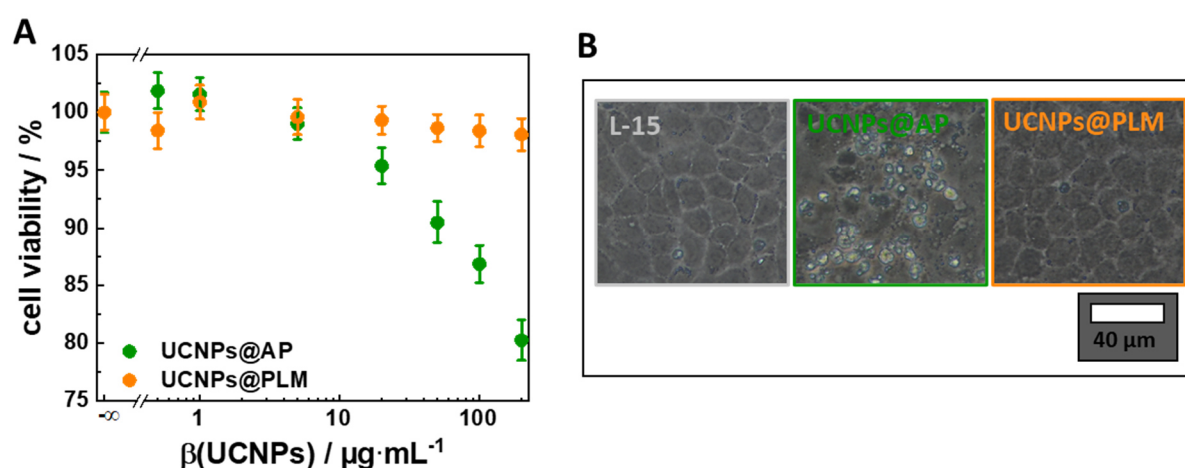


Figure 5.6. A) Cell viability of NRK cells incubated with 12 nm UCNPs@AP or UCNPs@PLM (mass concentrations (β) of 0.5 – 200 $\mu\text{g}\cdot\text{mL}^{-1}$, L-15, 5% FCS) at 37 °C for 24 h as determined by PrestoBlue™ assays (intensity weighted mean \pm error, three independent experiments with three replicates) and B) corresponding phase contrast micrographs (100 $\mu\text{g}\cdot\text{mL}^{-1}$).

However, the Presto Blue assay only reveals the cytotoxicity after a pre-defined exposure time and does not reveal neither the time course of toxicity nor the impact of the particles on cell viability for longer exposure times. Therefore, the ECIS assay was selected as a more comprehensive, time-resolved method to assess the cytotoxicity of the particles from changes in cell morphology, loss of adhesion and membrane rupture. NRK cells were grown to confluence on gold-film electrodes prior to their exposure to the different UCNPs preparations and their response was monitored for 72 h. The impedance was recorded at an AC frequency of 32 kHz as it provides the highest sensitivity for cell detachment (Lukic et al., 2015). **Figure 5.7A** and **Figure 5.7B** show representative time courses of the electrical impedance when the cells were treated with increasing concentrations of UCNPs@AP or UCNPs@PLM in DPBS (5% FCS). The impedance of the cells exposed to UCNPs@PLM or buffer remains at basal values

for 72 h, indicating no toxicity for these particles. In contrast, the impedance of the cells incubated with UCNPs@AP show a concentration-dependent response profile. Treated with the two highest concentrations ($\geq 50 \mu\text{g}\cdot\text{mL}^{-1}$), the impedance of the cells increases slightly after ~ 12 h before it drops after (26 – 36) h to values close to that of the cell-free electrode. Lower concentrations of UCNPs@AP initiated only the signal increase but led to no impedance decrease within the recorded time frame. The impedance drop indicates the loss of membrane integrity or detachment of the cells as a response to the particles (Lukic et al., 2015). The impact of different measurement buffers on the ECIS-readout was examined for the toxic UCNPs@AP (**Figure 5.7C**). The same concentration-dependent response profile with a transient increase prior to an impedance drop was recorded for UCNPs@AP in L-15 medium (5% FCS), but morphology changes were initiated by lower concentrations of UCNPs@AP ($\geq 5 \mu\text{g}\cdot\text{mL}^{-1}$) as compared to experiments performed in DPBS (5% FCS). The time courses in both buffers reveal a toxic impact of the UCNPs@AP, which is not of an immediate but rather intermediate nature. For the toxic UCNPs, a fit of the normalized impedance for 70 h exposure time as a function of the particle concentration (**Figure 5.7D**) provided an estimated EC_{50} value of $(45 \pm 7) \mu\text{g}\cdot\text{mL}^{-1}$ and $(15 \pm 2) \mu\text{g}\cdot\text{mL}^{-1}$ for NRK cells incubated with 33 nm UCNPs@AP in DPBS (5% FCS, $1 \text{ mg}\cdot\text{mL}^{-1}$ glucose) or in L-15 (5% FCS), respectively.

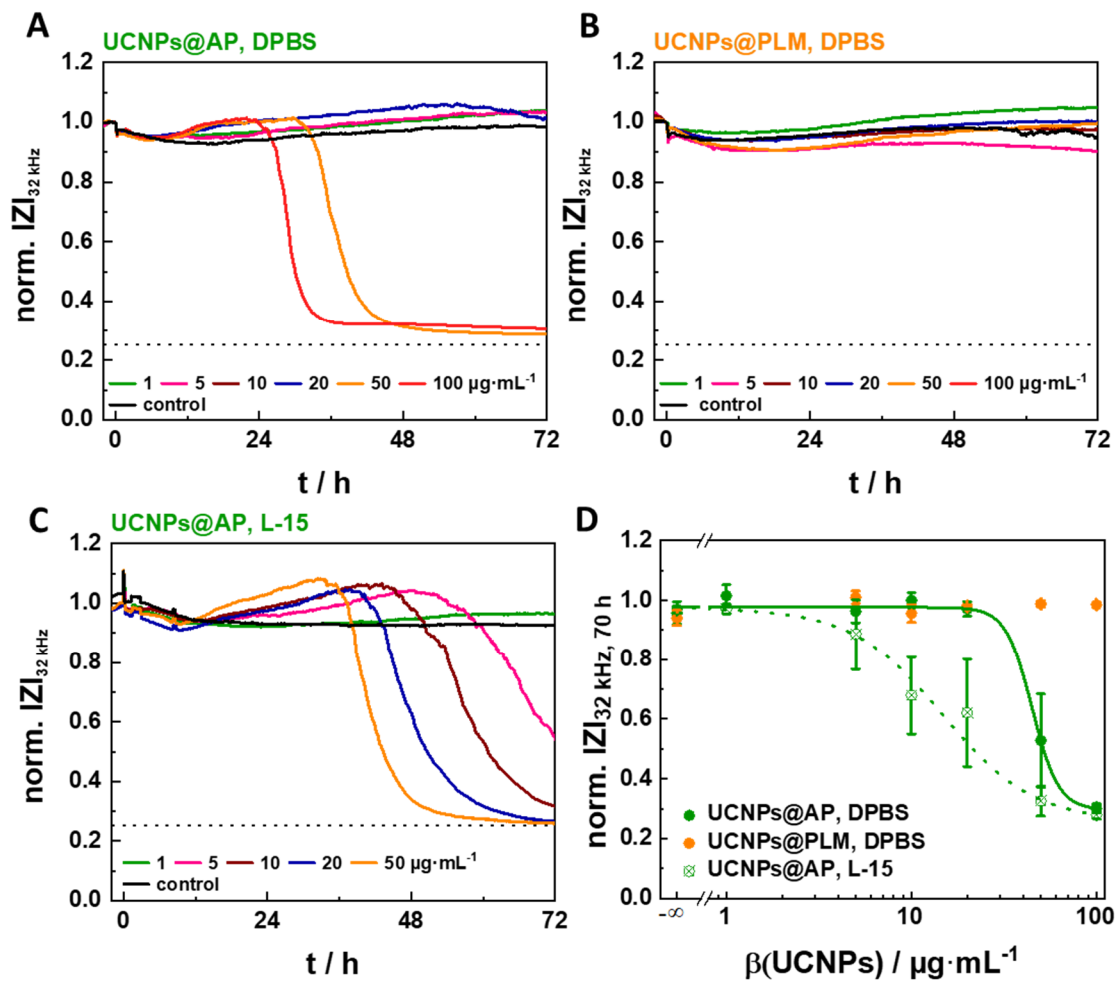


Figure 5.7. Representative time courses of impedance at 32 kHz of NRK cells, exposed to 33 nm A) UCNPs@AP in DPBS (5% FCS), B) UCNPs@PLM in DPBS (5% FCS), and C) UCNPs@AP at 37 °C in L-15 (5% FCS). Impedances were normalized to the initial value measured at 0 h. The baseline magnitude of impedance was (1.080 ± 0.007) kΩ before particle addition. The dashed line represents the impedance value of a cell-free electrode. D) Concentration-response relationship of the normalized impedance after exposing NRK cells for 70 h to 33 nm UCNPs. Potencies were calculated from the data of three measurements (mean \pm SEM) using a 4-parameter logistic model: $EC_{50}(\text{UCNPs@AP, DPBS, 70 h}) = (45 \pm 7) \mu\text{g}\cdot\text{mL}^{-1}$ (adjusted $R^2 = 0.999$) and $EC_{50}(\text{UCNPs@AP, L-15, 70 h}) = (15 \pm 2) \mu\text{g}\cdot\text{mL}^{-1}$ (adjusted $R^2 = 0.999$).

The time courses reveal a toxic impact of the UCNPs@AP to the cells in both media. This is not of an immediate but rather long-term nature. When the experiments were repeated with cells of higher passages, the time point of first decrease in impedance and the minimum concentration, which triggers this decrease, were different. The trend of shifted toxicity of UCNPs@AP for cells from a higher passage number was observed for both media (**Figure A 3**, **Figure A 4**). Moreover, in a few experiments with similar UCNPs but different cell batches, the

cells showed the same behavior (cf. **Chapter 6** and **Chapter 8**). The observed differences in cellular resilience to the particles might be due to a reduced capacity behavior of cells from higher subcultures and proceeded replicative senescence (Foroozandeh et al., 2019). This resulted in lower intracellular particle concentrations and hence lower toxicity values. This trend is analyzed in more detail in **Chapter 6**.

Differences in toxicity of UCNPs@AP suspended in serum-containing DPBS or L-15 might be caused by variations in the protein corona formed around the particles in the two media, leading to buffer-dependent internalization efficiency and cytotoxicity. A similar effect has already been observed for the DMEM and RPMI media by Pompa *et al.* for citrate-coated gold nanoparticles on HeLa and U937 cells. The authors showed a reduced protein corona formation in RPMI together with an improved uptake and higher cytotoxicity (Maiorano et al., 2010). Indeed, it is well-known that the uptake efficiency of nanoparticles and consequently their toxicity are reduced in the presence of a protein corona. The behavior of particles usually depends more on the amount of proteins adsorbed to the particle surface than on the nature of those proteins (Chandran et al., 2017; Cheng et al., 2015; Kelly et al., 2015; Lesniak et al., 2012). Particle internalization is also triggered in some cell lines by vitamins like folic acid, which are present in several cell culture media but not in DPBS (Sousa de Almeida et al., 2021). Additionally, the aggregation behavior of nanoparticles may vary in different media. As a consequence of the abundance of well-dispersed particles, smaller particle clusters, or large particle aggregates in different media, the toxicity may turn out to be media-dependent (Buford et al., 2007; DeLoid et al., 2017; Feliu et al., 2017). However, as the UCNPs do not tend to form large aggregates in any medium as revealed by DLS measurements (**Figure 5.2**), variations of the protein corona are more likely responsible for the buffer-dependent toxicity.

The electrical impedance of the cells, which were exposed to high concentrations of UCNPs@AP, increases transiently prior to a monotonic decrease to the values of a cell-free electrode (**Figure 5.7A,C**, **Figure A 3**, **Figure A 4**). This response profile might reflect the swelling of the cells, reducing the intercellular clefts as the major current pathway before membrane rupture, which is characteristic for necrosis (Zinkl et al., 2019). Indeed, such transient increase in impedance before cell death, induced by nanomaterials, has already

been reported for NRK cells exposed to C-Dots (Sperber et al., 2016), A549 cells treated with CuO or ZnO NPs (Seiffert et al., 2012), and HEPG2 cells incubated with ZnO NPs (Bartczak et al., 2015). This particular impedance profile has been associated to necrosis (Sperber et al., 2016). Thus, time resolved impedance data provide not only a detailed view on the time range during which the cells experience a toxic stress, they also give hints on the mechanism of cell death. Both assays demonstrated that in sharp contrast to UCNPs@PLM, UCNPs@AP strongly stress the cells, clearly indicating that surface modification is the key to success when it comes to the design of UCNPs for biological applications.

5.5 Internalization of Upconversion Nanoparticles with Amphiphilic Polymer or Phospholipid Membrane Coating

To determine whether the difference in toxicity between UCNPs@AP and UCNPs@PLM was related to a difference in uptake and availability of the two particles in the cytoplasm of NRK cells, we performed (i) an image-based quantification of particle uptake based on UCNP luminescence in individual cells by wide-field upconversion microscopy and (ii) an independent quantification of the total intracellular UCNP content by chemical extraction and subsequent quantification using inductively coupled plasma - mass spectrometry (ICP-MS). The microscopy approach was carried out using the 33 nm UCNPs that were allowed to interact with adherent NRK cells for 6 h. This short incubation time ensured no toxic cell damage and a sufficiently small number of internalized particles to avoid saturation of the detector. Cell bodies and nuclei were visualized using 1,1-dioctadecyl-3,3,3,3-tetramethylindotricarbocyanine iodide (DiR), incorporating into external and internal membranes and binding to hydrophobic molecules. A representative image of each experimental condition shows upconversion spots in the cells localized around the nucleus (**Figure 5.8, middle column**). The integrated upconversion intensity is higher for the UCNPs@PLM treated cells than for the UCNPs@AP treated ones. Note that the color scale is the same for all three experimental conditions and was adjusted to visualize the upconversion of the least bright sample (UCNPs@AP). The mean integrated upconversion intensity has been determined for 25 regions of interest (ROIs with 2 – 4 cells) from two independent experiments. The mean intensity was (700 ± 100) cts for the cells exposed to UCNPs@AP and

(2000 ± 400) cts for those exposed to UCNPs@PLM. Even if one keeps in mind that 33 nm UCNPs@AP are 20% less bright compared to UCNPs@PLM, (**Figure 5.3** and **Figure 5.4**) the upconversion intensity of internalized UCNPs@PLM is significantly higher than that of UCNPs@AP. Therefore, microscopic studies clearly indicate a reduced uptake of the toxic UCNPs@AP.

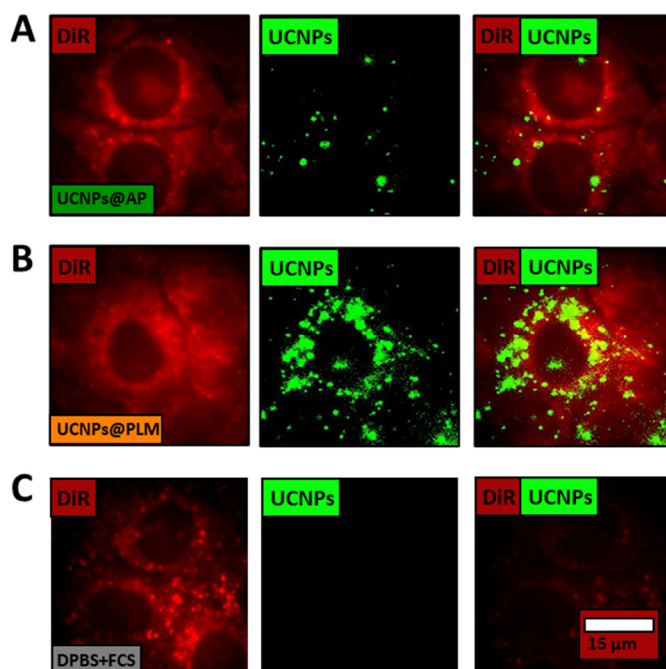


Figure 5.8. Representative wide-field microscopy images of NRK cells incubated with 33 nm A) UCNPs@AP and B) UCNPs@PLM ($5 \mu\text{g}\cdot\text{mL}^{-1}$) in DPBS (5% FCS, $1 \text{ mg}\cdot\text{mL}^{-1}$ glucose) for 6 h at 37°C and C) control. Upconversion luminescence ($\lambda_{\text{exc}} = 974 \text{ nm}$, cw, $8 \text{ kW}\cdot\text{cm}^{-2}$) is shown in green and co-staining with DiR ($\lambda_{\text{exc}} = 633 \text{ nm}$), visualizing the cell body and nucleus in red.

The number of internalized UCNPs per cell $N_{\text{UCNPs/cell}}$ was determined quantitatively by ICP-MS. The cells were incubated with the particles for 24 h as cellular uptake is known to saturate after $\sim 24 \text{ h}$ (Rojas-Gutierrez et al., 2019; Wang et al., 2020) and a significant fraction of the cells are still alive within 24 h of UCNP exposure. The cellular uptake was determined to $(160 \pm 45) \cdot 10^3 \text{ UCNPs@AP/cell}$ and $(420 \pm 90) \cdot 10^3 \text{ UCNPs@PLM/cell}$ (24 h, $100 \mu\text{g}\cdot\text{mL}^{-1}$ 12 nm-sized particles, L-15, 5% FCS). Both uptake studies, using independent means of analysis, revealed at least twice as many particles of the non-toxic UCNPs@PLM type in the cell as compared to the toxic UCNPs@AP type. This observation underlines that the amount of internalized UCNPs does not explain the different levels of cytotoxicity.

5.6 Stability of Upconversion Nanoparticles with Amphiphilic Polymer and Phospholipid Membrane Coating

The chemical stability of UCNPs@AP and UCNPs@PLM was analyzed at the single-particle level by wide-field upconversion microscopy. As demonstrated in a previous study (Dukhno et al., 2018), luminescence loss over time of individual UCNPs in aqueous solution is directly related to ion leakage. Differences in extracellular particle stability provide a direct indicator for the particles' individual tendency for intracellular ion leakage. The average luminescence intensity of spots attributed to single UCNPs@AP in H₂O at ambient temperature was observed to completely vanish within less than 5 h (**Figure 5.9A,B**). The time course of the average intensity loss was fitted with an exponential decay function and provided luminescence half-lives, $t_{1/2}$ (H₂O,rt), of (0.59 ± 0.05) h and (0.385 ± 0.002) h (two individual measurements, **Figure 5.9C**). Under the same conditions, the luminescence intensity of the UCNPs@PLM remains constant for at least 13 days. As a biomolecular corona might form around the UCNPs in cellular experiments, the dissolution rate of UCNPs was also studied in FCS-containing medium. The hydrodynamic diameter of the particles in the presence of FCS increased, indicating adsorption of proteins from solution onto the particle surface (**Figure 5.2**). The dissolution half-life of UCNPs@AP@FCS, $t_{1/2}$ (FCS,rt), was observed to be (1.3 ± 0.2) d and $(0.3) \pm 0.1$ d (two individual measurements) (**Figure 5.9D**). Compared to the data without FCS incubation, the dissolution half-life was significantly prolonged, suggesting a protecting effect of the protein corona on UCNPs, slowing down particle dissolution. The luminescence intensity of UCNPs@PLM@FCS was stable over the whole duration of the experiment (96 h). Repeating the same experiment at 37 °C, the UCNPs@AP@FCS dissolve faster than at rt with $t_{1/2}$ (FCS,37 °C) = (1.2 ± 0.1) h, indicating that the protecting effect of the FCS coating was reduced at physiological temperature (**Figure 5.9E**). Again, the luminescence of UCNPs@PLM@FCS remained constant at 37 °C over the time range of the experiment (72 h).

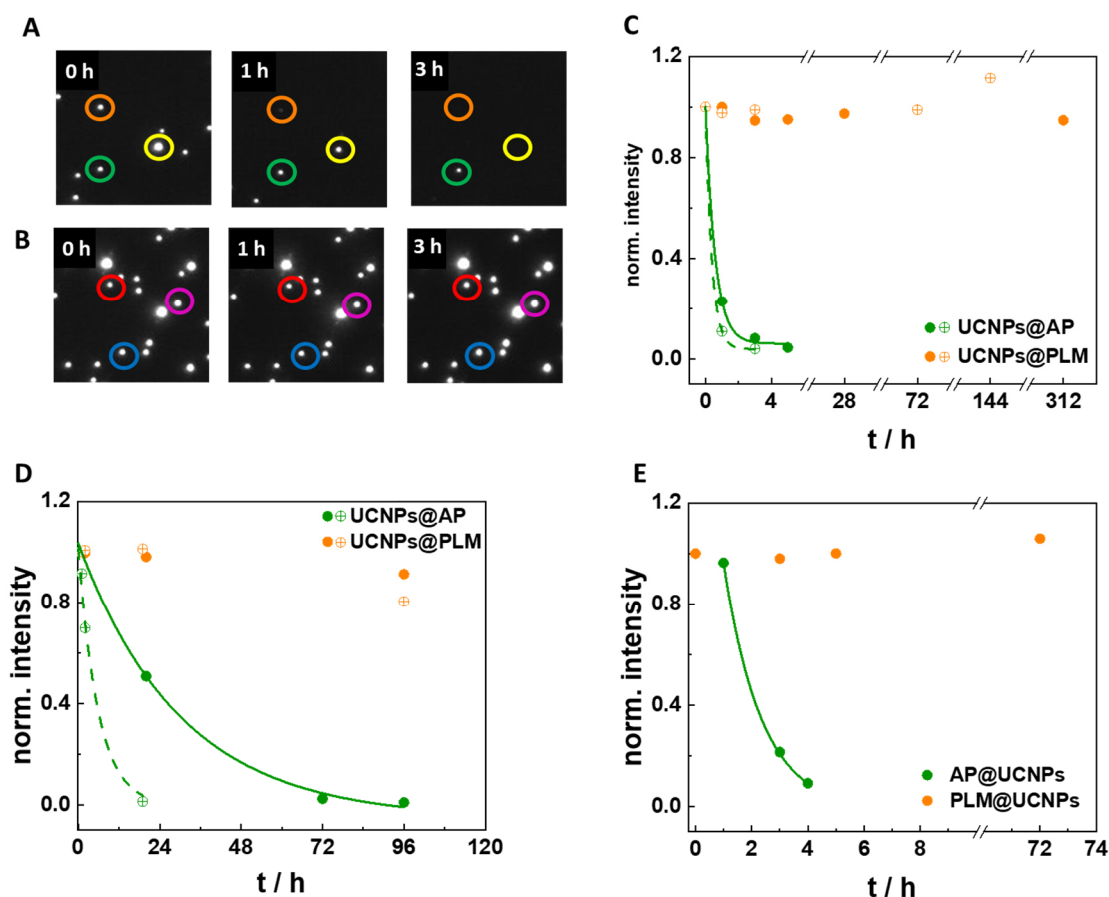


Figure 5.9. Representative wide-field upconversion micrographs (10 x 10 μm) of 33 nm A) UCNPs@AP and B) UCNPs@PLM in H₂O at rt at 0 h, 1 h and 3 h upon 974 nm irradiation (8 kW·cm⁻²). Normalized intensity of UCNPs@AP and UCNPs@PLM C) in H₂O at rt for 13 d, D) in H₂O at rt for 6 d after 30 min pre-incubation with FCS (5%, DPBS) and E) in H₂O at 37 °C for 3 d after 30 min pre-incubation with FCS (5%, DPBS) with exponential decay fit for AP@UCNPs to estimate dissolution half-lives ($t_{1/2}$) C) $t_{1/2} = (0.59 \pm 0.05)$ h and $t_{1/2} = (0.38 \pm 0.02)$ h, D) $t_{1/2} = (1.3 \pm 0.2)$ d and $t_{1/2} = (0.3 \pm 0.1)$ d and E) $t_{1/2} = (0.59 \pm 0.05)$ h. Experiments were performed once (E) or twice (colored and non-colored dots in C, D). The data points correspond to the luminescence intensity of single UCNPs averaged over 100 ROIs covering a total surface of 0.16 mm² (typically number of spots was 760 (H₂O) – 3600 (protein corona)).

According to the data presented in **Figure 5.9**, the protein corona was not sufficient to fully protect the UCNPs@AP from dissolution. Their dissolution was delayed at rt compared to physiological temperature, which is in accordance with studies revealing surface protection by protein corona and an enhanced dissolution at higher temperature (Saleh et al., 2020). In contrast, PLM-coated particles were perfectly stable under all experimental conditions, which confirmed the very good protecting properties of this surface modification. Similar observations in terms of brightness and colloidal stability in challenging phosphate buffers

have already been reported ((Märkl et al., 2020) cf. **Chapter 4**). The destabilizing effect of phosphates was also observed within cells. Indeed, the dissolved rare earth ions from NaYF₄-based UCNPs are known to form precipitating rare earth phosphates REPO₄ with the organic phosphates in *e.g.*, membrane lipids, nucleotide mono-, di-, and triphosphates, RNA, or DNA. This can even speed up particle disintegration, possibly impair cellular vesicles, and induce inflammatory effects (Li et al., 2015; Lisjak et al., 2021). The phosphate-enhanced particle disintegration is counteracted by making use of the strong attraction between rare earth ions and phosphates to design an efficient shielding of the particle surface from the media as shown for PLM. Also other phosph(on)ate based ligands as ethylenediaminetetra(methylenephosphonic acid) (EDTMP) or a modified 10-methacryoyldecylphosphate (HPS) have been proven to enhance the stability of UCNPs NaYF₄(Yb,Er) under these conditions (Li et al., 2015; Lisjak et al., 2021; Mendez-Gonzalez et al., 2022). The different dissolution tendency of UCNPs@AP and UCNPs@PLM in cell-free experiments may be likely observable within cells as well.

Additionally, metabolic degradation of the two types of particle-coating bilayers, AP and PLM, may be different within cellular vesicles. The AP coating is rather loose and not all functional groups may be involved in particle stabilization so that the polymer chains partly reach into solution. This may provide an easy access to the amide bonds for non-specific enzymes to induce a stepwise disintegration and pull-off from the particle. In contrast, the PLM coating is of non-polymeric nature and the phospholipids are close to the particle surface. Thus, the functional groups are sterically shielded, protected from enzymatic metabolization and they may not reach into the active center of the proteases. It seems plausible that individual biotransformation, vesicle membrane damage, and release of vesicle loading into the cytoplasm is the reason for the observed toxicity of poorly shielded particles. The lysosomal membrane leakage and release of lysosomal enzymes may trigger digestion of cellular components and cell death. A partial permeabilization of lysosomes results in apoptotic cell death, while a complete lysosomal breakdown triggers inflammatory processes and uncontrolled necrosis (Boya et al., 2008; Wang et al., 2018; Rock et al., 2008). UCNPs@AP did neither reduce significantly the metabolic activity of the cells within 72 h nor initiate cell shrinkage as sign of apoptotic cell death. In contrast, cell swelling prior to cell death was

observed after ~30 h of exposure. The latter may indicate the onset of necrosis, supporting the hypothesis of vesicular breakdown by dissolving UCNPs. Similar to these observations, a correlation between chemical stability of particles, cell viability, and inflammatory processes has been reported for UCNPs with non-perfect protective surface coatings, while NaYF₄(Yb,Er)@EDTMP showed no significant ion leakage or any impact on cell viability of human endothelial cells EA.hy926 and human myeloid cells THP-1 (Lisjak et al., 2021; Li et al., 2015). The experiments described above support the conclusion that the toxicity of UCNPs@AP, observed for epithelial NRK cells, was evoked by the formation of REPO₄, leading to lysosomal breakdown and necrosis.

5.7 Toxicity Evaluation of Released Ions

The possible impact on dissolving ions was evaluated by analyzing the toxicity of the rare earth and fluoride ions in contact to NRK cells *via* the ECIS approach. The rare earth ion mixture RE³⁺ (5.9 mM, 78% Y³⁺, 20% Yb³⁺, 2% Er³⁺) as RECl₃ and F⁻ (2 mM) as KF were chosen, representing the total dissolution of 100 µg·mL⁻¹ standard particles with average size and composition (25 nm NaYF₄:20%Yb,2%Er). The impedance of the cells, incubated with the RE³⁺ mixture or F⁻, does not change within at least 60 h (**Figure 5.10**). However, the possible internalization pathways of rare earth ions into NRK cells were unknown. To ensure the permeation of RE³⁺ into the cells, the cell membrane was permeabilized for a short period of time by applying a short electric pulse. Even under these conditions, the cells did not seem to be affected as the impedance courses did not change for at least 60 h.

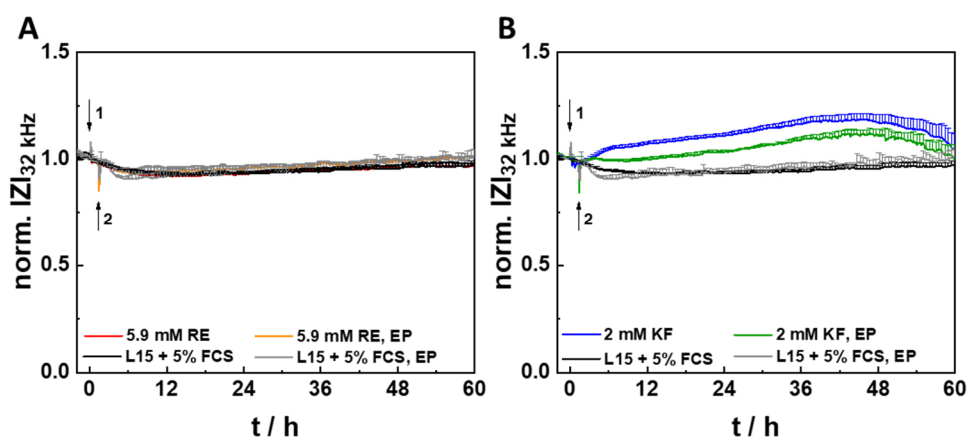


Figure 5.10. Normalized impedance time course at 32 kHz of NRK cells incubated with (A) RE^{3+} mixture (5.8 mM, 78% Y^{3+} , 20% Yb^{3+} , 2% Er^{3+} , L-15, 5% FCS) or (B) F^- (2 mM, L-15, 5% FCS) at 37 °C (mean \pm SEM, three independent experiments). Ion mixtures were added at time point 0 h (arrow 1) and introduced into the cytoplasm by electroporation (EP, arrow 2). The parameters of the electroporation pulses were as follows: 20 ms, 32 kHz, 1400 μA). Average baseline impedance magnitude was (1.084 ± 0.007) k Ω before addition ($N = 33$).

Nevertheless, as the availability of the RE^{3+} in the cells upon UCNPs dissolution might be different in terms of location, concentration, and formulation, a direct correlation of cytotoxicity with this artificial ion toxicity experiment might be not applicable. The different toxicity of nanoparticles and their metal chlorides has been shown for 17 nm ZnO particles and ZnCl_2 using macrophage-like cells (THP-1) and was attributed to different intracellular uptake and their final microenvironment in the cell. In contrast, 75 nm CoO particles and 29 nm CuO particles had a similar toxicity profile as their metal chlorides CoCl_2 and CuCl_2 . This study demonstrated that dissolving nanoparticles and the ions may not necessarily undergo the same interactions with the cell (Jeong et al., 2018). It seems indeed possible, that directly applied rare earth ions may complex with other biomolecules already in the cell medium prior to cell contact and, thereby, undergo different interactions than intracellularly formed RE^{3+} upon dissolution.

5.8 Possible Uptake Pathways of Non-Toxic Upconversion Nanoparticles

The internalization and fate of the non-toxic UCNPs@PLM in epithelial cells was further characterized by electron microscopy and wide-field upconversion microscopy. To identify uptake mechanisms, (i) NRK cells were incubated with UCNPs@PLM for 10 min or 60 min, (ii)

prepared for EM, and (iii) 70 nm ultrathin sections were examined by transmission electron microscopy. In the micrographs, macropinocytosis, identified by the membrane ruffles, and clathrin-mediated endocytosis (CME), identified by the dark clathrin-coated pits, were observed (**Figure 5.13**, red arrows). The UCNPs@PLM have been internalized as individual particles, and also as particle aggregates. Clustering of UCNPs@PLM during uptake from DMEM (5% FCS) is noteworthy as intensity weighted DLS measurements do not show any aggregate peak but only the presence of individual UCNPs in the cuvette (**Figure 5.2**).

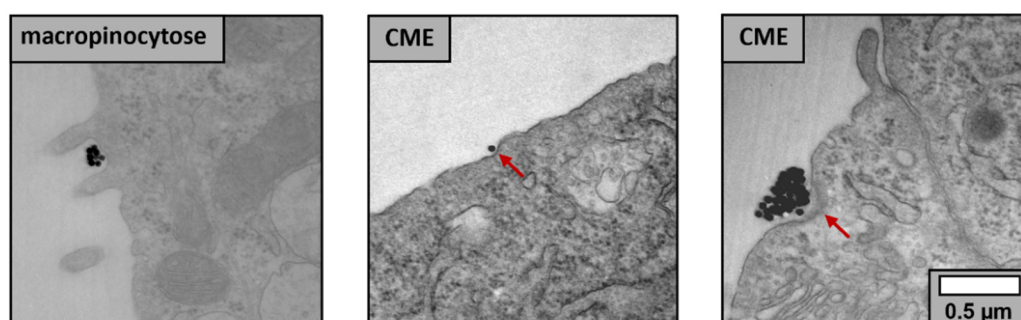


Figure 5.11. Representative electron micrographs of 70 nm ultrathin sections of NRK cells after 60 min incubation with 33 nm UCNPs@PLM ($200 \mu\text{g}\cdot\text{mL}^{-1}$, DMEM, 5% FCS) at 37°C show clear indications of macropinocytosis and clathrin-mediated endocytosis (CME). Red arrows point to clathrin coated pits.

Thus, aggregation was further analyzed by studying luminescence at a single particle level with a wide-field upconversion microscope upon 974 nm irradiation ($8 \text{ kW}\cdot\text{cm}^{-2}$) (**Figure 5.12**). The representative wide-field images of immobilized particles reveal individual luminescence spots of UCNPs in DMEM (5% FCS), which are mostly larger than those of individual UCNPs in H_2O and mask the small spots.

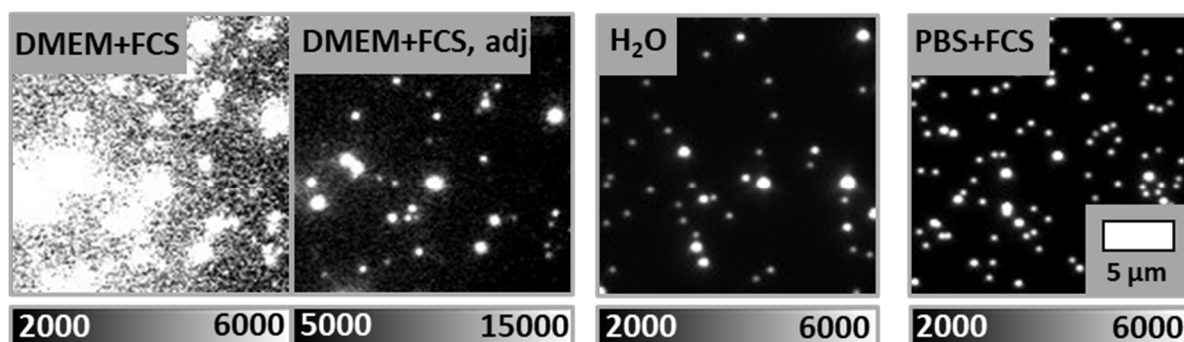


Figure 5.12. Representative wide-field upconversion microscopy images of 33 nm PLM@UCNPs at rt in DMEM (5% FCS) with single particle intensity range (2,000 – 6,000) and with adjusted intensity range (5,000 – 15,000), in H₂O (intensity range 2,000 – 6,000) and in DPBS (5% FCS) (intensity range 2,000 – 6,000).

The brighter spots are assigned to aggregates of a few particles in close contact (Dukhno et al., 2018). This indicates that UCNPs@PLM tend to form assemblies of a few UCNPs in the cell medium DMEM (5% FCS). Consequently, cells might not get in contact with only single particles of defined size and coating, as characterized by DLS, but they may also encounter clustered particles at the plasma membrane. Thus, it is useful to check the particle properties and aggregation on a single particle level prior to their application and adjust the medium to the application. For example, DPBS (5% FCS, 1 mg·mL⁻¹ glucose) does not induce cluster formation of UCNPs@PLM as shown by DLS and by wide-field microscopy (**Figure 5.2** and **Figure 5.12**).

The 70 nm ultrathin sections provide only access to 0.3% of a total cell with a mean diameter of 25 μm. Therefore, to collect more information from a higher number of cells, the different endocytosis pathways were analyzed by functional inhibitor studies on confluent NRK cell layers using wide-field upconversion microscopy as a readout. The uptake of 33 nm UCNPs@PLM by NRK cells at physiological temperature was first compared to the uptake at 4 °C to identify energy-dependent internalization processes. Undisturbed uptake was also compared to experiments, performed in presence of dynasore, a well-known inhibitor of dynamin, or in the presence of hypertonic sucrose solution, preventing the disassembly of the clathrin pits (Rennick et al., 2021). For a long time dynasore as well as hypertonic buffers have been considered as exclusive inhibitors of CME, but meanwhile they have been shown to also inhibit the *fast endophilin-mediated endocytosis* (FEME) as well as off-target

macropinocytosis (Rennick et al., 2021). Thus, the processes CME, FEME, and macropinocytosis were all studied as potential uptake mechanisms in these experiments. Some representative wide-field images with DiR co-staining are shown in **Figure 5.13**. The red dye visualizes the whole cell body and the green dots indicate upconversion luminescence. After incubation at 37 °C for 1 h, the UCNPs@PLM were detectable in high amounts within the cells. In comparison, at 4 °C almost no upconversion intensity was detected. Similarly, co-treatment with dynasore (200 µM) or hypertonic sucrose (0.45 M) reduced the number of internalized UCNPs significantly. Micrographs of at least 25 ROIs showing 2 – 4 cells each from two different experiments were included in the statistical analysis and interpretation. The mean upconversion intensity integrated over one cell was reduced under all inhibiting conditions from ~750 cts to ~250 – 375 cts, revealing that most of the UCNPs were taken up by NRK cells *via* an energy-dependent pathway and that CME/FEME as well as macropinocytosis were important endocytosis pathways for UCNPs@PLM.

Moreover, the 25 – 75% boxes show a high variance of the mean upconversion intensity per cell, indicating a high variation of the number of internalized UCNPs/cell. While some cells had internalized many UCNPs@PLM, other cells did not show any detectable upconversion luminescence. Even though the cells in a confluent monolayer are supposedly in stage G0 of the cell cycle (Khammanit et al., 2008), the high heterogeneity in particle internalization was apparent. This large variability between cells can have many reasons: (I) single-cell heterogeneity (Snijder et al., 2009), (II) differences in local particle concentrations (Åberg et al., 2021) and (III) different degrees of protein corona around particles (Forest et al., 2016), (IV) varying endocytic activity in different cell cycle phases together with individual cell size, (V) dilution of nanoparticles in daughter cells (Rees et al., 2019; Kim et al., 2011; Åberg et al., 2017; Panet et al., 2017; Hinze et al., 2018), and (VI) the stochastic nature of internalization (Åberg et al., 2021; Rees et al., 2019; Summers et al., 2011).

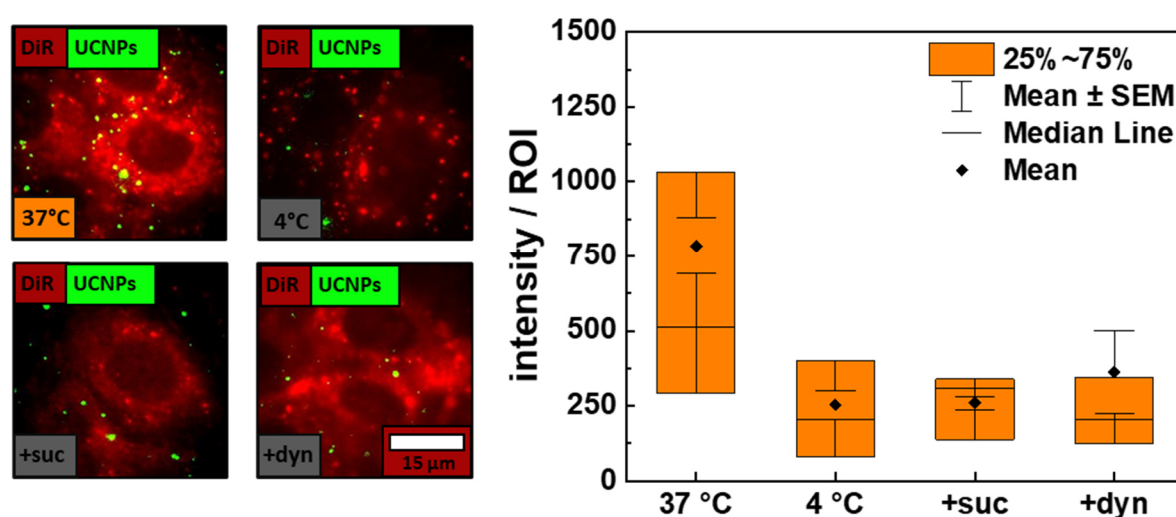


Figure 5.13. Representative wide-field upconversion microscopy images (one ROI) of NRK cells treated with 33 nm UCNPs@PLM in ($5 \mu\text{g}\cdot\text{mL}^{-1}$, DPBS, 5% FCS, $1 \text{ mg}\cdot\text{mL}^{-1}$ glucose) for 1 h at 37 °C or at 4 °C and or in presence of with additional sucrose (suc, 0.45 M) or dynasore (dyn, 200 μM) at 37 °C. Upconversion luminescence is shown in green ($\lambda_{\text{exc}}=974 \text{ nm}$, $8 \text{ kW}\cdot\text{cm}^{-2}$) and co-staining with DiR, visualizing the cell body and nucleus, in red ($\lambda_{\text{exc}}=633 \text{ nm}$). The mean upconversion intensity integrated over a one cell for each condition is presented in a box plot with mean \pm SEM, median (line) and boxes, representing 25 – 75% of the values. Data were extracted from 25 ROIs of two independent experiments.

The intracellular fate of the 12 nm and 33 nm UCNPs@PLM in NRK cells was analyzed by electron microscopy of 70 nm ultrathin sections, prepared from cells after 1 h or 24 h incubation time with the particles. The representative overview image (**Figure 5.14A**, 24 h) displays almost one whole cell with distinguishable cell compartments. After 1 h, the UCNPs@PLM are found as individual particles or particle agglomerates in early and late endosomes (EE, LE) (**Figure 5.14D,E**). After longer incubation times (24 h), they are identified mainly as aggregates in matured vesicles, such as the multivesicular bodies (MVB) and endolysosomes (EL) (**Figure 5.14B,C**). A deeper analysis of internalization and intracellular storage characteristics of the non-toxic UCNPs@PLM will be helpful for future particle designs.

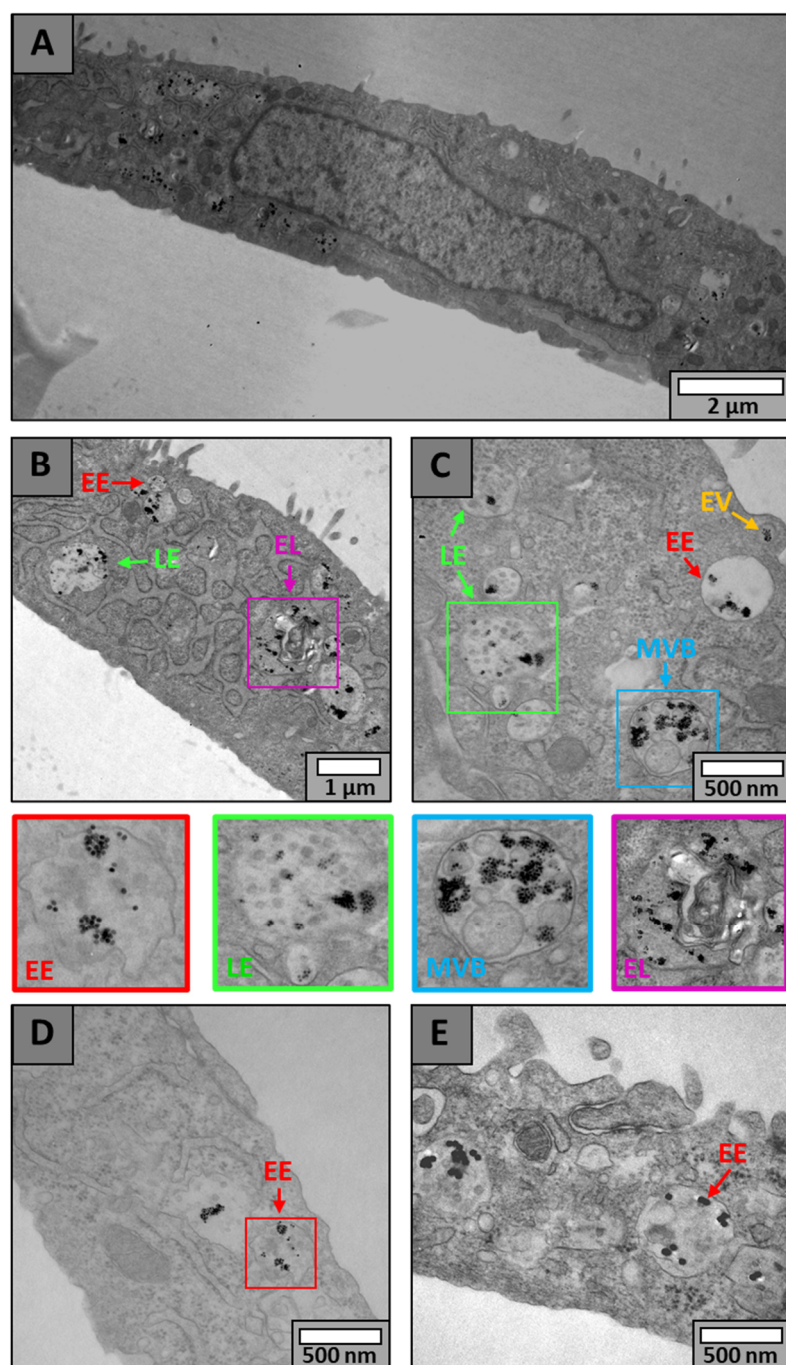


Figure 5.14. Representative electron micrographs captured from 70 nm ultrathin sections of NRK cells incubated with 12 nm UCNPs@PLM (DMEM, 5% FCS) at 37 °C for 24 h (A, B, C) or 1 h (D) or with 33 nm UCNPs@PLM for 1 h (E). The labels are defined as follows: endocytic vesicles (EV), early endosomes (EE), late endosomes (LE), multivesicular bodies (MVB) and endo-lysosome (EL). Some areas are enlarged for better visualization.

5.9 Conclusion

Both, intrinsically non-toxic PLM or AP surface modifications produce UCNPs with colloidal stability and brightness that is efficiently protected from water quenching. However, UCNPs@AP and UCNPs@PLM differ with respect to cytotoxicity. Viability and morphology of normal epithelial-like cells were strikingly affected by UCNPs@AP, while UCNPs@PLM did not induce any effect on NRK cells, even though they were internalized in higher amounts as compared to UCNPs@AP. Time resolved impedance analysis of cells revealed a delayed toxicity of the UCNPs@AP with an onset of cell death after around 30 h of exposure. The response profile shows a transient cell swelling prior to membrane permeabilization, suggesting necrosis as mechanism of cell death upon exposure to poorly shielded UCNPs@AP. Based on our data, the difference in toxicity is supposedly caused by a difference in chemical stability of the particles. UCNPs@PLM did neither disintegrate at room temperature in water nor in presence of serum at physiological temperatures. In contrast, UCNPs@AP dissolved under all conditions within hours. Their partial disintegration most likely also happens within the cells. Ion leakage from poorly shielded UCNPs@AP and their toxic effect might contribute to REPO4 formation in lysosomes, followed by lysosomal damage, which initiated necrosis in the epithelial cell line. This study clearly demonstrates that a toxicity analysis by common cell viability assays is not sufficient to provide a comprehensive picture of UCNPs biocompatibility. Microscopic analysis together with electrical cell-substrate impedance sensing revealed different interactions of epithelial cells with UCNPs, that was clearly dependent on the surface coating, leading to both, internalization of individual and agglomerated UCNPs. These findings stress out the importance of protective surface coatings on nanoparticle fate and interactions within the cell and might be helpful for surface engineering of inorganic nanoparticles suitable for long time applications in biological systems.

The promising results of **Chapter 4** on the water- and ion-protective characteristics of the phosphate-based PLM coating were supported in this chapter by the excellent chemical stability and non-toxicity of UCNPs@PLM in contact to epithelial cells although these particles were rapidly internalized. UCNPs@PLM convinced for further applications *in vitro* and possibly also *in vivo*, why UCNPs@AP should not be applied *in vivo* either. UCNPs@AP are suitable

particles to further analyze the impact of toxic UCNPs on this and other cell lines to deeply understand the fate of the UCNPs for a comprehensive toxicity evaluation.

6 Toxicity Profile of Poorly Surface-Protected Upconversion Nanoparticles in Contact to Epithelial Cells

6.1 Preface

Most of the experimental and theoretical work presented in this chapter was performed solely by the author. The PrestoBlue™ assays and some of the ECIS experiments were carried out by Lisa Tetek during her bachelor thesis under supervision by the author.

6.2 Introduction

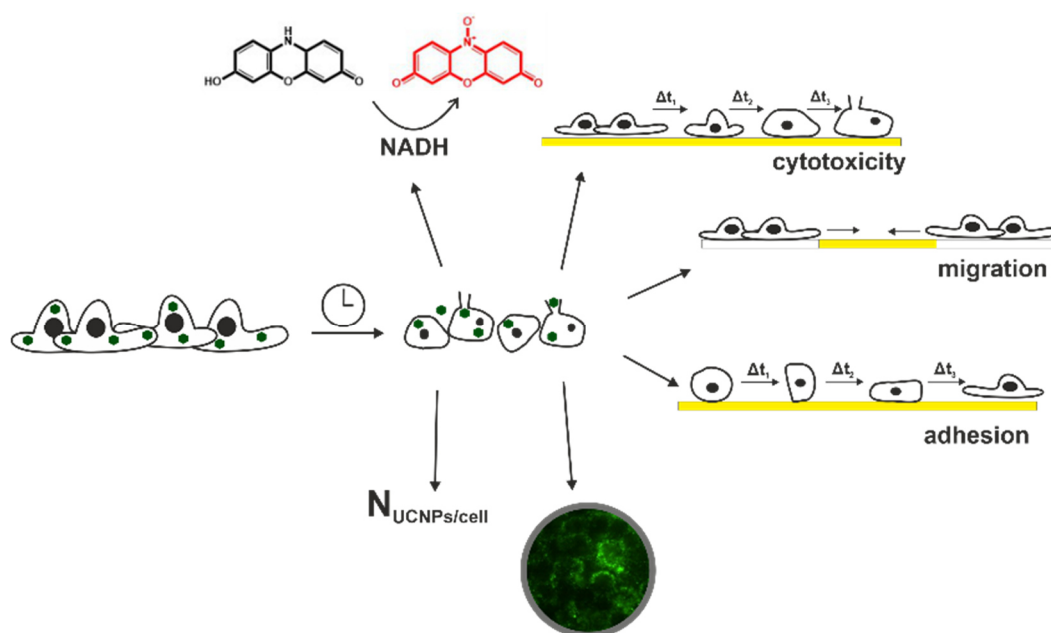
For a substantial introduction of the upconversion nanoparticles (UCNPs) into the biomedical field, their influence on cells and organisms has to be examined and understood in detail. So far, UCNPs have been considered in many *in vitro* and *in vivo* studies to be rather non-toxic (Guller et al., 2015). However, the toxicity studies have often been restricted to end-point studies of the cell viability on short-time scale. These were performed without assessing the toxicity in regard to the particle biotransformation. The cell models have been mostly restricted to cell lines for future application. These are often cancer cell lines, being known for their resilience (Torresan et al., 2021; Gnach et al., 2015; Guller et al., 2015; Tian et al., 2015). Moreover, the model cell line, the cell status and age (cf. **Chapter 1.4**), the UCNPs design, and the exposure mode vary highly in the relevant studies, making comparisons difficult. Therefore, it is rather difficult to make a general statement on the toxic properties of nanoparticles on the current data situation (Yang et al., 2021).

The main toxicity pathway of many inorganic particles, potentially leading to cell death, is the oxidative stress pathway. However, nanoparticles are also known to interfere with cellular mechanisms as cell signaling and normal cell functioning, which do not necessarily lead to cell death (Schrand et al., 2010). These pathways need to be taken into considerations, too. Especially when going from *in vitro* to *in vivo* measurements to test the functioning of modified UCNPs, a detailed *in vitro* study of UCNPs has to be performed in advance, including different assay formats on long-time scale. A differentiation of toxicity due to the nanoparticles themselves, their surface coating, or the disintegration products are required. Special focus

should lie on their potential interactions with cellular organelles, proteins, for instance enzymes, and the potential ROS formation due to ion leakage (Gnach et al., 2015).

Not only cancer cell lines are of interest but also those non-transformed cell lines, which are in contact to the particles after their (intravenous) injection and which are responsible for particle clearance or biodistribution. Depending on the particle size, the accumulation of nanoparticles has been reported in liver, spleen, kidney, heart, lung, bone marrow, and brain. Particles smaller as the filtration-size threshold for proteins (6 nm) have been reported to be partly excreted through the renal filter at the level of the proximal tubules (Bourquin et al., 2018). Therefore, the focus of toxicity research should lie on the barrier forming and sentineling cells, the nanoparticles have to cross to enter the organs, *e.g.* macrophages, endothelial cells, or organ lining epithelial cells (Bourquin et al., 2018). A detailed knowledge on the mechanisms of toxicity and cellular disfunctioning may enable the improvement of particle design for their future applications and pave the way to a more clinical relevance.

It was the aim of this project to carry out a detailed study on the toxicity of UCNPs on epithelial cells to reveal potential pathways, the UCNPs may trigger within non-transformed cells (**Scheme 6.1**). Normal rat kidney (NRK) cells from the proximal tubule were chosen as model epithelial cell line to test the toxicity of medium sized UCNPs NaYF₄(Yb,Er) with amphiphilic polymer coating. Different assays were performed, targeting the viability, the membrane integrity, and the adhesion as well as migration of the cells being exposed to the particles. Additionally, the internalization of the particles was determined qualitatively and quantitatively. The information about changes in metabolism, uptake, and cell physiology enabled the generation of a more comprehensive response profile of these cells to the UCNPs@AP.



Scheme 6.1. Overview of applied techniques to assess an *in vitro* toxicity profile of UCNPs for normal non-transformed cells, including a fluorescence-based cell viability assay (reading the metabolism with NADH), impedance-based cytotoxicity assays (reading cell morphology changes), impedance-based analysis of migration and adhesion of the cells, and the qualitative as well as quantitatively analysis of particle internalization.

6.3 Particle Preparation and Characterization

Ytterbium and erbium doped UCNPs from the type NaYF_4 were prepared. The synthesis was performed in high boiling solvent octadecene and oleic acid (Lin et al., 2008), resulting in oleate (OA)-coated particles UCNPs@OA. Transmission electron micrographs of UCNPs@OA reveal an average size of (25.0 ± 0.8) nm after statistical analysis (**Figure 6.1A,B**).

They were modified with an amphiphilic polymer (AP) to transfer them into aqueous media. Intensity weighted dynamic light scattering measurements of UCNPs@AP in water revealed a hydrodynamic diameter (d_{hydro}) of (50 ± 2) nm and a low polydispersity index (Pdl) of 0.22 ± 0.01 (**Figure 6.1C**), indicating the colloidal stability of the UCNPs@AP in H_2O . The d_{hydro} of UCNPs@AP in the measurement media Leibovitz L-15 (5% FCS, (v/v)) and DMEM (5% FCS, (v/v)) were (99 ± 1) nm (Pdl = 0.23 ± 0.01) and (87 ± 2) nm (Pdl = 0.18 ± 0.01), respectively. Compared to H_2O , the particles showed significant larger diameters in such media. This may be due to adsorbing media proteins and biomolecules, forming a bio-corona around the particles (Casals et al., 2010; Latreille et al., 2022). The particles were stable with this corona for at least 3 d (time of all experiments). The osmolarity of the particle suspension was

checked for the highest particle concentration to warrant the addition of isotonic dispersions to the cells. The osmolarities were found to be similar to those of the pure media with values around $320 \text{ mOsmol}\cdot\text{kg}^{-1}$. Upon 980 nm laser irradiation (cw, $85 \text{ W}\cdot\text{cm}^{-2}$) the spectra show similar intensity for the red and green luminescence with a ratio of green (500 – 600 nm) to red luminescence intensity (600 – 700 nm) close to 1. This indicates that the surface coating does not protect the particle surface from access of water as such values with reduced green emission are typically for a weak protection (S. Wilhelm et al., 2017) (**Figure 6.1D**). The particle diameter determined by TEM was used to calculate the number of particles (particle density $\rho = 4.23 \text{ g}\cdot\text{cm}^{-3}$ for NaYF_4 (Tan et al., 2011)) in a dispersion of $100 \mu\text{g}\cdot\text{mL}^{-1}$ UCNPs@AP as $2\cdot 10^{12}$ particles per 1 mL.

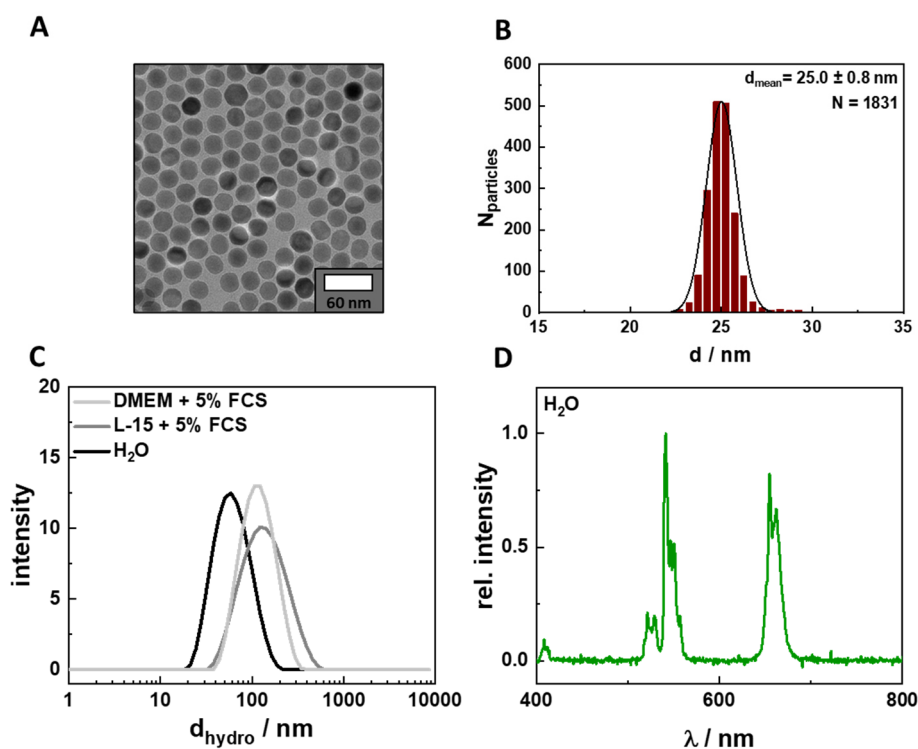


Figure 6.1. (A) TEM micrograph of $\text{NaYF}_4(\text{Yb,Er})@OA$ and (B) corresponding particle size distribution to determine $d_{\text{mean}} = 25.0 \pm 0.8 \text{ nm}$ (mean \pm SD). (C) Representative hydrodynamic diameter distribution (d_{hydro} , $N = 3$) of modified $\text{NaYF}_4(\text{Yb,Er})@AP$ ($1 \text{ mg}\cdot\text{mL}^{-1}$) at rt in H_2O , Leibovitz L-15 (5% FCS, (v/v)), and DMEM (5 % FCS, (v/v)). (D) Luminescence spectrum of $\text{NaYF}_4(\text{Yb,Er})@AP$ at rt in H_2O ($1 \text{ mg}\cdot\text{mL}^{-1}$) upon 980 nm excitation (cw, $85 \text{ W}\cdot\text{cm}^{-2}$).

The chemical stability of AP-coated UCNPs has been analyzed in **Chapter 5**. Although that study was carried out with particles of the same core but additionally equipped with an inert

shell of the same lattice for better sensitivity, the trend should be valid for all particles of the type NaYF₄, independent of the exact doping, architecture, and size. Rapid luminescence losses of the 33 nm UCNPs@AP were observed at rt in H₂O and attributed to particle dissolution with $t_{1/2}$ of ~0.5 h. A protein corona delayed particle degradation at rt but did not protect the particles at 37 °C. These results let assume that particle degradation at 37 °C can happen also when the particles are internalized by cells and stored in cellular vesicles. As the equilibrium in the cells is dynamic and RE³⁺ ions are known to be complexed by phosphates (Li et al., 2014), the dissolution process might be accelerated. The protein corona as well as the rather loose surface coating are likely degraded quickly within cells (Shang et al., 2014) so that the particle surface is accessible for degradation. These results are important when interpreting the toxicity of these nanoparticles.

6.4 Analysis of Nanoparticle Internalization

The internalization of UCNPs@AP into the cells was examined as the number of internalized UCNPs has been known to dictate their toxic affect to cells (Wang et al., 2020; Hemmer et al., 2013). To estimate the uptake of UCNPs@AP by the model cell line (NRK), the number of particles per cell was determined. An incubation time of 24 h was chosen so that uptake saturation for negatively charged UCNPs is likely (Rojas-Gutierrez et al., 2019; Wang et al., 2020). The NRK cells were incubated with UCNPs@AP (20 – 100 µg·mL⁻¹, L-15, 5% FCS, (v/v)) for 24 h. The RE ion concentration in the cell lysate was determined by inductively coupled plasma - mass spectrometry (ICP-MS) to calculate an average number of UCNPs per cell ($N_{\text{UCNPs/cell}}$). Around 3% of the UCNPs applied to the extracellular buffer were detected in the cell lysate after 24 h incubation time, resulting in $(1.9 - 4.0) \cdot 10^4$ UCNPs@AP per cell. The particles occupy ~0.03 % of the cell volume (**Table 6.1**).

Table 6.1. Mass of UCNPs per cell ($m_{\text{UCNP/cell}}$), number of UCNPs per cell ($N_{\text{UCNPs/cell}}$), recovery rate of UCNPs ($m_{\text{found}}/m_{\text{applied}}$) in the cell lysate, and the fraction of the volume that is occupied within a cell by UCNPs ($V_{\text{UCNPs}}/V_{\text{cell}}$) was determined from the UCNPs mass in cell lysates of the model cell line NRK obtained by ICP-MS measurements. Cell lysates (passage numbers 15 – 21) were prepared after incubation with UCNPs@AP (L-15, 5% FCS, (v/v)) at 37 °C for 24 h (mean \pm SEM, 10 repetitions in 5 independent experiments).

$\beta(\text{UCNPs})_{\text{applied}} / \mu\text{g}\cdot\text{mL}^{-1}$	20	40	100
$m_{\text{UCNPs/cell}} / \text{pg}$	0.81 ± 0.08	1.3 ± 0.1	1.7 ± 0.3
$N_{\text{UCNPs/cell}}$	$(1.9 \pm 0.2) \cdot 10^4$	$(2.9 \pm 0.3) \cdot 10^4$	$(4.0 \pm 0.7) \cdot 10^4$
$N_{\text{found}}/N_{\text{applied}} / \%$	4.5 ± 0.6	3.5 ± 0.4	1.9 ± 0.3
$V_{\text{UCNPs}}/V_{\text{cell}} / \%$	0.019 ± 0.004	0.029 ± 0.004	0.04 ± 0.01

The cells were washed several times before lysis to remove unbound UCNPs and the incubation time was set long enough to reach uptake saturation. Thus, most of the detected UCNPs@AP are attributed to be within the cells and not attached to the cell membrane (Rojas-Gutierrez et al., 2019). The cells, exposed to (20, 40, 100) $\mu\text{g}\cdot\text{mL}^{-1}$ UCNPs@AP, internalized (~ 2 , ~ 3 , ~ 4) $\cdot 10^4$ UCNPs/cell. A higher fraction of the applied UCNPs were taken up by the cells when the external particle concentration was lower. These three values suggested a non-linear internalization correlation.

The non-linear correlation between uptake efficiency and applied concentration has been reported several times, *e.g.* for 4 nm D-penicillamine coated quantum dots in epithelial cervix cancer cells HeLa, (Jiang et al., 2010) and for 35 nm polyethylene imine coated UCNPs in epithelial-like liver cancer cells HepG2 (NaYF₄(Yb,Er)@PEI, (Wang et al., 2020)). This relation was assigned to decreasing cellular ATP content, weakening energy-dependent uptake, and the reduction of receptors for receptor-mediated endocytosis on the cell surface. These hypotheses might explain the results of this study as well.

In other studies, different numbers of internalized particles were reported for cells exposed to UCNPs (100 $\mu\text{g}\cdot\text{mL}^{-1}$) for 24 h, like $\sim 8 \cdot 10^4$ UCNPs@PLM (91 x 53 nm) per epithelial lung cancer cell A549 (P. A. Rojas-Gutierrez et al., 2019) or ~ 275 pg 35 nm polyacrylic acid (PAA) coated UCNPs (100 $\mu\text{g}\cdot\text{mL}^{-1}$) per HepG2 cell (Wang et al., 2020). However, internalization is highly dependent on the cell type and nanoparticle characteristics as size, shape, surface coating, and biotransformation (Gnach et al., 2015). These parameters differed in the studies,

limiting the outcome of the comparison. Nevertheless, the conclusion applies that the number of particles per cell were in the same order of magnitude.

To prove that the number of particles per cell as quantified by ICP-MS corresponded mostly to internalized UCNPs and not to UCNPs attached to the cell membrane, upconversion microscopy images of NRK cells were taken after treatment with UCNPs@AP at 37 °C for 4 – 24 h (**Figure 6.2**). After 4 h, upconversion is not detectable. With rising incubation times, UCNPs luminescence increased and the UCNPs are found around the nucleus. Thus, the upconversion intensity is assigned to internalized UCNPs and not to UCNPs attached to the outer side of the membrane. This confirmed that the $N_{\text{UCNPs/cell}}$ determined by ICP-MS corresponded mainly to internalized UCNPs.

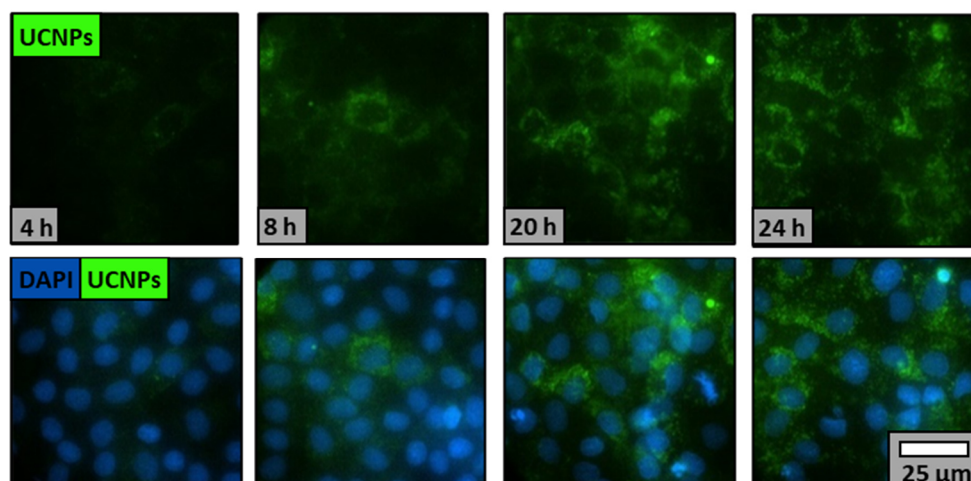


Figure 6.2 Wide-field upconversion micrographs of NRK cells (passage numbers 16 and 17) exposed to 25 nm UCNPs@AP ($50 \mu\text{g}\cdot\text{mL}^{-1}$) in L-15 at 37 °C for 4 – 24 h. Upconversion intensity upon irradiation with 980 nm (cw, $640 \text{ W}\cdot\text{cm}^{-2}$) is shown in green and DAPI stained nuclei in the overlay in blue.

6.5 End-Point Cell Viability Assay

The cytotoxicity of the UCNPs@AP was analyzed by their impact on metabolic activity of NRK cells *via* the PrestoBlue™ assay. The end-point assay reads the cellular redox metabolism at a predefined time by detecting fluorometrically the amount of resazurin, which was converted intracellularly by reduced redox coenzymes to resorufin. The viability of the cells was determined after different incubation times (24 h, 72 h) with the particles UCNPs@AP

(0.5 – 400 $\mu\text{g}\cdot\text{mL}^{-1}$, L-15, 5% FCS, (v/v)) at 37 °C. After an incubation time of 24 h, the cells have already a reduced viability when UCNPs@AP were applied in concentrations $\geq 10 \mu\text{g}\cdot\text{mL}^{-1}$ (**Figure 6.3A**). The cell population treated with the highest UCNPs@AP (400 $\mu\text{g}\cdot\text{mL}^{-1}$) shows 75% viability. When the cells (passage numbers 33 – 36) are exposed to the particles for 72 h, a concentration dependent reduction in cell viability is observed with the half-maximal effective concentration (EC_{50}) of $(103 \pm 8) \mu\text{g}\cdot\text{mL}^{-1}$. The cells treated with 0.5 or 10 $\mu\text{g}\cdot\text{mL}^{-1}$ show a slightly higher cell viability as those with lower particle concentrations or control L-15. The performance of the PrestoBlue™ assay was verified with the positive control Triton X-100 (0.5% (v/v), L-15, 5% FCS (v/v)). A conversion from resazurin directly by the UCNPs is excluded by the outcome of a cell-free control (data not shown here).

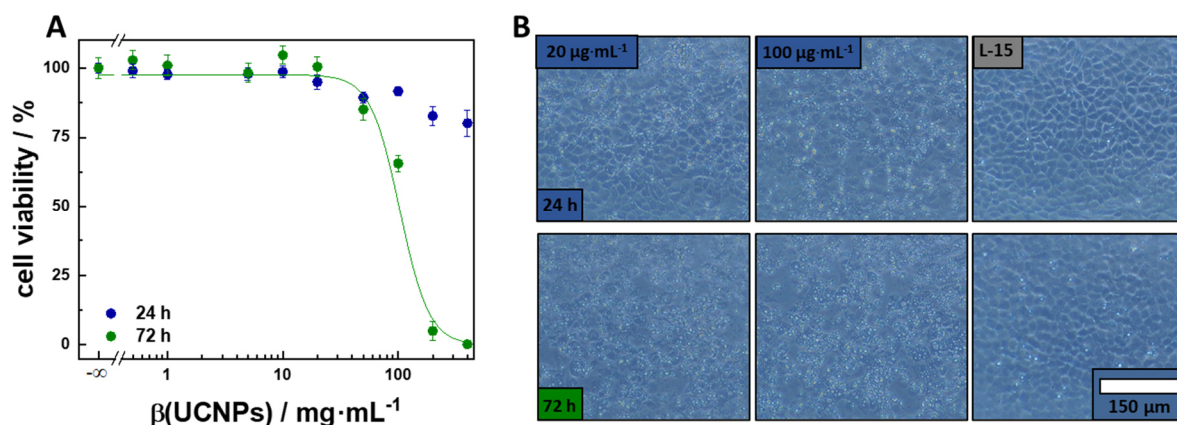


Figure 6.3. (A) Viability of NRK cells (passage numbers 33 – 36) after incubation with UCNPs@AP (0.5 – 400 $\mu\text{g}\cdot\text{mL}^{-1}$) at 37 °C in L-15 medium (5% FCS (v/v)) at 37 °C for 24 h or 72 h. The sigmoidal concentration response relation is approximated by a 4-parameter logistic model ($R^2 = 0.99$) to determine the EC_{50} after 72 h as $(103 \pm 8) \mu\text{g}\cdot\text{mL}^{-1}$ (intensity weighted mean \pm error, three independent experiments with three replicates). (B) Phase contrast microscopy images of NRK cells incubated with UCNPs@AP (20 $\mu\text{g}\cdot\text{mL}^{-1}$ or 100 $\mu\text{g}\cdot\text{mL}^{-1}$ in L-15 + 5% FCS (v/v)) or control at 37 °C for 72 h.

Cells incubated with low particle concentrations (0.5 and 10 $\mu\text{g}\cdot\text{mL}^{-1}$) for 72 h exhibited a cell viability higher than that of control cells. This typical effect of a boosted metabolic response upon low dose stimulation (0.5 $\mu\text{g}\cdot\text{mL}^{-1}$) by potentially toxic substances has been explained by hormesis (Stebbing, 1982). It has also been reported for nanoparticles as well (Iavicoli et al., 2010; Jiao et al., 2014; Stebbing, 1982).

Many cell viability studies on UCNPs have already been performed with end-point assays like MTT or MTS assays (Wang et al., 2020; Guller et al., 2015). However, the comparison of different cell viability studies with UCNPs of different sizes and surfaces in different cells is not

possible. Moreover, most of the assays were performed in cancer cells and the results may not be transferred easily to non-transformed cells (Guller et al., 2015). However, in a large number of these short-time experiments only a very low toxicity of UCNPs was observed within 24 – 48 h, which was similar to the outcome of the PrestoBlue™ assay within the current study.

The representative phase contrast micrographs of the cell layers after incubation with a particle concentration of $20\ \mu\text{g}\cdot\text{mL}^{-1}$ for 24 h show only a few detached cells in an intact cell layer (**Figure 6.3B**). When exposed to high particle concentrations ($100\ \mu\text{g}\cdot\text{mL}^{-1}$), mostly spherical and detached cells as well as cell fragments are visible. After 72 h also the cell layers incubated with $20\ \mu\text{g}\cdot\text{mL}^{-1}$ UCNPs@AP mainly consist of rounded cell fragments with only a few cells, attached to the substrate, in between.

In comparison to the phase contrast micrographs, which revealed only a low number of fully attached cells, the cell viability was close to 100% for the cells exposed to $100\ \mu\text{g}\cdot\text{mL}^{-1}$ UCNPs@AP for 24 h. The same contradictory result was obtained for the cells after 72 h incubation with $20\ \mu\text{g}\cdot\text{mL}^{-1}$ UCNPs@AP with a cell viability of ~100% and a fragmented cell layer. A conversion of resazurin by the particles themselves could be excluded by cell-free measurements (data not shown). Therefore, it was required to check on these contradictory results of intact energy metabolism mitochondria and dramatic cell morphology changes with another assay format.

6.6 Impedance-Based Cell Analysis

To check the suitability of the PrestoBlue™ assay, the toxicity of UCNPs at NRK cells was assessed by the wholistic impedance-based cell analysis. This non-invasive approach provides real-time information of cellular morphology changes by on-line monitoring of the electrical impedance and supplies time-resolved information about the onset of cell death. The ECIS assay was used to examine the toxicity of resting cells as well as the impact of the UCNPs@AP on the migration and adhesion behaviour. The latter phenotypes require active cells. To mirror the cell coverage of the electrode and the membrane integrity, the impedance or capacitance of the NRK cells at 32 kHz were recorded as the capacitance has the largest sensitivity at this AC frequency (**Figure 6.4A,C**). Changes on the intercellular clefts defined by cell-cell and cell-

substrate contacts were monitored with the impedance at 4 kHz when the influence of resistance is maximal (**Figure 6.4A,B**).

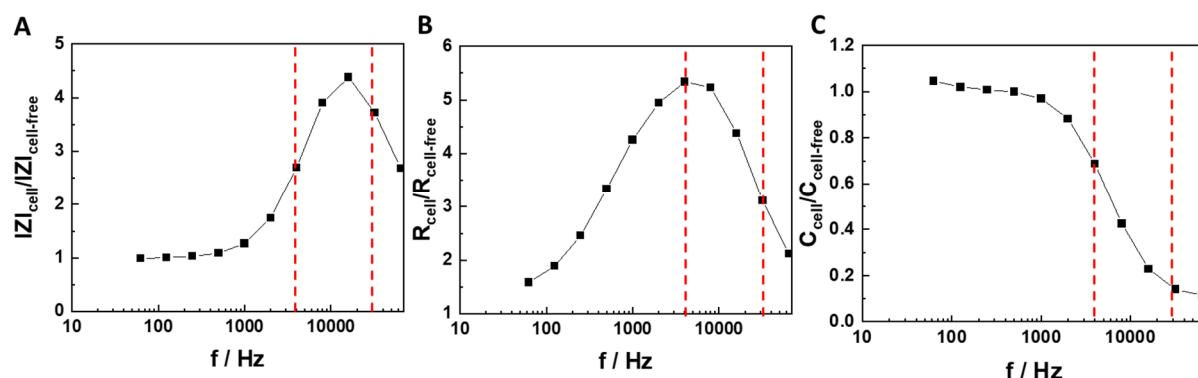


Figure 6.4. AC frequency-dependent ratio (A) impedance $|Z|$, (B) resistance R , and capacitance C of cell-covered and cell-free electrodes for the model cell line NRK at 37 °C. Red dashed lines mark 4 kHz and 32 kHz.

6.6.1 Toxicity

The toxicity of the particles was analyzed for confluent NRK cell layers by the normalized impedance at 32 kHz. Representative normalized impedance ($|Z|_{\text{norm.}} = |Z|_t/|Z|_0$) time courses of NRK cells treated with UCNPs@AP ($0.5 - 100 \mu\text{g}\cdot\text{mL}^{-1}$, L-15, 5% FCS (v/v)) are shown in **Figure 6.5A**. After addition of L-15 or particles at time point 0 h, the normalized impedance decreases slightly until new basal values were obtained. Concentration-dependent changes of the impedance courses can be identified a few hours after particle addition. The normalized impedance curves of cells with high particle concentrations ($10 - 100 \mu\text{g}\cdot\text{mL}^{-1}$) start to rise after ~6 h to maximum values after ~18 h. This level is maintained for a few hours until the impedance curves decrease monotonically, cutting the impedance time course of untreated cells after ~34 h and reaching values of a cell-free electrode after 48 h. A medium concentration of $5 \mu\text{g}\cdot\text{mL}^{-1}$ triggers a slight increase with the maximum reached after 18 h and stays around this value for at least 72 h. The impedance time courses of cells treated with low concentration ($0.5 - 1 \mu\text{g}\cdot\text{mL}^{-1}$) are not distinguishable from the ones of the control measurement. The UCNPs@AP induce a weaker response in cells from higher passage numbers (P35 vs P33) (**Figure 6.5B**). Medium concentrations applied to these cells delays the particle induced impedance decrease ($20 \mu\text{g}\cdot\text{mL}^{-1}$) or do not trigger the decrease at all ($10 \mu\text{g}\cdot\text{mL}^{-1}$).

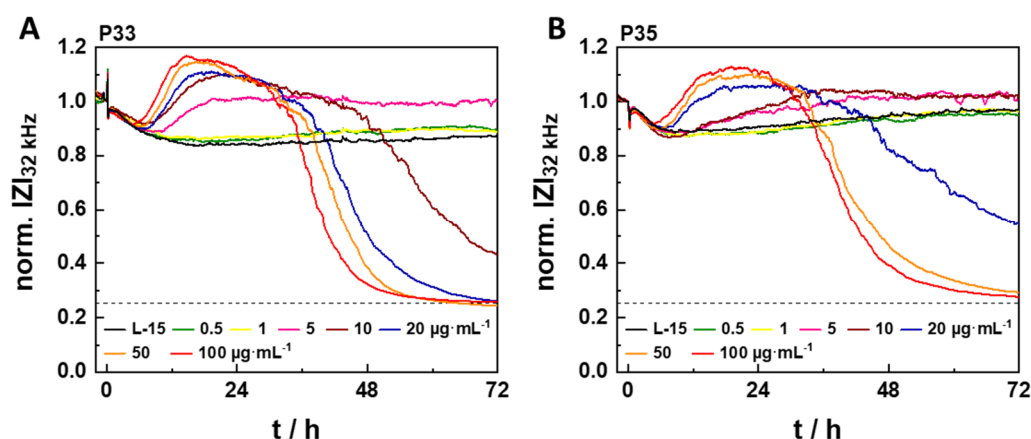


Figure 6.5. Normalized time courses recorded for impedance at 32 kHz of NRK cells (passage number (A) P33 and (B) P35), treated with UCNPs@AP ($0.5 - 100 \mu\text{g}\cdot\text{mL}^{-1}$, L-15, 5% FCS (v/v)) or control at time point 0 h at 37°C for 72 h. Average baseline impedance magnitude was $(1.070 \pm 0.008) \text{ k}\Omega$. Dashed lines indicate impedance values of cell-free electrodes.

In general, the decrease of the cellular impedance as response to a toxic substance can be attributed only to disrupted cell-cell and cell-substrate contacts or also to losses of the cell membrane integrity. These effects can be captured by the ECIS assay at different AC frequencies. The capacitance at 32 kHz reflects the electrode coverage and the membrane capacitance of the NRK cells as indicator for membrane integrity. The changing impedance at 4 kHz mirrors mainly the resistance of changing cell-cell and cell-substrate contacts when the capacitance at 32 kHz is maintained. Therefore, the time courses are analyzed in more detail at the time point of onset cell death. In the current toxicity study, the impedance of the cells at 4 kHz (**Figure 6.6B**) as well as the capacitance at 32 kHz (**Figure 6.6C**) show the same monotonic changes to values of a cell-free electrode, starting after ~ 34 h in a concentration-dependent manner, as the impedance at 32 kHz (**Figure 6.6A**). This indicated that the total impedance decrease of the NRK cells, initiated by UCNPs@AP, can be attributed to a loss of membrane integrity and changes on the intercellular cleft as well as the cell-substrate cleft.

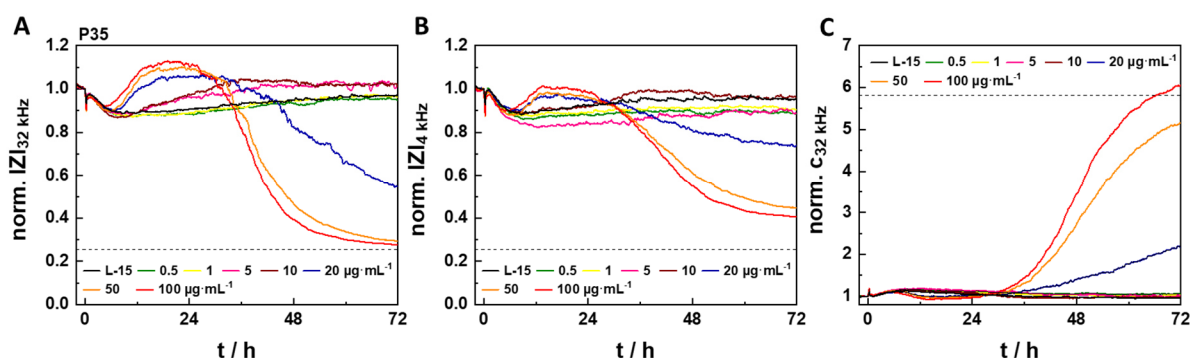


Figure 6.6. Normalized time courses of impedance (A) at 32 kHz, (B) at 4 kHz and (C) of capacitance at 32 kHz of NRK cells (passage number 35), treated with UCNPs@AP (0.5 – 100 $\mu\text{g}\cdot\text{mL}^{-1}$, L-15, 5% FCS (v/v)) or control at time point 0 h at 37 °C for 72 h. Average baseline magnitude of impedance at 32 kHz was (1.070 ± 0.008) k Ω , at 4 kHz (1.76 ± 0.07) k Ω and for capacitance at 32 kHz (7.48 ± 0.05) nF (N = 32). Dashed lines indicate impedance and capacitance of cell-free electrodes.

Before the monotonic impedance drop at 32 kHz, the cells show a transient increase. This characteristic cell response is analyzed in more detail to unveil details of the cell death mechanism. A similar response profile has been already reported for different cells and nanomaterials, such as NRK cells exposed to C-Dots, HepG2-cells incubated with ZnO nanoparticles (Bartczak et al., 2015), or A549 cells treated with CuO or ZnO NPs (Seiffert et al., 2012). The transient increase in impedance was addressed in more detail by Seiffert et al. They have proposed that the release of glutathione, a second messenger of apoptosis, was associated to impedance-increasing rearrangements of the plasma membrane, including the exposure of phosphatidylserine on the outer leaflet of the plasma membrane as well as changes in the distribution of cholesterol (Seiffert et al., 2012). However, the proposed rearrangements of the cell membrane are not likely to be visible in the capacitance since almost all cell types with unfolded membrane have a cell membrane capacitance of around $1 \mu\text{F}\cdot\text{cm}^{-2}$, independent of their exact membrane composition (Reiss et al., 2015). Moreover, apoptosis and early apoptosis events usually accompany with cell shrinkage (Bortner et al., 1998), which should result in a broadening of the extracellular current path and an impedance decrease instead of an increase prior to cell death. In contrast, cell swelling, leading to narrowing of the intercellular cleft and an impedance increase, is a marker for onset of necrosis and has been indeed discussed for the transient impedance increase prior to cell death (Zinkl et al., 2019).

A validation of these theories should be accessible by extracting cell-related parameters out of the impedance courses in the time interval of the transient increase. Three cell-related parameters are accessible *via* fitting the impedance spectra with an appropriate transfer function (Giaever et al., 1991), containing the following cell-related parameters: the specific resistance in cell-cell (R_b) and cell-substrate contacts (α) and the cell membrane capacitance (C_m). A custom-developed fitting algorithm was applied on the time courses of impedance of NRK cells with exposure to UCNPs@AP to translate the frequency-dependent normalized impedance spectra into α , R_b , and C_m for the first 30 h of the experiment to capture the initial impedance increase (**Figure 6.7**, corresponding errors of reactance and resistance are given in **Figure A 5**). The transient increase in the normalized impedance is found to be concentration-dependent and lasts around 24 h with a maximum value of +20% of basal impedance values for the highest UCNPs@AP concentration after 15 h (**Figure 6.7A**). During this time frame, concentration-dependent changes of the three cell-related parameters are observed. The cells treated with the lowest concentrations ($0.5 - 1 \mu\text{g}\cdot\text{mL}^{-1}$) exhibit similar courses for R_b , C_m , and α than the control. Maximal differences were obtained for cells incubated with the highest UCNPs@AP concentration ($100 \mu\text{g}\cdot\text{m}^{-1}$). R_b and α increased with around 50% and 30 %, respectively, in comparison to the control course, while C_m dropped by 50% at maximum. The time courses of cells with exposure to medium concentrations are in between.

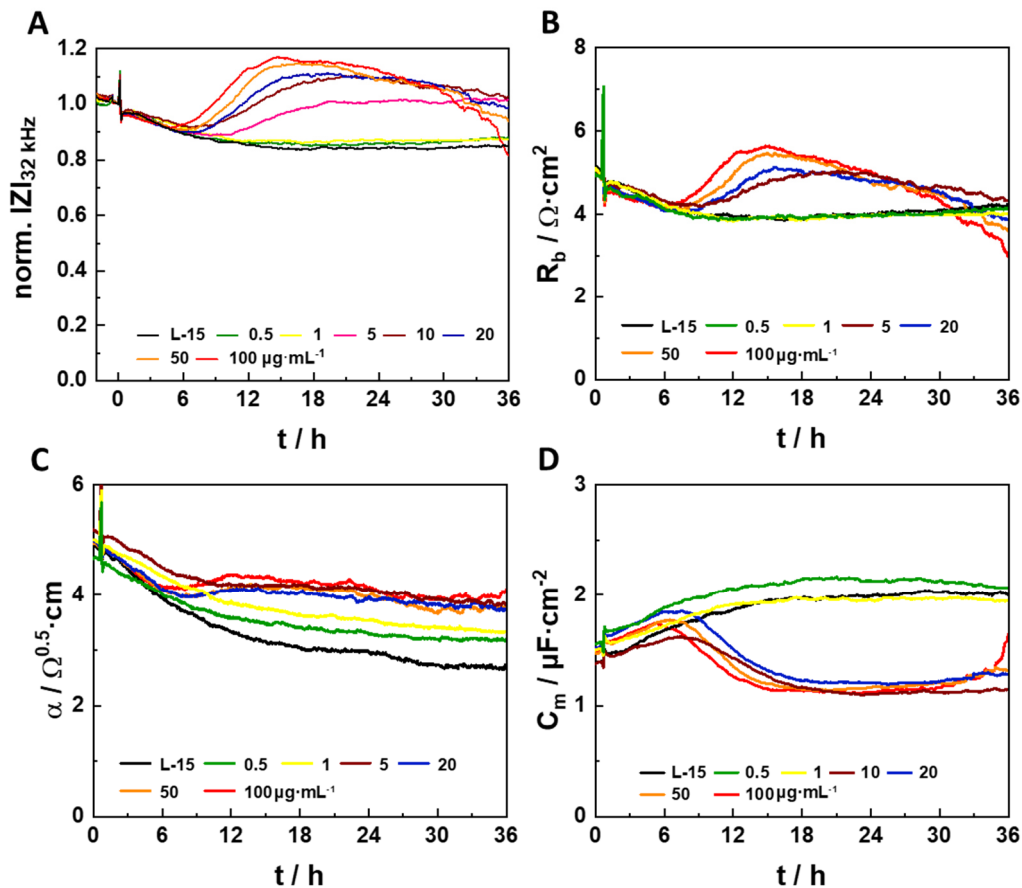


Figure 6.7. (A) Representative normalized impedance time course at 32 kHz of NRK cells (passage 33) with exposure to UCNPs@AP (0.5 – 100 $\mu\text{g}\cdot\text{mL}^{-1}$, L-15, 5% FCS (v/v)) or control at 37 °C at time point 0 h. The frequency-dependent normalized impedance spectra were fitted with an appropriate transfer function to obtain the specific resistance in the cell-cell (R_b) and cell-substrate contacts (α) and the specific cell membrane capacitance (C_m). R_{bulk} was kept static with 360 Ω and the electrode parameters A_{CPE} and n_{CPE} were fitted continuously with mean values of $(1.8 \pm 0.2) \cdot 10^{-5} \text{ F}\cdot\text{s}^{n-1}\cdot\text{cm}^{-2}$ for A_{CPE} and 0.94 ± 0.01 for n_{CPE} (mean \pm SD, 8W10E array with 8 wells).

The increase in R_b demonstrated the narrowing of the intercellular cleft and the slight increase in α the narrowing of the cell-substrate cleft. The decrease in C_m is associated to a reduced membrane folding. When a cell swells, its volume increases and the cell expands in all directions, coming closer to the substrate and the neighboring cells. Folded membrane had to unfold for these expansions and C_m was found to decrease. These three changes are indicators of cell swelling, which may be linked to necrosis.

Necrosis has been reported for dissolving lanthanide-based particles. Especially, rare earth oxide particles like LaO_3 , EuO_3 , ErO_3 , YO_3 , and YbO_3 are known to degrade in the lysosomes of macrophages. They form rare earth phosphates REPO_4 by dephosphorylating the membrane

lipids. The damage of the lysosomal membrane leads to the release of the lysosomal loading into the cytoplasm, triggering inflammation and necrosis (Gao et al., 2017; Li et al., 2014). The formation of REPO₄ followed by inflammation has also been observed for the more stable rare earth fluoride particles NaYF₄(Yb,Er) in macrophages (Li et al., 2015). As the UCNPs@AP tended to degradation in cell-free tests (cf. **Chapter 5**) and necrosis was identified as the major form of cell death from the impedance course, it is reasonable to assume that UCNPs@AP triggered similar cascades in the NRK cells including ion leakage, REPO₄ formation, vesicle damage, and necrosis.

The concentration-dependent impedance time courses of the cells during exposure to UCNPs@AP at 37 °C were different for cells of different passages (cf. passage number 33 vs 35 in **Figure 6.5**). The minimum concentration inducing cell death changed and the time point of cell death was delayed. This might be the result from more pronounced senescence in cells with a higher passage number. To evaluate the hypothesis of replicative senescence and hence, the less sensitivity to the UCNPs, the passage number-dependent toxicity was further analyzed by repeating the toxicity experiments with cells from low passage numbers (14 – 17) and from higher passage numbers (37) (**Figure 6.8**). Alterations in the main features of the passage-dependent impedance time courses, the transient impedance increase, and the minimum concentration triggering cell death, were analyzed. The cells used directly after recultivation (passage number 14) show a retarded response to the UCNPs as the transient impedance increase maximum is detected after ~48 h and the monotonic decrease, mirroring cell death, is only indicated within the 90 h measurement time (**Figure 6.8A**). When cells undergo a few more divisions (passage number 17), UCNPs@AP are toxic at high concentrations (**Figure 6.8B**). UCNPs@AP have a distinct toxicity to the cells of passage number 31 with cell death inducing concentrations $\geq 5 \mu\text{g}\cdot\text{mL}^{-1}$ and no visible transient impedance increase prior to cell death (**Figure 6.8C**). The transient impedance increase is most pronounced for slightly “older” cells (passage number 33) with $10 \mu\text{g}\cdot\text{mL}^{-1}$ as minimum concentration triggering cell death (**Figure 6.8D**). With further rising passage number, the cells are less affected by the UCNPs@AP as only the highest concentration induced cell death for the senescent phenotype (passage number 37) (**Figure 6.8E**).

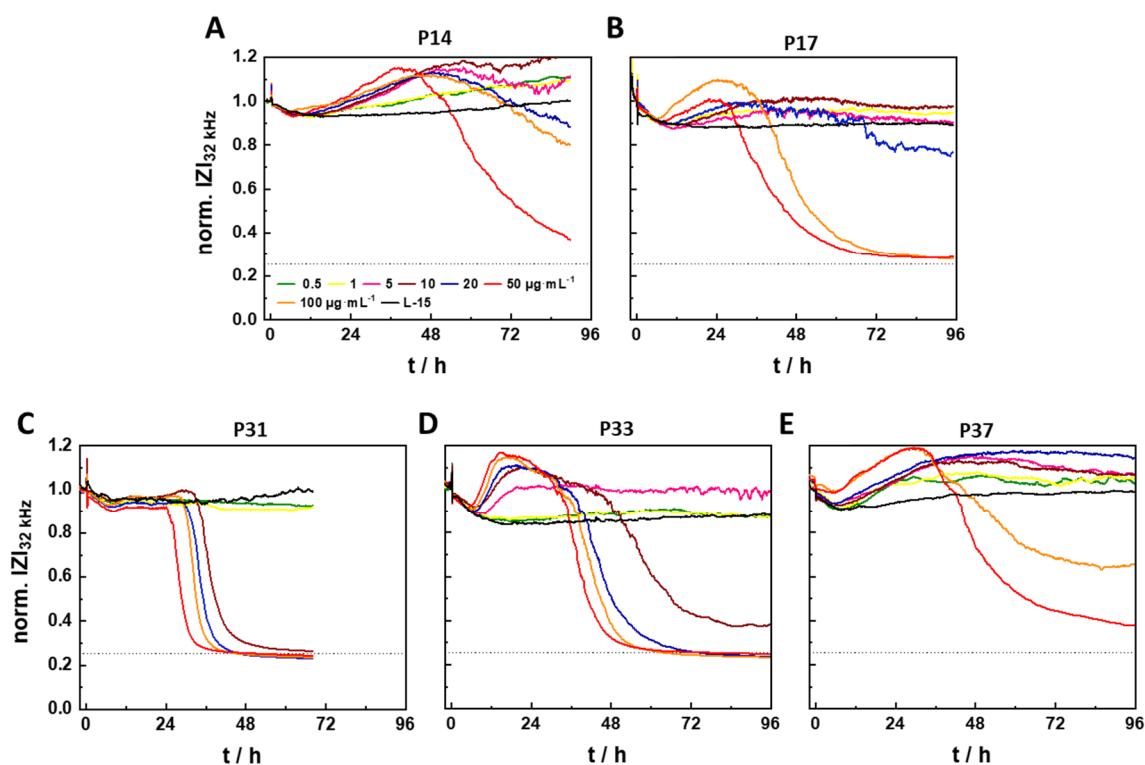


Figure 6.8. Normalized impedance time course at 32 kHz of NRK cells exposed to UCNPs@AP ($0.5 - 100 \mu\text{g}\cdot\text{mL}^{-1}$, L-15 + 5% FCS (v/v)) or control at time point 0 h at 37°C . NRK cells were from low (A, B) (P14 and P17), (C, D) medium (P31 – P33), or (E) high passage numbers (P37). Dashed lines represent impedance values of a cell-free electrode. All y-axes have the same scale.

Altogether, cells from low passage numbers were less affected by the UCNPs@AP as they might be more robust to toxicants or not as active in terms of internalization when they had undergone only a few replications after recultivation. The toxic impact of UCNPs@AP on NRK cells increased with rising number of replications and reached a maximum at passage number ~ 31 . The cells from passage numbers, which were influenced the most, might be not covered here as no cells from passage numbers between 17 and 31 were tested. After a maximum cell response was reached, the influence of UCNPs@AP was reduced again for the cells from highest passage numbers. The same trend of age-dependent impedance time courses for NRK cells of different passage numbers was observed for 33 nm UCNPs@AP in **Chapter 5** and for 24 nm UCNPs@AP-RB in **Chapter 7**. A reason for the reduced response from cells of higher passage numbers could be a slower metabolism with a reduced particle internalization of older cells and hence, a lower number of intracellular particles, potentially interacting with the cells. The different internalization of NP by replicative senescent cells has been already

reported for quantum dots with poly(ethylene glycol) coating in human lung fibroblast cells (IMR90) and in human colon epithelial cells (CCD841CoN) (Foroozandeh et al., 2019). A lower particle uptake has been reported to be accompanied by reduced toxicity (Wang et al., 2020). Thus, the reduced cell response for cells from different passage number seems valid.

A verification of this hypothesis was conducted by microscopic studies of cells from low and high passage numbers, which were incubated with the UCNPs@AP for 4 – 24 h (**Figure 6.9**). In comparison, the micrographs of cells from higher passage numbers (P35, P36) show no or a strongly reduced upconversion intensity at all time points compared to those cells from lower passage numbers (P15, P16). This indicates a lower UCNP internalization of cells from higher passage numbers and substantiates the theory that UCNPs@AP might have a lower impact to replicative senescent cells due to reduced particle uptake.

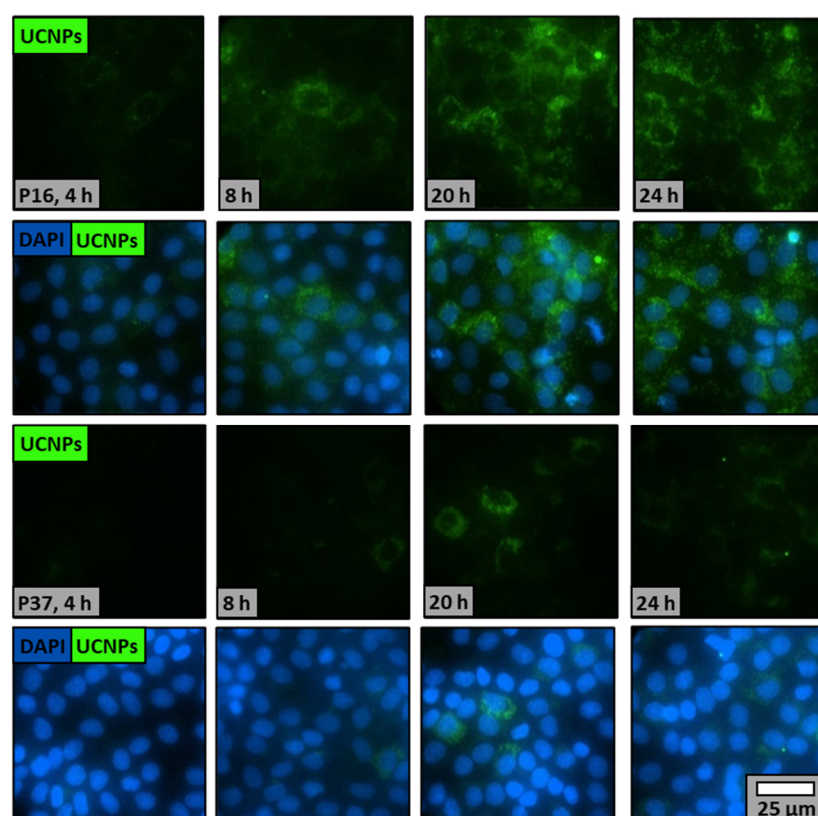


Figure 6.9. Wide-field upconversion micrographs of NRK cells (passage numbers P16 and P37) exposed to 25 nm UCNPs@AP ($50 \mu\text{g}\cdot\text{mL}^{-1}$, in L-15, 5% FCS) at 37°C for 4 – 24 h. Upconversion intensity upon excitation with 980 nm (cw, $640 \text{ W}\cdot\text{cm}^{-2}$) is shown in green and DAPI stained nuclei in the overlay in blue.

To enable comparisons of the impedance-based toxicity analysis to the results of the end-point cell viability assay after 72 h incubation time (**Figure 6.3**), the potencies of both methods

with cells from the same passage numbers were compared. The EC_{50} of UCNPs@AP was determined by plotting the concentration-dependent normalized impedance values at 32 kHz after 72 h incubation time (**Figure 6.5**). The sigmoidal cell response-related data was fitted *via* a 4 parametric logistic function to obtain an EC_{50} of $(17 \pm 15) \mu\text{g}\cdot\text{mL}^{-1}$ (**Figure 6.10**). The error for the calculated EC_{50} is rather high as the medium concentrations were toxic cell-age dependently in just a few of the experiments. The minimum UCNPs@AP concentration affecting the cells is around $10 \mu\text{g}\cdot\text{mL}^{-1}$ and the EC_{100} amounts to around $30 \mu\text{g}\cdot\text{mL}^{-1}$.

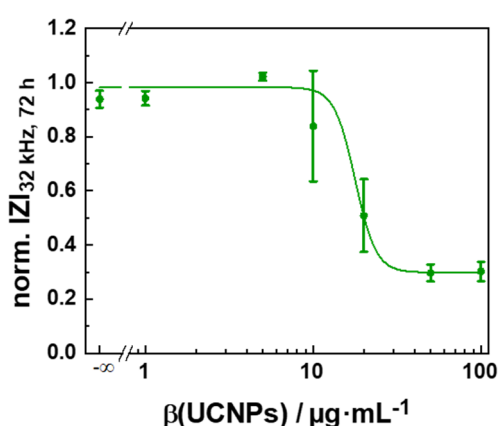


Figure 6.10. Concentration-dependent response of NRK cells (passage numbers 33 – 36) treated with UCNPs@AP (L-15, 5% FCS (v/v)) at 37 °C, using normalized impedance values at 32 kHz after 72 h to determine an EC_{50} of $(17 \pm 15) \mu\text{g}\cdot\text{mL}^{-1}$ (mean \pm SEM, four independent experiments), 4-parameter logistic model, adjusted $R^2 = 0.96$).

The EC_{50} determined by ECIS after 72 h ($(17 \pm 15) \mu\text{g}\cdot\text{mL}^{-1}$) is significantly lower than the value obtained by the endpoint assay PrestoBlue™ ($(103 \pm 8) \mu\text{g}\cdot\text{mL}^{-1}$) after 72 h. As an interference of the dye with UCNPs@AP themselves was excluded, the conversion had to be carried out by the cells. The concentrations inducing cell death after ~36 h in the ECIS assay matched the phase contrast images after 24 h incubation, revealing stressed and dead cells for medium and high concentrations ($100 \mu\text{g}\cdot\text{mL}^{-1}$, shown in **Figure 6.3B**). These results indicated that even if the cells reduced contacts, rounded up, and partly detached from the substrate, as observed with the ECIS approach and visible by microscopy, the cell metabolism was still intact to produce enough NADH to convert resazurin in amounts similar to the control. Thus, the particles and their disintegration side products seemed to limit the cells in a pathway, which does not affect the cell metabolism. These findings matched the impedance profile indicating necrosis, which does not primarily harm the mitochondria and the redox metabolism, and the

fact that UCNPS@AP showed the tendency for dissolution and can potentially damage the lysosomal membranes (cf. **Chapter 5**).

6.6.2 Cell Migration

The recording of cell migration enables the study of complex cellular processes as (I) protrusion of the plasma membrane, driven by polymerization of cytoskeletal actin filaments, (II) formation of large adhesive complexes of integrin, actin filament, and other proteins, and (III) retraction of the cell body after detaching (Horwitz et al., 1999; Pollard et al., 2003). The migration of NRK cells upon exposure to UCNPs@AP for different time frames was analyzed in an electrical wounding assay by studying the impedance at 32 kHz (representative courses in **Figure 6.11**). After incubation with UCNPs@AP for 4 – 24 h (data not shown), an electrical pulse (2.400 μ A, 32 kHz, 30 s) was applied to kill the cells attached to the electrode. The migration of the surrounding cells to re-populate the electrode was monitored for 15 h. Directly after applying the electrical pulse, the impedance of the cells drops down to ~40% of the starting value, close to values of a cell-free electrode. It recovers within 4 – 5 h to the values before wounding for the control cells and recovers in a concentration- and incubation time-dependent manner for UCNPs@AP-treated cells. After 4 h incubation time with UCNPs@AP, all cell populations can close the wound although some have a short time delay, which is found to be dependent on the applied particle concentration (**Figure 6.11A**). After 8 h exposure the impedance of the cells treated with high concentrations (20 – 100 μ g·mL⁻¹) does not increase at all. Those with medium concentration (10 μ g·mL⁻¹) starts to recover in the recorded time frame. The cells treated with low concentrations (\leq 5 μ g·mL⁻¹) recovers totally to starting values within the 15 h of the experiment (**Figure 6.11B**). After 20 h incubation time only the impedance of the cells with exposure to UCNPs@AP \leq 5 μ g·mL⁻¹ reaches the starting values within the observed time (**Figure 6.11C**). The recovery time of cells treated with 5 μ g·mL⁻¹ is already retarded for an incubation time of 24 h (**Figure 6.11D**).

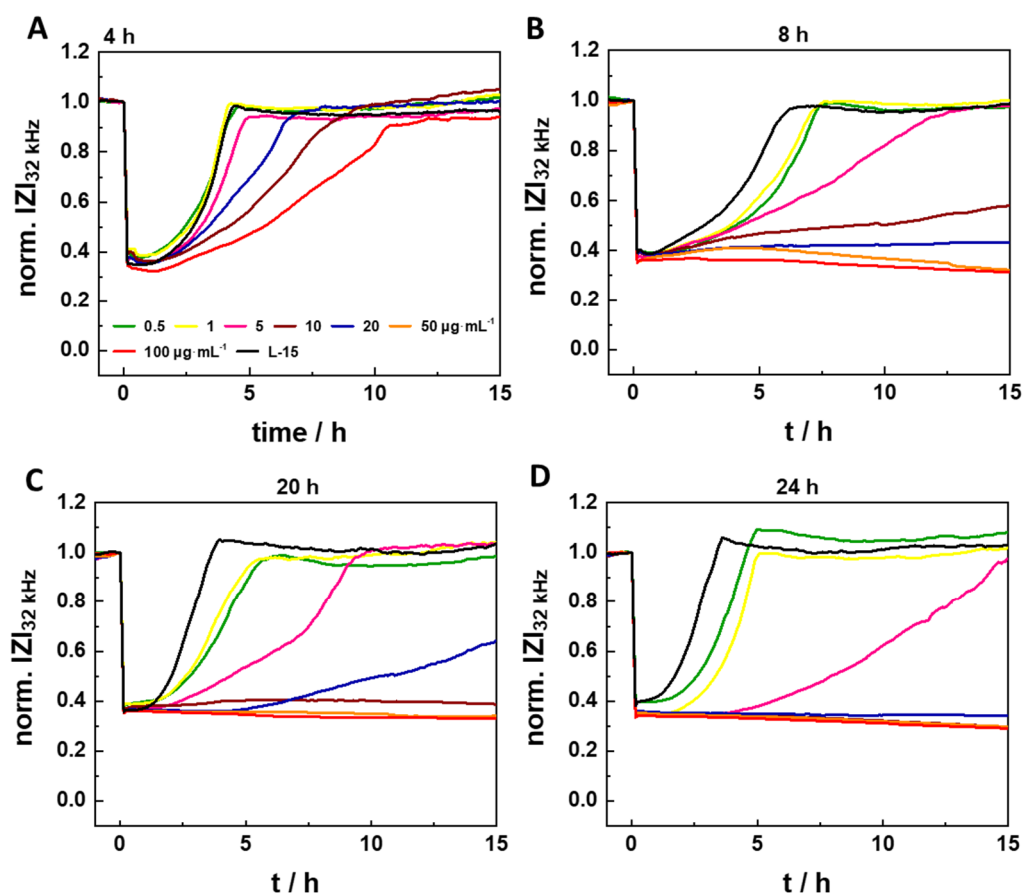


Figure 6.11. Typical normalized impedance time course at 32 kHz of NRK cells (passage number 33) exposed to UCNPs@AP ($0.5 - 100 \mu\text{g}\cdot\text{mL}^{-1}$, L-15 + 5% FCS, (v/v)) or control at 37°C for (A) 4 h, (B) 8 h, (C) 20 h or (D) 24 h prior to the wounding with an electrical pulse ($2,400 \mu\text{A}$, 32 kHz, 30 s) at time point 0 h. Baseline impedance magnitude before wounding was $(6.27 \pm 0.03) \text{ k}\Omega$ ($N = 32$).

The potency for each incubation time was determined for a better comparison of the effect of UCNPs@AP exposure time on the migration of NRK cells. The area under the curve (AUC) from 0 – 15 h after the wounding pulse was calculated and shown concentration-dependently to determine the half-maximal effective concentrations (**Figure 6.12**). NRK cells (passage numbers 24 – 33) with exposure to UCNPs@AP for 4 h were all able to close the wound and EC_{50} is not determined within the concentration range of this experiment. The EC_{50} values range from $(11 \pm 3) \mu\text{g}\cdot\text{mL}^{-1}$ for 8 h and $(9 \pm 3) \mu\text{g}\cdot\text{mL}^{-1}$ for 20 h to $(3.6 \pm 0.8) \mu\text{g}\cdot\text{mL}^{-1}$ for 24 h incubation time.

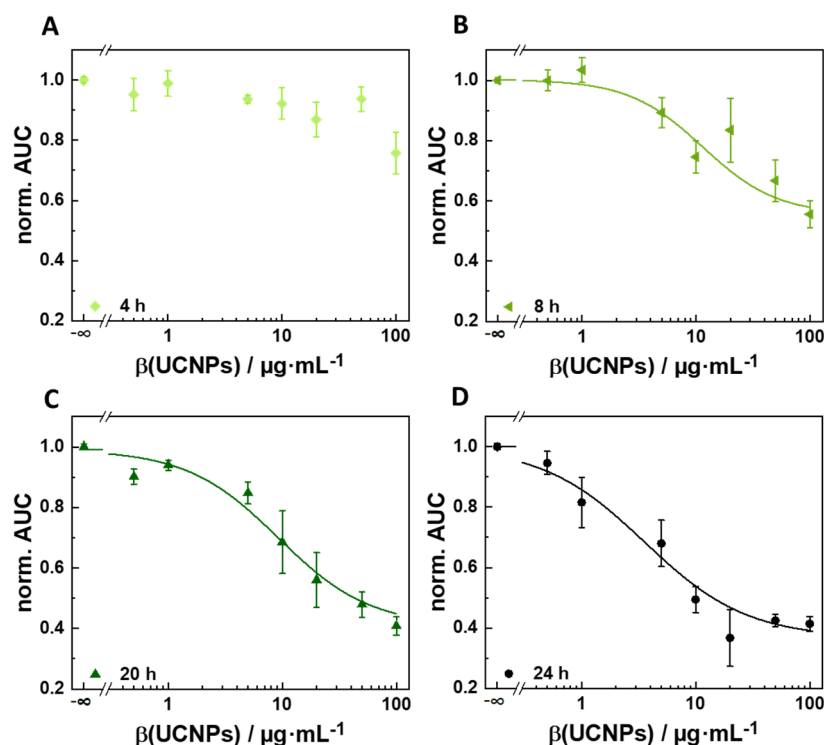


Figure 6.12. Normalized area under the curve of the impedance time course at 32 kHz (norm. AUC, 0 – 15 h after wounding with baseline norm. $I_{Z|32\text{ kHz}} = 0$, normalized to AUC of NRK cells without exposure to UCNPs@AP) of NRK cells (passage numbers 24 – 33) exposed to UCNPs@AP ($0.5 - 100\text{ }\mu\text{g}\cdot\text{mL}^{-1}$, L-15, 5% FCS (v/v)) or control at 37 °C for (A) 4 h, (B) 8 h, (C) 20 h or (D) 24 h prior to the wounding pulse. EC_{50} values were determined as $(11 \pm 3)\text{ }\mu\text{g}\cdot\text{mL}^{-1}$, $(9 \pm 3)\text{ }\mu\text{g}\cdot\text{mL}^{-1}$ and $(3.6 \pm 0.8)\text{ }\mu\text{g}\cdot\text{mL}^{-1}$ for an incubation time of 8 h, 20 h and 24 h (adjusted $R^2 = 0.950, 0.965$ and 0.994 ; mean \pm SEM, three independent experiments).

The recovery of the signal was possible with some time delays for almost all cells after 4 h incubation time, while the minimum concentration preventing the migration of the surrounding NRK cells to the electrode was found to vary between $5\text{ }\mu\text{g}\cdot\text{mL}^{-1}$ and $10\text{ }\mu\text{g}\cdot\text{mL}^{-1}$ for incubation times $\geq 8\text{ h}$. This indicated that enough UCNPs were internalized by the cells after $\geq 8\text{ h}$ to reduce or inhibit processes being required for cellular movements. Thus, the number of internalized particles seem to be more relevant for reduced cell migration than the number of extracellularly available particles. As migration of cells upon particle treatment was reduced or not possible at all, it is assumed that UCNPs@AP or their side products affected or impaired the cell machinery required for migration, including the actin filament cytoskeleton, the anchoring proteins, and the protein biosynthesis.

The reduction of migration has been reported to be accompanied by cytoskeleton disruption in lung epithelial cells upon exposure to 25 nm TiO_2 or 100 nm SiO_2 particles (Déciga-Alcaraz

et al., 2020a; Déciga-Alcaraz et al., 2020b). The disruption of the cytoskeleton by metallic or metal oxide particles, followed by the intracellularly generated reactive oxygen species (ROS), has been described as well. For example, reorganization of the actin filament leading to cell stiffness was observed for ROS-stimulated kidney epithelial cells (PtK1, (Taulet et al., 2012)). Epithelial cancer cells MCF-7, treated with Ag NPs, and A549 cells upon exposure to ZnO particles have also shown disturbances in cytoskeletal functions and a reduced cell elasticity. These changes resulted in necrosis and were traced back to ROS production by the nanoparticles (Matteis et al., 2018; García-Hevia et al., 2016). Changes of proteins related to migration together with alterations of the actin und tubulin networks, were observed in A549 cells upon 60/175 nm SiO₂ particle treatment or in papillary thyroid cancer (TPC-1) cells upon exposure to 8 nm AuNP (Vuong et al., 2016; Gonzalez et al., 2015; Liu et al., 2019). As cytoskeletal disruption was observed for many inorganic nanoparticles, it is plausible that UCNPs@AP impacted the cell cytoskeleton in a similar way, hindering cell migration. However, this remained an assumption and could not be verified within the scope of this thesis by a detailed analysis of ROS levels, expression levels of corresponding proteins, and cell cytoskeleton staining.

The wound healing assay of NRK cells, incubated with UCNPs@AP for different periods of time, revealed that the migration of the cells was strongly limited by the internalized particles in a time- and concentration-dependent manner. The restrictions in migration were assumed to correspond to a disrupted cytoskeleton or to changes of contributing proteins, related to cell migration. In comparison to the cell viability and the impedance-based cytotoxicity assays, the potencies were shifted to lower concentrations and the impact of the UCNPs@AP on the cells was visible at shorter incubation times. The reason for the differently pronounced impact may be found in the cellular states. PrestoBlue™ and the impedance-based cytotoxicity assay targets resting cells in a confluent monolayer, whereas the wound healing assay detects active cells which might be restricted earlier in their functioning and are more sensitive to toxicants.

6.6.3 Cell Adhesion

Another assay format targeting cells and their biological phenotypes is the impedance-based adhesion assay. Here, the kinetics of cell spreading are monitored and give access to cell-

matrix as well as cell-cell interactions, the involved cytoskeleton, and anchoring proteins. The adhesion of cells to extracellular matrix substrates and neighboring cells is enabled by the protrusion of their leading edge with filopodia and lamellipodia. This process is driven by polymerization of the actin filament and involves a broad variety of proteins, such as cadherins, integrins, vinculin, and α -actinin (Parsons et al., 2010). Especially epithelial cells are known to form strong adhesive contacts, mainly supported by E-cadherins, which are stabilized by actin filaments *via* catenines (Guillot et al., 2013). The adhesion of NRK cells exposed to UCNPs@AP was analyzed with the impedance-based cell assay (**Figure 6.13**). The cell attachment was monitored *via* the capacitance time courses at 32 kHz and the formation of cell-cell contacts with the impedance time courses at 4 kHz. The capacitances of cells in cell culture medium and those exposed to low UCNPs@AP concentrations ($\leq 10 \mu\text{g}\cdot\text{mL}^{-1}$) decrease to minimum values after ~ 6 h and stay around these values for 18 h (**Figure 6.13A**). This indicates the successful adhesion of the NRK cells to the electrode. An impairment of cell adhesion is observed for the cell suspension with $20 \mu\text{g}\cdot\text{mL}^{-1}$ UCNPs@AP. The cells with $50 \mu\text{g}\cdot\text{mL}^{-1}$ UCNPs@AP exposure are partly able to adhere to the electrode but detach again after 9 h until capacitance values of a cell-free electrode are obtained. The cells from the suspension with the highest particle concentration start to adhere for ~ 3 h before they detach again.

The impedance at 4 kHz shows a bimodal increase for the cells with UCNPs@AP concentrations $\leq 10 \mu\text{g}\cdot\text{mL}^{-1}$. The bimodal curve is related to the initial cell adhesion (first increase, also visible in the capacitance course) and to the formation of cell-cell contacts for a cell monolayer (second increase) (**Figure 6.13B**). Cells with a medium concentration of UCNPs@AP ($10 \mu\text{g}\cdot\text{mL}^{-1}$) can adhere and spread but show a slightly delayed monolayer formation. Cell contacts were not formed for cells with exposure to $\geq 20 \mu\text{g}\cdot\text{mL}^{-1}$ UCNPs@AP. The normalized area under the impedance course at 4 kHz is shown in a concentration-dependent manner to determine the EC_{50} value for UCNPs@AP-treated NRK cells during adhesion with $(28 \pm 6) \mu\text{g}\cdot\text{mL}^{-1}$ (**Figure 6.13C**).

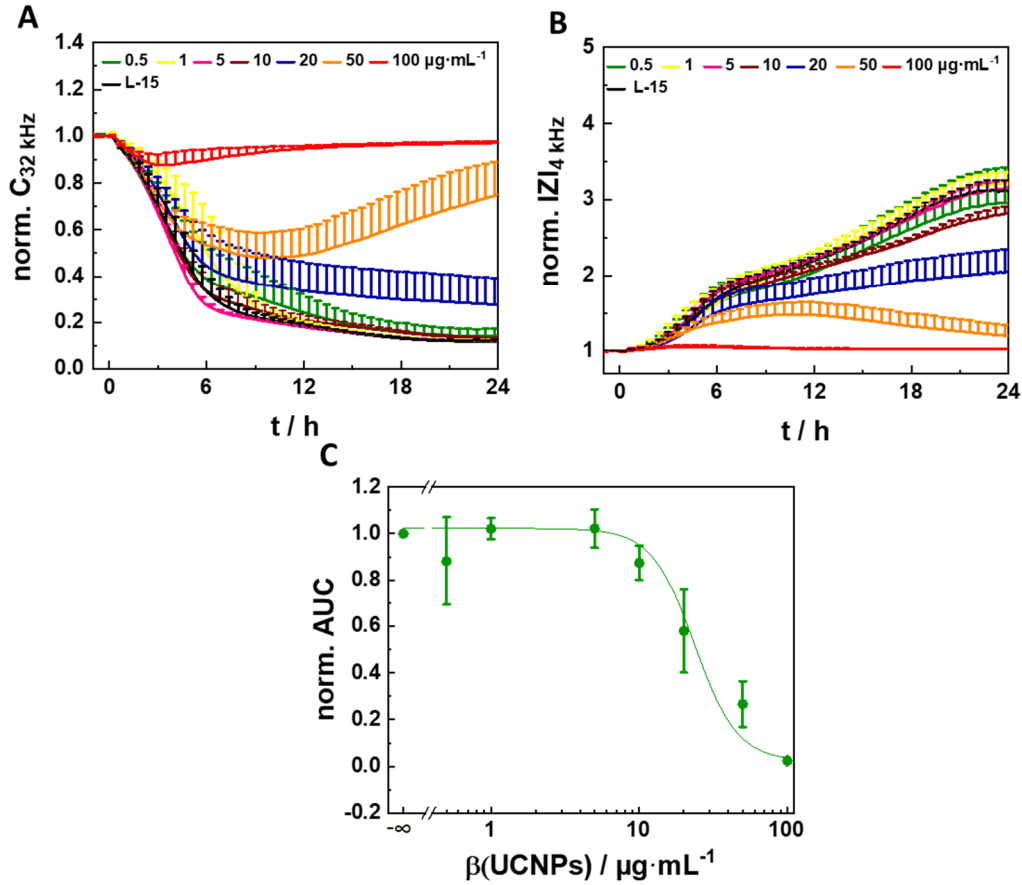


Figure 6.13. Normalized time courses of (A) capacitance at 32 kHz and (B) impedance at 4 kHz of initially suspended NRK cells (passage numbers 33 – 36) adhering to the electrode during exposure to UCNPs@AP (0.5 – 100 $\mu\text{g}\cdot\text{mL}^{-1}$, cell culture medium) at 37 °C. NRK cells in suspension were added at time point 0 h (mean + SEM, three individual experiments). Average baseline magnitude of impedance and capacitance of the cell-free electrode were (0.74 ± 0.01) k Ω (N = 24(8)) at 4 kHz and (50.0 ± 0.2) nF (N = 24) at 32 kHz. (C) Normalized area under the impedance time course at 4 kHz (norm. AUC, from 0 – 24 h with baseline norm. $|Z|_{32 \text{ kHz}} = 0$, normalized to AUC of NRK cells without exposure to UCNPs@AP) of adhering cells to determine the EC_{50} as (28 ± 6) $\mu\text{g}\cdot\text{mL}^{-1}$ (adjusted $R^2 = 0.998$, mean \pm SEM, three independent experiments).

In general, restrictions in cell spreading might be attributed to changes of the cell cytoskeleton or proteins involved in cell-matrix adhesion. The impedance-based adhesion assay targets very similar processes as the impedance-based migration assay since both processes are assisted by the formation and re-organization of cytoskeletal actin filaments. The discussion in the previous chapter on cell migration and cytoskeletal disruption are valid for the findings of the impedance-based cell adhesion assay as well.

Indeed, the impact of UCNPs@AP on adhering cells was found to be similar to that on migrating cells. Both assay formats revealed early restrictions of active cells by UCNPs@AP in

a similar time frame and rather low potencies. The harmful effect of high concentrations of UCNPs@AP and their disintegration products was visible strongly in the cell adhesion experiment after ~3 h and on cell migration also slightly after 4 h and strongly after ≥ 8 h UCNPs incubation time. However, the potencies were slightly lower for migrating than for adhering cells. The reason for this could be found in the cellular conditions at the beginning of the assay. In the migration assay resting cells were pre-treated with UCNPs@AP before they were active again, while in the adhesion assay UCNPs@AP were exposed directly to the active cells without pre-treatment.

6.7 Toxicity Profile and Summary

The influence of UCNPs@AP on epithelial NRK cells was analyzed with different assays, targeting the cell metabolism, cell morphology changes, and the fundamental processes of cell adhesion as well as cell migration (**Scheme 6.2**).

i) The cell metabolism and NADH production was reduced slightly after exposure to particles for 24 h, indicating cells under stress (cf. **Figure 6.3A**). After 72 h incubation time the cell energy metabolism was limited with an EC_{50} value of $(103 \pm 8) \mu\text{g}\cdot\text{mL}^{-1}$ (passage numbers 33 – 36) and was increased for cells with particle treatment in low concentration, which was attributed to hormesis.

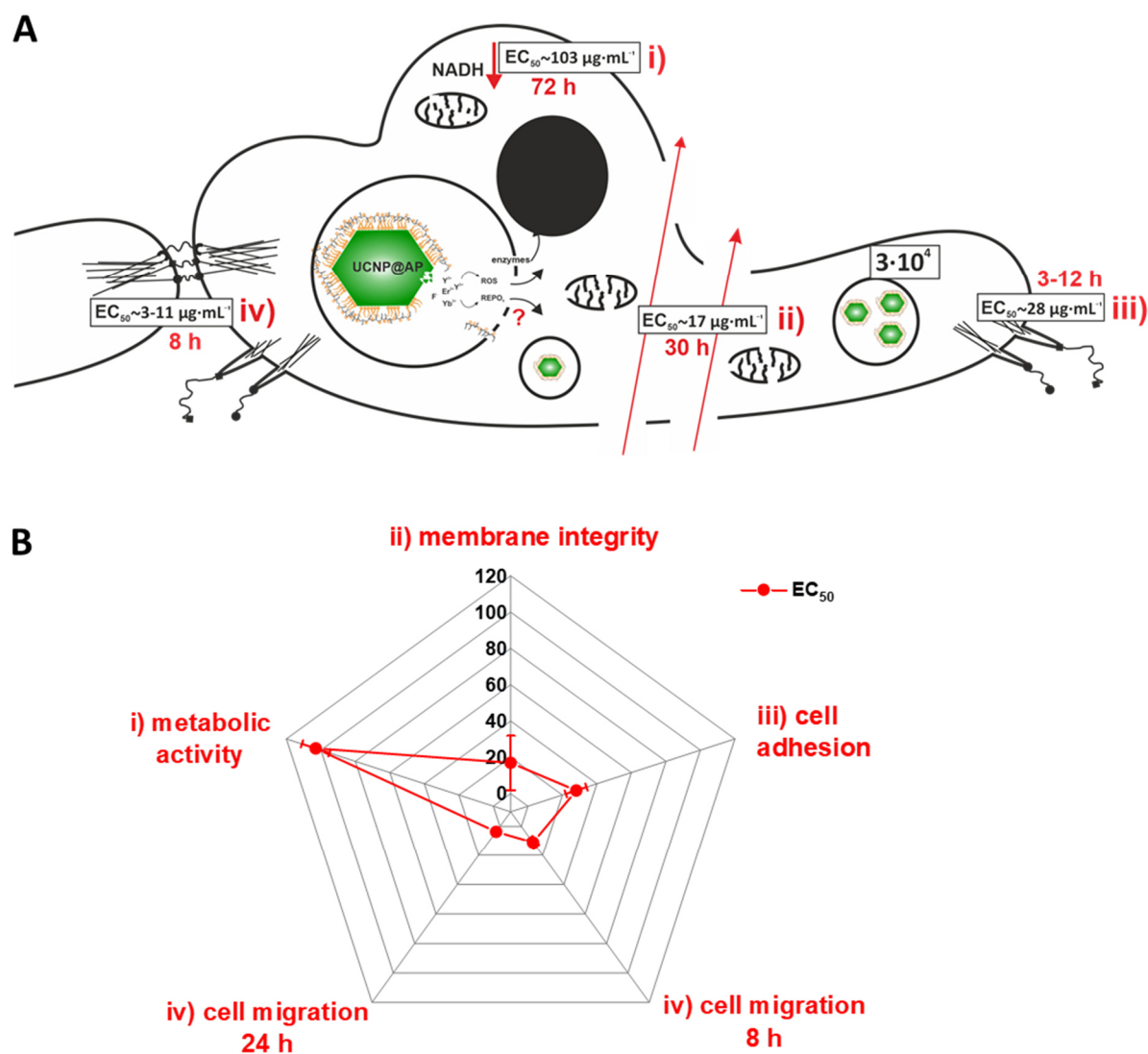
In contrast, the corresponding phase contrast micrographs showed detaching cells already after 24 h incubation time when treated with high particle concentrations and after 72 h incubation time when treated with low particle concentrations (cf. **Figure 6.3B**).

ii) The results of the toxicity measurement with the impedance-based cell assay matched the micrographs. Cell death occurred after ~34 h with an EC_{50} of $(17 \pm 15) \mu\text{g}\cdot\text{mL}^{-1}$ (passage numbers 33 – 36) (cf. **Figure 6.3**). The time courses of impedance implied that the cells died due to necrosis (cf. **Figure 6.7**).

iii) The UCNPs@AP affected cell adhesion with an EC_{50} of $(28 \pm 6) \mu\text{g}\cdot\text{mL}^{-1}$ (passage numbers 33 – 36) after 3 – 12 h (cf. **Figure 6.13**).

iv) The migration of the NRK cells was affected slightly by UCNPs@AP for a low incubation time of 4 h but highly for incubation times of 8 – 24 h with EC_{50} values between $(3.6 \pm 0.8) \mu\text{g}\cdot\text{mL}^{-1}$ and $(11 \pm 3) \mu\text{g}\cdot\text{mL}^{-1}$ (passage numbers 33 – 36) (cf. **Figure 6.11**, **Figure**

6.12). This time dependency demonstrated that the impact of UCNPs was more dependent on the intracellular number of UCNPs@AP than on the number of UCNPs applied extracellularly. Cellular uptake of the UCNPs was confirmed by upconversion microscopy and the number of internalized particles per cell was determined by ICP-MS to be around $3 \cdot 10^4$ UCNPs@AP per cell after 24 h incubation time (cf. **Figure 6.2, Table 6.1**).



Scheme 6.2. (A) Toxicity profile and (B) spider blot of NRK cells with exposure to UCNPs@AP. The impact of internalized particles ($\sim 3 \cdot 10^4 \mu\text{g}\cdot\text{mL}^{-1}$ UCNPs/cell, determined after 24 h), their metabolites and side products (AP, ROS, REPO_4) was examined on i) metabolic activity, ii) membrane integrity, iii) cell adhesion, and iv) cell migration with their individual EC_{50} values.

UCNPs@AP and their disintegration products restricted cell physiology of active cells more strongly than resting cells in monolayers. The time scale of a detectable impact of UCNPs@AP on adhering/migrating cells was visible within 8 h. In contrast, cell morphology changes were observed after > 30 h and a slight reduction in cell metabolism was visible after 72 h. Limitations of the cellular adhesion and migration might be contributed to changes of the cytoskeleton and proteins involved in the development of contacts to substrate and neighbored cells. These restrictions might also occur at resting cells, visible at later times.

An intrinsic toxicity of the amphiphilic polymer could be excluded by the results described in **Chapter 5** so that toxicity pathways were supposed to be triggered mainly by UCNPs themselves and not by the coating. The UCNPs@AP showed a high colloidal stability in the applied medium within the time frame of the experiment (cf. **Figure 6.1**). Metabolization of protein corona and surface coating may take place within the cellular vesicles so that the particle surface is available for degradation (Shang et al., 2014). Indeed, dissolution of protein corona coated UCNPs@AP was observed to take place at physiological temperature until no luminescence was detectable anymore within 2 h (cf. **Chapter 5**). Beneath the potential formation of ROS by leaking ions, the RE ions have been known to form REPO_4 with phosphates being provided from, *e.g.* ATP or the cell membrane (Li et al., 2014). An increase of the ROS level can lead to vesicle membrane rupture as well as the escape of metabolized particle products and endosomal/lysosomal enzymes into the cytosol, which can end-up in necrosis (Gao et al., 2017). Therefore, the UCNPs@AP themselves, their disintegration products, RE ions, REPO_4 , and vesicle enzymes had to be considered as possible initiators of adhesion/migration impairment, losses of membrane integrity, reduced cell metabolism, and final cell death.

The potential pathways, the UCNPs@AP trigger in epithelial NRK cells, arose out of these studies together with published ones. To confirm the discussed hypotheses, more experiments are required, including the analysis of cytoskeletal changes of particle-treated cells, the detection of UCNPs@AP metabolites, the potential formation of REPO_4 , the determination of vesicle rupture, and the release of endosome loading.

7 Upconversion Nanoparticles for Photodynamic Therapy

7.1 Preface

Most of the experimental and theoretical work presented in this chapter was performed solely by the author. The 24 nm core-shell UCNPs were provided by Alexandra Schroter. The synthesis of the 15 nm core-shell UCNPs as well as the modification with a rose bengal functionalized amphiphilic polymer (AP-RB) was carried out by Jannik Feiler during a scientific internship under supervision by the author. First reactive oxygen species (ROS) and PrestoBlue™ experiments were done by Jannik Feiler and completed by the author. The analysis of cellular UCNPs internalization *via* laser ablation - inductively coupled plasma - mass spectrometry (LA-ICP-MS) and the corresponding data procession was carried out by Svenja Berit Seiffert at the BASF in Ludwigshafen.

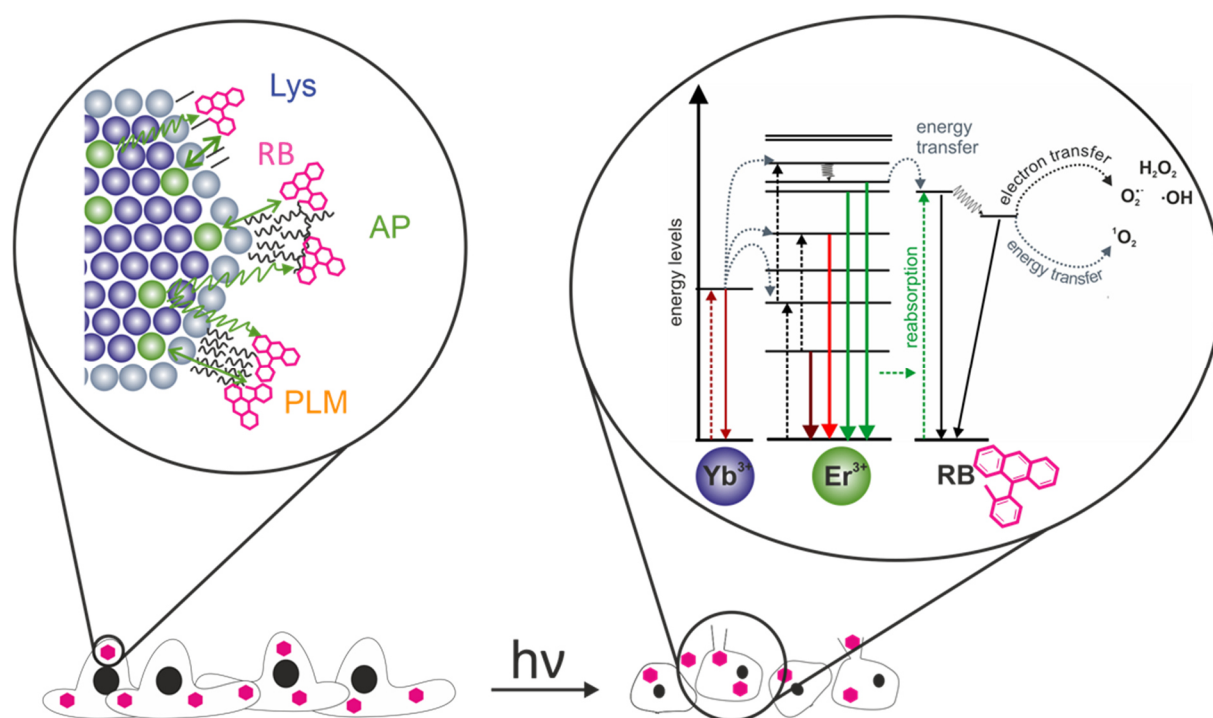
7.2 Introduction

The minimal invasive photodynamic therapy (PDT) is an alternative treatment to radio- and chemotherapy in clinical practice for destroying specifically cancerous tissue by locally confined reactive oxygen species (ROS) generation. Non-toxic photosensitizers (PS) are administered intravenously or superficially to the desired tissue. The accumulated photosensitizers are activated by local excitation and can change from a short time singlet state ($^1\text{PS}^*$) into a relatively long-lived electronically excited triplet state ($^3\text{PS}^*$), from which they can undergo two types of reactions, initiating cell death (Dougherty et al., 1998). The type I reaction describes the transfer of electrons to cellular substrates to form radicals, which generate oxygenated products, such as superoxide anion ($\text{O}_2^{\bullet-}$) and hydroxyl radicals ($\bullet\text{OH}$) or hydrogen peroxide (H_2O_2) (**Scheme 7.1**). The photosensitizers can also directly transfer the triplet state energy to oxygen (O_2), which is known as type II reaction, and produces singlet oxygen ($^1\text{O}_2$). The cytotoxic ROS, generated by these two reaction types, are characterized by a short half-life of $< 0.4 \mu\text{s}$, beneficial in only inducing cell damage in the surrounding cells ($< 0.02 \mu\text{m}$ radius) as apoptosis, necrosis, or autophagy (Moan et al., 1991). Due to the small radius of administered photosensitizer, irradiation, and photodamage, the adverse side effects of this treatment are highly reduced compared to other cancer therapies based on

drugs without tissue specificity and large radius of damage. However, PDT has to deal with some drawbacks, like hydrophobicity of the PS, low stability in the biological environment with half-lives of around 30 min, tendency for aggregation, and low cell specificity (Demartis et al., 2021a). These limitations can be overcome *e.g.*, by precisely transporting the PS into the target cells with nanomaterials as carriers. So far, nanoparticles (NP), such as gold NPs, silver NPs, silica NPs, quantum dots, upconversion NPs (UCNPs), carbon-based materials, or two-dimensional nanosheets (NS) as manganese dioxide NS or dichalcogenide NS are reported as delivery systems in PDT (Demartis et al., 2021a). They can be equipped with hydrophilic coatings for an increased stability of PS in the *in vitro* tumor environment as well as long circulatory lifetime and functionalized with specific targeting moieties for an enhanced tissue targeting efficiency (Chen et al., 2020). The problem of phototoxicity and limited penetration depth of the excitation light in UV/VIS can be circumvented by designing photosensitizers, excitable by light within the optical window of biological tissues (Zhu et al., 2019). The NIR light interacts only minimally with endogenous molecules, enabling penetration depth up to 10 cm (Weissleder, 2001). This rises the interest in UCNPs as they combine I) the benefits of nanocarriers and II) the excitation by light with deep tissue penetration with emissions in the visible range, which are useful for the excitation of attached PS to generate ROS *in situ* (Wang et al., 2013). These are most often based on NaYF₄ or LiYF₄ host crystals doped with sensitizing ions (*e.g.* Yb³⁺ or Nd³⁺) and activating ions (*e.g.* Er³⁺ or Tm³⁺). They have a perfect spectral overlap with the absorbance of photosensitizers such as rose bengal, merocyanine (MC540), chlorin e6 (Ce6), methylene blue, or temoporfin (*m*-THPC) (Wang et al., 2011; Valenzano et al., 1987; Chen et al., 2020; Chen et al., 2012; Yu et al., 2014). **Scheme 7.1** shows exemplary the simplified energy level diagram of Yb³⁺ and Er³⁺ doped nanocrystals functionalized with rose bengal. The Yb³⁺ ions absorb photons of 980 nm and transfer the energy of two or more photons subsequently to neighbored Er³⁺ ions, which get excited to higher states. In addition to non-radiative relaxations, Er³⁺ ions emit photons in the green and red. The energy of the green emissions can be either transferred directly to rose bengal by non-radiative resonance energy-transfer (RET) or radiative energy transfer (reabsorption). Excited singlet states can emit the energy or undergo intersystem crossing to triplet states, from which type I (energy transfer) and especially type II (electron transfer) reactions can occur to produce ROS.

The PS-functionalized UCNPs have already entered *in vivo* studies. In the last years, the research of UCNPs is based on designing smart UCNPs with multimodalities for image-guided PDT combining two or more therapeutic strategies as photothermal therapy, chemotherapy, or radiotherapy. However, besides the fast progresses in multifunctional designs, nanomaterials like UCNPs still deal with many challenges, especially in terms of colloidal and chemical stability or unknown biotransformation in biological environment.

In this project, rose bengal-functionalized UCNPs are designed in two different sizes (15 nm and 24 nm) with different surface coating strategies (lysine, amphiphilic polymer, and phospholipid membrane) to analyze the impact of surface properties on the photosensitizer loading efficiency, biotransformation, colloidal stability in biological media, the delivery efficiency of the photosensitizers into the cells, the intrinsic cytotoxicity without illumination, the efficiency in ROS production, and the resulting cell death.



Scheme 7.1. *In vitro* photodynamic therapy with UCNPs, functionalized with rose bengal (RB) by different strategies (lysine (Lys), amphiphilic polymer (AP), phospholipid membrane (PLM)). Cells with internalized UCNPs@RB undergo cell death due to the formation of reactive oxygen species ($^1\text{O}_2$, H_2O_2 , $\text{O}_2^{\cdot-}$, $\cdot\text{OH}$) upon excitation with NIR light at 980 nm. The energy level diagram, showing the photophysical processes leading to ROS generation by irradiation of UCNPs@RB, includes absorbance (dashed straight arrows), emissions (lined arrow), non-radiative relaxation, intersystem crossing (wavy arrows), and energy (type I) as well as electron transfer (type II) (dashed curvy arrows) events.

7.3 Particle Functionalization and Characterization

Oleate coated core-shell UCNPs@OA were chosen as precursor particles for the modification and functionalization with the photosensitizer dye rose bengal. The core particles were additionally surrounded by a NaYF₄ shell to increase the brightness of the particles. The particles were prepared in two different sizes according to reported procedures (Schroter et al., 2022; Rinkel et al., 2014). The transmission electron micrographs of the core and core-shell particles reveal an average diameter of 15 nm for core-shell particles NaYF₄(20%Yb,2%Er)@NaYF₄, synthesized from 10 nm core particles NaYF₄(20%Yb,2%Er) with a 2.5 nm thick shell (**Figure 7.1A,C**). The 24 nm NaYbF₄(20%Er)@NaYF₄ were prepared from 19 nm cores NaYbF₄(20%Er) with a 2.5 nm thick shell (**Figure 7.1C,D**). The particle diameter determined by TEM was used to calculate the number of particles in a dispersion of 100 µg·mL⁻¹ 15 nm and 24 nm UCNPs as 1.1·10¹³ and 2.6·10¹² particles per mL, corresponding to a molar concentration of 18 nM and 4.4 nM.

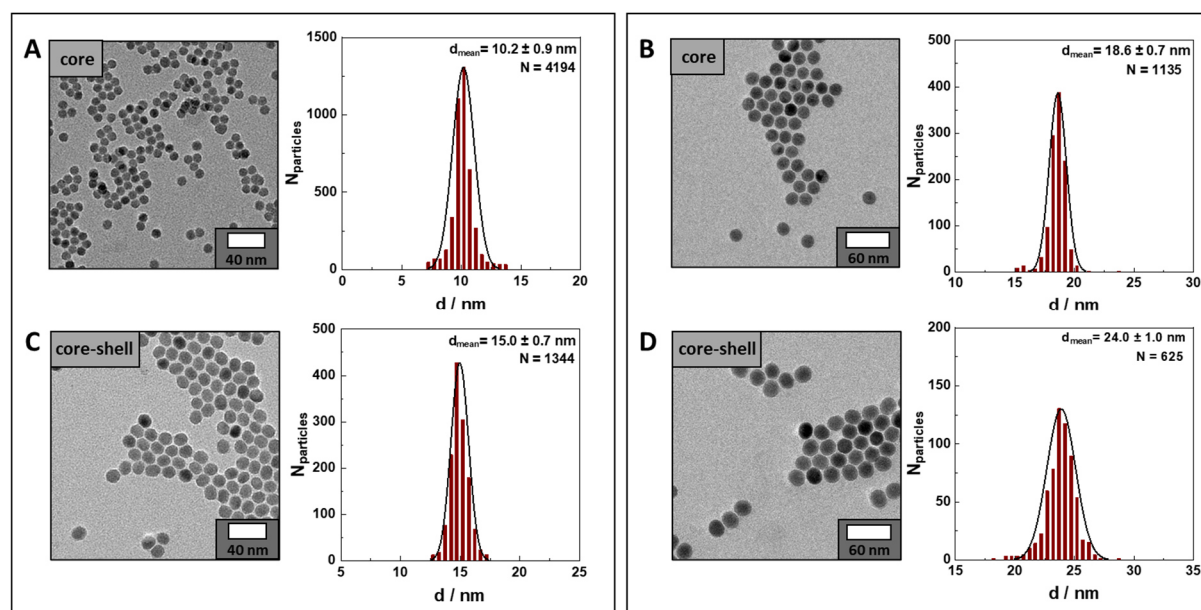


Figure 7.1. Transmission electron micrographs of core particles (A) NaYF₄(Yb,Er) as well as (B) NaYbF₄(Er) and core-shell particles (C) NaYF₄(Yb,Er)@NaYF₄ as well as (D) NaYbF₄(Er)@NaYF₄ with corresponding particle size distribution (mean \pm SD), revealing average particle diameters of (A) (10.2 \pm 0.9) nm, (B) (18.6 \pm 0.7) nm, (C) (15.0 \pm 0.7) nm, and (D) (24.0 \pm 1.0) nm.

The overlap of the green emission of Er³⁺ doped UCNPs with the absorbance band of rose bengal (**Figure 7.2**) enables the non-radiative as well as radiative energy-transfer from excited UCNPs to rose bengal, in analogy to **Scheme 7.1**, and proves the suitability of the particles for

PDT. Luminescence spectra of UCNPs were not shown in H₂O but in cyclohexane to allow the comparison of the luminescence intensities of both UCNPs in a medium without water quenching and varying surface protection effects.

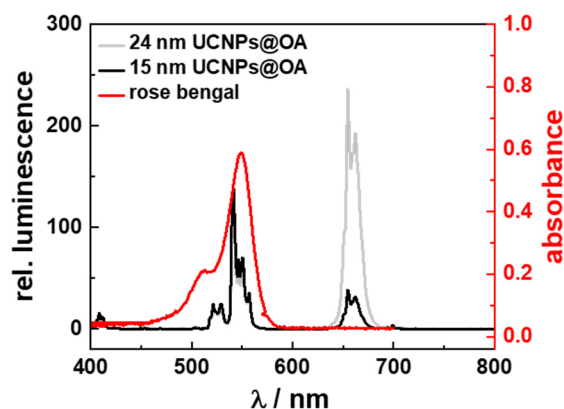
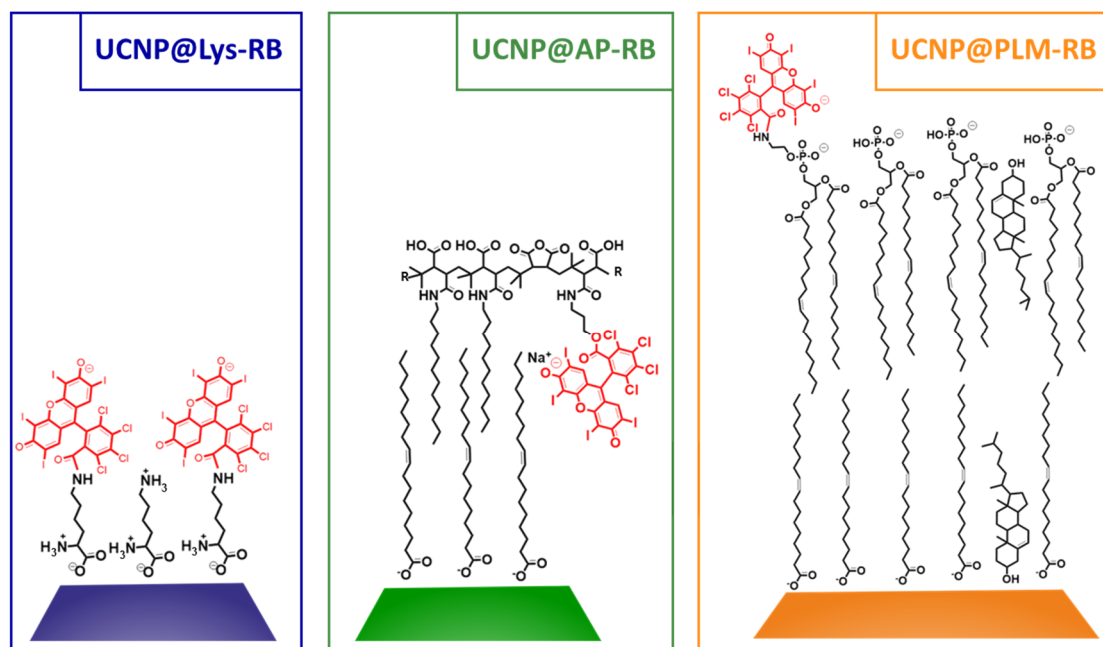


Figure 7.2. Overlay of luminescence spectra of 15 nm and 24 nm core-shell UCNPs@OA upon excitation with 980 nm (cw, 144 W·cm⁻²) at rt in cyclohexane and absorbance spectrum of rose bengal (5 μM, water). Luminescence spectra were normalized to the particle mass concentration.

The photosensitizer rose bengal (RB) was attached covalently to particles modified with monolayer coatings as lysine (Lys) or bilayer coatings composed of amphiphilic polymer (AP) or phospholipid membrane (PLM) (**Scheme 7.2**).



Scheme 7.2. Surface functionalization strategies to attach rose bengal (red) to the particles, resulting in UCNPs@Lys-RB, UCNPs@AP-RB and UCNPs@PLM-RB.

Rose bengal was attached to the ϵ -amine groups of lysine-modified 24 nm particles UCNPs@Lys *via* EDC/NHS chemistry (Buchner et al., 2019) to obtain particles UCNPs@Lys-RB (cf. procedure in **Scheme 3.5**). The large hydrodynamic diameter and the high polydispersity index (Pdl) demonstrates that they are not long-time water-dispersible (**Figure 7.3C**). Thus, these UCNPs should be stored in DMSO to prevent aggregation before usage. Directly after dilution in Leibovitz L-15 (5% FCS) the polydispersity index (Pdl) increases to values >0.7 , indicating particle aggregation.

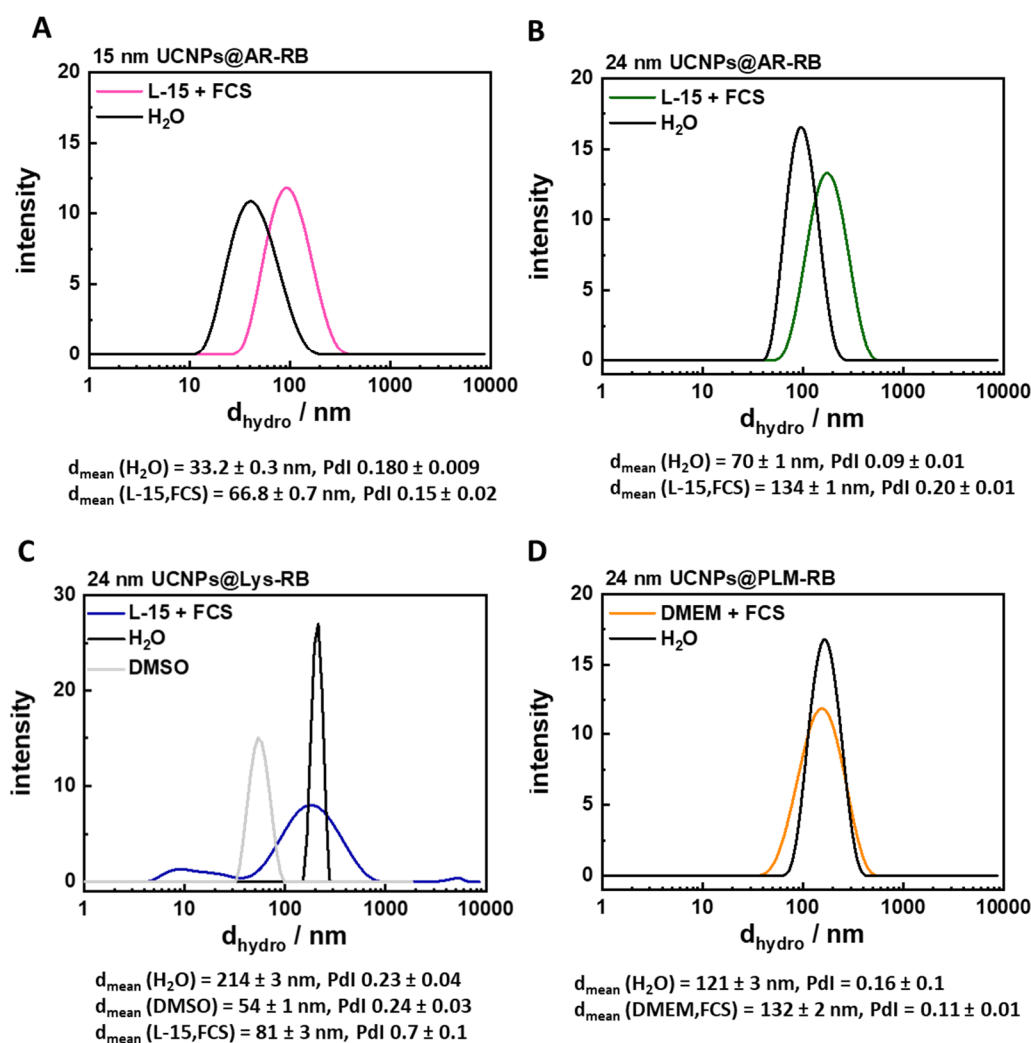


Figure 7.3. Representative intensity weighted hydrodynamic diameter (d_{hydro}) distribution with corresponding d_{hydro} and polydispersity indices (Pdl) obtained by dynamic light scattering measurements (mean \pm SD, $N = 3$) of (A) 15 nm UCNPs@AP-RB, (B) 24 nm UCNPs@AP-RB, (C) 24 nm UCNPs@Lys-RB, and (D) 24 nm UCNPs@PLM at rt in H_2O and medium L-15 (5% FCS) or DMEM (5% FCS).

UCNPs@OA in two sizes (15 nm and 24 nm) were coated with an RB-functionalized amphiphilic polymer (RB-AP) to form bilayer coated particles UCNPs@AP-RB (cf. procedure in **Scheme 3.7**). To prepare RB-AP, rose bengal had to be functionalized with an amino group in advance, which was conducted by a substitution reaction (cf. reaction in **Scheme 3.6**). RB-AP was synthesized with poly(isobutyl-maleic anhydride (PIBMAD)), dodecyl amine (50%), and amino-functionalized rose bengal (25%). The hydrodynamic diameters of the particles with Pdl's <0.2 (5% FCS) (**Figure 7.3A,B**) confirmed the colloidal stability of both UCNPs@AP-RB in H₂O and in Leibovitz L-15 (5% FCS), which was the medium of choice for cell applications. The amino groups of 24 nm UCNPs@PLM were used to link RB directly to the particles with their carboxy moieties *via* an EDC/NHS coupling reaction (cf. procedure in **Scheme 3.8**). The hydrodynamic diameter of UCNPs@PLM-RB were ~121 nm in H₂O and ~132 nm in DMEM (5% FCS) with Pdl's <0.2, indicating the colloidal stability of the particles (**Figure 7.3D**).

The number of attached rose bengal molecules per particle were determined from absorbance measurements of the dye. Free RB in H₂O has an absorption maximum at 549 nm for the S₀ → S₁ transition with a shoulder at 515 nm (Fleming et al., 1977). The absorbance spectrum changes when RB is attached to the UCNPs with a differently pronounced shoulder and a shifted absorbance band to slightly higher wavelengths. The maxima are found at $\lambda_{\text{exc,max}} = 555 \text{ nm}$ for UCNPs@Lys-RB, $\lambda_{\text{exc,max}} = 571 \text{ nm}$ for UCNPs@AP-RB, and $\lambda_{\text{exc,max}} = 564 \text{ nm}$ for UCNPs@PLM-RB (**Figure 7.4**). This effect is similar to the bathochromic shift of maximal absorbance values of rose bengal when comparing $\lambda_{\text{exc,max}}$ in water and in hydrophobic solvents (Martin, 1975; Fleming et al., 1977; Ludvíková et al., 2016). Here, the bathochromic shift can be explained by a changed local environment of the dye and the esterification (AP-RB) or amidation (Lys-RB, PLM-RB). For example, a red-shift of ~13 nm was already reported for rose bengal methyl ester (Pereira et al., 2017). Although the absorbance band of rose bengal was slightly shifted upon particle attachment, an overlap with the luminescence bands of UCNPs was still given, enabling the energy transfer.

The absorbance maxima together with the particle concentration, estimated from ICP-OES and TEM data of RB functionalized UCNPs, enabled the rough estimation of the average number of attached rose bengal molecules per particle. However, this estimation does not consider the differently changed photophysical properties of attached RB in terms of different

absorbance shifts as well as extinction coefficients for each particle type. Exact values were not determined in the scope of this thesis. The calculations are done equally for each particle type and thereby, enable a comparison of the obtained numbers. It was 1,100 RB molecules per 15 nm UCNPs@AP-RB, 1,500 RB molecules per 24 nm UCNPs@AP-RB, 1,200 RB per 24 nm UCNPs@PLM-RB, and 200 RB per 24 nm UCNPs@Lys-RB. Rose bengal could be attached in ~ 6 times larger amounts to bilayer modified UCNPs (AP, PLM) than to UCNPs@Lys. A higher number of attached RB molecules is in the 15 nm UCNPs@AP-RB dispersion than in the 24 nm UCNPs@AP-RB dispersion. This fact can be partly attributed to the higher surface to volume ratio of the smaller UCNPs (**Figure 7.4**).

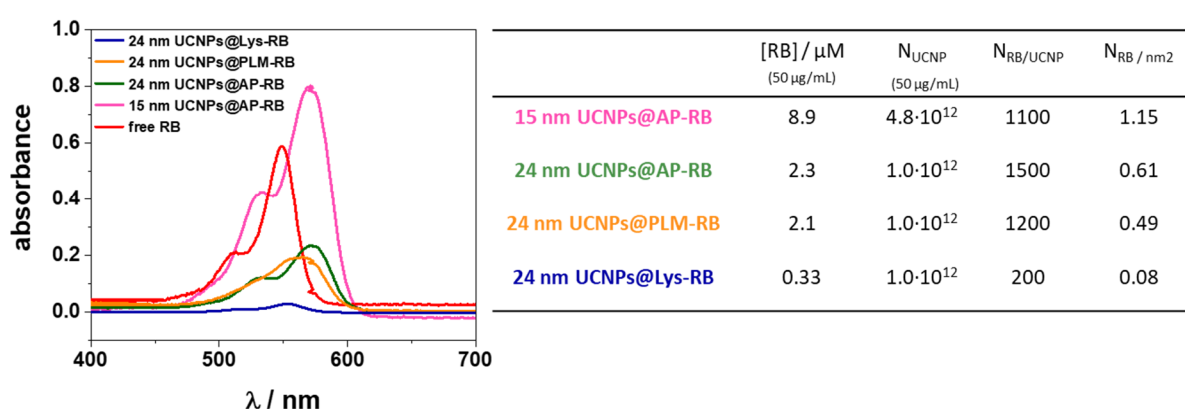


Figure 7.4. Absorption spectra of free rose bengal (5 μM) and RB-functionalized particles: 15 nm UCNPs@AP-RB, 24 nm UCNPs@AP-RB, and 24 nm UCNPs@PLM-RB at rt in H_2O (50 $\mu\text{g} \cdot \text{mL}^{-1}$) and 24 nm UCNPs@Lys-RB in DMSO (50 $\mu\text{g} \cdot \text{mL}^{-1}$). Maximal absorbance values were used to estimate the amount of attached rose bengal molecules per particle ($N_{\text{RB/UCNP}}$) and the number of rose bengal molecules per nm^2 ($N_{\text{RB}/\text{nm}^2}$).

Due to limited colloidal stability in water, the luminescence properties of UCNPs@Lys-RB is characterized only in DMSO. As such data are not of any practical importance for bioapplications, only the upconversion luminescence characteristics of those particles, which were colloiddally stable in H_2O , have been studied with and without attached RB (**Figure 7.5**). In comparison to the spectra without RB, the green emission is highly reduced by 87% for 24 nm UCNPs@AP-RB, by 76% for 24 nm UCNPs@PLM-RB and by 98% for the 15 nm UCNPs@AP-RB. In addition, a weak emission band of rose bengal at 595 – 625 nm arises in the spectrum of the larger UCNPs@AP-RB, which is not visible in the spectrum of the other particles.

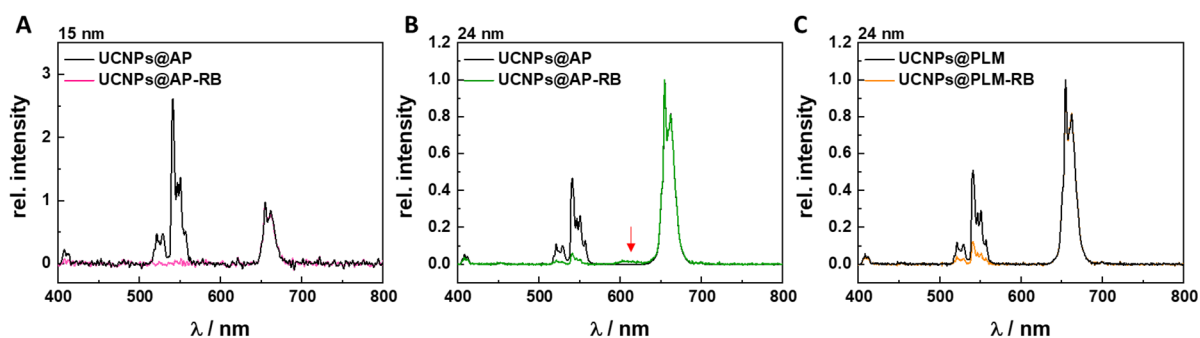


Figure 7.5. Luminescence spectra of (A) 15 nm UCNPs@AP and UCNPs@AP-RB, (B) 24 nm UCNPs@AP and UCNPs@AP-RB and (C) 24 nm UCNPs@PLM and UCNPs@PLM-RB at rt in H₂O upon excitation with 980 nm (cw, 85 W·cm⁻²). Spectra were normalized to red emission. Red arrow highlights emission of rose bengal. Y-axes have the same scale.

In general, photodynamic therapy requires the efficient excitation of photosensitizers *via* non-radiative RET as well as radiative energy transfer processes (Ding et al., 2015). The reduction of the green emission as well as the emerging rose bengal emission band reveal the successful reabsorption or non-radiative energy transfer of the upconversion luminescence in the green range by rose bengal. However, the rose bengal emission band can be only detected for the brightest UCNPs with the highest number of attached rose bengal per particle (24 nm UCNPs@AP-RB). This observation is consistent with the photophysical characteristics of rose bengal with low fluorescence efficiency. The S_1T_1 energy gap of RB is rather low due to the four iodine substituents and further decreases in water as hydrogen bonds poorly stabilizes T_1 . The fluorescence life time of free rose bengal in water is very low (0.018 ps) while the intersystem crossing rate of rose bengal is high, leading to low radiative decay constants ($1.9 \cdot 10^{-8} \text{ s}^{-1}$) and high non-radiative decay constant ($103 \cdot 10^{-8} \text{ s}^{-1}$) (Fleming et al., 1977). Thus, it is assumed that the attached RB may mostly undergo non-radiative decay with energy transfers of type I and II for ROS production and only low levels of fluorescence may occur.

The functionalization of the particles with RB was confirmed by UV/Vis spectroscopy, luminescence spectroscopy, and dynamic light scattering. The (non-) radiative transfer of energy from Er^{3+} ions to rose bengal for PDT was confirmed for bilayer coated UCNPs. The bilayer coated particles outperform the monolayer coated UCNPs in terms of attached $N_{\text{RB/UCNPs}}$ and colloidal stability in isotonic media (with 5% FCS) (cf. **Chapter 4**), making them to promising candidates for cellular applications.

7.4 Rose Bengal Uptake by Cells

The delivery efficiency of rose bengal by 24 nm UCNPs into normal rat kidney (NRK) cells was studied by confocal fluorescence microscopy with direct excitation of rose bengal. In the scope of this project, it was not possible to excite and image UCNPs luminescence.

The uptake of the particle-attached RB in various ways was compared to the uptake of free RB after different incubation times (**Figure 7.6**, gain and intensities are adjusted to visualize low as well as high signal intensities). Lysine-attached rose bengal emission is neither imaged in the NRK cells after 5 h nor after 10 h incubation time (**Figure 7.6**, first row, blue), while the emission of AP-attached RB is already detected in low intensities around the cell nuclei for both incubation time frames (**Figure 7.6**, second row, green). Incubating the cells for 5 h with UCNPs and allowing them to regenerate for 20 h, AP-attached rose bengal intensities are slightly increased, indicating that RB is not removed by the cells in this time frame but that it remains within the cells and may be associated to the cell membrane. Some red spots are found around the cells and may belong to UCNPs@AP-RB attached to the glass substrate. In contrast, PLM-attached rose bengal emission is imaged in higher intensities after 5 h and does almost not change for 10 h of incubation time or 5 h incubation time followed by 20 h regeneration time (**Figure 7.6**, third row, orange). This demonstrates that rose bengal is kept within the cells and the cells do not eliminate RB. When rose bengal is applied freely to the cells in the same amount as it is attached to the particles (40 μM), no RB emission is imageable (**Figure 7.6**, fourth row, red). Free RB may not be internalized in high amounts as the poorly amphiphilic RB has a high hydrophilic tendency and hence low membrane transfer ability (Demartis et al., 2021a). The local intracellular concentration of free RB might be lower than that of particle-attached RB and potentially too low for visualization.

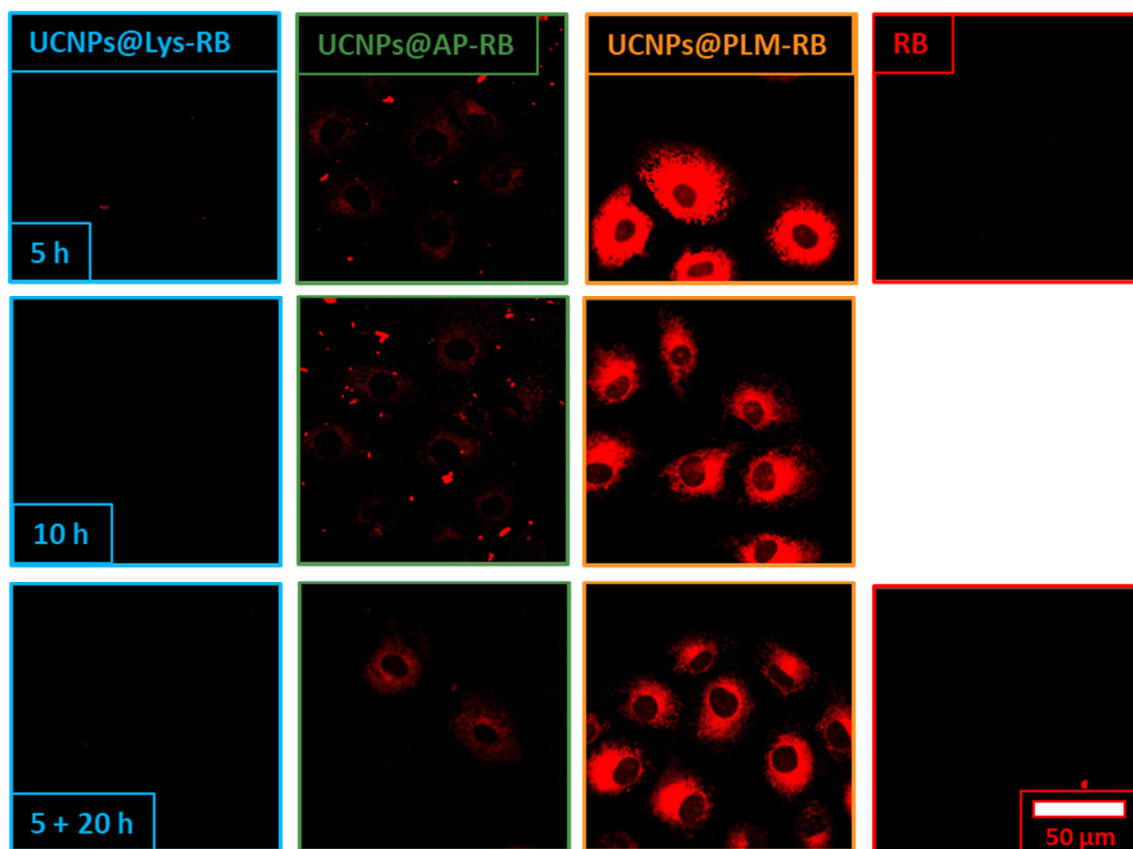


Figure 7.6. Confocal laser scanning micrographs of NRK cells (passage number 23, 24) exposed to free rose bengal (40 μM , DMEM, 5% FCS) or particles UCNPs@Lys-RB, UCNPS@AP-RB, or UCNPs@PLM-RB (50 $\mu\text{g}\cdot\text{mL}^{-1}$, DMEM, 5% FCS) at 37 $^{\circ}\text{C}$ for 5 h, 10 h, or 5 h + 20 h regeneration time under DMEM (5% FCS). RB was excited at 543 nm and emission was collected around 650 nm. Intensity was adjusted to visualize low as well as higher amounts of internalized RB.

Lysine-attached RB was not found within the cells. The reason for this may be either a very low internalization of UCNPs@Lys-RB at all or that lysine detached extracellularly from the particles and the UCNPs were internalized without lysine and Lys-RB. The monolayer ligand lysine was only loosely attached to the particle with its carboxy group and cannot be stabilized laterally by neighboring lysine molecules as lysine is a rather small amino acid. The detaching RB from the particles appeared possible since the DLS revealed a poor colloidal stability of these particles and cell medium contains high concentrations of lysine and many more biomolecules with suitable functional groups for particle attachment. Thus, surrounding amino acids, sugars, peptides, or proteins from DMEM (5% FCS) might easily replace lysine or Lys-RB from the particle surface and hindered the transport of rose bengal into the cells.

However, a verification of these two hypotheses by microscopy was not possible as a microscope equipped with a laser for direct excitation of the UCNPs was not available.

AP-attached RB was internalized and mostly stayed within the cells for 20 h, showing that UCNPs@AP were indeed suitable as delivery system. Nevertheless, the efficiency was rather poor compared to the uptake of RB by UCNPs@PLM-RB as signal intensities are even imaged supersaturated under similar conditions.

The nanocarriers UCNPs@AP were further used to compare the impact of UCNPs with different sizes on rose bengal delivery. Confocal fluorescent micrographs of NRK cells exposed to 15 nm UCNPs@AP-RB or 24 nm UCNPs@AP-RB were taken after 3 – 24 h (**Figure 7.7**). The small UCNPs@AP-RB enable the detection of rose bengal already after 3 h while at least 6 h incubation time is required for the bigger particles until it can be detected. The rose bengal intensities within the cells increase for both particles from 6 h to 24 h and remain higher for 15 nm UCNPs@AP-RB than for 24 nm UCNPs@AP-RB.

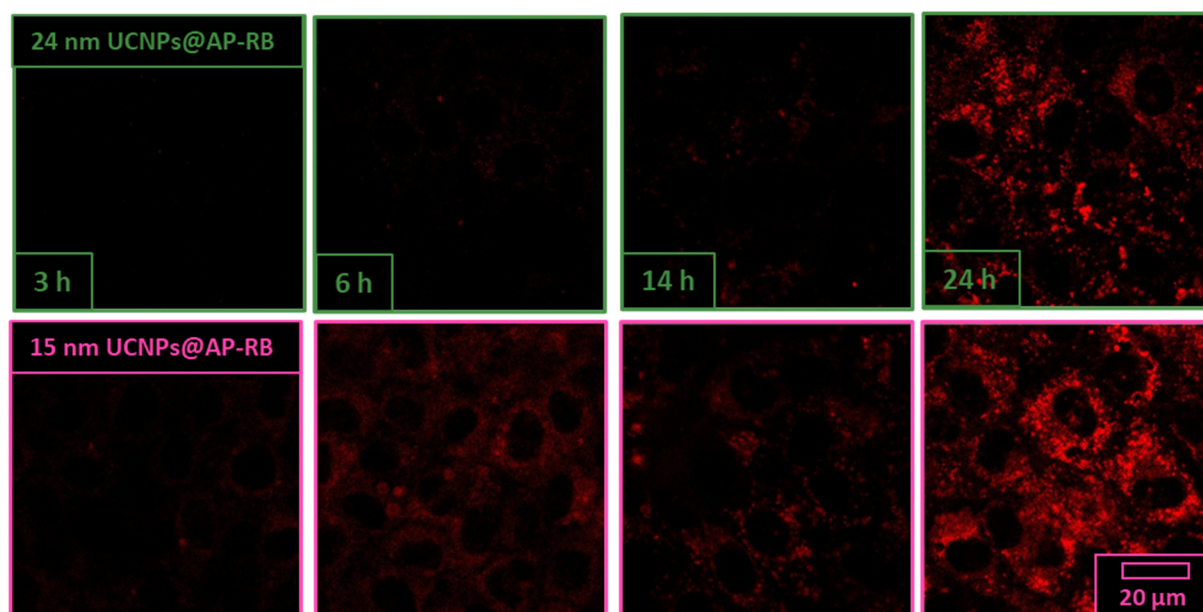


Figure 7.7. Confocal images of NRK cells (passage number 20 – 23) exposed to 15 nm or 24 nm UCNPs@AP-RB ($100 \mu\text{g}\cdot\text{mL}^{-1}$, DMEM, 5% FCS) at 37°C for 3 – 24 h. Rose bengal was excited at 543 nm and emission was collected around 650 nm.

This indicates that the smaller UCNPs might be internalized more efficiently when the cells were exposed to the same particle mass concentration. The comparison of the uptake of RB

by different sized UCNPs in the same mass concentration ($100 \mu\text{g}\cdot\text{mL}^{-1}$) results in five times more individual particles of 15 nm UCNPs ($\sim 5\cdot 10^{12}$) than 24 nm UCNPs ($\sim 1\cdot 10^{12}$). Therefore, the probability of a higher number of internalized small particles is more likely for statistical reasons. Moreover, a higher number of RB molecules per particle was found ($8.9 \mu\text{M}$ vs $2.3 \mu\text{M}$ RB per $50 \mu\text{g}\cdot\text{mL}^{-1}$ for 15 nm and 24 nm particle suspension, respectively), which led to a higher delivery efficiency for smaller particles.

To confirm this hypothesis, an ICP-MS study of UCNP internalization by NRK cells was performed with similar sized UCNPs@AP without attached rose bengal (12 nm or 25 nm particles, cf. **Chapter 4** and **Chapter 5**) by applying UCNP dispersions with same mass concentration (**Table 7.1**). The comparison revealed that in total a higher mass of larger UCNPs was found in the cell lysates. However, considering the particle mass (m_{UCNPs}), a larger number of the smaller UCNPs with a higher S/V ratio was taken up by the cells ($\sim 180\cdot 10^3$ vs $40\cdot 10^3$ UCNPs per cell). The results of this ICP-MS study using AP-coated UCNPs are in accordance with the observations of the RB microscopy study. The internalization of small UCNPs@AP by particle is higher than that of larger UCNPs@AP, enabling in total a higher rose bengal uptake by the cells when exposed to the smaller UCNPs@AP-RB.

Table 7.1. ICP-MS analysis of NRK cells (passage numbers 15 – 21) exposed to 12 nm $\text{NaYF}_4(\text{Yb},\text{Er})@\text{NaYF}_4$ or 25 nm $\text{NaYF}_4(\text{Yb},\text{Er})$ UCNPs ($50 \mu\text{g}\cdot\text{mL}^{-1}$, L-15, 5% FCS) at 37°C for 24 h with total mass of UCNPs in the whole cell lysate (m_{UCNPs}) and number of UCNPs per cell ($N_{\text{UCNPs/cell}}$) (mean \pm SEM, ten independent experiments with two replicates).

	12 nm UCNPs@AP	25 nm UCNPs@AP
$m_{\text{UCNPs}} / \mu\text{g}$	0.19 ± 0.05	0.38 ± 0.09
$N_{\text{UCNPs/cell}} / 10^3$	180 ± 50	40 ± 9

The microscopy study addressing the impact of particle size and surface properties on the delivery efficiency of rose-bengal functionalized UCNPs revealed that bilayer modifications with a larger amount of stably bound photosensitizer were the favorable particle coatings. Due to the increased surface to volume ratio, the smaller particles could transport higher amounts of rose bengal into the cells.

7.5 Toxicity of Rose Bengal Functionalized Nanoparticles

The photosensitizer functionalized UCNPs should not be intrinsically toxic in the dark in the desired time if cell death by ROS production is intended to be monitored. Therefore, the toxic effect of the various rose bengal-functionalized UCNPs on NRK cells was analyzed *via* the impedance-based cell assay in the dark. The impedance time courses of cells exposed to 24 nm UCNPs@AP-RB and UCNPs@Lys-RB ($50 \mu\text{g}\cdot\text{mL}^{-1}$) show a monotonic decrease after 30 – 40 h. Values of a cell-free electrode are obtained after > 42 h incubation time (**Figure 7.8**). In contrast, the exposure to UCNPs@PLM-RB does not change the impedance courses of the cells, similar to the control with DMEM (5% FCS, with/without 1% DMSO).

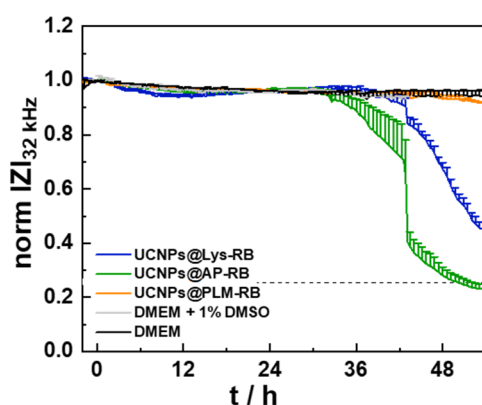


Figure 7.8. Normalized time courses of impedance at 32 kHz of NRK cells (passage numbers 24, 25) exposed to 24 nm UCNPs@Lys-RB ($50 \mu\text{g}\cdot\text{mL}^{-1}$, DMEM, 5% FCS, 1% DMSO), UCNPs@AP-RB, UCNPs@PLM-RB ($50 \mu\text{g}\cdot\text{mL}^{-1}$, DMEM, 5% FCS) or control DMEM (5% FCS) and DMEM (5% FCS, 1% DMSO) at time point 0 h at 37 °C in the dark (mean + SEM, triplicates from two independent experiments). Dashed line indicates the impedance value of a cell-free electrode. Average baseline magnitude of impedance was $(1.66 \pm 0.03) \text{ k}\Omega$ ($N = 18$) before addition.

The toxicity of UCNPs@Lys-RB in the dark is unexpected as no RB was imaged within the cells after exposure to UCNPs@Lys-RB. However, only the RB emission and not the UCNPs emission was collected in the microscopy study and therefore, the experiment enabled only hints on the fate of RB and not on the fate of UCNPs. According to the DLS analysis of less stable UCNPs@Lys-RB (cf. **Figure 7.3**), demonstrating poor colloidal stability, and the UCNPs/RB uptake study by LA-ICP-MS (cf. following **Chapter 7.6**), demonstrating no RB but an high UCNPs uptake, it is valid that loosely bound lysine as well as Lys-RB were stripped off or exchanged from the particle surface by medium components before entering the cell and

particle aggregates were internalized without significant amounts of rose bengal. Thus, the observed death of cells exposed to UCNPs@Lys-RB was assumed to result from internalized particles. This is in accordance with the toxicity study in the dark using poorly shielded UCNPs in **Chapter 6**.

The UCNPs@AP-RB stressed the cells in an earlier stage compared to UCNPs@Lys-RB, which might be due to the higher internalization rate of UCNPs@AP-RB. The UCNPs@PLM-RB did not affect the cells at all, which was remarkable as the uptake efficiency of RB by UCNPs@PLM-RB was the highest (**Figure 7.6**). The non-toxicity of UCNPs@PLM compared to UCNPs@AP in the dark was discussed in detail in **Chapter 5** and was related to the protection of the particle surface by the PLM coating, hindering particle degradation.

In terms of toxicity, the Lys as well as AP coating should not be applied *in vivo* at all but may be applicable in short-time *in vitro* tests with concentrations $< EC_{50}$ and proof-of-concept studies. In this first study the PLM turned out to be a suitable coating for functionalizing UCNPs with photosensitizers for further *in vitro* and maybe *in vivo* studies as it did not trigger cell death itself in the dark at any concentration up to $50 \mu\text{g}\cdot\text{mL}^{-1}$ for at least 54 h.

The size-dependent toxicity of 15 nm and 24 nm UCNPs@AP-RB on NRK cells was examined with the impedance-based cell assay in the dark. The impedance of electrodes with attached cells exposed to 15 nm UCNPs@AP-RB ($50 - 100 \mu\text{g}\cdot\text{mL}^{-1}$, L-15, FCS) starts to increase slightly after 12 h and fluctuates around the maximum normalized impedance value of 1.2 for at least 72 h (**Figure 7.9A**). Lower concentrations show an impedance time course not different to the one of the control L-15 (5% FCS). When cells of low subcultures (P18) were exposed to 24 nm UCNPs@AP-RB, the impedance increases only slightly for at least 72 h and does not decrease at all (**Figure 7.9B**). After a transient increase, the impedance of electrodes with cells from higher passage numbers (P22 - P24) decreases monotonically to values of cell-free electrodes with exposure to 24 nm UCNPs@AP-RB in a concentration-dependent manner (**Figure 7.9C**). For those, cell death is initiated by concentrations $\geq 20 \mu\text{g}\cdot\text{mL}^{-1}$. The stepwise impedance decrease over time can lead to the wrong conclusion of a stepwise cell-death. However, the steps are only visible after averaging the individual time courses of the independent measurements with cells from higher passage numbers and slightly different time points of starting impedance decreases and are not interpretable. The area under the curve was used

to determine an EC_{50} value of $(14 \pm 4) \mu\text{g}\cdot\text{mL}^{-1}$ for the 24 nm particles UCNPs@AP-RB in L-15 for NRK cells (passage number 22-24) (Figure 7.9D).

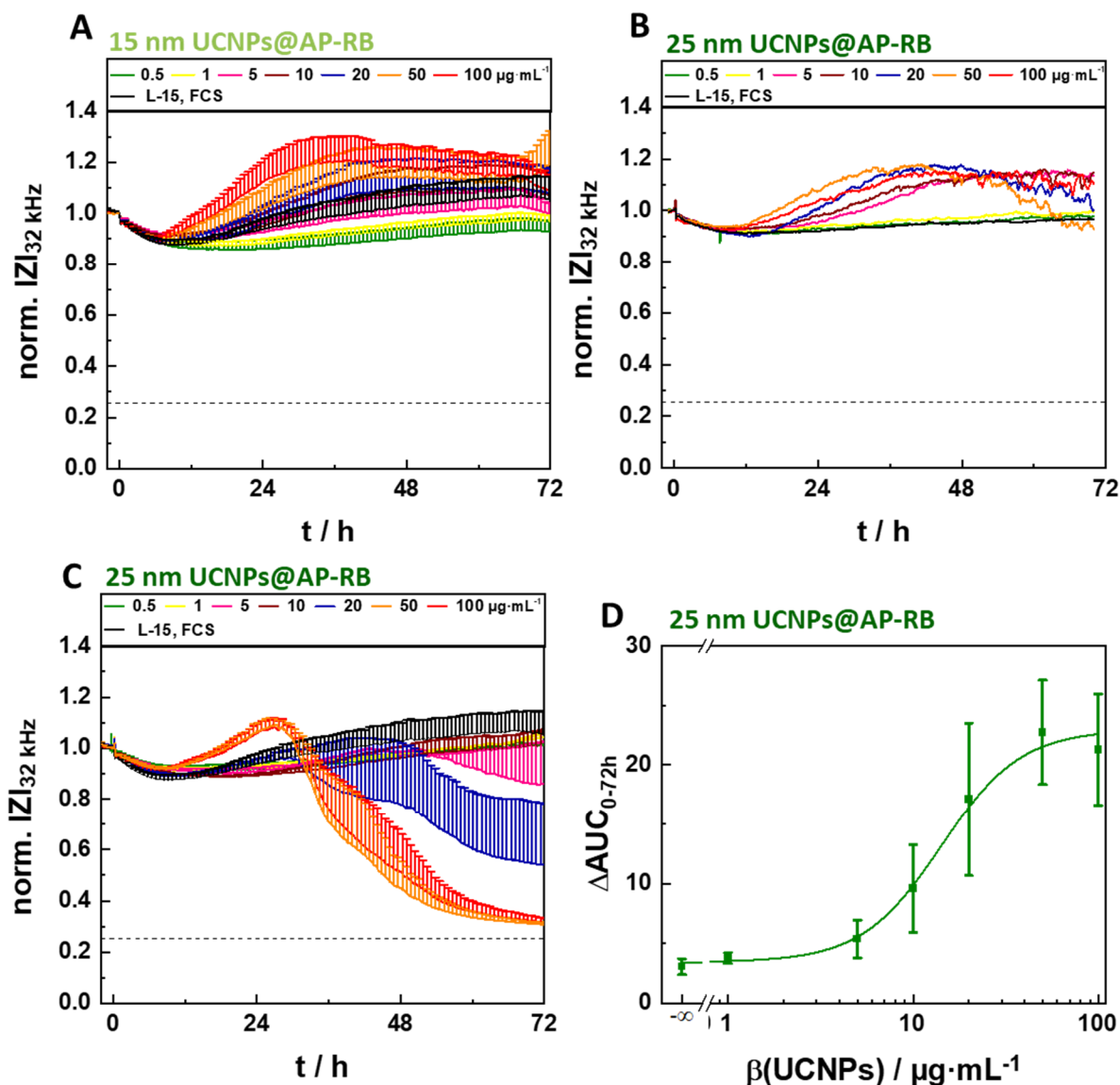


Figure 7.9. Normalized time courses of impedance at 32 kHz of NRK cells (passage number 22 - 24) exposed to (A) 15 nm and (C) 24 nm UCNPs@AP-RB ($0.5 - 100 \mu\text{g}\cdot\text{mL}^{-1}$, L-15 + 5 % FCS) (mean \pm SEM, three individual experiments) or (B) NRK cells (passage number 18) exposed to 24 nm UCNPs@AP-RB or control at time point 0 h (black arrow) at 37°C in the dark for at least 72 h. Dashed lines indicate impedance of cell-free electrodes. (D) Concentration-dependent area under the normalized impedance curve (0 - 72 h) of NRK cells (passage number 22 - 24) with 24 nm UCNPs@AP-RB exposure to determine an $EC_{50} = (14 \pm 4) \mu\text{g}\cdot\text{mL}^{-1}$ (mean \pm SEM, three independent experiments). The average baseline magnitude of impedance was $(1.075 \pm 0.005) \Omega$ (mean \pm SEM, $N = 60$).

The cell age-dependent toxicity in the dark, which was monitored for the 24 nm UCNPs@AP, was also observed for 33 nm UCNPs@AP and 25 nm UCNPs@AP (cf. **Chapter 5** and **Chapter 6**).

While the larger particles with lower RB internalization triggered cell death in the dark, the 15 nm UCNPs@AP-RB with a relative higher rose bengal load did only initiate cell stress but no death within 72 h in the dark. Impedance just increases, which may be related to swelling cells under stress due to a large number of vesicle-internalized UCNPs (Zinkl et al., 2019).

The size-dependent toxicity of metal-based nanoparticles has been well-described, but the results were controversial and do not enable a common statement. Some studies reported a higher toxicity of smaller nanoparticles (Feng et al., 2018; Li et al., 2011; Zhang et al., 2011) while there are also plenty of studies claiming a higher toxicity of larger nanoparticles (Kim et al., 2015; Kim et al., 2012; Mironava et al., 2010). In general, smaller particles have a higher surface area for reactivity for the same mass concentration as larger particles, which was often attributed to favor adverse chemical reactions (Shang et al., 2014). The mainly proposed mechanism of nanotoxicity were based on the generation of ROS due to oxidations triggered by the nanoparticle surface, released ions, or due to mitochondrial membrane damage by particles, leading to mitochondrial ROS release into the cytoplasm (Yang et al., 2021). Ion release takes place for all particles until the saturation concentration of equilibrium is reached. However, kinetics might be different and degradation should be faster for smaller nanoparticles with larger surface area (Nel et al. 2009; Carlson et al. 2008). In a dynamic system with continuously changing vesicles, undergoing maturation (early endosome, late endosome, and lysosome) or recycling processes, the equilibrium is constantly adjusted, which accelerates dissolution.

The surface-dependent dissolution of the particles was also reported for fluoride based UCNPs with an increase of particle disintegration for 20 nm vs 33 nm polyacrylic acid (PAA) coated UCNPs ($\text{NaYF}_4(\text{Yb},\text{Er})@\text{PAA}$, (Saleh et al., 2020)) and for 10 nm vs 33 nm ethylene glycol (EG) coated UCNPs ($\text{NaYF}_4(\text{Yb},\text{Tm})@\text{EG}$, (Lisjak et al., 2016)). So far, the toxic effect due to intracellular ion leakage of fluoride based UCNPs has not been well-documented and, thus, does not allow a comparison to extracellularly applied ion solutions (Rim et al., 2013; Wysokińska et al., 2019). Nevertheless, a possible toxicity pathway of in situ generated RE ions has been reported. The RE ions have a high binding affinity to phosphates and forms RE phosphates (REPO_4) with cellular phosphates as DNA, ATP or membrane lipids (Li et al., 2015). Thus, the endosomal membranes can be destroyed by dissolving ions so that the REPO_4

structures as well as the endosomal enzymes can escape into the cytoplasm, causing further membrane damage and pro-inflammatory effects. Together with the classical ROS pathways, observed in many other nanoparticles (cf. **Chapter 1.5**), this scenario is plausible for fluoride based RE particles (cf. **Chapter 5** and **Chapter 6**).

Here, the larger UCNPs had a higher toxicity than the smaller ones, which did not fit to the theory of surface area dependent particle disintegration and toxicity. However, the total mass of ~25 nm internalized particles was higher than the one of ~15 nm particles, yielding a similar total surface area for both particle systems (both $\sim 2.4 \cdot 10^{10} \text{ nm}^2$) with a mass difference of a factor of 5 – 10 (**Table 7.1**). Membrane-wrapping effects and ligand receptor interactions may be favored for larger particles (Shang et al., 2014), accelerating the internalization process and triggering toxicity cascades faster. Confocal fluorescence microscopy studies of direct excitation of rose bengal does not confirm these theories as RB loading efficiency was larger for small UCNPs and excitation of upconversion luminescence was not possible due to experimental limitations. Nevertheless, the faster internalization rate of 33 nm UCNPs@PLM than of 15 nm UCNPs@PLM by NRK cells was observed by electron microscopy studies after 10 – 60 min (data not shown here).

Since the internalization of the larger particles occurred faster, the release of RE ions into the cell followed by ROS production and membrane damage might have happened faster compared to smaller UCNPs. However, a confirmation of this hypothesis was impossible within this work due to limited spectroscopic as well as microscopic possibilities.

In terms of toxicity and photosensitizer delivery, the application of smaller 15 nm UCNPs may be preferred over 24 nm UCNPs. For studying photodynamic therapy, a pre-exposure time of < 24 h should be chosen for 24 nm UCNPs@AP-RB to ensure no intrinsic toxicity in the dark (ROS production, membrane rupture cell death), falsifying the results.

7.6 Rose Bengal and Upconversion Nanoparticle Uptake by Cells

To validate the microscopic results on rose bengal delivery efficiency by UCNPs decorated with RB by different strategies (24 nm UCNPs@Lys-RB, UCNPs@AP-RB, UCNPs@PLM-RB), the internalization and intracellular fate of these UCNPs was further analyzed by a luminescence-independent technique with a highly sensitive determination of the local chemical composition: the laser ablation – inductively coupled plasma – mass spectrometry (LA-ICP-

MS). The RB modified UCNPs are a suitable nanoparticle-ligand model to examine the fate of particles and attached ligand separately with this method. The ligand rose bengal contains four iodine per RB molecule, which is reliably detectable by ICP-MS with the stable isotope $^{127}\text{I}^+$ after appropriate sample preparation. The UCNPs are easily quantified by ICP-MS due to their high amounts of the rare earth ions yttrium, ytterbium, and erbium. Here, the most sensitive oxygenated yttrium isotope ($^{89}\text{Y}^{16}\text{O}^+$) was chosen for analysis. Thus, LA-ICP-MS enables the determination of the rose bengal to UCNPs ratio, accessible by the iodine to yttrium intensity ratio (I/Y with intensities of $^{127}\text{I}^+$ and $^{89}\text{Y}^{16}\text{O}^+$) under cell-free conditions and *in vitro* and, thereby, gives hints to the intracellular fate of nanoparticles and the attached ligands on cells seeded in low density.

The cell-free I/Y ratio of the UCNPs, embedded in gelatine, was determined *via* LA-ICP-MS as $1.4 \cdot 10^{-3}$ for UCNPs@Lys-RB and around $22 \cdot 10^{-3}$ for UCNPs@PLM-RB as well as for UCNPs@AP-RB (**Table 7.2**). These values confirm the clear tendency, obtained from rose bengal absorbance measurements and ICP-OES measurements of the UCNPs ($N_{\text{RB/UCNPs}}$), that a similar amount of RB is attached to UCNPs@PLM-RB and UCNPs@AP-RB, while significantly less RB is bound to UCNPs@Lys-RB (cf. **Chapter 7.4**). The $N_{\text{RB/UCNPs}}$ was converted to RB/Y ratio and a (I/Y)' ratio, considering the four iodine per RB (**Table 7.2**). However, the iodine concentrations, obtained from the absorbance data of particle-attached RB, are only rough estimates and do not consider the changed photophysical properties of RB attached to the UCNPs as these are difficult to characterize (cf. **Chapter 7.1**). Therefore, these (I/Y)' ratios as determined by UV/VIS are approximately four times higher than the more precise values obtained by LA-ICP-MS, which is independent of any photophysical changes of RB. Regardless of exact values for $N_{\text{RB/UCNPs}}$ and I/Y ratio, both methods reveal the same trend (low I/Y for UCNPs@Lys-RB, high and similar I/Y for UCNPs@PLM-RB and UCNPs@AP-RB) and demonstrate that LA-ICP-MS is indeed suitable to capture changing I/Y ratios of the different particles.

Table 7.2. Rose bengal to yttrium (RB/Y) and iodine to yttrium (I/Y) ratio of UCNPs@AP-RB, UCNPs@PLM-RB, and UCNPs@Lys-RB obtained either by LA-ICP-MS ($^{127}\text{I}^+$ and $^{89}\text{Y}^{16}\text{O}^+$) or absorbance measurements of rose bengal (λ_{max} between 555 nm and 571 nm) together with ICP-OES measurements of the UCNPs. $(\text{I/Y})'$ was determined from RB/Y ratio of absorbance data by considering the four iodine per RB.

	$\text{I/Y} \cdot 10^{-3}$	$\text{RB/Y} \cdot 10^{-3}$	$(\text{I/Y})' \cdot 10^{-3}$
	LA-ICP-MS	absorbance, ICP-OES	absorbance, ICP-OES
24 nm UCNPs@AP-RB	21	26	104
24 nm UCNPs@PLM-RB	22	19	76
24 nm UCNPs@Lys-RB	1.4	3	12

These cell-free I/Y ratios, determined by LA-ICP-MS, were compared to the ratios obtained from individual cells after a certain UCNP incubation time. The individual NRK cell bodies are clearly defined by the phosphorus distribution ($^{31}\text{P}^{16}\text{O}^+$) in false colored images as exemplary shown in **Figure 7.10** for the UCNPs@PLM treated cells in comparison to the light micrographs. Yttrium ($^{89}\text{Y}^{16}\text{O}^+$) as marker for the UCNPs is highly found in areas where cells are identified *via* the phosphorus content and the phase contrast micrograph. False colored images of iodine ($^{127}\text{I}^+$) as marker for rose bengal are not shown here as intensities were only high enough for a reliable quantification of the total ($^{127}\text{I}^+$) per cell but too low for precise imaging with spatial resolution. The $^{89}\text{Y}^{16}\text{O}^+$ and $^{127}\text{I}^+$ signals can be assigned to internalized or cell membrane attached UCNPs, rose bengal, and their biotransformed products. Some UCNPs are also found around the cells, randomly bound to the microscopic slide. However, these are clearly distinguishable from cell bound UCNPs by comparison with the phosphor/phase contrast images.

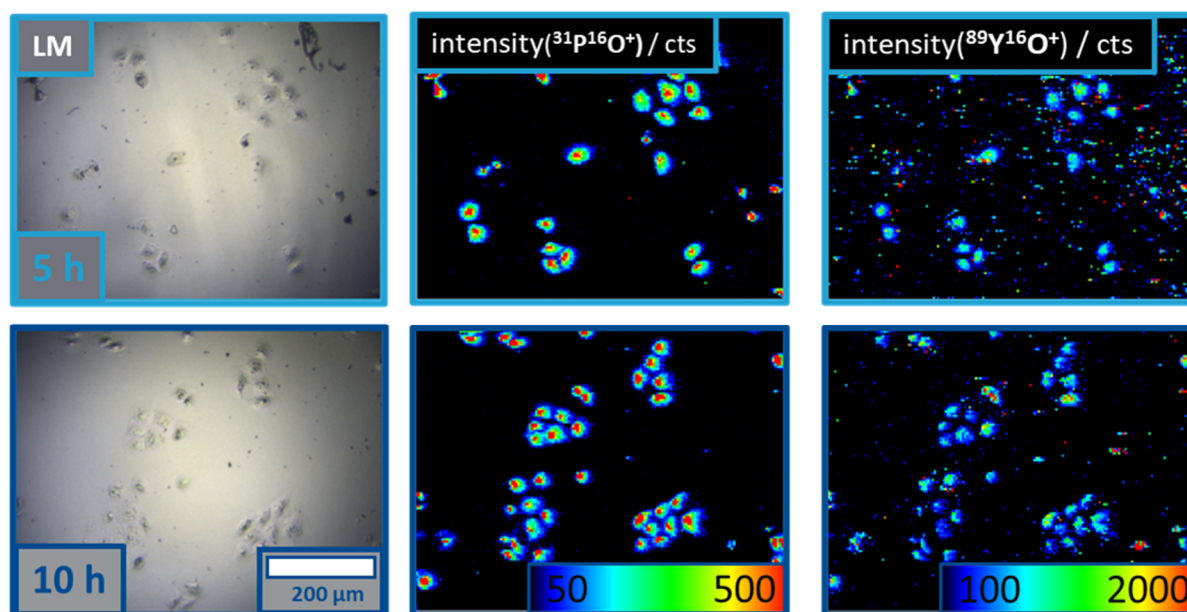


Figure 7.10. Representative bright field micrographs (LM) of NRK cells after exposure to UCNPs@PLM ($50 \mu\text{g}\cdot\text{mL}^{-1}$, DMEM, 5% FCS) at 37°C for 5 h or 10 h with corresponding false colored images of the phosphorous ($^{31}\text{P}^{16}\text{O}^+$) intensity to visualize cell bodies and of the ($^{89}\text{Y}^{16}\text{O}^+$) yttrium as marker for UCNPs, obtained by LA-ICP-MS. Signal intensities are color-coded with increasing intensity from blue (low intensities) to red (high intensities).

The iodine content ($\text{intensity}(^{127}\text{I}^+)$), the yttrium content ($\text{intensity}(^{89}\text{Y}^{16}\text{O}^+)$), and the corresponding I/Y ratio per cell were determined for 100 individual cells, incubated with one of the three particles for 5 h or 10 h. The distributions of these values are visualized as box plot in **Figure 7.11** (cf. corresponding histograms in **Figure A 8**). In the case of UCNPs@Lys-RB, ~ 80 cts iodine and $\sim 300 \cdot 10^3$ cts yttrium are found per cell after 5 h and 10 h of incubation, resulting in a cellular I/Y ratio of $\sim 0.5 \cdot 10^{-3}$. This I/Y ratio is 65% lower than the corresponding ratio of the UCNPs@Lys-RB found in cell-free experiments ($\sim 1.4 \cdot 10^{-3}$, cf. **Table 7.2**). Cells exposed to UCNPs@AP-RB for 5 h or 10 h show ~ 300 cts iodine and $\sim 30 \cdot 10^3$ cts yttrium with a I/Y ratio of $\sim 6 \cdot 10^{-3}$ per cell, which is 70% lower than the corresponding ratio in cell-free experiments ($\sim 21 \cdot 10^{-3}$, cf. **Table 7.2**). In contrast, the amount of iodine in UCNPs@PLM-RB treated cells increases with longer incubation time from ~ 800 cts after 5 h to ~ 2000 cts after 10 h, while the yttrium content remains constant at $\sim 20 \cdot 10^3$ cts. Thus, the I/Y ratio is shifted in this time range from $50 \cdot 10^{-3}$ to $100 \cdot 10^{-3}$ and hence, is at least two times higher than the cell-free determined I/Y value.

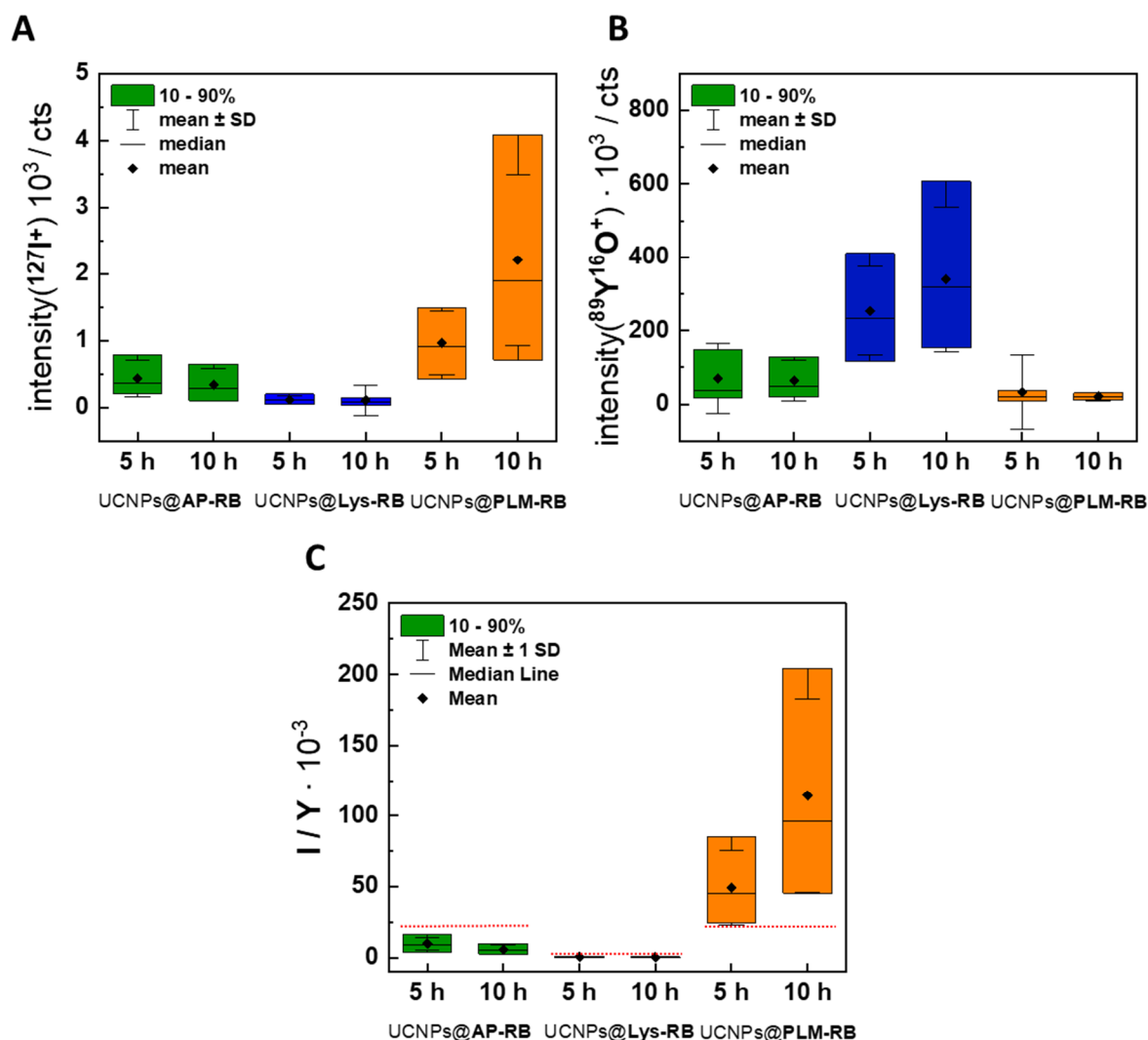


Figure 7.11. Box plot of the cellular (A) iodine content (intensity($^{127}\text{I}^+$)), (B) yttrium content (intensity($^{89}\text{Y}^{16}\text{O}^+$)), and the (C) corresponding I/Y ratio of 100 individual NRK cells determined *via* LA-ICP-MS after incubation with 24 nm UCNPs@Lys-RB (50 $\mu\text{g}\cdot\text{mL}^{-1}$, DMEM, 5% FCS, 1% DMSO), UCNPs@AP-RB, or UCNPs@PLM-RB (each 50 $\mu\text{g}\cdot\text{mL}^{-1}$, DMEM, 5% FCS) at 37 $^{\circ}\text{C}$ for 5 h or 10 h. The boxes visualize the values of 10 – 90% of the cells with the median and mean value \pm SD. I/Y ratios of the UCNPs determined under cell-free conditions in gelatine are shown as red line in (C).

These results clearly indicate that the cellular I/Y ratio is lower than the corresponding cell-free determined ratios for toxic as well as instable UCNPs@Lys-RB and toxic UCNPs@AP-RB, while the values of the non-toxic UCNPs@PLM-RB increased in the cells. The amount of iodine per NRK cell is at least three to ten times higher after 5 h incubation with UCNPs@PLM-RB than with UCNPs@AP-RB and UCNPs@Lys-RB, respectively. Thus, UCNPs@PLM-RB seem to deliver significantly higher amounts of RB to the cells than the UCNPs with the other surface modifications. This is in accordance with the CLSM study (cf. **Figure 7.6**).

The strongly reduced *in vitro* I/Y ratio of UCNPs@Lys-RB and UCNPs@AP-RB is not due to a high overestimation of the cell-free determined ratios due to insufficient washing steps of the particles since purification was carried out until the supernatant was approximately clear by bare eye. More likely is that loosely bound Lys-RB was partly exchanged by medium contained lysine or other biomolecules available in high amounts so that the UCNPs@Lys-RB were internalized as aggregates with changed and unknown surface characteristics. This hypothesis is supported by the DLS data of UCNPs@Lys-RB, revealing ongoing aggregation of these particles in the medium (cf. **Figure 7.3**). A ligand exchange of a bilayer forming AP-RB for the colloidal stable UCNPs@AP-RB is less probable as for UCNPs@Lys-RB due to the more stable bilayer of the surface modification. However, the AP-RB polymer chains may not stick totally to the particle but reach into solution so that extracellular available proteases may cleave some amide bonds and UCNPs@AP-RB are internalized with lower RB levels.

In contrast, the *in vitro* I/Y ratios of non-toxic UCNPs@PLM-RB are higher than those of the gelatine standards. The ratios further increase with longer incubation times (10 h), indicating an accumulation of rose bengal but not of UCNPs. An extracellular separation of rose bengal and particles by extracellular proteases, followed by a high internalization rate of free RB, is not likely as the hydrophilic RB has been shown to be not taken up in detectable amounts without a carrier such as the UCNPs (cf. **Figure 7.6**). The extracellular destruction of membrane bound UCNPs@PLM-RB by splitting the PLM at the hydrophobic core during cell washing into phospholipid-RB, sticking to the membrane, and UCNPs with one lipid layer is very improbable. UCNPs@PLM have been shown to be very stable during harsh treatments such as washing or centrifugation and should withstand the careful washing of the cells for sample preparation. Thus, the separation of UCNPs@PLM-RB may rather happen intracellularly to achieve an accumulation of RB in the cell, while UCNPs were exocytosed from the viable cells. A partial cleavage of RB from the UCNPs@PLM at the amide bond may be enabled by intracellular proteases within cellular vesicles and allows a different fate of UCNPs and RB. RB is known to intercalate into lipid bilayers with its hydrophobic part (Demartis et al., 2021b), cross membranes without a dense lipid, protein, or carbohydrate content as diffusion barrier (Feenstra et al., 1992b), accumulate in the cell cytoplasm, and stains cell nuclei by tightly binding to nuclear histone proteins (Feenstra et al., 1992a; Doughty, 2013). Indeed, RB fluorescence was observed in the cell nuclei after exposure to UCNPs@PLM-RB for 5 h and

more pronounced after 10 h incubation by CLSM images of a medium focus plane (cf. **Figure 7.6**). As nuclear pore complexes (NPC, diameter < 9 nm) enable the passive diffusion into the nucleus only for substances with a diameter smaller than the NPCs (Paine et al., 1975), the nanoparticles used in this study are not supposed to enter the nuclei (cf. microscopy study in **Chapter 5**). Thus, the RB emission in the nuclei may demonstrate a separation of RB and UCNPs@PLM-RB. A reduction of the internalized nanoparticle amount is in general possible by proliferation and exocytosis (Kang et al., 2022). However, proliferation would lead to the equal reduction of RB and UCNPs, which was not observed, and hence, exocytosis of the UCNPs after separation may be the more probable pathway. Exocytosis is exhibited by all cells to deliver membrane proteins and is especially important for endothelial and epithelial cells of respiratory and gastrointestinal organs for the transcytosis of any substances. Thereby, nanoparticles in vesicles, like early endosomes or lysosomes, can be transported back to the cellular membrane (Sakhtianchi et al., 2013; Jaiswal et al., 2002). UCNPs@PLM have been localized in these vesicles in NRK cells by electron microscopy (cf. **Chapter 5**) and hence, exocytosis of UCNPs from the normal kidney cells is likely to happen. This seems to be only the case for UCNPs@PLM-RB treated cells with increasing I/Y ratio and not for the cells exposed to the toxic UCNPs@AP-RB or UCNPs@Lys-RB with reduced I/Y ratio as those cells might be too affected by the particles and had already slowed down transport processes.

The UCNPs@Lys-RB treated cells show the highest yttrium intensities. This may be due to the transformation of UCNPs@Lys-RB in cell medium, forming large aggregates as determined by DLS (cf. **Figure 7.3**). The individual particle aggregates have different surface and mass characteristics than the well-dispersed individual UCNPs, leading to an altered abundance, uptake probability, and toxic impact to the cells (Buford et al., 2007; DeLoid et al., 2017; Feliu et al., 2017). The UCNPs@Lys-RB are determined in cellular proximity and can be either attributed to internalized or cell membrane attached particles.

The lower amount of UCNPs@PLM-RB compared to the one of UCNPs@AP-RB was not expected since wide-field upconversion microscopy and ICP-MS analysis of cell lysates revealed at least twice as many UCNPs@PLM than UCNPs@AP in NRK cells after 6 h and 24 h (cf. **Chapter 5**). However, depending on the cell cycle stage, exocytosis is differently pronounced. The ICP-MS and wide-field upconversion microscopy studies were performed with cells in confluency, which are supposed to mainly stick in G0 phase of cell cycle with a

reduced tendency for mitosis (Khammanit et al., 2008). The cells for the LA-ICP-MS measurement were seeded in low density and thus, the cell cycle was still ongoing. Exocytosis is highest for cells during cytokinesis due to the required membrane recycling (Tanaka et al., 2020) and may happen more likely with proliferating cells like in the LA-ICP-MS experiments. Thus, the results of the three experiments performed with cells in different states are not necessarily comparable.

This study on changing ratios of the UCNP and the surface functionalization (here: rose bengal) demonstrates that the overall particle properties change during cell exposure and internalization and reveals the different delivery by using several surface modification strategies. It was observed that transport processes as exocytosis may differ for viable and stressed cells. However, the model of exocytosis as reason for increasing I/Y ratios need to be verified by extended exocytosis studies with LA-ICP-MS and additional techniques.

7.7 Production of Reactive Oxygen Species upon Irradiation of Rose Bengal

After particle characterization and analyzing the photosensitizer (PS) loading efficiency, PS uptake into the cells and intrinsic toxicity of particles, their phototoxicity was examined size-dependently with 15 nm and 24 nm UCNP functionalized with RB. UCNP@AP-RB were used in this first proof-of-concept study, verifying the assay functioning and choosing suitable parameters, as their preparation is much cheaper than that of UCNP@PLM-RB. Initially, rose bengal was excited directly to prove reactive oxygen species (ROS) production with the RB-modified particles and to optimize the analysis of cellular ROS production and cell viability. The direct excitation was chosen for a proof-of-concept study to induce a maximum of ROS production and to quantify any UCNP-mediated ROS generation relative to this. Moreover, the 980 nm excitation can only be performed in a small area of one well with a homemade, difficult to control set-up as NIR light sources are not commonly found in microplate readers so far. This makes any high throughput screening upon 980 nm excitation impossible while direct excitation can be performed in multiple wells of a microplate at once. However, it is desired to excite the PS indirectly by UCNP emission for later approaches to use the particles not only as transporter but also as excitation source *via* upconversion of NIR light to create further options for photodynamic therapy.

7.7.1 Fluorometric Detection of Cellular Levels of Reactive Oxygen Species

Evaluation of Assay Conditions

ROS generated upon excitation of rose bengal within the cells were detected spectroscopically by the dye 2',7'-dihydrodichlorofluorescein (H_2DCF). This probe is oxidized by various ROS into its fluorescent derivative DCF, enabling the quantification of cellular ROS. The lipophilic precursor molecule 2',7'-dihydrodichlorofluorescein diacetate (H_2DCFDA) needs to be converted into its non-permeable hydrophilic H_2DCF by cellular esterases to enable its oxidation to dichlorofluorescein (DCF) (**Scheme 3.13**). The dye mainly detects the ROS produced within the cells (Eruslanov et al., 2010), which was confirmed with cell-free experiments at the beginning to avoid misinterpretation. These cell-free values of non-specific DCF conversion in aqueous solution with particles are used to correct the measurement data. A particle incubation time of 14 h using different concentrations was chosen to enable a high uptake of the RB-functionalized particles for ROS production upon excitation. In this time frame, particle induced cell death was not observed in the dark. As two protocols for ROS detection with molecular probes have been reported, incubating the cells with the dye either prior or after irradiation, the detectability of ROS was tested with these two approaches. The H_2DCFDA treatment was done either 2 h after 10 min irradiation at 528 nm (**Figure 7.12A**) or prior to the 10 min irradiation (**Figure 7.12B**). When H_2DCFDA was applied 2 h after irradiation, almost no DCF intensity is detected within 5 h and no significant difference between UCNPs@AP-RB and L-15 treated cells are visible. DCF fluorescence in control cells with or without irradiation at 528 nm for 10 min is equal, confirming that the irradiation itself under these conditions does not harm the cells for at least 7 h. The slight increase of DCF fluorescence in the control- as well as in particle-treated cells may be due to low levels of ROS present in the cells anyhow or produced during H_2DCFDA treatment.

By incubating the cells with H_2DCFDA before irradiation, the DCF intensity immediately increases after irradiation for particle-treated cells until a maximum value is obtained after 2 h (**Figure 7.12B**). With a difference of one order of magnitude, non-irradiated cells or cells without particle incubation are not able to convert the H_2DCF to fluorescent DCF. Only slight increases of DCF fluorescence are visible, attributed to the ubiquitous presence of low levels of ROS in the cells.

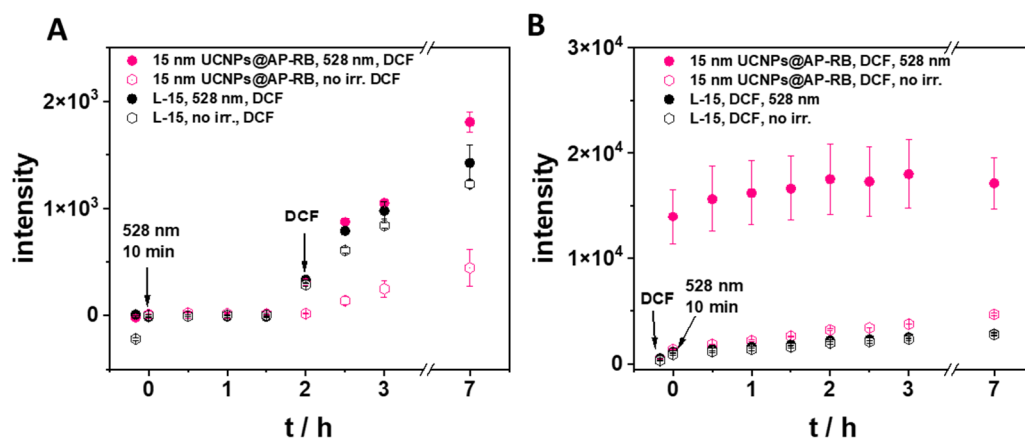


Figure 7.12. Time-dependent luminescence intensity of DCF converted by cells exposed to 15 nm UCNPs@AP-RB ($100 \mu\text{g}\cdot\text{mL}^{-1}$, L-15, 5% FCS) or control (L-15, 5% FCS) at 37°C and irradiated with 528 nm at time point 0 h or not (A) 2 h before DCFDA incubation or (B) directly after DCFDA incubation at 37°C ($\lambda_{\text{exc}} = 485 \text{ nm}$, $\lambda_{\text{em}} = 535 \text{ nm}$, mean \pm SD, triplicate in one experiment).

In comparison, the H_2DCFDA treatment of cells after irradiation was not suitable to detect ROS produced upon irradiation since the cells might get rid of ROS in the meantime and no conversion to DCF by ROS was possible anymore. Additionally, the fact that no ROS were detectable under these conditions provides evidence that the particles did not trigger intrinsically the production of significant amounts of ROS after an incubation time of 14 h. The incubation of the cells with H_2DCFDA before irradiation was more appropriate as produced ROS immediately oxidize H_2DCF to DCF and ROS production was not masked. Thus, the assay was suitable to detect ROS with H_2DCFDA incubation prior to any irradiation.

The DCF emission band overlaps (here: readout at $\lambda_{\text{em}} = 535 \text{ nm}$) with the absorbance band of rose bengal (here: excitation at 528 nm). Thus, it is possible that RB gets excited and induces cellular ROS production during each fluorescent readout of DCF. However, the DCF emission intensity is expected to be low in comparison to the LED intensity. Only a very low DCF conversion, slightly rising over time with each measurement, is observed in the control measurement with DCF and particles but without 528 nm excitation (**Figure 7.2B**). This low DCF conversion possibly arise from the undesired chain reaction after each fluorescence measurement. One can get rid of the falsifying effect of this possible chain reaction by normalizing the DCF luminescence intensities of particle-treated and irradiated cells (I_x) with the luminescence intensities of particle-untreated but irradiated cells (I_0). The ratio I_x/I_0 is reduced over time as the amount of DCF in the cells slightly rises without additional treatment

(**Figure 7.13A**). Thus, I_x/I_0 directly after 528 nm excitation of RB was chosen for further data evaluation when the possible chain reaction does not occur anyhow.

To prove the functioning of the intracellular DCF conversion, the tert-butyl hydroperoxide (tBHP) was chosen as positive control. NRK cells without further particle treatment were exposed to tBHP after H₂DCFDA incubation and the amount of intracellular DCF was detected. DCF levels within the cells and thus I_x/I_0 increases over time until a maximum level is reached (**Figure 7.13B**). This confirms the suitability of the assay to detect intracellular DCF converted *e.g.*, by ROS generated by RB after direct excitation.

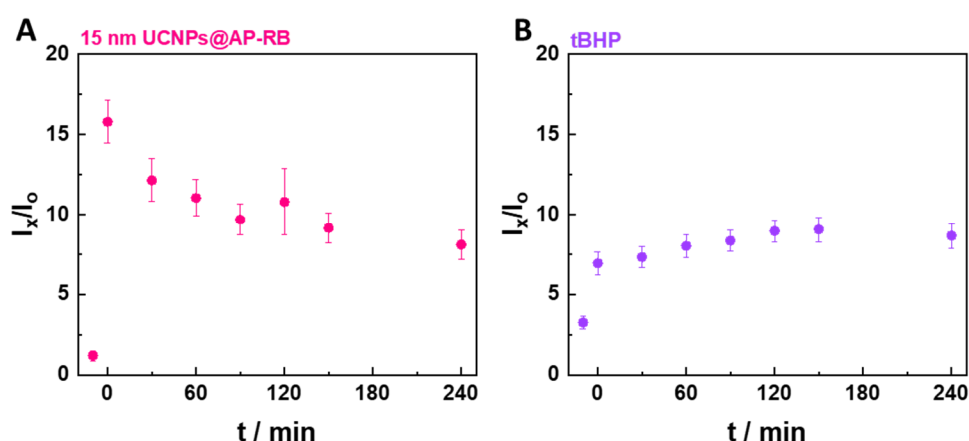


Figure 7.13. (A) Time dependent DCF intensity ratio I_x/I_0 of NRK cells with exposure to 15 nm UCNPs@AP-RB at 37 °C and irradiation (I_x) and cells without particle treatment but irradiation (I_0). (B) Time dependent luminescence intensity ratio I_x/I_0 of DCF at 528 nm of NRK cells exposed to tert-butyl hydroperoxide (I_x , tBHP, 100 μ M, L-15, 5% FCS) or not (I_0 , L-15, 5% FCS) (λ_{exc} = 485 nm, λ_{em} = 528 nm, mean \pm SD, triplicate of one experiment).

Detection of Cellular Reactive Oxygen Species Upon Photosensitizer Activation

The suitability of 15 nm and 24 nm UCNPs@AP-RB to induce ROS production by direct excitation of rose bengal was analyzed with the DCF assay. The NRK cells being incubated with the UCNPs@AP-RB (10 – 100 μ g·mL⁻¹) for 14 h were irradiated with 528 nm for 0 – 10 min before the DCF conversion was detected. The 15 nm UCNPs@AP-RB trigger high ROS levels, which are dependent of the applied particle concentration and the irradiation time (**Figure 7.14A**). The highest particle concentration of 100 μ g·mL⁻¹ with 10 min photosensitizer excitation induces the highest I_x/I_0 ratio of ~11. Reducing the number of internalized particles results in I_x/I_0 ratios of ~7 (50 μ g·mL⁻¹) and ~2 (10 μ g·mL⁻¹), close to values related to non-excited control cells. Shortening the irradiation time to 5 min, the I_x/I_0 (5 min) ratios are lower

than 50% of the I_x/I_0 (10 min) ratios. All concentrations of 15 nm UCNPs@AP-RB and irradiation times of 5 – 10 min triggered cellular ROS production, distinguishable from control cells without irradiation.

The 25 nm UCNPs@AP-RB induce an I_x/I_0 ratio of ~5 for the highest particle concentration (100 $\mu\text{g}\cdot\text{mL}^{-1}$) and longest irradiation time (10 min). I_x/I_0 decreases with decreasing particle concentrations and irradiation time until no detectable ROS levels were produced by the cells for 10 $\mu\text{g}\cdot\text{mL}^{-1}$ particles and 5 min irradiation time (Figure 7.13B).

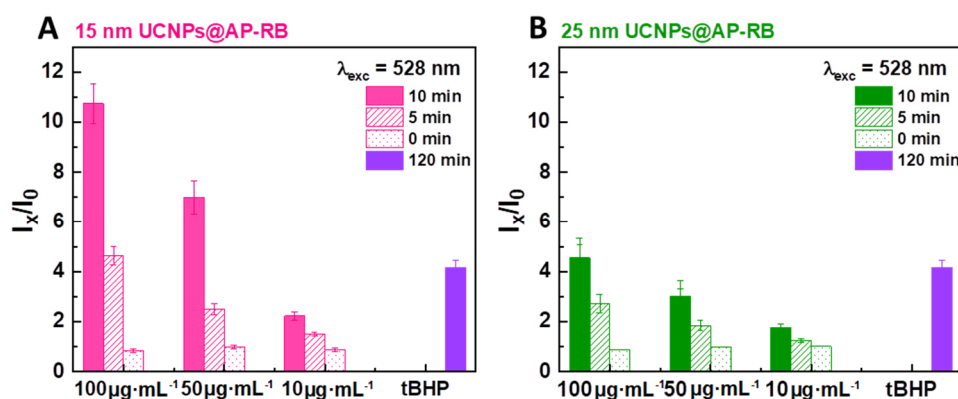


Figure 7.14. Luminescence intensity ratio I_x/I_0 of NRK cells (passage numbers 20 – 24) incubated with (A) 15 nm UCNPs@AP-RB, (B) 24 nm UCNPs@AP-RB (10 – 100 $\mu\text{g}\cdot\text{mL}^{-1}$, L-15, 5% FCS) or positive control tert-butyl hydroperoxide (tbHP, 100 μM , L-15, 5% FCS) at 37 °C for 14 h prior to incubation with H_2DCFDA and irradiation with 528 nm for 0 – 10 min ($\lambda_{\text{exc}} = 485 \text{ nm}$, $\lambda_{\text{em}} = 528 \text{ nm}$, intensity weighted mean \pm error, eight measurements of three experiments).

In comparison, the ROS production of directly activated rose bengal was more efficient for the 15 nm UCNPs@AP-RB than for 24 nm UCNPs@AP-RB, which is in line with the facts that relatively more RB was attached to smaller UCNPs and that more RB was internalized with the smaller UCNPs. However, the ROS production of 15 nm or 24 nm UCNPs@RB may differ for indirect excitation of rose bengal *via* the UCNPs emissions upon NIR irradiation as the intensity of the green upconversion emission is size-dependent and lower for the smaller UCNPs. Therefore, it is instructive to analyze the size-dependent experiment upon indirect excitation to find the optimal size for UCNP-mediated RB excitation.

7.7.2 Detection of Cell Death upon Production of Reactive Oxygen Species

Cell death caused by ROS production upon excitation of the PS rose bengal was validated by the cell viability assay PrestoBlue™. Similar to the DCF assay the cells were exposed to 15 nm or 24 nm UCNPs@AP-RB for 14 h and irradiated with 528 nm light for 0 – 10 min. After a regeneration of 2 h the viability of the cells was analyzed. Small UCNPs initiate cell death of the whole population when irradiated for 5 min ($100 \mu\text{g}\cdot\text{mL}^{-1}$) or 10 min ($50 - 100 \mu\text{g}\cdot\text{mL}^{-1}$) (**Figure 7.15A**). The cell viability is reduced to ~70 % after 5 min irradiation for particle pre-treatment at $50 \mu\text{g}\cdot\text{mL}^{-1}$. Lower concentrations of 15 nm UCNPs@AP-RB do not trigger cell death when irradiated for 5 – 10 min. In contrast, the 25 nm UCNPs@AP-RB are not able to initiate cell death of the whole population (**Figure 7.15B**). Only a reduction of cell viability to 20% after 10 min irradiation and to 50% after 5 min irradiation is observed for the highest particle concentration, while lower particle concentrations do not trigger cell death, independent of the irradiation time.

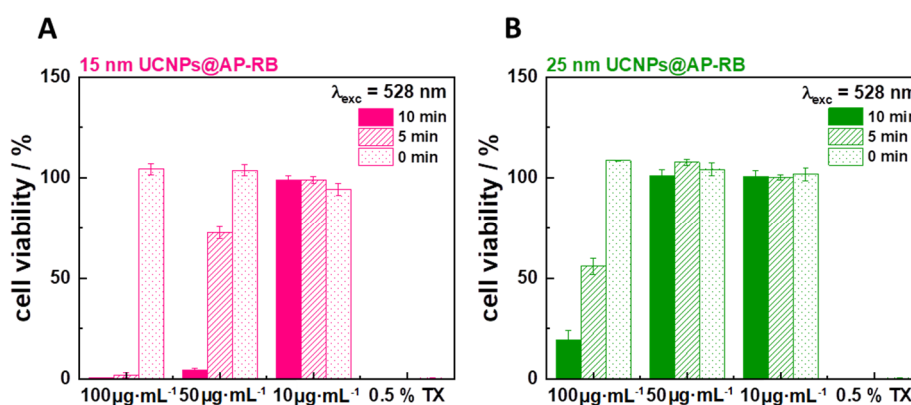


Figure 7.15. Cell viability of NRK cells (passage numbers 20 – 24) exposed to (A) 15 nm UCNPs@AP-RB or (B) 24 nm UCNPs@AP-RB ($10 - 100 \mu\text{g}\cdot\text{mL}^{-1}$, L-15, 5% FCS) for 14 h and triton X-100 (0.5%, w/v, DPBS⁺⁺) as positive control at 37 °C before irradiation at 528 nm for 0 – 10 min (intensity weighted mean \pm error, eight measurements of three independent experiments).

The viability of cells exposed to higher concentrations of particles and no irradiation or short irradiation times ($100 \mu\text{g}\cdot\text{mL}^{-1}$ 15/24 nm UCNPs, no irradiation.; $50 \mu\text{g}\cdot\text{mL}^{-1}$ 25 nm UCNPs, 5 min irradiation) is $>100\%$, which is attributed to hormesis (cf. **Chapter 5** and **Chapter 6**) (Iavicoli et al., 2010). The 25 nm UCNPs@AP-RB produce not enough ROS under the tested irradiation conditions to initiate death of the whole cell population, while the 15 nm

UCNPs@AP-RB trigger 100% cell death when exposed to high particle concentrations and irradiated for 5 min or 10 min with 528 nm.

Identifying the ROS levels inducing cell death, the DCF ratio I_x/I_0 was correlated with the corresponding cell viability (**Figure 7.16**). A ratio $I_x/I_0 < 3$ results in cell viabilities of ~100 % and $I_x/I_0 \geq 7$ in cell viabilities of ~0 %. The relation of I_x/I_0 to cell viability of directly irradiated rose bengal can be approximated by a logistic model. It needs to be verified if the relation between I_x/I_0 and cell viability applies also under other experimental conditions, as for indirect excitation of RB by UCNPs emission, or if it is only valid for direct excited RB.

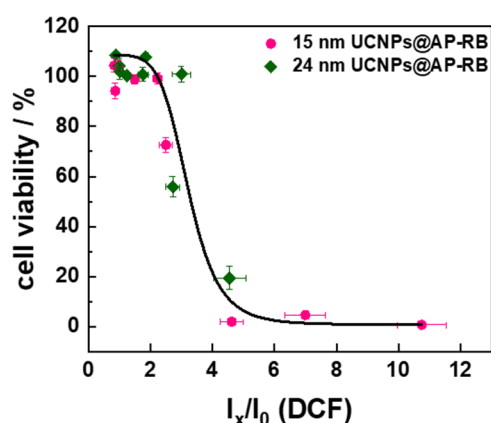


Figure 7.16. Relation of luminescence intensity ratio I_x/I_0 and cell viability of NRK cells exposed to 15 nm or 24 nm UCNPs@AP-RB ($10 - 100 \mu\text{g}\cdot\text{mL}^{-1}$, L-15, 5% FCS) at 37 °C for 14 h before irradiation with 528 nm for 0 – 10 min (intensity weighted mean \pm error, eight measurements of three independent experiments) was approximated with a 4-parameter logistic model (adjusted $R^2 = 0.999$).

This study demonstrated that UCNPs@AP transported RB in therapeutically relevant amounts into cells. Depending on the size and irradiation time, UCNPs@AP-RB produced enough ROS upon RB excitation to kill cells. The workaround and assay parameters developed in this study are expected to be adaptable to similar studies with any other RB functionalized particle. As RB was internalized in even higher amounts into cells by the carrier particles UCNPs@PLM, the intracellular generation of sufficient amounts of ROS is expected for these particles as well.

7.8 Conclusion and Outlook

Rose bengal-functionalized UCNPs were used to analyze the impact of surface properties on the performance of UCNPs in photodynamic therapy. Differently sized core-shell UCNPs (15 nm and 24 nm) were rendered water-dispersible with monolayer (lysine) and bilayer protective coatings (amphiphilic polymer and phospholipid membrane) and functionalized with the photosensitizer rose bengal. The successful attachment of rose bengal to all particle modifications was verified and quantified by UV-Vis spectroscopy and LA-ICP-MS of purified UCNPs. Rose bengal was attached most efficiently to AP, followed by PLM and only poorly to lysine. Smaller UCNPs were loaded with a relatively higher number of photosensitizer molecules due to their higher surface to volume ratio. The uptake of rose bengal into the cells was poor for aggregating UCNPs@Lys-RB, higher for UCNPs@AP-RB and highest for UCNPs@PLM-RB. Moreover, the uptake efficiency of RB from smaller UCNPs was higher than from larger UCNPs, which fits to the fact that dye loading was higher at smaller particles. The 24 nm UCNPs@AP-RB with higher uptake rate had a slightly increased toxicity compared to 24 nm UCNPs@Lys-RB. 24 nm UCNPs@PLM-RB with best RB uptake efficiency did not show any toxic effect to the cells. Smaller UCNPs@AP-RB with a higher numeric uptake had a lower toxicity than 24 nm UCNPs@AP-RB. First studies on changing iodine to yttrium ratios (I/Y corresponding to RB/UCNP) upon particle internalization implied that the RB content of the toxic particles (UCNPs@Lys-RB, UCNPs@AP-RB) was reduced extracellularly and that particles as well as RB accumulated in the cells. In contrast, the changing I/Y ratio of non-toxic UCNPs@PLM-RB indicated the successful internalization of UCNPs and RB in high amounts. As iodine levels increased relatively, a partly intracellular separation of UCNPs and RB was hypothesized, resulting in the intracellular accumulation of RB and the possible exocytosis of UCNPs with reduced amounts of attached RB.

In conclusion, the primary surface coating, rendering UCNPs water-dispersible, dictates ROS production efficiency after photosensitizer attachment and hence cell death. In detail, they affect (I) luminescence intensity (cf. **Chapter 4**), (II) colloidal stability, (III) the number of covalently attached RB to UCNPs, (IV) the uptake efficiency of RB and UCNPs@RB into the cells, and (V) the intrinsic particle toxicity. The bilayer modified UCNPs were the most suitable candidates for PDT due to their colloidal stability in culture medium and high photosensitizer

loading efficiency as well as delivery efficiency into the cells. In terms of toxicity, 24 nm UCNPs@PLM-RB or smaller UCNPs@AP-RB should be chosen in future applications.

The ROS generation by rose bengal and the initiation of cell death was verified by a ROS sensitive assay and a cell viability assay. This has been accomplished so far in an assay, which may be suitable for high throughput screening, using 15 nm and 24 nm UCNPs@AP-RB with direct excitation and by considering the different loading and delivery efficiency of the colloidal stable particles.

These novel insights on surface characteristics in terms of particle stability, dye loading, delivery efficiency, and toxicity may improve future particle designs for photodynamic therapy and other biomedical applications. Further studies are required to extend the promising results and pave UCNPs the way into photodynamic therapy. The study enabled first insights about the intracellular fate of UCNPs and photosensitizer in terms of accumulation and potentially occurring exocytosis. The ROS assay can be performed upon 980 nm irradiation in future applications to use UCNPs not only as transporter but to shift the excitation wavelength of the photosensitizer to higher wavelengths within the biological window. These results can be used to tailor the architecture of the UCNPs (size, dopant ratio) for an increased intracellular ROS production. Moreover, the photosensitizer functionalized UCNPs can be further equipped with ligands for specific cells or tissues, enabling a very local photodynamic therapy. The functioning of the particles should be tested on different cell lines of interest with individual resilience to ROS levels.

.

8 Upconversion Nanoparticles to Study G Protein-Coupled Receptors

8.1 Preface

The content of this chapter was worked out in cooperation and discussion with PD Dr. Max Keller. Most of the experimental and theoretical work presented in this chapter was performed solely by the author. Jakob Gleixner and Lisa Schindler prepared the NT(8-13) derivatives. Lisa Schindler carried out the radioligand competition binding assay.

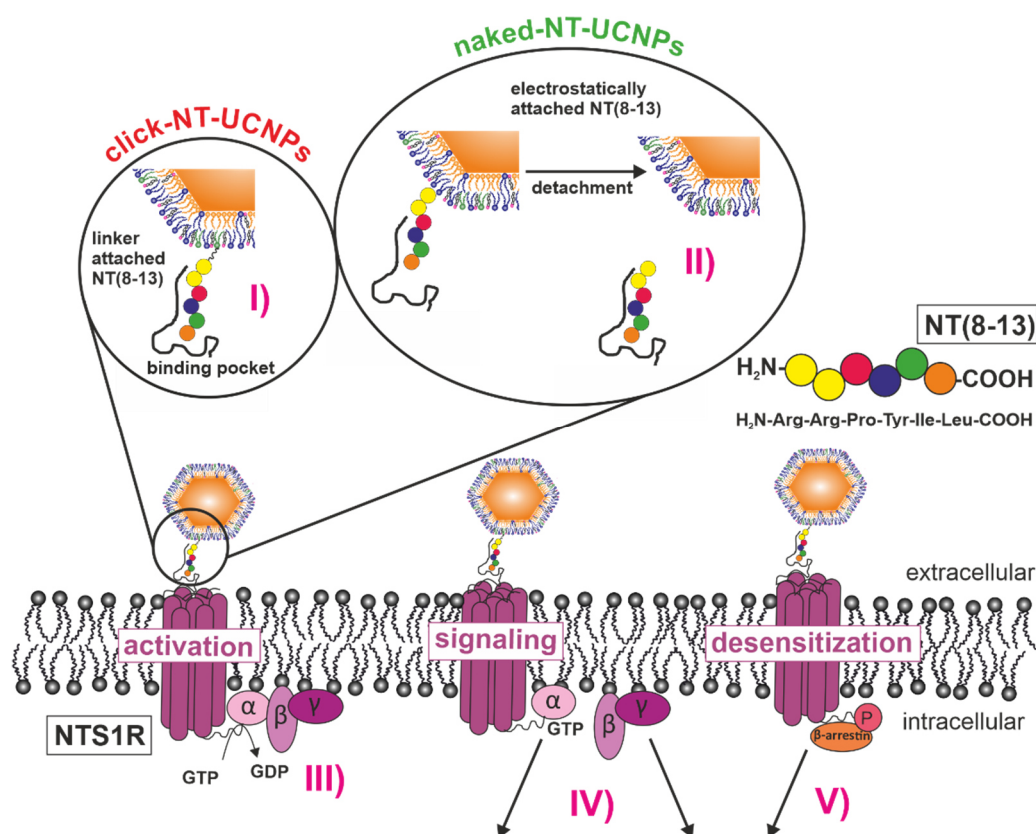
8.2 Introduction

G protein-coupled receptors (GPCRs) form the largest family of membrane proteins with around 800 members in humans and regulate many cellular functions and cell-specific responses in diverse signaling mechanisms, making them the most heavily addressed targets in therapy. To develop new drugs and identify new therapeutic pathways of unknown GPCRs, a broadening of the analysis techniques and tools is required, *e.g.* by expanding the toolbox to the field of nanomaterials. Nanomedicine can solve some of the current issues and enables the design of multifunctional probes by attaching (ant-) agonists to (luminescent) nanoparticles for 1) enhanced solubility of the drug, 2) increased bioavailability, 3) multivalence for increased receptor affinity to improve stimulation efficacy and internalization efficiency, 4) targeted drug delivery, 5) controlled drug release, 6) improved imaging by distinct photophysical characteristics, and 7) localization and tracking of the drug and its fate in elongated time frames (Patra et al., 2018; Hild et al., 2010). Choosing upconversion particles (UCNPs) as tool, expands the list of advantages for imaging and tracking by the benefits of NIR excitation, which are 8) low background fluorescence, 9) deep tissue penetration, 10) no photobleaching, and 11) reduced photodamage in comparison to probes excitable by UV/Vis irradiation (Yang, 2014).

In this project, the well-studied human neurotensin 1 receptor (hNTS₁R) with the peptidyl agonist neurotensin (NT) was chosen as model system to examine the suitability of UCNPs as luminescent probe with drug delivery features and to study GPCR-mediated internalization. The endogenous agonist neurotensin consists of thirteen amino acids with only six C-terminal amino acids required for the binding and stimulation of NTS₁R, making NT(8-13) an equi-active

agonist to neurotensin (Furuta et al., 1984). According to crystal structures of the binding pocket of the neurotensin receptor with NT(8-13), the agonist binds in an extended conformation to the receptor with the C-terminus oriented towards the electropositive receptor core and the N-terminal arginine (Arg), which is stabilized by the electronegative rim of the binding pocket (White et al., 2012). Thus, the N-terminus is the suitable docking side to anchor fluorescent labels by maintaining its affinity to the receptor and agonistic activity (Keller et al., 2016). So far, fluorophores, chemotherapeutics, and macromolecules have been attached successfully to the NT(8-13) at the N-terminal amino acids as molecular tools and for targeted drug delivery (Keller et al., 2020; Bird et al., 2017; Brunetti et al., 2015).

Here, UCNPs were modified with a phospholipid membrane (PLM) to enable its functionalization with linker-attached and electrostatically bound NT(8-13). The affinity of these particles to the receptor and their stimulation abilities were studied in absence and presence of serum proteins by radioligand binding as well as by impedance-based cell analysis. The results and theories were substantiated by upconversion microscopy. An overview of the proposed receptor activation by the particles and the reported signaling pathways, activated at hNTS₁R by NT(8-13) (detailed transcription in **Chapter 1.6.**), is depicted in **Scheme 8.1**.



Scheme 8.1. Activation of NTS₁ receptor by NT(8-13)-functionalized UCNP with proposed receptor binding behavior (I, II) to trigger well-reported signaling cascades (III – V) (Besserer-Offroy et al., 2017). Binding of NT(8-13) ((I) covalently attached to click-NT-UCNPs or II) stripped off the naked-NT-UCNPs) to NTS₁R enables the III) exchange of GDP by GTP at the Gα of the trimeric G-protein (activation). IV) Activated Gα-subunit separates from Gβγ subunit and triggers several signaling pathways. (V) After phosphorylation NTS₁R recruits β-arrestin1 and 2, triggering β-arrestin-coupled signaling pathways, the desensitization of the receptor and its recycling. These targets can activate transcription factors and downstream effectors, leading to the transcription of genes for cell survival, proliferation, cell migration and cytoskeletal dynamics. Black arrows indicate activated signaling pathways.

8.3 Particle Functionalization with an Agonist

General Considerations on Particle Design

As a label for agonists in GPCR studies, the UCNP need to fulfil several requirements: (I) The particles should be bright enough for particle tracking under physiological conditions in aqueous media *via* microscopy techniques. (II) The surface coating should provide a high colloidal stability of the particles in the desired medium so that the UCNP are available as individual particles for the cells and not as aggregates. The administration of aggregated particles may reduce stimulation efficiency as many attached agonist molecules are hidden

within the aggregate, the steric demand of the label is increased, and the receptor binding probability is reduced due to the lower number of dispersed particles. Moreover, (III) the ligand at the particle surface must provide functional groups to attach the agonist molecules covalently or electrostatically to the particle.

In this project, the photophysical requirements were met with medium sized particles in a core-shell architecture $\text{NaYF}_4(\text{Yb,Er})@\text{NaYF}_4$ to reduce the surface quenching of the upconversion luminescence by water (Wiesholler et al., 2018). The nanoparticles were coated with a phospholipid membrane (PLM), consisting of oleate, cholesterol, DOPA and DOPE, for high colloidal stability in phosphate buffer with Ca^{2+} (DPBS⁺⁺: DPBS⁻ with 0.18 mM CaCl_2 1 mg·mL⁻¹ glucose) without the need of fetal calf serum (FCS) (cf. **Chapter 4**). The ethanolamine as part of the PLM coating enables the covalent attachment of biomolecules with carboxy moieties.

The preparation and characterization of core-shell UCNPs@PLM (naked-UCNPs) are discussed in detail in **Chapter 6**. The mean diameter of the particle was determined from the transmission electron microscopy (TEM) images as (33 ± 1) nm (**Figure 8.1A**). The dynamic light scattering (DLS) measurement of the PLM modified UCNPs in water revealed a hydrodynamic diameter (d_{hydro}) of (125 ± 2) nm ($\text{Pdl} = 0.197 \pm 0.008$) (**Figure 8.2A**). Peaks at higher diameters, assigned to aggregates, were not visible. These particles have similar d_{hydro} and Pdl values in DPBS⁺⁺ and in DPBS⁺⁺ supplemented with bovine serum albumin (BSA, 0.5% (w/v)) or fetal calf serum (FCS (5% (v/v))), demonstrating their colloidal stability under measurement conditions. The peak observed at $d_{\text{hydro}} < 10$ nm, occurring in BSA containing buffer, can be assigned to the free protein (cf. DLS measurement of BSA, **Figure A 6**). The zeta potential of the particles (200 $\mu\text{g}\cdot\text{mL}^{-1}$) in H_2O (10 mM NaCl) was $-(63 \pm 3)$ mV.

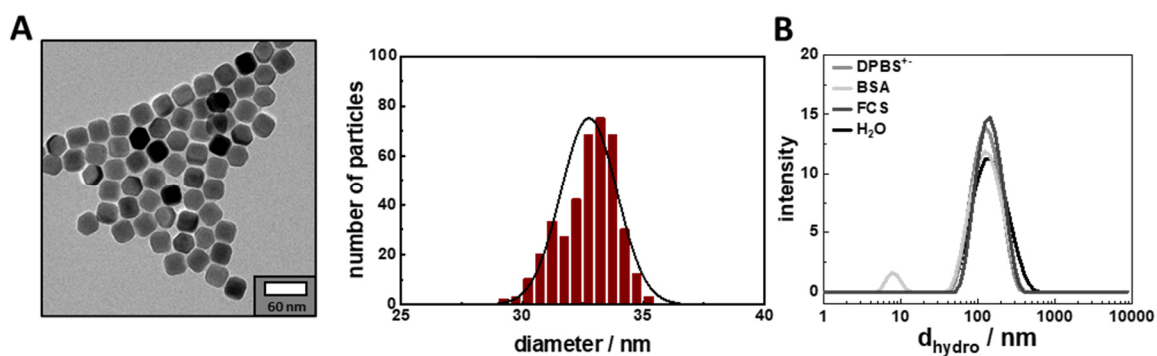
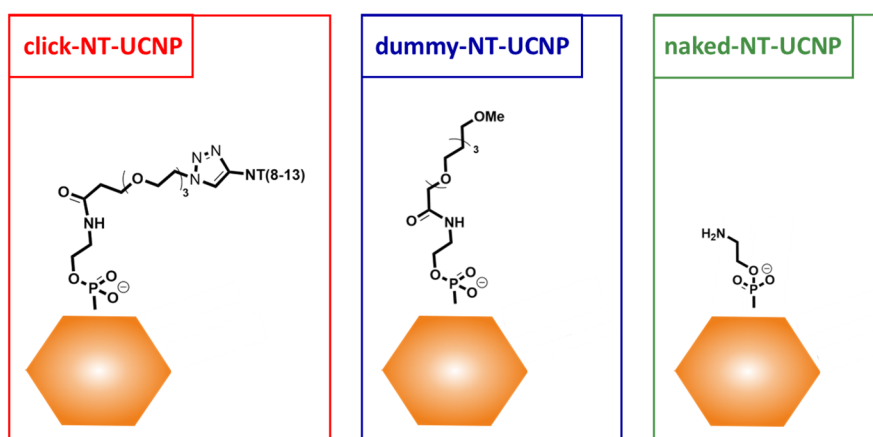


Figure 8.1. (A) TEM micrograph and corresponding particle size distribution (mean \pm SD) of unmodified particles $\text{NaYF}_4(\text{Yb,Er})@\text{NaYF}_4$ (UCNPs@OA) in cyclohexane with a mean diameter of (33 ± 1) nm ($N = 395$) and (B) Representative intensity weighted hydrodynamic diameters (d_{hydro} , mean \pm SD, $N = 3$) of UCNPs@PLM ($500 \mu\text{g mL}^{-1}$) at rt in H_2O with $d_{\text{hydro}} = (125 \pm 2)$ nm ($\text{Pdl} = 0.197 \pm 0.008$) and in DPBS^+ and DPBS^+ supplemented with BSA (0.5% (v/v)) or FCS (5% (v/v)) with similar d_{hydro} .

Both, the intensity weighted DLS with low Pdl and no aggregate peak as well as the highly negative zeta potential, indicated well-dispersed UCNPs@PLM in aqueous media and under measurement conditions, making them suitable for further particle functionalization with alkyne-NT(8-13). The UCNPs@PLM before any further functionalization or incubation are referred as naked-UCNPs.

Particle Functionalization

The naked-UCNPs were modified or incubated with alkyne-NT(8-13) to obtain click-NT-UCNPs and the control particles dummy-NT-UCNPs and naked-NT-UCNPs. A schematic overview of the particle types and their characterization by DLS are given in **Scheme 8.2** and **Figure 8.2**.



Scheme 8.2. Overview of particles with the neurotensin derivative alkyne-NT(8-13) treatment for the stimulation and binding studies at the hNTS_1R receptor: click-NT-UCNPs, dummy-NT-UCNPs and naked-NT-UCNPs.

The naked-UCNPs were further functionalized with an azido linker to enable the attachment of alkyne-NT(8-13) *via* copper-mediated click chemistry. The reactions of this two-step modification are depicted in **Scheme 3.9**. Firstly, the amine groups of the PLM coating were used to attach the azido linker using NHS coupling chemistry. After purification, the azido-linker-UCNPs were modified with the alkyne-functionalized NT(8-13) in a copper(I)-catalyzed alkyne-azido (“click”) cycloaddition according to a recently described procedure (Spinnler et al., 2020). The stability of NT(8-13)-azido-linker-UCNPs (click-NT-UCNPs) got weaker by centrifugation and precipitated irreversibly after the second centrifugation step. This was not observed for naked-UCNPs and, thus, may already be a first indication that NT(8-13) was attached successfully. Thus, the stepwise dialysis against H₂O or buffer was chosen as purification method. The stability of purified click-NT-UCNPs in H₂O and DPBS⁺ was verified by DLS (**Figure 8.2A**). Compared to naked-UCNPs the zeta potential slightly increased from $-(63 \pm 3)$ mV to $-(46 \pm 3)$ mV, revealing that the charges provided by phosphate groups were at least partly compensated.

UCNPs@PLM were modified with a dummy linker with an ether instead of an azido group to obtain control particles, making surface functionalization *via* click-chemistry not possible. Additionally, they were stirred with the NT(8-13) reaction solution according to the described protocol for click-NT-UCNPs, but the NT(8-13) was not supposed to attach to the ether linker (**Scheme 3.10**). DLS confirmed stable particles without aggregation in H₂O and in DPBS⁺ (**Figure 8.2B**). These reference particles were referred as dummy-NT-UCNPs.

A second control particle system was prepared without linker, just by analogous stirring of UCNPs@PLM in the NT(8-13) solution and purification (**Scheme 3.11**). Changes on the particle surface upon NT(8-13) treatment were identified as the zeta potential increased to -32 mV. DLS again revealed colloidal stability of the particles in H₂O and in DPBS⁺ (**Figure 8.2C**). They were referred as naked-NT-UCNPs.

A quantification of attached NT(8-13) was not possible with the available methods. Therefore, all functionalized particles were tested for binding and receptor agonism, respectively, with the radioligand competition binding assay and the ECIS assay.

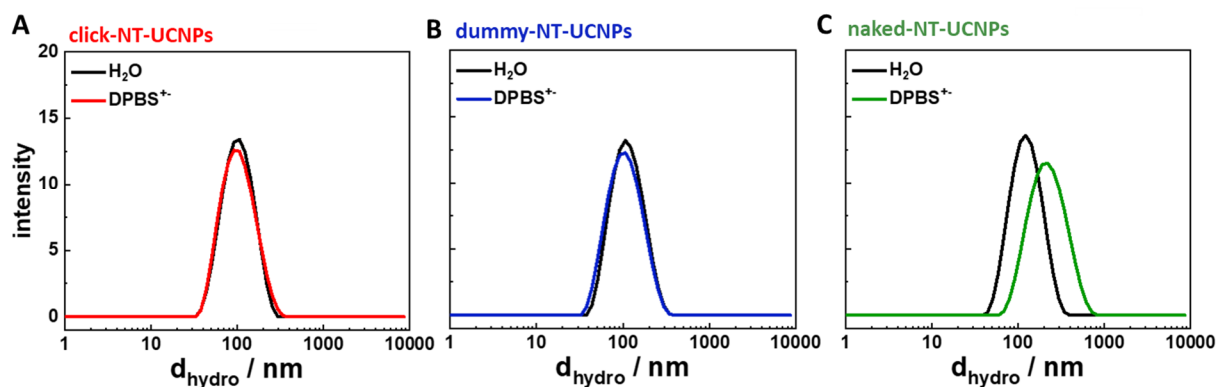


Figure 8.2. Representative intensity weighted hydrodynamic diameter (d_{hydro}) distribution of (A) click-NT-UCNPs, (B) dummy-NT-UCNPs, and (C) naked-NT-UCNPs ($500 - 1500 \mu\text{g}\cdot\text{mL}^{-1}$) at rt in H_2O with (A) $d_{\text{hydro}} = (92 \pm 2) \text{ nm}$ ($\text{Pdl} = 0.18 \pm 0.01$), (B) $d_{\text{hydro}} = (99 \pm 1) \text{ nm}$ ($\text{Pdl} = 0.157 \pm 0.009$), and (C) $d_{\text{hydro}} = (112 \pm 2) \text{ nm}$ ($\text{Pdl} = 0.187 \pm 0.008$) (mean value \pm SD, $N = 3$). D_{hydro} of the particles in experimental buffer DPBS^{+-} are similar.

8.4 Characterization of Cell Stimulation by Free Agonist

At first, the response of the model GPCR hNTS_1R was evaluated by impedance-based cell analysis when exposed to the agonist NT(8-13). The hNTS_1R expressing cells need to undergo morphology changes upon receptor-mediated activation of the specific signaling cascade, which are detectable *via* the ECIS approach. HT-29 cells, endogenously expressing $\sim 45,000$ hNTS_1R per cell, and CHO cells, stably transfected with around 300,000 hNTS_1R per cells (CHO- hNTS_1R), served as model cell lines. To be consistent with later particle experiments, the cells (I) were pretreated with BSA supplemented DPBS^{+-} (0.5% (v/v)) for 20 min (II) before stimulation was carried out with the free agonist NT(8-13) in DPBS^{+-} (DPBS^{+-} , 0.18 mM Ca^{2+} , 1 $\text{mg}\cdot\text{mL}^{-1}$ glucose). In the first feasibility check the use of BSA or FCS was avoided as a protein corona around the particles may hide the agonist and the particle may lose its agonism (Tonigold et al., 2018) and DPBS^{+-} was chosen as experimental buffer. However, as naked-UCNPs were identified to heavily bind unspecific to cells (microscopic study not shown here) and to avoid unspecific binding of the particles to the well walls, the cell surface and well walls were saturated with BSA before the stimulation experiment.

Figure 8.3A shows the time courses of the impedance change of the HT-29 cells upon stimulation with NT(8-13) at the frequency of maximum sensitivity (8 kHz). The baseline impedance magnitude before stimulation was $(5.33 \pm 0.02) \text{ k}\Omega$ ($N = 33$) and slightly decreased

for cells grown on reused arrays to $(4.94 \pm 0.02) \text{ k}\Omega$ ($N = 35$). It was in all experiments in this range. Directly after addition of the agonist, the impedance increases transiently by $\sim 1,500 \text{ }\Omega$ for the four highest concentrations (10 – 300 nM) before it decreases again to $\sim 150 \text{ }\Omega$ within 6 min. Afterwards the impedance rises slightly to $\sim 250 \text{ }\Omega$. Cells with exposure to medium concentrations (1 – 3 nM) behave similar with maxima at (500 – 1,000) Ω and final values around 150 Ω . The impedance of the cells exposed to 0.1 – 0.3 nM NT(8-13) slightly increases and approaches values similar to the time course of the control. The cells with 0.03 nM NT(8-13) addition do not differ significantly to the control DPBS⁺ with a continuous impedance decrease after addition until around -200 Ω are reached after 30 min. The transient impedance maximum within the first 2 min was plotted against the concentration and fitted by a 4P-logistic model to determine the EC₅₀ value for NT(8-13) and HT-29 cells with $(1.7 \pm 0.4) \text{ nM}$ (**Figure 8.3B**).

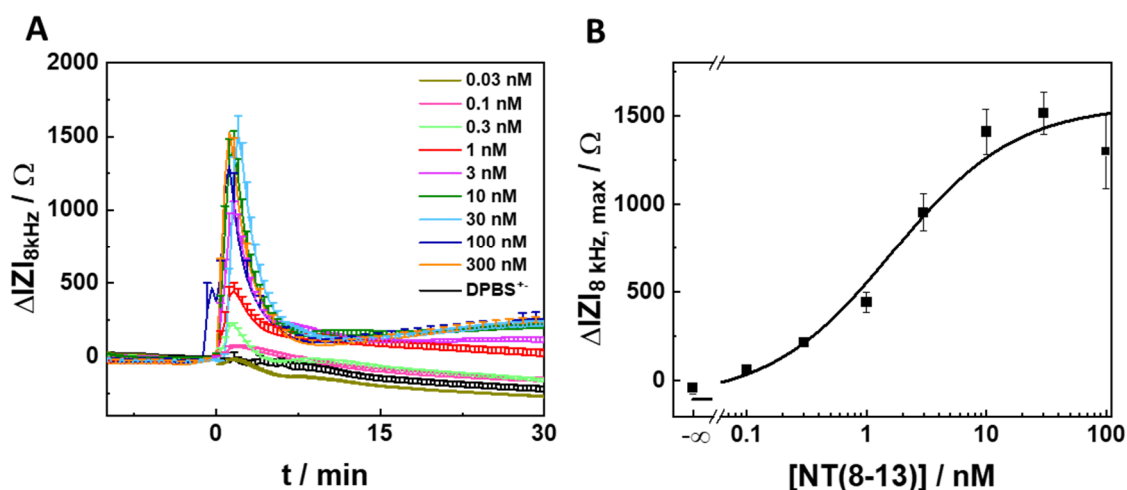


Figure 8.3. (A) Time courses of the change in impedance magnitude at 8 kHz of HT-29 cells, stimulated with NT(8-13) (0.03 – 300 nM) or control DPBS⁺ at time point 0 min at 37 °C (mean + SEM, at least eight measurements from three independent experiments). Baseline impedance magnitude of all measurements before stimulation was $(5.12 \pm 0.02) \text{ k}\Omega$ ($N = 84$). (B) The maximum impedance changes after around 2 min were plotted against the concentration and approximated with a 4-parameter logistic model to determine the potency with $(1.7 \pm 0.4) \text{ nM}$ (adj, $R^2 = 0.98$).

The time courses of the impedance change at the frequency of maximum sensitivity (12 kHz) of the CHO-hNTS_{1R} cells, exposed to NT(8-13) (0.03 – 100 nM, DPBS⁺), are shown in **Figure 8.4A**. The baseline impedance magnitude was $(3.80 \pm 0.03) \text{ k}\Omega$ ($N = 64$) with lower values for cells grown on a reused array ($3.48 \pm 0.05 \text{ k}\Omega$, $N = 32$) than for cells on new arrays

((3.80 ± 0.04) k Ω , N = 32). It was in all experiments in this range. After addition of NT(8-13) or the control (DPBS⁺), the impedance magnitude decreases to values between -300 Ω and -500 Ω . The impedance time courses recorded for the cells stimulated with the three highest concentrations (10 – 100 nM) form a dip and increase within 15 min to a maximum value of ~1,500 Ω before it decreases to values close to the baseline after 60 min. The stimulation of the cells with 3 nM of NT(8-13) results in a similar time course with a maximum at ~500 Ω . The two lower concentrations (0.3 and 1 nM) induce only a recovery of the impedance to basal values after the initial dip, while the impedance curves of the lowest NT(8-13) concentrations (0.03 and 0.1 nM) and the buffer treated cells decrease slightly after the initial drop until the end of the experiment.

The EC₅₀ value of NT(8-13)-stimulated CHO-hNTS₁R cells was calculated with the maximal impedance changes after around 15 min by approximation with a 4P-logistic model as (2.4 ± 0.9) nM.

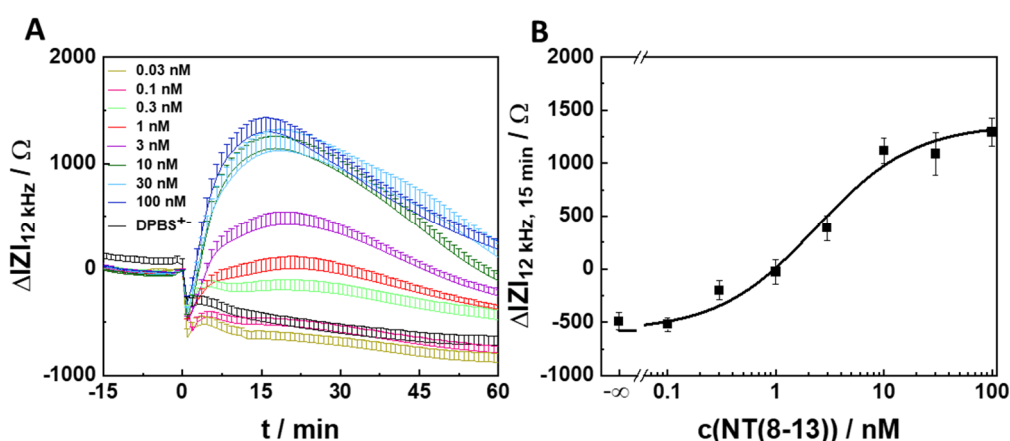


Figure 8.4. (A) Time courses of the change in impedance magnitude at 12 kHz of CHO-hNTS₁R cells, exposed to NT(8-13) or control (DPBS⁺) at time point 0 min at 37 °C (mean + SEM, at least seven measurements from three independent experiments). Baseline impedance magnitude before stimulation was (3.80 ± 0.03) k Ω (N = 88). (B) The impedance values after 15 min were plotted against the concentration to determine EC₅₀ as (2.4 ± 0.9) nM by approximation with a 4-parameter logistic model ($R^2_{\text{adj}} = 0.96$).

Both cell lines had characteristic impedance response profiles, which were well-distinguishable even though the same hNTS₁ receptor was stimulated in both cell lines. The impedance changes of HT-29 cells were visible only for ~5 min with a maximal response after 2 min. In contrast, the impedance changes of CHO-hNTS₁R cells were observable for at least

60 min with an initial dip prior to a maximal response after ~15 min and a slow decrease close to basal values. A similar impedimetric time profile of the CHO-hNTS₁R cells upon stimulation with NT(8-13) has been reported with the same characteristic dip, maximal response after ~15 min and a slow signal depletion (Besserer-Offroy et al., 2017). The transient minimum of impedance after compound addition was reported to be characteristic for GPCRs, predominantly coupling to G_q, for example on CHO-M1 cells with acetylcholine stimulation or on U-373 MG cells with histamine treatment (Scott et al., 2010; Stolwijk et al., 2019; Lieb et al., 2016). Indeed, the hNTS₁ receptor has been known to trigger the G_q-coupled pathway, amongst others (cf. **Chapter 1.7**, (Besserer-Offroy et al., 2017)) so that the dip could be assigned to this pathway, next to slight changes upon medium addition itself. HT-29 cells showed a completely different impedance time course than the CHO-hNTS₁R cells upon NT(8-13) stimulation although a similar variety of pathways is triggered in both cell lines (Qiu et al., 2017). However, the triggered pathways may be differently pronounced due to a cell-type specific biased signaling, which has been already demonstrated for U-2 cells and SK-N-MC cells upon dopamine stimulation (Peters et al., 2009).

The pEC₅₀ of NT(8-13) for HT-29 cells with 8.8 ± 0.1 was similar to the potency for CHO-hNTS₁R with 8.6 ± 0.2 . Another impedance-based analysis of CHO-hNTS₁R stimulation with NT(8-13) revealed a potency of around 7 (Besserer-Offroy et al., 2017). The variation might occur due to a different genetic origin of the CHO cells (CHO-K1 vs CHO-FRT cells) and different experimental parameters and cell conditions. These potencies determined in a wholistic cell response readout are in the same range as those obtained from assay formats, specifically targeting an individual signaling molecule. Exemplarily reported potencies are 8.92 ± 0.12 for HT-29 cells, determined in a fura-2-based Ca²⁺ assay, and 10.16 ± 0.14 for CHO-hNTS₁R cell, determined in a fluo-4-based Ca²⁺ assay (Keller et al., 2020). The free alkyne-NT(8-13), used for particle functionalization, is in the same range as NT(8-13) with a pEC₅₀ of 8.7 in HT-29 cells in a fura-2-based Ca²⁺ assay (Keller et al., 2016).

Altogether, the morphology changes of the HT-29 as well as CHO-hNTS₁R cells upon activation of hNTS₁R with the agonist NT(8-13) can be monitored *via* the ECIS assay. Thus, the receptor, the agonist and both cell lines were suitable model systems to evaluate receptor activation by agonist modified UCNPs.

8.5 Characterization of Cell Stimulation and Receptor Binding by Agonist-Functionalized Nanoparticles

The intrinsic agonism of naked-UCNPs with respect to hNTS₁R were evaluated by the ECIS assay to assess the suitability of these particles for this study. The endogenously hNTS₁R expressing HT-29 cells were exposed to the two concentrations of the naked UCNPs, being equal to the highest and a moderate concentration of UCNPs in other experiments. The particle treated cells exhibit a similar impedance time course as the particle-free control experiment with almost no impedance changes after compound addition (**Figure 8.5**). Thus, the nanoparticles with the PLM coating triggered no detectable morphology changes within these cells. Therefore, they are suitable for functionalization with an agonist.

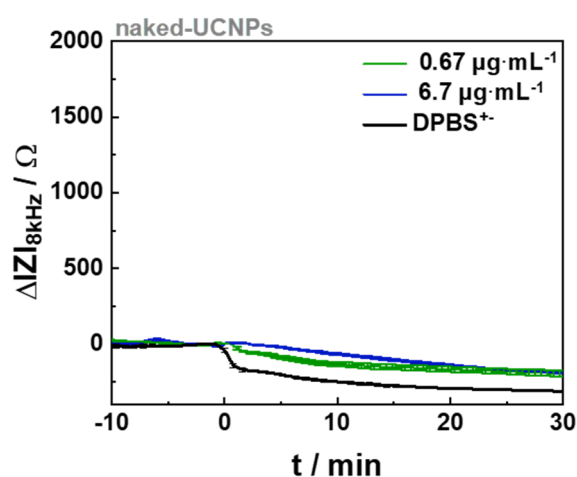


Figure 8.5. Time courses of the change in impedance magnitude at 8 kHz of HT-29 cells exposed to naked-UCNPs (0.67 and 6.7 µg·mL⁻¹, DPBS⁺) or control (DPBS⁺) at time point 0 min at 37 °C (mean ± SD, three measurements in one experiment).

The attachment of alkyne-NT(8-13) to the UCNPs and the agonistic activity of click-NT particles and the control particles (dummy-NT-UCNPs, naked-NT-UCNPs) were analyzed with HT-29 cells by the ECIS assay and partly verified *via* the radioligand competition binding assay. The impedance time courses of the HT-29 cells, stimulated with click-NT-UCNPs (**Figure 8.6A**) were similar to those of free NT(8-13) (**Figure 8.3A**). The maximum response of ~1,500 Ω is obtained for 2 µg·mL⁻¹ and 6.7 µg·mL⁻¹ of UCNPs while 0.2 µg·mL⁻¹ and 0.67 µg·mL⁻¹ of click-NT-UCNPs show only a slight increase to ~200 Ω and a small increase for the 0.67 µg·mL⁻¹ after around 7 min. The cells, exposed to the lowest UCNP concentration (0.02 µg·mL⁻¹), exhibit the same

impedance course as the DPBS⁺ control. The EC₅₀ was calculated using the concentration-dependent maximal impedance changes within the first 2 min as $(1.2 \pm 0.4) \mu\text{g}\cdot\text{mL}^{-1}$ (Figure 8.6).

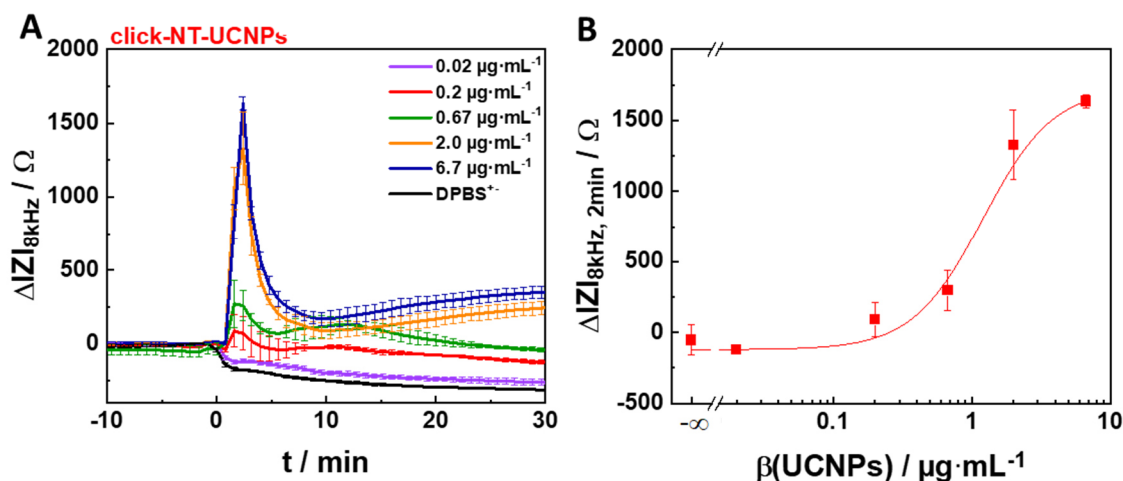


Figure 8.6. (A) Time courses of the change in impedance magnitude at 8 kHz of HT-29 cells exposed to click-NT-UCNPs (diluted in DPBS⁺) or control DPBS⁺ at time point 0 min at 37 °C (mean \pm SD, three measurements in one experiment). (B) Concentration response curve of the maximal impedance magnitude after 2 min to determine the EC₅₀ as $(1.2 \pm 0.4) \mu\text{g}\cdot\text{mL}^{-1}$ with a 4-parameter logistic model ($R^2_{\text{adj}} = 1.00$).

The similarity of the impedimetric response profile of the NT(8-13) and the click-NT-UCNPs treated HT-29 cells, including maximal impedance values and time profile, confirmed the agonistic activity of the click-NT-UCNPs. It indicates the successful attachment of alkyne-NT(8-13) to the azido-linker-UCNPs *via* click chemistry. A comparison of the potencies ((1.7 ± 0.4) nM for NT(8-13) and $(1.2 \pm 0.4) \mu\text{g}\cdot\text{mL}^{-1}$ for the click-NT-UCNPs) was difficult as the amount of NT(8-13) and lipids per particle could not be quantified. However, based on the applied lipid ratios for the UCNPs@PLM synthesis, the amount of attached agonist can be estimated roughly. In a particle dispersion with $1.2 \mu\text{g}\cdot\text{mL}^{-1}$ UCNPs@PLM ($3.5 \cdot 10^{10}$ UCNPs $\cdot\text{mL}^{-1}$), the lipid DOPE available for binding reactions on the particle surface should be in the range of (28 – 36) nM (cf. **Chapter 4** for details of UCNPs@PLM design with (7 – 10)% DOPE on the particle surface). Assuming a saturation of all ethanolamine groups with azido-linker and alkyne-NT(8-13), (28 – 36) nM of NT(8-13) should be available in the click-NT-UCNPs dispersion ($1.2 \mu\text{g}\cdot\text{mL}^{-1}$), which would result in a number of 660 NT(8-13) ligands per particle. However, only one of the eight particle sides (hexagonal prism, cf. **Figure 8.1**) might be

available for cellular interactions so that receptor binding and the number of NT(8-13), available for stimulation, is supposed to be reduced to ~80 NT(8-13) ligands per particle (~4 nM NT(8-13) in particle dispersion). As not all attached NT(8-13) might reach a hNTS₁R for stimulation, the number of agonist being capable of stimulating a receptor might be even lower. In contrast, many particle-attached NT(8-13) ligands might simultaneously come in close proximity to the cell surface, leading to multivalent ligand-receptor interactions for an improved potency (Hild et al., 2010). Particle-bound agonists might have a lower receptor affinity as shown for Qdots@EXP3174 in contact to NCI-H295R cells but due to multivalency, the potencies of free and nanoparticle-bound agonist could be in a similar range (Weissleder et al., 2005). It was rather difficult to quantify all the contradictory effects and estimate the number of stimulating agonists at all. Altogether, these effects might balance out and the potency of NT(8-13), which might be attached on the DOPE of click-NT-UCNPs and reach the receptors, could be in a similar range as free NT(8-13). By rough calculation, the potency of the dispersion of click-NT-UCNPs with $(1.2 \pm 0.4) \mu\text{g}\cdot\text{mL}^{-1}$ may be attributed to a potency of 4 nM NT(8-13) in a solution of free ligand. In contrast, the potency of free NT(8-13) was determined as $(1.7 \pm 0.4) \text{ nM}$.

To confirm that the stimulation of HT-29 cells was achieved by the conjugated alkyne-NT(8-13) and not by the alkyne linker or click reaction solution, different particles and solutions were tested with respect to their agonistic ability. The control particles dummy-NT-UCNPs with a dummy linker without ability to click alkyne-NT(8-13) were added to the HT-29 cells in high concentrations ($1 - 100 \mu\text{g}\cdot\text{mL}^{-1}$) and the impedance changes were monitored (**Figure 8.7A**). All tested concentrations trigger the characteristic pattern of NT(8-13) stimulated HT-29 cells. As dummy-NT-UCNPs evoked the full response of HT-29 cells, alkyne-NT(8-13) had to be available in the particle dispersion, which was added to the cells. A possible reason for this might be either an incomplete purification or the attachment of alkyne-NT(8-13) to the particles, independently of which linker was bound to the PLM@UCNPs.

The hypothesis of stimulation by residual unbound alkyne-NT(8-13) in the particle suspension due to an insufficient purification by dialysis was examined with a dialyzed click reaction solution without UCNPs. HT-29 cells were stimulated with the remaining dialysis tube solution of the click reaction without particles (dialyzed against water) and their response tracked by

the ECIS assay (**Figure 8.7B**). Except a minimal impedance increase directly after compound addition, the time courses are similar to the one of the controls. Thus, the dialysis against water seemed to be sufficient to remove unbound alkyne-NT(8-13) from the bulk phase. Therefore, it could be concluded that no NT(8-13) was present in the solution anymore and, hence, the reason for the stimulation of click-NT-UCNPs and dummy-UCNPs had to be something else.

The unspecific attachment of alkyne-NT(8-13) was tested with the naked-UCNPs without any linker, which were incubated with the click reaction solution and purified analogously by dialysis (naked-NT-UCNPs). The surface zeta potential of these particles was changed upon incubation with alkyne-NT(8-13) from -68 mV to -32 mV, indicating changes on the particle surface. Their agonistic activity was monitored by the ECIS assay (**Figure 8.7C**). The two highest concentrations ($2 \mu\text{g}\cdot\text{mL}^{-1}$ and $6.7 \mu\text{g}\cdot\text{mL}^{-1}$) trigger full response of the HT-29 cells with an impedance peak of $\sim 1,500 \Omega$. After 5 – 10 min, a short dip to $\sim 200 \Omega$ is visible before final values of around $(300 - 400) \Omega$ are obtained. A peak with $250 - 500 \Omega$ is induced by medium concentrations ($0.2 \mu\text{g}\cdot\text{mL}^{-1}$ and $0.67 \mu\text{g}\cdot\text{mL}^{-1}$) with a subsequent smaller maximum for $0.67 \mu\cdot\text{mL}^{-1}$ and final values around 200Ω . The impedance time course of the lowest concentrations ($0.02 \mu\text{g}\cdot\text{mL}^{-1}$) is similar to the control, keeping baseline values for the whole experiment time.

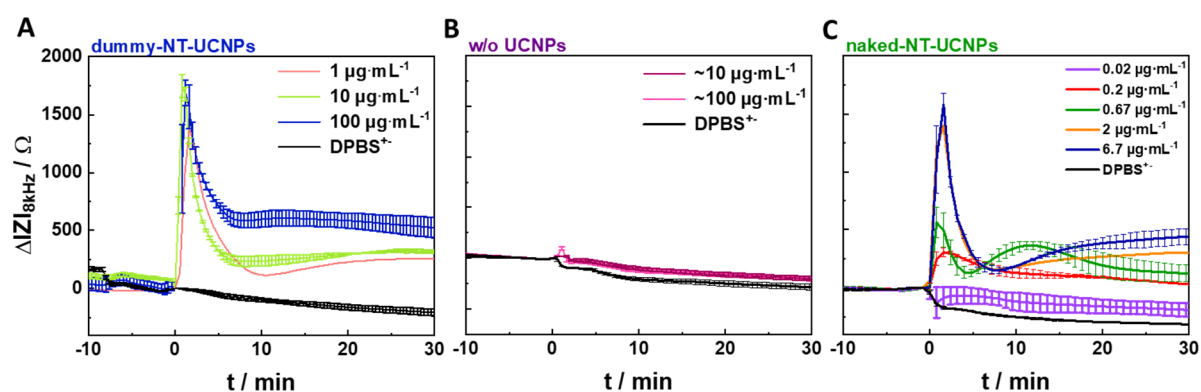


Figure 8.7. Time courses of the change in impedance magnitude at 8 kHz for HT-29 cells, stimulated with (A) dummy-NT-UCNPs (DPBS⁺), (B) particle-free click reaction solution (concentrations similar to particle dilutions), (C) naked-NT-UCNPs (DPBS⁺) or control DPBS⁺ at time point 0 min at 37 °C (mean \pm SD, three measurements in one experiment). All y-axes have the same scale.

The HT-29 cells show the characteristic impedance time course of hNTS₁R activation upon addition of naked-NT-UCNPs. Thus, alkyne-NT(8-13), bound to the naked-UCNPs, did not detach during dialysis against water, and was able to activate NTS₁R. For a better comparison of the agonistic activity of the particles, the maximum impedance changes of the stimulated HT-29 cells were plotted in relation to the concentration (**Figure 8.8 A**). All alkyne-NT(8-13) treated UCNPs evoke similar changes of impedance magnitude in a concentration dependent manner. Untreated naked-UCNPs did not stimulate at all, confirming that the stimulation occurred by alkyne-NT(8-13). Independent of an attached azido linker, alkyne-NT(8-13) seemed to be bound to the click-NT-UCNPs, dummy-NT-UCNPs as well as to the naked-NT-UCNPs and induced the same morphology changes as free NT(8-13) in all cases.

Competition binding studies at the hNTS₁R expressing HT-29 cells with a radiolabeled NT(8-13) derivative were performed to verify the results of the impedance-based stimulation cell analysis with receptor binding affinities of the UCNPs. The displacement of the tritiated NT(8-13) derivative [³H]27 by the UCNPs (click-NT, dummy-NT, naked, naked-NT) in different concentrations was determined from the specific binding of the radioligand (**Figure 8.8B**). The naked-UCNPs displace the [³H]27 for the lower concentrations ($\leq 0.2 \mu\text{g}\cdot\text{mL}^{-1}$) by 20% but not for the highest concentrations ($2 - 20 \mu\text{g}\cdot\text{mL}^{-1}$). Alkyne-NT(8-13) treated UCNPs are able to displace the tritiated NT(8-13) derivative when applied in high concentrations ($2 - 20 \mu\text{g}\cdot\text{mL}^{-1}$). With $0.02 \mu\text{g}\cdot\text{mL}^{-1}$ the naked-NT-UCNPs displace ~75% of the radioligand. Click-NT-UCNPs and dummy-NT-UCNPs have a lower displacement rate of ~40%. UCNPs in concentrations $<0.02 \mu\text{g}\cdot\text{mL}^{-1}$ do not displace [³H] anymore.

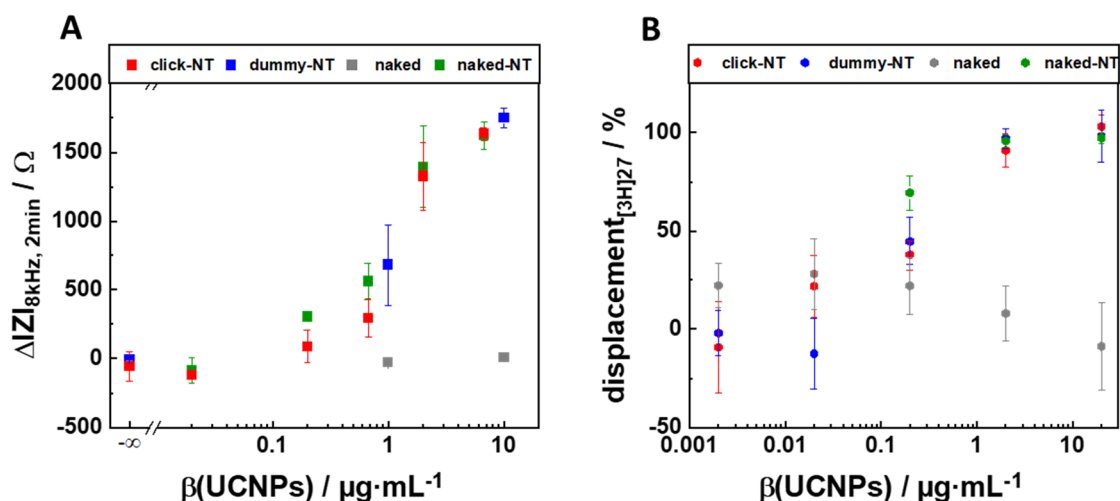
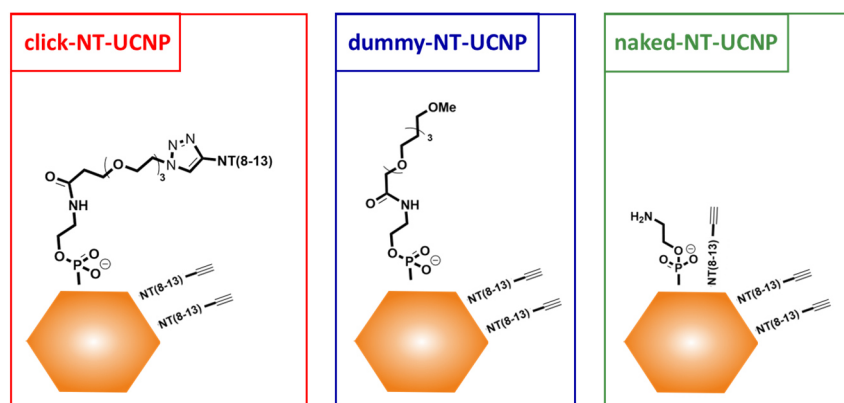


Figure 8.8. (A) Maximal impedance changes of HT-29 cells 2 min after stimulation with click-NT-UCNPs, dummy-NT-UCNPs, naked-UCNPs, and naked-NT-UCNPs in DPBS⁺⁺ at 37 °C (mean \pm SD, three measurements in one experiment). (B) Radioligand binding assay for displacement of tritiated NT(8-13) derivative $[^3\text{H}]27$ (1 nM) from hNTS₁R (HT-29) cells by click-NT-UCNPs, dummy-NT-UCNPs, naked-UCNPs, and naked-NT-UCNPs in DPBS⁺⁺ at 37 °C (mean \pm SD, three measurements in one experiment).

As the tritiated NT(8-13) derivative was displaced by all UCNPs with NT(8-13) treatment but not by naked-UCNPs, the alkyne-NT(8-13) non-covalently attached to the particles seemed to have a high affinity to the hNTS₁ receptor. Within the errors, click-NT-UCNPs and dummy-UCNPs had almost the same receptor binding affinity. The naked-NT-UCNPs might have a slightly higher one, which should be verified by repetitions of the experiment to reduce the error. However, independently of the errors, these results agreed with the impedance-based stimulation assay and showed that alkyne-NT(8-13) was available to bind to the NTS₁R in all particle dispersions. The hypothesis of residual agonist due to insufficient dialysis was rejected as alkyne-NT(8-13) could be separated by dialysis without the presence of UCNPs (**Figure 8.7B**). Therefore, the conclusion was that the NT(8-13) attached non-covalently to the particles.

NT(8-13) consists of hydrophobic (Ile, Leu, Pro) and uncharged (Tyr) amino acids at the C-terminus and two neighbored positively charged arginine amino acids at the N-terminus, which can undergo electrostatic interactions. The surface of PLM@UCNPs consists of DOPE (~10%) and mainly of DOPA (~90%) with around 90% free phosphate groups, resulting in highly negative charged particles with a zeta potential of $-(63 \pm 3)$ mV ($200 \mu\text{g}\cdot\text{mL}^{-1}$, 10 mM NaCl). Therefore, electrostatic attraction between negative charged UCNPs and the amine

groups may occur, resulting in NT(8-13) bound to linker-free particles. In addition to the electrostatic interactions, the phosphatic acid (PA) is known to form hydrogen bonds to arginine, which are further intensified by neighboring phosphatidyl ethanolamine (PE), a component of the PLM coating (Kooijman et al., 2005). Ethanolamine favors the dissociation of the second PA proton by their competing hydrogen bonds so that arginine and PA undergo interactions of “covalent-like” stability with hydrogen bond lengths with 2.9 Å (Kooijman et al., 2007; Woods et al., 2005), potentially strengthening the attachment of NT(8-13) to the particles. These findings agree with the observations that alkyne-NT(8-13) seemed to attach to the highly negatively charged particles with and without the presence of a linker and did not detach easily during dialysis against H₂O. An updated overview of the expected particle functionalization is given in **Scheme 8.3**. A comparison of the amount of stimulating particle-bound NT(8-13) with the potency of free NT(8-13) is not possible and useful anymore as more unknown parameters on the nature of particle-bound agonist occurred.



Scheme 8.3. Updated overview of particles with the neurotensin derivative alkyne-NT(8-13) treatment for the stimulation and binding studies at the hNTS₁R receptor: click-NT-UCNPs (covalently and electrostatically bound alkyne-NT(8-13)), dummy-NT-UCNPs (electrostatically bound alkyne-NT(8-13)) and naked-NT-UCNPs (electrostatically bound alkyne-NT(8-13)).

Nevertheless, it might be possible that NT(8-13) detached during storage or in the high ionic buffer solution during the experiment and freely available agonist activates the receptor instead of bound agonist. Thus, it was required to prevent the non-covalent attachment of the peptide to the particles.

8.6 Particle Functionalization for Reduced Non-Specific Binding

Several strategies were tested with click-NT-UCNPs and naked-NT-UCNPs to reduce unspecific binding of NT(8-13) to the UCNPs@PLM. They were characterized by DLS and zeta potential measurements and evaluated by the competition binding assay with [^3H]27 at HT-29 cells.

At first, the sample was dialyzed in phosphate buffer to purify the particles by reducing the electrostatic interactions between phosphoric acid and arginine by surrounding phosphates in the bulk phase. DLS confirmed the colloidal stability in H_2O and in DPBS^{++} (data not shown) after the modified particle purification method. Compared to the initial conditions, a reduction of 25% displacement of the radioligand at HT-29 is obtained by the naked-NT-UCNPs in moderate concentrations (**Figure 8.9B**), while this effect cannot be seen for click-NT-UCNPs. The data of concentrations $>0.2 \mu\text{g}\cdot\text{mL}^{-1}$ show no differences to untreated click-NT-UCNPs and only the value of $0.2 \mu\text{g}\cdot\text{mL}^{-1}$ reveals a slight increase in the displacement of 30% (**Figure 8.9A**).

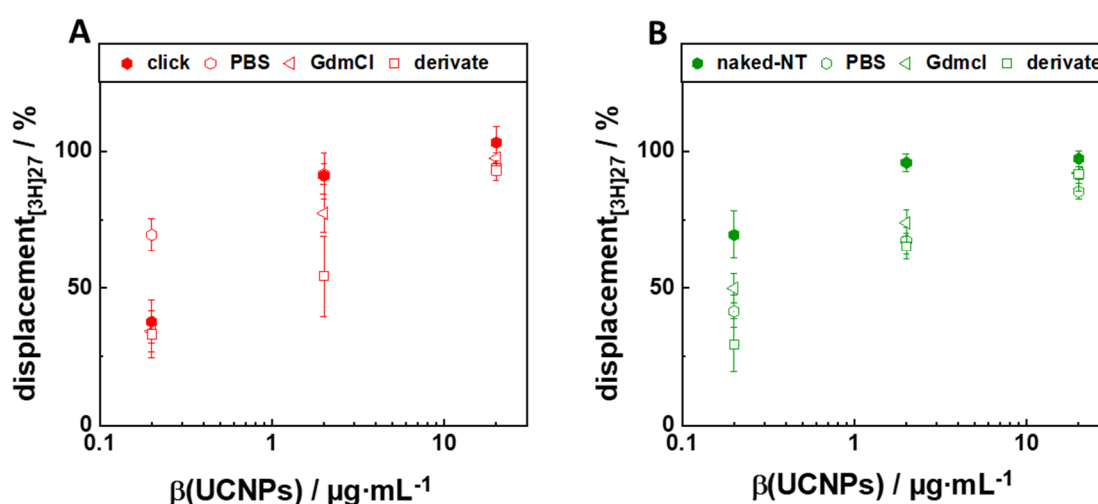


Figure 8.9. Displacement of [^3H]27 (1 nM) from hNTS₁R (HT-29 cells) by (A) click-NT-UCNPs or (B) naked-NT-UCNPs ($0.02 - 20 \mu\text{g}\cdot\text{mL}^{-1}$, DPBS^{++}), prepared under initial conditions (dialysis in H_2O) or with replacement and saturation strategies: dialysis in PBS, pretreatment with guanidinium chloride (GdmCl, 3 mM) or less-affine derivative N(Me)-Leu-NT-(8-13) (200 μM) (mean \pm SD, three measurements in one experiment).

The positively charged guanidino group of the two arginine amino acids seemed to be the most suitable group in NT(8-13) to interact with the negatively charged UCNPs@PLM. Therefore, the particle surface was saturated with guanidinium chloride in excess (3 mM) prior to the click reaction with alkyne-NT(8-13) (300 μM). Particles were stable in H_2O and DPBS^{++} as the corresponding DLS measurements revealed (data not shown here). The displacement

of the radioligand at HT-29 cells was not reduced by the pre-saturated particles (**Figure 8.9A,B**).

As another saturation strategy, particles were incubated with the less stimulating derivative N(Me)-Leu-NT(8-13) (200 μ M) (no attachment *via* click chemistry possible) prior to alkyne-NT(8-13) treatment (100 μ M). Incubation with higher peptide concentrations was not possible as particles started to precipitate. The N(Me)-Leu-NT(8-13) derivative has also two neighboring arginine amino acids for PA interactions but a N-methylated leucine for a reduced binding affinity to NTS₁R (receptor affinity reduced by factor 500). The stability of the prepared particles in H₂O and DPBS⁺ was verified by DLS (data not shown). HT-29 cells were exposed to these particles and the displacement of the radioligand was monitored. In this case, a small decrease of (10 – 40)% was achieved in the displacement ability of radioligand by naked-NT-UCNPs or click-NT-UCNPs (**Figure 8.9A,B**).

Altogether, the binding affinities of the pretreated UCNPs did not change enormously, for the described strategies. Nevertheless, a small improvement was obtained by partly saturation with the less stimulating derivative N(Me)-Leu-NT(8-13) and by dialysis in PBS. Thus, both strategies were combined and the final alkyne-NT(8-13) treated particles were prepared with partly saturation with derivative N(Me)-Leu-NT(8-13) (no attachment *via* click chemistry possible) and purification in phosphate buffer. They are used from now on in this project and are referred as UCNPs (der,PBS). Their zeta potentials were lower than that of the naked-UCNPs ($\zeta_{\text{naked}} = (-68 \pm 2) \text{ mV}$, $\zeta_{\text{naked-NT(der,PBS)}} = (-28 \pm 3) \text{ mV}$ and $\zeta_{\text{click(der,PBS)}} = (-44 \pm 1) \text{ mV}$), confirming that the particle surface changed during the preparation. The colloidal stability of these particles (der, PBS) as well as the naked-UCNPs in water, DPBS⁺, 0.5% BSA and 5% FCS in DPBS⁺ was verified *via* DLS (**Figure 8.10A,B**). A small peak < 10 nm is visible for the particle samples in BSA and FCS, assigned to unbound proteins (DLS measurement of free BSA, FCS in **Figure A 6**).

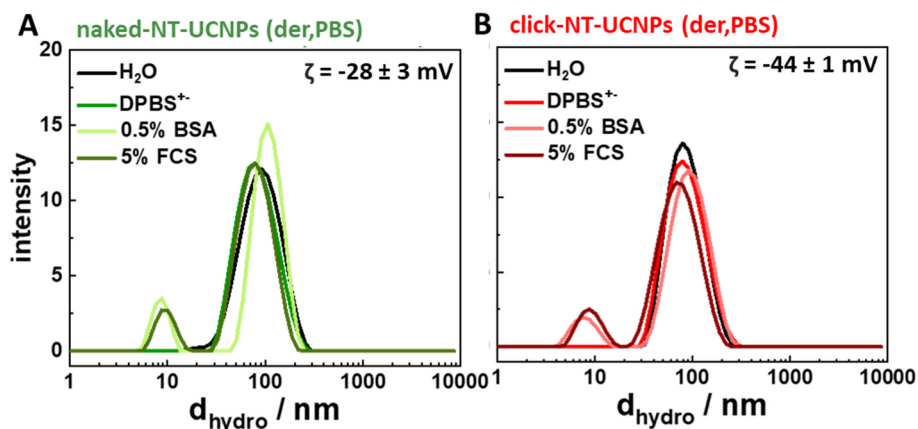


Figure 8.10. Hydrodynamic diameters (d_{hydro} , mean \pm SD, $N = 3$) of (A) naked-NT-UCNPs (der,PBS), and (B) click-NT-UCNPs (der,PBS) were determined in H_2O ($500 - 1500 \mu\text{g}\cdot\text{mL}^{-1}$), experimental buffer DPBS^{++} or DPBS^{++} supplemented with BSA (0.5%, w/v) or FCS (5%, v/v)-equipped DPBS^{++} ($50 \mu\text{g}\cdot\text{mL}^{-1}$) by dynamic light scattering measurements. d_{hydro} in H_2O are (A) $(83 \pm 3) \text{ nm}$ ($\text{Pdl} = 0.179 \pm 0.006$) and (B) $(77 \pm 2) \text{ nm}$ ($\text{Pdl} = 0.15 \pm 0.02$) and of similar value in the buffers. Zeta potentials (ζ , mean \pm SD, $N = 3$) of the particles ($50 \mu\text{g}\cdot\text{mL}^{-1}$) were determined in saline (10 mM NaCl in H_2O) at $\sim 1.2 \text{ mS}\cdot\text{cm}^{-1}$.

The agonistic properties of the particles prepared according to the modified synthesis protocol were verified with HT-29 cells by impedance-based cell analysis. The maximal impedance values after 2 min were plotted in a concentration-dependent manner (**Figure 8.11**). In comparison, the click-NT-UCNPs and the naked-NT-UCNPs, both prepared using the saturation protocol, were less potent than the particles of the first generation at the same concentrations. At the highest concentration ($6.7 \mu\text{g}\cdot\text{mL}^{-1}$), the naked-NT-UCNPs (der, PBS) still triggered the full response while click-NT-UCNPs (der, PBS) did not. Thus, potencies could not be determined exactly but were estimated by a 4-parametric logistic model with the top asymptote set to $1,500 \Omega$. The potency of click-NT-UCNPs changed from $\sim 1.2 \mu\text{g}\cdot\text{mL}^{-1}$ to $\sim 6 \mu\text{g}\cdot\text{mL}^{-1}$ for click-NT-UCNPs (der,PBS). The EC_{50} of naked-NT-UCNPs from $\sim 1.1 \mu\text{g}\cdot\text{mL}^{-1}$ to $\sim 1.6 \mu\text{g}\cdot\text{mL}^{-1}$ for naked-NT-UCNPs(der-PBS).

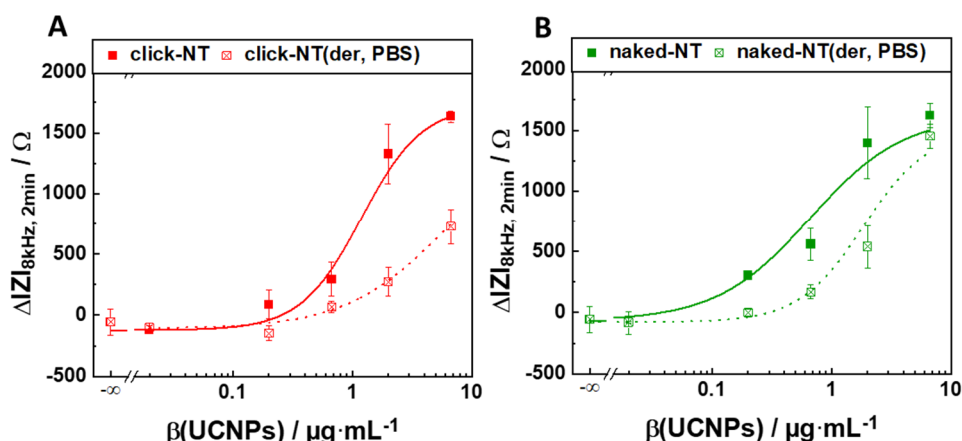


Figure 8.11. Maximal impedance changes after 2 min recorded for HT-29 cells, stimulated with (A) click-NT-UCNPs and (B) naked-NT-UCNPs (DPBS^{+-}) at 37°C , prepared under initial conditions (dialysis against H_2O) or improved conditions (partly covered with a less-affine NT(8-13) derivative ($200 \mu\text{M}$) and dialysis against PBS) (mean \pm SD, three measurements in one experiment). Potencies were determined or estimated (assuming an upper asymptote of $1,500 \Omega$, dashed line) as (A) $(1.2 \pm 0.4) \text{ nM}$ for click-NT-UCNPs (adjusted $R^2 = 0.996$), $(6 \pm 2) \text{ nM}$ for click-NT-UCNPs(der,PBS) (adjusted $R^2 = 0.91$), (B) $(1.1 \pm 0.3) \text{ nM}$ for naked-NT-UCNPs (adjusted $R^2 = 0.96$), and $(1.9 \pm 0.42) \text{ nM}$ for naked-NT-UCNPs(der,PBS) (adjusted $R^2 = 0.97$).

These results indicate a reduction of non-covalently attached alkyne-NT(8-13) on the surface of both particles with the improved procedure. With and without improved procedure, the naked-NT-UCNPs with only electrostatically bound peptide showed a better agonism than the click-NT-UCNPs with electrostatically bound and covalently attached peptide. This seemed counterintuitive, especially when one keeps in mind that NT(8-13) needs to penetrate fully into the NTS_1 receptor binding pocket for a successful receptor activation (Figure 8.12, (Hübner et al., 2016; White et al., 2012)). The alkyne-NT(8-13) without attached linker had a high steric hindrance due to the large particle in close contact and it was unlikely that the bound peptide could enter completely the binding pocket for stimulation in this environment. Therefore, it was hypothesized that attached alkyne-NT(8-13) without linker had still a high affinity to the NTS_1 receptor and started to penetrate with the C-terminus into the binding pocket. The established interactions of the receptor with the amino acids on the C-terminus were already strong enough to capture the peptide and pull it off the particle, even though it was attached to the particles by hydrogen bonding and electrostatics. As naked-NT-UCNPs were more agonistic than click-NT-UCNPs, it is straightforward to assume that the

electrostatically attached and upon receptor binding stripped off NT(8-13) had a higher agonistic activity as the linker-attached NT(8-13).

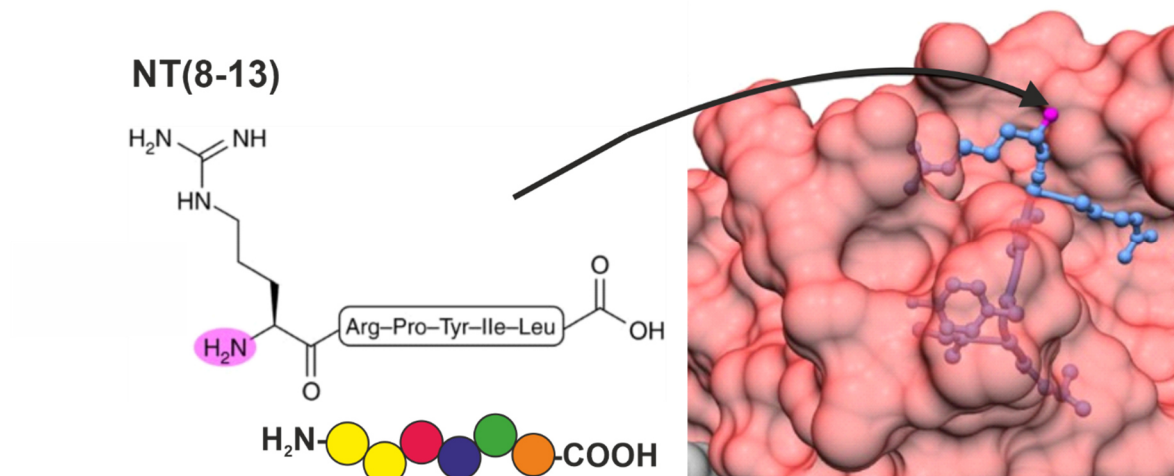


Figure 8.12. The binding pocket of the NTS₁ receptor with the agonist NT(8-13), revealed by crystal structure analysis (adapted from (Hübner et al., 2016)).

To confirm the hypothesis, microscopic studies of the HT-29 cells, exposed to click-NT-UCNPs (der,PBS) and naked-NT-UCNPs (der,PBS), were performed. NT-conjugated macromolecules were known to be internalized upon NTS₁R stimulation, as shown for NTS₁R transfected HEK293 cells (Bird et al., 2017). Thus, there might be a difference in internalization for linker-attached peptide at click-NT-UCNPs and for electrostatically attached peptide at naked-NT-UCNPs. The click-NT-UCNPs might show receptor-induced internalization, while the naked-NT-UCNPs might not be internalized if they were separated from the ligands upon NTS₁R binding. Wide-field upconversion microscopy images of HT-29 cells, incubated with naked-UCNPs, click-NT-UCNPs (der, PBS) or naked-NT-UCNPs (der, PBS) for 40 min, were recorded as 3D-stack to identify internalized and membrane-/receptor-attached UCNPs. The cell bodies were visualized by the dye DiR, which intercalates into the exo- and endo-membrane but does not enter the nucleus. Thus, the cell bodies (red) and the nucleus (black) could be visualized upon 633 nm excitation so that the planes of interest (within and above the cells) could be identified easily. In **Figure 8.13** the fluorescence images upon 980 nm excitation of HT-29 cells being exposed to the three particle systems are shown. In general, the upconversion spots are in focus above the cells but they shine through the planes below so that blurry upconversion can be detected within the cells. The images of the click-NT-UCNPs treated cells show distinguishable upconversion spots on the apical side, belonging to individual UCNPs or small

agglomerates. Naked-NT-UCNPs are hardly found at the cell surface. The highest upconversion intensity is detected for the naked-UCNPs, adhering in large amounts to the cells even if they had been pre-treated with BSA to reduce non-specific binding. The partly agglomerated or individual naked-UCNPs were in proximity so that their bright luminescence shined through all z planes. Thus, naked-UCNPs are not found within the cells but attached in different amounts on the cells. The HT-29 cells seem to form strong cell-cell contacts so that UCNPs could not enter the intercellular gap as they are not found between the cells. Control images of HT-29 cells without particle incubation, showing only DiR stained cells but no particle luminescence, are not depicted here.

As internalized UCNPs cannot be identified for all three cases, additional micrographs of HT-29 cells were taken after 3 h of incubation time with the particles. However, the same trend was visible: no internalization of any particle but attachment to the plasma membrane in large amounts. The upconversion intensity was so high that the detector was saturated, no images suitable for comparison could be taken and, hence, are not shown here.

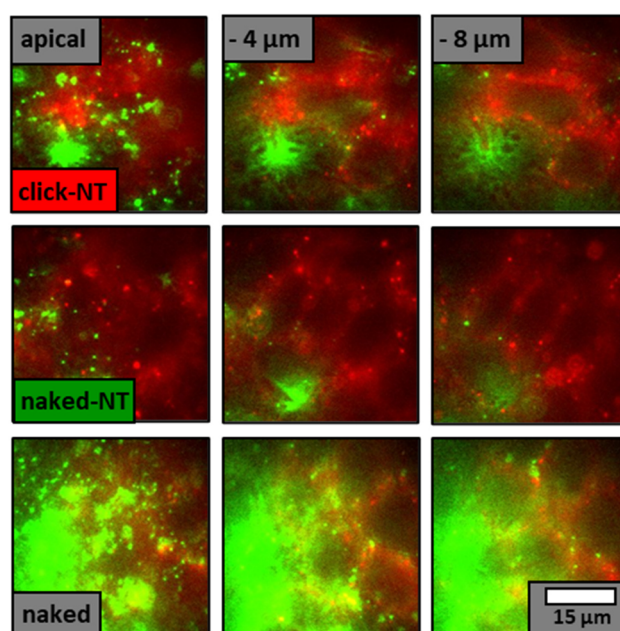


Figure 8.13. Representative wide-field upconversion micrographs of HT-29 cells (apical, -4 μm , -8 μm), incubated with click-NT-UCNPs (der, PBS), naked-NT-UCNPs (der, PBS) or naked-UCNPs ($6.7 \mu\text{g}\cdot\text{mL}^{-1}$, DPBS⁺) at 37 °C for 40 min and co-stained with DiR (at least 25 images from 3 independent experiments). The images show the upconversion intensity (green) upon 980 nm excitation (cw, $8 \text{ kW}\cdot\text{cm}^{-1}$) and the DiR emission (red) upon 633 nm excitation. Upconversion intensity was adjusted to visualize small single spots.

The HT-29 cells did not seem to internalize any of the three particle types upon NTS₁R stimulation at all and, hence, it was not possible to make a receptor-mediated internalization study. Moreover, it was not possible to correlate the binding or activation characteristics of the particles with their different internalization behavior. Nevertheless, less naked-NT UCNPs with higher agonistic activity were found to be attached on the plasma membrane than click-NT-UCNPs with lower agonistic activity. This may indicate that NT(8-13) could penetrate deeply in the binding pocket for stimulation and the UCNPs with residual NT(8-13), which was not involved in receptor-binding, separated and diffused away. Afterwards the particles may be available for further receptor binding and stimulation. Different to that, it may be possible that linker-attached NT(8-13) of click-NT-UCNPs with less sterical hindrance could penetrate deeply in the binding pocket without particle cleave-off and escape so that they were found in higher amounts on the cell surface. Despite the BSA preincubation, the naked-UCNPs strongly attached to the cell surface without receptor affinity or activation properties towards the hNTS₁ receptor. Similar to Arg-DOPA, the strong binding to the cells might be due to the high electrostatic attraction of amine groups of lipid headgroups, proteins, or sugars on the cell surface and the freely available phosphate groups on the particle surface without sterically hindrance by headgroups.

8.7 Characterization of Cell Stimulation by Agonist-Functionalized Nanoparticles with a Second Cell Model

The hypothesis that non-covalently attached alkyne-NT(8-13) was removed from the UCNPs upon receptor binding was further validated by examining the receptor binding and activation properties of the particles on another NTS₁R expressing cell line. A CHO cell line, stably transfected with the hNTS₁R (CHO-hNTS₁R) and providing a seven times higher receptor density on the cell surface than the native HT29 cell line, was chosen to verify the stimulation and binding characteristics of the particles with the protocols, applied to the HT-29 cells.

At first the agonistic activity of naked UCNPs@PLM itself without functionalization was verified by the impedance-based analysis (**Figure 8.14A**). Upon compound addition the impedance of CHO-hNTS₁R drops to around -500 Ω for all tested concentrations and stays around this value for at least 60 min, similar to the control sample with DPBS⁺⁻ addition.

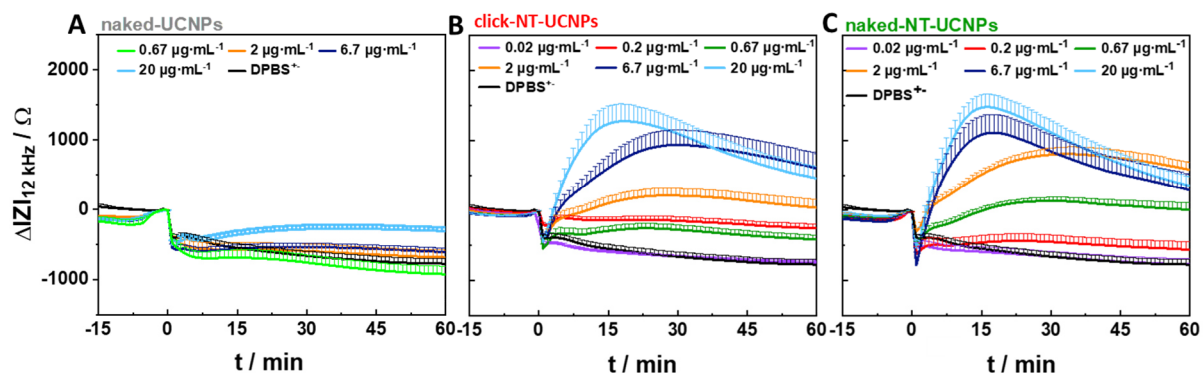


Figure 8.14. Time courses of impedance change at 12 kHz of CHO-hNTS₁R cells stimulated with (A) naked-UCNPs, (B) click-NT-UCNPs (der, PBS), (C) naked-NT-UCNPs (der, PBS) in DPBS⁺⁺ or DPBS⁺ alone at time point 0 min at 37 °C (mean + SEM, at least six measurements from three independent experiments).

Here again, the naked-UCNPs were identified as suitable particle for NT(8-13) functionalization as they did not provoke cellular morphology changes due to NTS₁R activation by themselves or any interactions with the cells.

The morphology changes of CHO-hNTS₁R cells upon stimulation with the functionalized click-NT-UCNPs (der,PBS) and naked-NT-UCNPs (der,PBS) were also analyzed with the ECIS assay. The click-NT-UCNPs and the naked-NT-UCNPs triggered a transient impedance decrease after compound addition of ~500 Ω, followed by a concentration-dependent impedance increase with a maximum after 15 min and a slow impedance decrease until the end of the experiment (**Figure 8.14B, C**). These impedance courses are similar to the impedance profile of NT(8-13)-activated CHO-hNTS₁R (**Figure 8.4A**). The cells, exposed to the two highest concentrations of click-NT-UCNPs (6.7 μg·mL⁻¹ and 20 μg·mL⁻¹), exhibit a maximal impedance change of 1,500 Ω and 1,000 Ω. The medium concentrations of the click-NT-UCNPs (0.2 – 2 μg·mL⁻¹) trigger a recovery of the impedance to baseline values after the dip but no impedance increase. The cells with the lowest concentration treatment (0.02 μg·mL⁻¹) remain at the baseline impedance value after the dip and stays around this value for 60 min as the control does.

The naked-NT-UCNPs induce a maximum response of CHO-hNTS₁R at the two highest concentrations (6.7 μg·mL⁻¹ and 20 μg·mL⁻¹) and a medium response of 1,000 Ω at 2 μg·mL⁻¹. The impedance changes of the cells stimulated with naked-NT-UCNPs in low concentrations recovers after the dip to baseline level (0.67 μg·mL⁻¹) or remains at this value (0.02 – 0.2 μg·mL⁻¹).

The maximal change in impedance after 15 min particle treatment was plotted in relation to the concentration for a better comparison of their agonistic activities (**Figure 8.14D**). It can be clearly seen that naked-NT-UCNPs triggered a higher impedance response than click-NT-UCNPs for all concentrations except for the lowest concentration ($0.2 \mu\text{g}\cdot\text{mL}^{-1}$). The response of the naked-UCNPs initiated a response, similar to the control. A slightly higher impedance change was observed only for the cells with exposure to the highest concentration of naked-UCNPs ($20 \mu\text{g}\cdot\text{mL}^{-1}$). However, this value is also very close to the control and indicates no intrinsic stimulation by the particles. The highest particle concentrations were still part of the linear slope so that estimation of potencies were impossible. However, as free NT(8-13) triggered no impedance change higher than $1,500 \Omega$, this value was set as upper limit to estimate the potencies as $\sim 5 \mu\text{g}\cdot\text{mL}^{-1}$ for click-NT-UCNPs and $\sim 1.1 \mu\text{g}\cdot\text{mL}^{-1}$ for naked-NT-UCNPs.

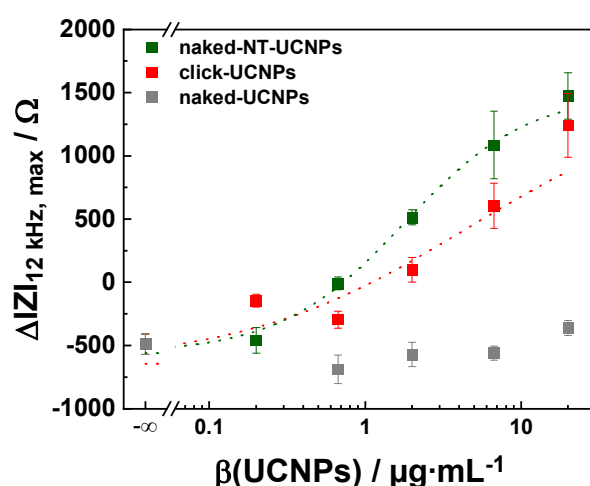


Figure 8.15. Maximal impedance changes at 12 kHz after 15 min of CHO-hNTS₁R cells upon exposure to naked-UCNPs, click-NT-UCNPs (der, PBS) and naked-NT-UCNPs (der, PBS) at 37 °C in DPBS⁺ (mean + SEM, at 4-parameter logistic model (final value 1,500 Ω , dashed line) as $5 \pm 3 \mu\text{g}\cdot\text{mL}^{-1}$ for click-NT-UCNPs (adjusted $R^2 = 0.76$) and $1.1 \pm 0.1 \mu\text{g}\cdot\text{mL}^{-1}$ for naked-NT-UCNPs (adjusted $R^2 = 0.990$).

These results were in good agreement with those of HT-29 cells ($\sim 6 \mu\text{g}\cdot\text{mL}^{-1}$ for click-NT-UCNPs (der,PBS) and $\sim 1.6 \mu\text{g}\cdot\text{mL}^{-1}$ for naked-NT-UCNPs(der-PBS), cf. **Figure 8.8**). Alkyne-NT(8-13) treated UCNPs provoked the same characteristic impedance profile for CHO-hNTS₁R cells as free NT(8-13), indicating the successful attachment of the peptide to the UCNPs *via* click chemistry and/or non-covalently binding. Moreover, the click-NT-UCNPs were less stimulative

than naked-NT-UCNPs with estimated potencies in the same range. Naked-UCNPs did not cause any detectable morphology changes at all.

Wide-field microscopy images were taken of the CHO-hNTS₁R, incubated with the click-NT-UCNPs (der, PBS), naked-NT-UCNPs (der, PBS) or naked-UCNPs. **Figure 8.16** summarizes representative stacks of cells incubated with each of the particles (2.2 $\mu\text{g}\cdot\text{mL}^{-1}$). It rather seems that particles are distributed around the cells and are not internalized. However, as the spatial resolution was not high enough and the DiR staining did not work well for CHO-hNTS₁R cells, it was not possible to exclude the internalization of at least some particles. Individual click-NT-UCNPs spots are in focus around the cells and some above the cells (blurry spots are from planes below and above). Naked-NT-UCNPs are hardly found, neither attached at the apical side nor around the cells. Although cells were pre-treated with BSA to reduce non-specific binding, the unmodified naked-UCNPs are clearly seen as single spots on the apical side and around the cells after washing. This indicates that they bind strongly to the cells.

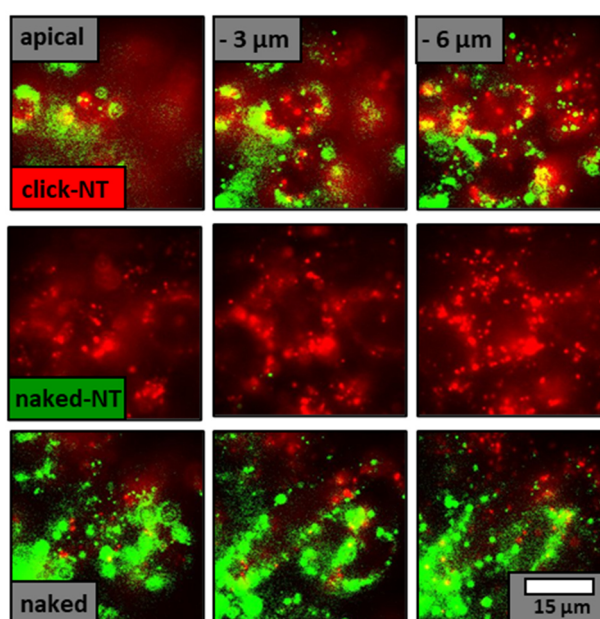


Figure 8.16. Representative wide-field upconversion images of CHO-hNTS₁R cells (apical, -3 μm , -6 μm), incubated with click-NT-UCNPs (der, PBS), naked-NT-UCNPs (der, PBS) or naked-UCNPs (2.2 $\mu\text{g}\cdot\text{mL}^{-1}$, DPBS⁺) at 37 °C for 20 min and co-stained with DiR (at least 20 images from two independent experiments). The images show the upconversion intensity (green) upon 980 nm excitation (cw, 8 kW·cm⁻²) and the DiR emission (red) upon 633 nm excitation. Control images without particle incubation are not shown here. Upconversion intensity was adjusted to visualize small single spots.

The different binding behavior of the particles in contact to the cells revealed that the NT(8-13) incubated particles may have a completely different surface than the naked particles. Despite BSA pretreatment before incubation, the non-stimulative naked-UCNPs bound unspecifically to the cells while the NTS₁R-activating click-NT-UCNPs were clearly identified at the plasma membrane and agonistic naked-NT-UCNPs hardly attached to the cells. These were the same trends, which were observed for the HT-29 cells, except that the UCNPs could enter the intercellular cleft and were also found around the cells. Receptor-mediated internalization was not studied as HT-29 did not internalize the particles at all and the CHO-hNTS₁R did not seem to internalize the particles, too. This was not expected as the NTS₁R receptor has been reported to undergo internalization *via* clathrin-mediated endocytosis for its recycling (Navarro et al., 2006; Wu et al., 2012; Keller et al., 2020), taking along the ligand and attached macromolecules (Bird et al., 2017). However, this was reported for smaller cargo, *e.g.* for U2OS, HT-29, CHO-hNTS₁R, or Caco-2 cells and may be dependent on the cargo type as well as the cell model. It has been assumed that a limit of size for cargo internalization *via* the hNTS₁ receptor might be present (Bird et al., 2017) but no exact values were determined so far. This could already be exceeded with the UCNPs@PLM having a 33 nm UCNP core and a 3 – 4 nm thick PLM coating. However, this theory needs to be verified by a detailed study with particles of different size to answer the question.

8.8 Characterization of Cell Stimulation by Agonist-Functionalized Nanoparticles in the Antagonism Assay

To confirm the agonistic activity of the particles, a competitive antagonist assay of particles with an appropriate antagonist were carried out with the CHO-hNTS₁R cells, recording the cell response by impedance-based readout. At first, the protocol for the antagonist assay as well as the antagonistic activity of the hNTS₁R antagonist SR142948 was confirmed, using the free NT(8-13) as competing agonist. Analogously to the agonist assay, the CHO-hNTS₁R cells were pre-treated with the BSA-containing measurement buffer (0.5% BSA (w/v), DPBS⁺, 20 min). Prior to the addition of NT(8-13) in a concentration triggering maximal impedance response (10 nM, DPBS⁺) at time point 0 min, the cells are exposed to SR142948 (4 µM) in 400-fold excess at time point -5 min. When the antagonist is added, the impedance rises about

(400 – 1000) Ω but drops down back to baseline level upon buffer addition and stays around this value for 60 min (**Figure 8.17A**). In the case of NT(8-13) treatment, there is a small impedance dip at baseline level before a slight rise of ~ 300 Ω due to NTS₁R activation.

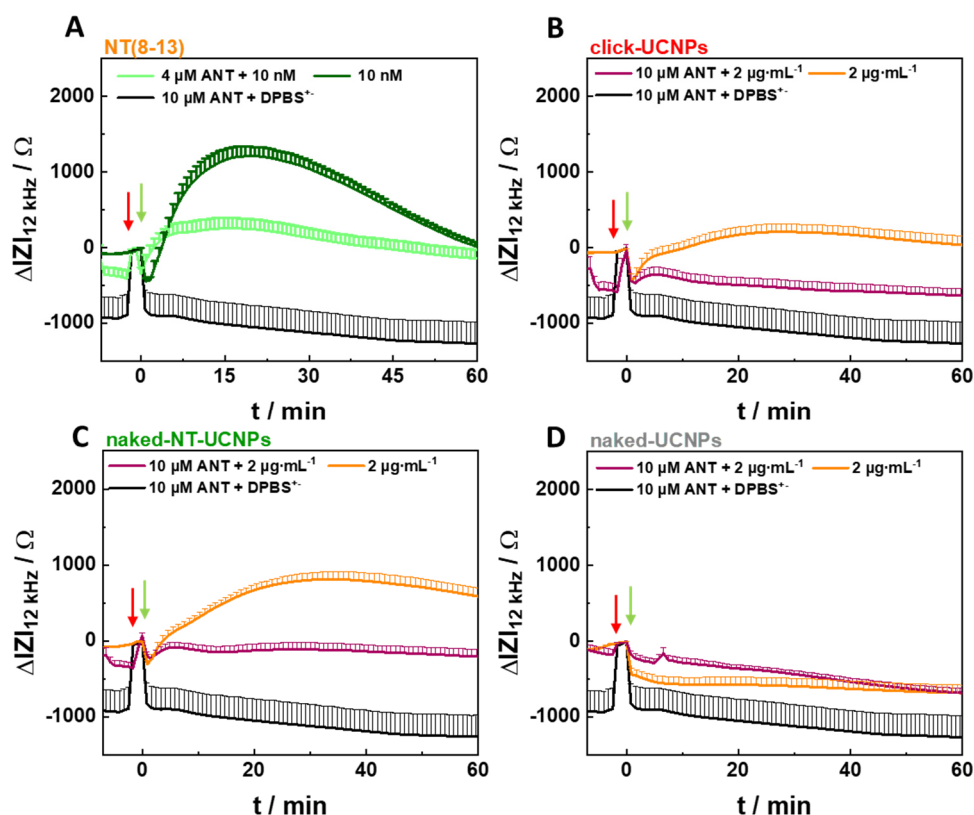


Figure 8.17. Time courses of impedance change of CHO-hNTS₁R cells at 12 kHz, pretreated (red arrow) with the antagonist SR142948 (ANT, 4 μ M or 10 μ M) 5 min prior to the stimulation (green arrow) with (A) free NT(8-13) (10 nM, DPBS⁺) (B) click-UCNPs ((der, PBS), 2 μ g·mL⁻¹, DPBS⁺), (C) naked-NT-UCNPs ((der, PBS), 2 μ g·mL⁻¹, DPBS⁺), (D) naked-UCNPs (2 μ g·mL⁻¹, DPBS⁺) or control DPBS⁺ at time point 0 min at 37 °C (mean + SEM, at least six measurements from two independent experiments).

After addition of the agonist, the impedance time courses of antagonist pre-treated cells were similar to those of antagonist-free CHO-HNTS₁R cells at the same concentration but with lower maximum impedance values. The activation of NTS₁R was still possible in the tested concentration ranges of agonist and antagonist but the maximal impedance change after 15 min was reduced by 70%. This visualized the competing antagonist binding to the receptor and confirmed that the impedance changes of the cells after NT(8-13) addition can be attributed to morphology changes upon NTS₁R receptor activation. Moreover, the suitability of the antagonist in competitive stimulation experiments with particles was demonstrated.

The same protocol was applied to test the binding of the antagonist and the particles in concentrations with medium agonistic power (**Figure 8.17B-D**). The impedance of the cells rises upon SR142948 (10 μM) addition by 200 – 1000 Ω and falls back to baseline level when particles are added (2 $\mu\text{g}\cdot\text{mL}^{-1}$) in all cases. In the case of cells exposed to naked-UCNPs, the impedance slightly decreases until values similar to those of cells without additional antagonist treatment are reached after 50 min. In contrast, the impedance rises slightly for those cells being stimulated with click-NT-UCNPs or naked-NT-UCNPs and antagonist pre-treatment. The maximal impedance changes are strongly reduced in comparison to those without antagonist treatment.

The reduction of the maximal response confirms the competitive hNTS₁ receptor binding and activation of the receptor by the particles click-NT-UCNPs or naked-NT-UCNPs.

The binding of UCNPs to the CHO-hNTS₁R cells was examined microscopically to find out whether the reduced receptor stimulation upon antagonist pre-treatment is supported by binding data. As the naked-NT-UCNPs did almost not bind to the cells at all, microscopic competitive binding studies were not conducted with these particles. Instead, naked-UCNPs were used as control. Representative wide-field upconversion micrographs of the particle-treated cells are shown for a medium cell plane with surrounding UCNPs and cell bodies in focus and upconversion intensity set to visualize small single spots (**Figure 8.18.A**). The upconversion intensity is high around the cells when exposed to naked-UCNPs, while those with prior antagonist SR142948 treatment show only a few upconversion spots. The micrographs of cells exposed to click-NT-UCNPs or click-NT-UCNPs with antagonist pre-treatment are similar as in both cases upconversion spots are identified around the cell bodies. A clear tendency was visible for the cells incubated with naked-UCNPs and antagonist. The drastic reduction of detected upconversion was unexpected as they could only bind randomly to the cells in both cases and should not show any agonistic effect at all. Having a look at the molecular structure of SR142948, a tertiary amine group was identified, which might form salt bridges to the phosphate groups of UCNPs@PLM, too (**Figure 8.18.B**). Additional electrostatic attraction could occur with carboxy groups of the antagonist and the ethanolamine moieties of DOPE of the UCNPs@PLM. SR142948 may equip the UCNPs@PLM with a new surface coating, masking the phosphate groups for high unspecific binding to amines at the cell

surface. A detailed study with dynamic light scattering and zeta potential measurements might give deeper insights in the change of particle surface upon the binding of molecules. In contrast, the number of attached particles was not reduced drastically for antagonist and click-NT-UCNPs treated cells. To make a clear statement with a precise determination of small differences, the experiments will have to be repeated with a microscope technique enabling a good spatial resolution and an easy data deconvolution, which was not able with the setup used for this experiment together with the poor cell body staining. Moreover, the particle concentrations might be inappropriate for this microscopy experiment. The wide-field upconversion images did not clearly confirm or deny the reduced binding in the presence of a competitive inhibitor.

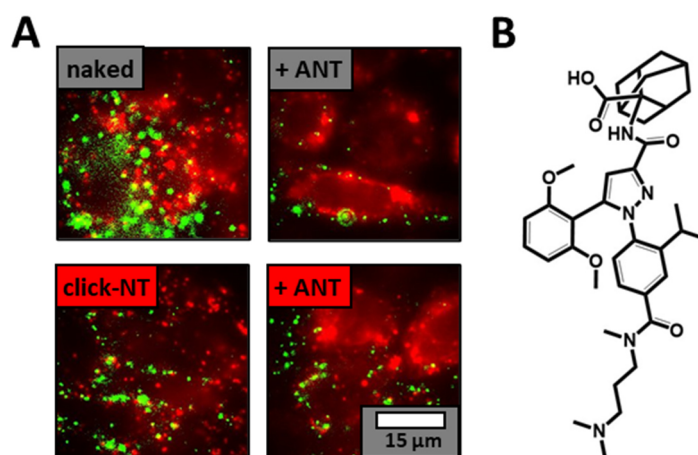


Figure 8.18. (A) Representative wide-field microscopic images of CHO-hNTS₁R cells, incubated with click-NT-UCNPs (der, PBS) or naked-UCNPs (2.2 $\mu\text{g}\cdot\text{mL}^{-1}$, DPBS⁺) at 37 °C for 20 min with or without preceding antagonist treatment (ANT, 10 μM) and co-stained with DiR (at least 20 images of two independent experiments). The images show the upconversion intensity (green) upon 980 nm excitation (cw, 8 $\text{kW}\cdot\text{cm}^{-2}$) and the DiR emission (red) upon 633 nm excitation. Micrographs without particle incubation are not shown here. Upconversion intensity was adjusted to visualize small single spots. (B) Molecule structure of NTS₁R antagonist SR142948.

8.9 Characterization of Cell Stimulation by Agonist-Functionalized Nanoparticles in the Presence of Serum Proteins

Finally, the agonistic activity of the particles was tested under more physiological conditions by monitoring the cell responses to the particles in the presence of serum proteins, which might form a protein corona around the particles.

At first, the stimulation of free NT(8-13) in presence of BSA (0.5%, DPBS⁺) or FCS (5%, DPBS⁺) was analyzed with CHO-hNTS₁R and compared to protein free conditions (**Figure 8.19**). In the presence of BSA a slight decrease of maximal impedance change values is observed for cells exposed to medium concentrations (0.3 nM and 3 nM), while cells being exposed to 30 nM of NT(8-13) have the same impedance course as those with DPBS⁺ (**Figure 8.19B**). Different to that, cells exposed to 0.3 nM and 3 nM NT(8-13) in FCS-containing DPBS⁺ were not stimulated, while cells with 30 nM NT(8-13) treatment show a significantly lower impedance increase (**Figure 8.19C**).

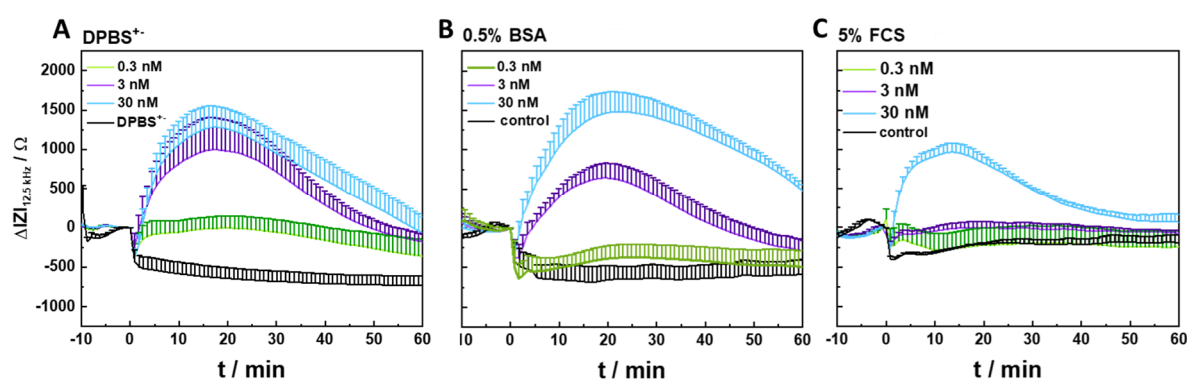


Figure 8.19. Time courses of impedance change at 12.5 kHz of CHO-hNTS₁R cells exposed to NT(8-13) or the control in (A) DPBS⁺, (B) DPBS⁺ (0.5% (w/v) BSA), or (C) DPBS⁺ (5% FCS (v/v)) at time point 0 min at 37 °C (mean + SEM, at least five measurements from two independent experiments). Baseline impedance magnitude before stimulation at time point 0 min was (3.66 ± 0.06) kΩ (N = 15) in DPBS⁺, (4.09 ± 0.04) Ω (N = 19) in DPBS⁺ (0.5% BSA), and (4.43 ± 0.06) Ω (N = 17) in DPBS⁺ (5% FCS).

BSA had only a slight reductive impact on the agonistic activity of NT(8-13) while FCS highly decreased the maximum impedance values of stimulation for a given concentration. Proteolytic degradation of neurotensin is reported to occur at the peptide bond between Arg⁸-Arg⁹, Pro¹⁰-Tyr¹¹ and Tyr¹¹-Ile¹² (García-Garayoa et al., 2001). Thus, proteases, present in FCS

but not in BSA, might slowly degrade the agonist within the time frame of dilution and measurement (30 min) so that stimulation was reduced or not possible anymore.

It had to be tested whether BSA or serum proteins degrade the particle-attached NT(8-13) or cover the particles and, hence, affect their agonistic activity. Thus, CHO-hNTS₁R cells were exposed to the particles in concentrations, inducing either low, medium, or maximal impedance response in BSA (0.5%)- or FCS (5%)-containing DPBS⁺⁺ buffer and compared to protein-free conditions. In the case of click-NT-UCNPs, the cells in BSA-containing buffer show an increase of maximum impedance changes of around 500 Ω for all applied concentrations, while the experiment performed in FCS reveal impedance time courses similar to those in DPBS⁺ (**Figure 8.20A-C**). Similarly, an impedance increase of the cells is visible for naked-NT-UCNPs in all applied concentrations in BSA-containing buffer but not in FCS containing buffer, compared to the experiment in protein-free buffer (**Figure 8.20D-F**). The maximal differences of impedance changes in BSA were observed for those cells with exposure to the medium particle concentration ($2 \mu\text{g}\cdot\text{mL}^{-1}$), which might be closest to the EC₅₀. The impedance time courses of cells, exposed to naked-UCNPs in DPBS⁺⁺ with or without FCS or BSA, are all similar with impedance changes slightly higher than of the control cells with buffer treatment (**Figure 8.20G-I**).

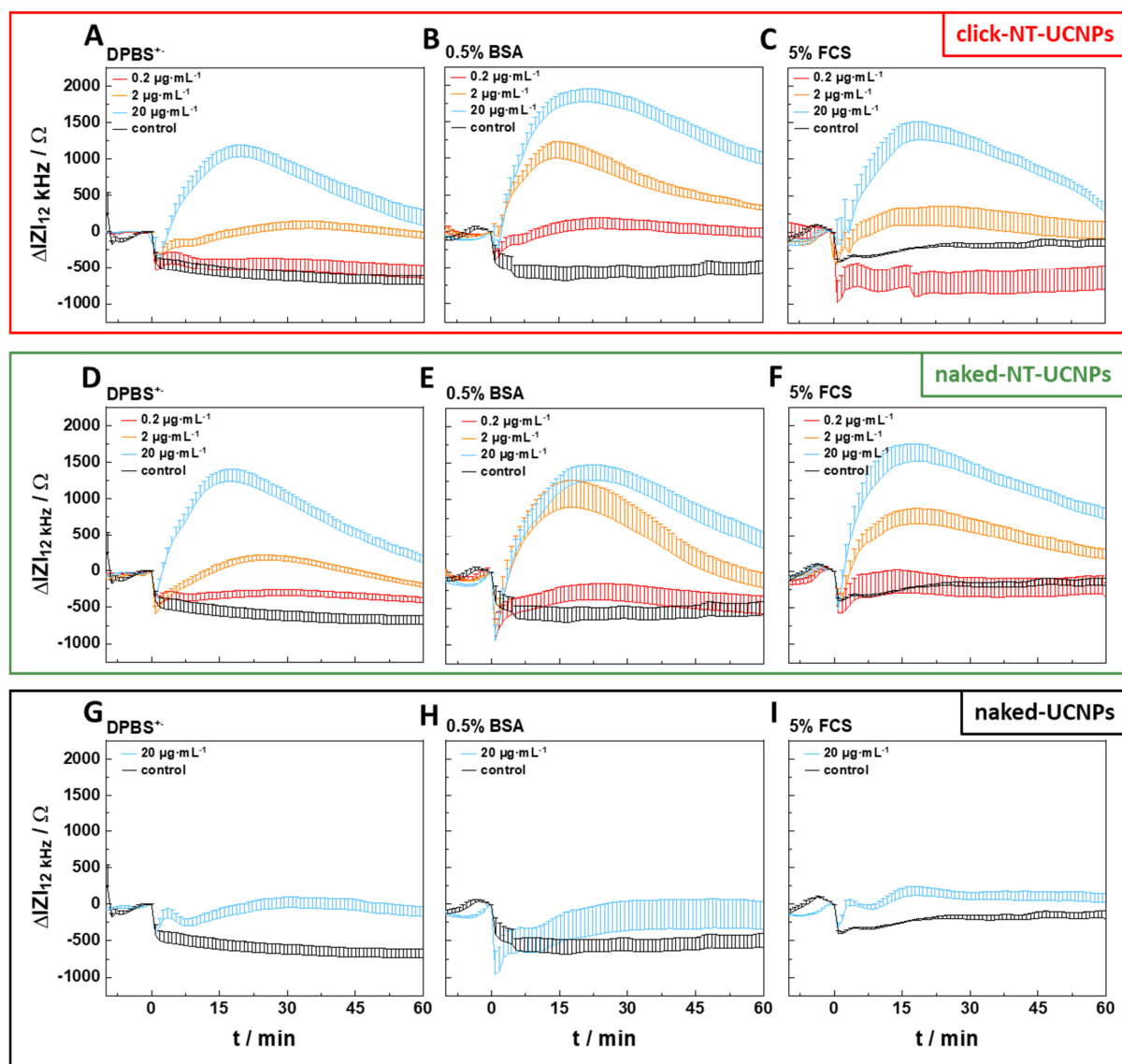


Figure 8.20. Time courses of impedance change at 12 kHz of CHO-hNTS₁R cells, exposed to click-NT-UCNPs, naked-NT-UCNPs, naked-UCNPs (0.2 – 20 $\mu\text{g}\cdot\text{mL}^{-1}$) or control in (A, D, G) DPBS⁺, (B, E, H) DPBS⁺ (0.5% BSA), or (C, F, I) DPBS⁺ (5% FCS) at time point 0 min at 37 °C (mean + SEM, at least six measurements from two independent experiments). Baseline impedance magnitude before stimulation at time point 0 min was (3.63 ± 0.04) k Ω (N = 40) in DPBS⁺, (4.30 ± 0.4) k Ω (N = 46) in DPBS⁺ (0.5% BSA), and (4.63 ± 0.04) k Ω (N = 43) in DPBS⁺ (5% FCS).

The agonistic activity of the particle-attached NT(8-13) was not reduced but increased in the presence of BSA or FCS. This indicated that NT(8-13) was not hidden under a protein corona to hinder stimulation and that a degradation of the NT(8-13) by serum proteases did not take place. This is different to the fate of free NT(8-13) in FCS being degenerated quickly by FCS (**Figure 8.19**) within the time frame of dilution and measurement (30 min). Proteolytic degradation of NT occurs at the peptide bond between Arg⁸-Arg⁹, Pro¹⁰-Tyr¹¹ and Tyr¹¹-Ile¹²

(García-Garayoa et al., 2001). As Arg was attached to the particle surface and the agonist was highly sterically hindered, the proteases might have limited access to the peptide. Moreover, the surface of the particles had been covered with NT(8-13) almost completely, reaching with the uncharged C-terminus into solution. Thus, the binding positions on the particle for strong interactions might be limited and the affinity of serum proteins to particles might be rather low. This may have led to the formation of a rather soft (loose) and dynamic corona rather than a hard (tight) and static corona around the particles. The DLS measurements substantiated this hypothesis as they revealed a small peak of serum proteins <10 nm in the samples naked-NT-UCNPs and click-NT-UCNPs, which was not observed for naked-UCNPs with plenty of phosphate and amino groups being freely available for electrostatic interactions (**Figure 8.2A,E,F** and **Figure A 2**). This indicated that serum proteins were bound with high affinity to highly charged naked-UCNPs so that the protein peak diminished. With lower affinity to the peptide-saturated particles plenty of proteins remained unattached in solution.

The particles had a higher agonistic activity in BSA-containing buffer and naked-NT-UCNPs led to higher impedance signal changes than click-NT-UCNPs. This indicates that NT(8-13) was not totally hidden under a serum albumin corona. Moreover, besides the attachment of a low number of proteins, the exchange of alkyne-NT(8-13) by “multivalent” BSA with neighboring arginine amino acids might be possible, too. Similar to the detachment of electrostatically bound NT(8-13) from the particle by strong receptor binding, the NT(8-13) could be detached due to simultaneous binding of many Arg (or other amino acids) of one BSA molecule. This might result in freely available NT(8-13), stimulating hNTS₁R more actively than the particle-attached NT(8-13). The hydrodynamic diameter from the particles in BSA was slightly shifted to higher values, which visualized the change of the particle surface decoration and may indicate the attachment of additional BSA or the replacement of small peptides by larger BSA (**Figure 8.2B,E**). The more pronounced interactions with the particles by BSA and not by FCS, visible in the impedance assay, may be due to the fact that the particles were the only binding partner for electrostatic interactions in the BSA dispersion, while a great number of different proteins were available in the FCS particle dispersion. These were, next to the particles, possible binding partner to each other and, hence, decrease the electrostatic attraction to the particles. The replacement of NT(8-13) by serum proteins could be possible as well but might

not be as strong to be detectable as impedance changes or might even be masked as free NT(8-13) can be degraded proteolytically in FCS.

The stronger cell response for naked-NT-UCNPs than for click-NT-UCNPs in BSA-containing buffer might be found in the nature of the agonist attachment. Naked-NT-UCNPs have a higher amount of electrostatically-attached NT(8-13) than click-NT-UCNPs with electrostatically-attached as well as covalently-anchored NT(8-13). Thus, the naked-NT-UCNPs have a higher amount of the type of NT(8-13), which can be displaced by BSA proteins and stimulate as free agonist.

Contradictory results on the impact of adsorbed proteins on the receptor binding capability of nanoparticles carrying targeting ligands have been extensively reported. The cell recognition of transferrin-functionalized NPs has been shown to be blocked by protein corona (Salvati et al., 2013). In contrast, the targeting moieties of particles against the epidermal growth factor receptor were maintained upon protein binding (Zarschler et al., 2014). The targeting capability of non-covalently attached antibodies against the receptor CD63 was retained while covalently conjugated ones lost their targeting ability (Tonigold et al., 2018). Additionally, a size dependent impact of protein adsorption on folic acid-coated NPs was reported with a reduction for 5 nm NPs and an enhancement for 40 nm NPs due to multivalence (Su et al., 2016). Even if the targeting capability seemed to be maintained in many internalization studies due to the highly dynamic nature of protein adsorption, misinterpretations might occur as it was also possible that the targeting moiety was masked or replaced by serum proteins, triggering another type of receptor of the same cell. The question whether the targeting moiety was masked under the protein corona or just replaced by other non-targeting proteins, cannot be answered easily and is often not commented. Moreover, the type of targeting (or stimulating) molecule, the nature of its receptor interaction, and the tendency for protein corona formation or replacement are very individual and may highly vary for each example. Thus, it is rather difficult to interpret the observed targeting of the different UCNPs and compare to the results from other studies as different ligands, ligand carriers, cells, and experimental setups have been used.

To sum up, the particles with electrostatically (naked-NT-UCNPs) or electrostatically as well as covalently bound agonist (click-NT-UCNPs) were able to trigger the full cell response under all

tested conditions. This demonstrates that the proteins could neither form a strong corona around the agonist coated particles nor degrade the agonist to diminish their agonistic activity. Moreover, the stimulating properties increased for the particles in BSA containing buffer. The reason remained elusive but the prediction was made that serum albumin partly displaced NT(8-13) and enabled the activation of NTS₁R by free and possibly more stimulating NT(8-13). The trend was more pronounced for naked-NT-UCNPs than for click-NT-UCNPs, which may confirm again the differences in the nature of the agonist attachment (electrostatically vs covalently attached). The partial displacement of agonist from the particles was only visible in BSA containing buffer and not under the physiological serum conditions. This demonstrated the suitability of UCNPs@PLM as protective carrier for the peptidyl agonist for extracellular stimulation.

8.10 Conclusion and Outlook

In this project, the suitability of UCNPs@PLM as label and carrier for GPCR agonists was analyzed. The functioning of the applied techniques was confirmed with the free NTS₁R agonist NT(8-13) and the hNTS₁R antagonist SR142948 using the two model cell lines HT-29 and CHO-hNTS₁R. The suitability of the UCNPs@PLM (naked-UCNPs) as basic particle for agonist functionalization was verified as they had almost no receptor affinity and did not trigger any morphology changes being detectable *via* the impedance-based cell analysis. In contrast, linker-attached alkyne-NT(8-13) (click-NT-UCNPs) and electrostatically bound alkyne-NT(8-13) (naked-NT-UCNPs) had a high receptor affinity and provoked the characteristic impedance pattern upon hNTS₁R activation. Due to the high steric hindrance imposed on electrostatically-bound alkyne-NT(8-13), a deep penetration into the binding pocket for NTS₁R activation might be rather improbable. Therefore, it was hypothesized that sterically hindered NT(8-13) might start to enter the binding pocket from the C-terminus but might get stripped off the particle by the interaction with the receptor. Particle and NT(8-13) might separate and the NT(8-13) was retracted in the binding pocket for stimulation. Micrographs of cells and UCNPs substantiated this hypothesis as click-NT-UCNPs were found at the cell surface and naked-NT-UCNPs were hardly detected, indicating the separation of particles and NT(8-13) upon receptor binding. These results could be validated for both cell models. Additionally, an antagonistic assay with an appropriate antagonist against hNTS₁R

confirmed that the NT(8-13)-functionalized particles activated the hNTS₁ receptor. The particles kept their agonistic activity under more physiological conditions in the presence of BSA or FCS, indicating that serum proteins could not degrade the agonist proteolytically when attached to particles. Moreover, the established BSA or FCS based protein corona around the particles appeared rather soft and dynamic as d_{hydro} did not change drastically and the particles were still able to activate the receptors. BSA seemed to partly replace NT(8-13) when purely applied to particles but not severely when applied in FCS.

It was validated that the UCNPs@PLM equipped with the agonist were capable of successfully binding as well as stimulating a GPCR and protecting the agonist from proteolytic degradation. Thus, these particles might be good candidates as carriers for drugs and targeting moieties to their target location, even in the presence of serum proteins. This can be faced either with linker attached agonists or with electrostatically attached agonists. Both functionalization methods may enable the intended receptor stimulation. However, non-covalently bound particles might diffuse away quickly and might be secreted, while covalently bound particles might remain for a longer time at the cell surface. Regarding the application, it can be advantageous that the particles are not internalized and stay extracellularly for stimulation followed by secretion.

The particles did not seem to be the ideal candidates for studies of receptor-mediated internalization processes as they were not uptaken by the two model cell lines of this project. Nevertheless, this might be also due to an unsuitable model receptor and agonist or model cell line for these large UCNPs. Thus, it could be very valuable to test different particle sizes, GPCRs and cell lines.

As the naked UCNPs@PLM strongly bound to the cell surface despite BSA pretreatment, they might disturb microscopy studies and might not be suitable luminescent probes. To further improve the particles in terms of non-specific binding to cells or to arginine-containing peptides, particles with a different bilayer coating should be prepared without phosphatic acid as main component. However, if one wants to take advantage of the benefits of UCNPs@PLM in terms of outstanding chemical and colloidal stability as well as brightness, the system can be applied and tested on other types of (biased) agonists. Moreover, one can also take advantage of this strong binding ability and prepare peptides based on arginine-PA interactions for a different linkage method. Another improvement of the particle design could

be obtained by elongating the NT(8-13) on the C-terminus with native amino acid sequences or any other linker moiety and end up with at least two arginine so that a peptide with strong particle attachment but reduced steric hindrance for a high receptor binding and agonistic activity might be available.

9 Summary

This thesis demonstrated the importance of surface protecting ligands for the preparation of upconverting nanoparticles (UCNPs) with high brightness, colloidal and chemical stability, biocompatibility, and efficient biomolecule functionalization for cellular uptake or targeting a receptor.

The surface protection abilities of different ligands were analyzed with UCNPs of 12 nm diameter as these are very sensitive towards luminescence quenching effects at the particle surface when suspended in water. The UCNPs were modified by ligand exchange or ligand addition strategies with poly(acrylic acid) (PAA), amphiphilic polymer (AP), and a biomimetic phospholipid membrane coating (PLM). The PLM is the only coating, which provides an efficient hydrophobic barrier against water quenching and particle dissolution. In contrast to UCNPs@PAA and UCNPs@AP, the UCNPs@PLM showed a seven times more intense upconversion luminescence in aqueous media and colloidal stability in a much wider range of solutions, including phosphate buffer as well as solutions of high ionic strength, a wide pH range, and complex cell culture medium. UCNPs@PLM turned out to be suitable for biosensing applications in cells and tissues under serum-free conditions and in serum-supplemented media, while UCNPs@AP were only stable in serum-containing media and UCNPs@PAA were not suitable for *in vitro* experiments at all.

The importance of surface-shielding ligands on the biocompatibility of UCNPs was demonstrated by UCNPs with the intrinsically non-toxic bilayer coatings AP and PLM in contact to non-transformed epithelial kidney cells (NRK). The chemically stable UCNPs@PLM had no toxic effect on the mammalian model cell line although these particles were efficiently internalized *via* macropinocytosis and clathrin-dependent pathways. In contrast, the viability and morphology of the cells changed upon uptake of UCNPs@AP with their low chemical stability. UCNPs@AP induced cell swelling and cell death after around 30 h with an EC₅₀ value of $(45 \pm 7) \mu\text{g}\cdot\text{mL}^{-1}$ in L-15 (5% FCS) and $(15 \pm 2) \mu\text{g}\cdot\text{mL}^{-1}$ in DPBS⁺ (5% FCS) even though their internalization was ~3 times less efficient compared to non-toxic UCNPs@PLM.

The impact of UCNPs on cell physiology, metabolism, and morphology changes was analyzed in more detail with the poorly shielded medium sized UCNPs@AP with a diameter of 25 nm. The UCNPs@AP interfered strongly with cell adhesion (EC_{50} of $(28 \pm 6) \mu\text{g}\cdot\text{mL}^{-1}$) and migration within < 8 h (EC_{50} of $(4 - 11) \mu\text{g}\cdot\text{mL}^{-1}$). Resting cells were less sensitive to the particles showing onset of cell death only after ~ 30 h (EC_{50} of $(17 \pm 15) \mu\text{g}\cdot\text{mL}^{-1}$) and reduction of metabolism after 72 h (EC_{50} of $(103 \pm 8) \mu\text{g}\cdot\text{mL}^{-1}$). It was observed that the cell age had a significant impact on the outcome of the toxicity experiments. The detailed analysis of the impedance profiles with transient cell swelling and the very late reduction of metabolic activity argued against apoptosis and indicated a necrotic cell death. The observed dissolution of the UCNPs@AP in H_2O , their cytotoxicity, and the cell response profile supported the hypothesized toxicity pathway of poorly shielded UCNPs: ion leakage within the vesicles, REPO_4 formation with phosphates of vesicle membrane, lysosomal damage, followed by necrosis. These studies revealed potential toxic pathways of poorly shielded UCNPs in contact to a non-transformed cell line.

The suitability of several UCNPs surface modifications (Lys, AP, PLM) for functionalization and subsequent cellular uptake by NRK cells was analyzed with the photosensitizer rose bengal (RB). UCNPs@Lys with a monolayer-like particle coating had the lowest RB binding efficiency and a non-detectable RB transport into NRK cells. Nevertheless, UCNPs@Lys-RB induced cell stress. RB was strongly attached to bilayer coated UCNPs@AP, were internalized in higher amounts by the cells and initiated cell death. In contrast, binding of RB and its transport into the cells was highly efficient by bilayer coated UCNPs@PLM without triggering any cell response. The amount of RB uptake by bilayer coated UCNPs was sufficient for the light-induced generation of reactive oxygen species at levels, high enough to initiate cell death. The UCNPs@PLM are considered as promising drug carrier for efficient transport into cells and light-activated therapy.

The potential of UCNPs@PLM as label and carrier for GPCR agonists (here: neurotensin-derivative NT(8-13)) was analyzed for two different cell lines expressing the model GPCR hNTS₁R. UCNPs with linker-bound alkyne-NT(8-13) (click-NT-UCNPs) and/or with electrostatically attached alkyne-NT(8-13) (naked-NT-UCNPs) had a high receptor affinity and

provoked the characteristic impedance pattern upon hNTS₁R activation. Reduced receptor activation in presence of an antagonist confirmed their successful binding by the functionalized particles. The separation of electrostatically bound NT(8-13) from the particle before receptor binding was hypothesized and supported by microscopy studies. This concept was substantiated as BSA was likely to replace partly electrostatically bound alkyne-NT(8-13) from the particle. Serum proteins could neither form a dense protein corona around the particles, hindering receptor activation, nor degrade the particle-attached agonist proteolytically. In conclusion, UCNPs@PLM can be considered as protective carriers for drugs with extracellular targets as for instance, cell surface receptors.

10 Zusammenfassung

Diese Arbeit zeigt die Bedeutung von oberflächenschützenden Liganden für die Herstellung aufkonvertierender Nanopartikel (UCNPs) mit hoher Helligkeit, kolloidaler und chemischer Stabilität, Biokompatibilität und effizienter Anbindung von Biomolekülen für deren Aufnahme in tierische Zellen und die Stimulation von Zelloberflächenrezeptoren.

Die oberflächenschützenden Eigenschaften unterschiedlicher Liganden wurden mit 12 nm großen UCNPs analysiert, welche starke Lumineszenzlöschung an der Partikeloberfläche zeigten. Die Partikel wurden über Ligandenaustausch oder durch das Hinzufügen einer zusätzlichen Ligandenschicht aus Polyacrylsäure (PAA), einem amphiphilen Polymer (AP) oder einer biomimetischen Phospholipidmembran (PLM) modifiziert. PLM ist die einzige Modifizierung, die eine hydrophobe Barriere gegen Wassermoleküle, welche Lumineszenz löschen und Partikelauflösung initiieren können, bildet. Im Vergleich zu PAA- und AP-umhüllte Nanopartikel weisen PLM-ummantelte Partikel eine siebenfach höhere Lumineszenz in wässrigen Medien auf. Außerdem sind diese in einer Vielfalt an Lösungsmitteln kolloidal stabil, was für Nanopartikel oftmals herausfordernd ist, wie z.B. in Lösungen mit hoher Ionenstärke, in Phosphatpuffer, in extremen pH Werten und in komplexen Zellkulturmedium. PLM modifizierte Nanopartikel stellten sich als geeignet heraus für zelluläre Anwendungen in FCS-freien und FCS-supplementierten Medien, wohingegen AP ummantelte Partikel nur in FCS-haltigen Medien stabil und PAA umhüllte Partikel unter diesen Bedingungen gar nicht für *in vitro* Experimente geeignet waren.

Die Wichtigkeit von oberflächenschützenden Liganden für die Biokompatibilität von UCNPs wurde anhand der intrinsisch nicht toxischen Liganden AP und PLM an nicht-transformierten Epithelzellen demonstriert. Die chemisch stabilen PLM umhüllten Partikel zeigten keine toxische Wirkung in der Säugetiermodellzelllinie, obwohl sie in großen Mengen über Makropinozytose und Clathrin-abhängige Wege internalisiert wurden. Im Gegensatz dazu veränderte sich die Viabilität und die Morphologie der Zellen nach Exposition zu AP modifizierten Partikeln mit geringer chemischer Stabilität. AP ummantelte Partikel erzeugten ein Anschwellen der Zellen und induzierten deren Tod nach etwa 30 h mit EC₅₀ Werten von

(45 ± 7) $\mu\text{g}\cdot\text{mL}^{-1}$ in L-15 Medium (5% FCS) und von (15 ± 2) $\mu\text{g}\cdot\text{mL}^{-1}$ in DPBS⁺ (5% FCS), obwohl diese Partikelsorte dreifach weniger effizient aufgenommen wurde als die nicht toxischen PLM umhüllten Partikel.

Der Einfluss aufkonvertierender Nanopartikel auf die Funktionstüchtigkeit der Zellen, den Metabolismus und die Morphologie wurde im Detail mit den wenig schützenden AP umhüllten Partikeln in mittlerer Größe gezeigt. Diese Partikel schränkten die aktiven Zellen stark in ihrer Adhäsions- (EC_{50} von (28 ± 6) $\mu\text{g}\cdot\text{mL}^{-1}$) und Migrationsfähigkeit innerhalb weniger als 8 h ein (EC_{50} von ($4 - 11$) $\mu\text{g}\cdot\text{mL}^{-1}$). Der Partikel-induzierte Zelltod von Zellen in der Ruhephase fand nach ca. 30 h (EC_{50} of (17 ± 15) $\mu\text{g}\cdot\text{mL}^{-1}$) statt. Eine Verringerung der metabolischen Aktivität konnte nach 72 h (103 ± 8) $\mu\text{g}\cdot\text{mL}^{-1}$) festgestellt werden. Es wurde beobachtet, dass das Alter der Zellen einen signifikanten Einfluss auf die Ergebnisse der Toxizitätsexperimente hatte. Die detaillierte Analyse des Zellantwortprofils mit dem vorübergehenden Anschwellen der Zellen und der spät eintretenden Reduzierung der metabolischen Aktivität sprechen gegen Apoptose und für einen nekrotischen Zelltod. Die beobachtete Auflösung der Partikel in zell-freien Experimenten, deren Toxizität und das Zellantwortprofil unterstützten die aufgestellte Hypothese zum Toxizitätsweg von wenig geschützten aufkonvertierenden Nanopartikeln: Austreten von Ionen in Vesikeln, Ausbildung von REPO_4 mit den Phosphatgruppen der Vesikelmembran, Beschädigung der Lysosomen und darauffolgende Nekrose. Diese Studien zeigten die potenziellen Toxizitätswege von wenig geschützten, AP ummantelten UCNPs in nicht-transformierten Zelllinien.

Die Eignung unterschiedlicher Oberflächenmodifizierungen für aufkonvertierende Nanopartikel (Lysin (Lys), AP, PLM) zur Funktionalisierung und für deren Aufnahme in tierische Zellen wurde mit dem Photosensibilisator Rose Bengal (RB) an einer Säugetiermodellzelllinie untersucht. Nanopartikel, welche mit der Monoschicht ausbildenden Liganden Lys modifiziert wurden, zeigten die geringste Anbindungseffizienz von RB und einen nicht nachweisbaren RB Transport in die Zellen. Trotzdem induzierten diese Partikel Stress in den Zellen. Im Gegensatz dazu konnte RB in großen Mengen an den Doppelschichten ausbildenden Liganden AP gebunden und von den Zellen aufgenommen werden. Diese Partikel initiierten den Zelltod. Die Anbindung und der Transport von RB in die Zellen war höchst effizient mit Partikeln mit Phospholipiddoppelschicht (PLM), ohne dabei eine toxische Zellantwort

hervorzurufen. Die Mengen an intrazellulärem RB war bei den Liganden, die Doppelschichten ausbildeten, ausreichend, um Licht-induzierte reaktive Sauerstoffspezies in Konzentrationen zu erzeugen, die hoch genug waren, um den Zelltod auszulösen. Aufgrund dieser Ergebnisse könnten die PLM modifizierten Partikeln vielversprechende Transporter für pharmakologische Wirkstoffe sein, um deren effizienten Transport in Zellen und darüber hinaus eine Licht-aktivierte Therapie zu ermöglichen.

Das Potential von PLM ummantelten Partikeln als Label und Transporter für G Protein-gekoppelter Rezeptoren (GPCRs) Agonisten (hier: ein Neurotensinderivat NT(8-13)) wurde mit zwei verschiedenen Zelllinien untersucht, die den humanen Neurotensin 1 Rezeptor (hNTS₁R) exprimieren. Nanopartikel mit Linker gebundenem Alkin-NT(8-13) (click-NT-UCNPs) und/oder elektrostatisch gebundenem Alkin-NT(8-13) (naked-NT-UCNPs) hatten eine hohe Affinität zum Rezeptor und lösten das charakteristische Impedanz Profil nach Aktivierung des hNTS₁R in den Zellen aus. Die reduzierte Fähigkeit, den Rezeptor in Anwesenheit eines Antagonisten zu aktivieren, bestätigte die spezifische Rezeptoraktivierung durch die funktionalisierten Partikel. Eine potentielle Trennung des elektrostatisch gebundenem NT(8-13) vom Partikel nach Rezeptorbindung wurde postuliert und unterstützt durch Mikroskopie Studien, die keine naked-NT-UCNPs, allerdings click-NT-UCNPs in großer Anzahl an der Zelloberfläche zeigten. Diese Theorie wurde weiter verifiziert, da es so schien als würde Serumalbumin teilweise elektrostatisch gebundenes Alkin-NT(8-13) vom Partikel verdrängen. Serumproteine formten weder eine dichte Proteincorona um die Partikel, was die Rezeptoraktivierung verhindern hätte können, noch konnten sie den partikelgebundenen Agonist proteolytisch abbauen. Zusammenfassend können PLM modifizierte Partikel als schützende Transporter für pharmakologische Wirkstoffe mit extrazellulären Targets, wie z.B. Rezeptoren an der Zelloberfläche, betrachtet werden.

References

- Åberg C, Kim JA, Salvati A, Dawson KA. Reply to 'The interface of nanoparticles with proliferating mammalian cells'. *Nat. Nanotechnol.* **2017**; 12(7): 600–3.
- Åberg C, Piattelli V, Montizaan D, Salvati A. Sources of variability in nanoparticle uptake by cells. *Nanoscale* **2021**; 13(41): 17530–46.
- Alsop RJ, Maria Schober R, Rheinstädter MC. Swelling of phospholipid membranes by divalent metal ions depends on the location of the ions in the bilayers. *Soft Matter* **2016**; 12(32): 6737–48.
- Arppe R., Hyppänen I., Perälä N., Peltomaa R., Kaiser M., Würth C., et al. Quenching of the upconversion luminescence of $\text{NaYF}_4:\text{Yb}^{3+},\text{Er}^{3+}$ and $\text{NaYF}_4:\text{Yb}^{3+},\text{Tm}^{3+}$ nanophosphors by water: the role of the sensitizer Yb^{3+} in non-radiative relaxation. *Nanoscale* **2015**; 7(27): 11746–57.
- Augustine R, Hasan A, Primavera R, Wilson RJ, Thakor AS, Kevadiya BD. Cellular uptake and retention of nanoparticles: Insights on particle properties and interaction with cellular components. *Mater. Today. Commun.* **2020**; 25: 101692.
- Auzel F. Upconversion and anti-Stokes processes with f and d ions in solids. *Chem Rev* **2004**; 104(1): 139–73.
- Bakshi AK, Haider T, Tiwari R, Soni V. Critical parameters for design and development of multivalent nanoconstructs: recent trends. *Drug Deliv Transl Res* **2022**; 12(10): 2335–58.
- Balfourier A, Luciani N, Wang G, Lelong G, Ersen O, Khelifa A, et al. Unexpected intracellular biodegradation and recrystallization of gold nanoparticles. *Proc Natl Acad Sci U S A* **2020**; 117(1): 103–13.
- Banerjee I, Pangule RC, Kane RS. Antifouling coatings: recent developments in the design of surfaces that prevent fouling by proteins, bacteria, and marine organisms. *Adv. Mater.* **2011**; 23(6): 690–718.
- Barak LS, Bai Y, Peterson S, Evron T, Urs NM, Peddibhotla S, et al. ML314: A Biased Neurotensin Receptor Ligand for Methamphetamine Abuse. *ACS Chem Biol* **2016**; 11(7): 1880–90.

- Bartczak D, Baradez M-O, Goenaga-Infante H, Marshall D. Label-free monitoring of the nanoparticle surface modification effects on cellular uptake, trafficking and toxicity. *Toxicol. Res.* **2015**; 4(1): 169–76.
- Bastos V, Oskoei P, Andresen E, Saleh MI, Rühle B, Resch-Genger U, et al. Stability, dissolution, and cytotoxicity of NaYF₄-upconversion nanoparticles with different coatings. *Sci Rep* **2022**; 12(1): 3770.
- Behzadi S, Serpooshan V, Tao W, Hamaly MA, Alkawareek MY, Dreaden EC, et al. Cellular uptake of nanoparticles: journey inside the cell. *Chem Soc Rev* **2017**; 46(14): 4218–44.
- Berezin MY, Achilefu S. Fluorescence lifetime measurements and biological imaging. *Chem Rev* **2010**; 110(5): 2641–84.
- Besserer-Offroy É, Brouillette RL, Lavenus S, Froehlich U, Brumwell A, Murza A, et al. The signaling signature of the neurotensin type 1 receptor with endogenous ligands. *Eur J Pharmacol* **2017**; 805: 1–13.
- Binder H, Zschörnig O. The effect of metal cations on the phase behavior and hydration characteristics of phospholipid membranes. *Chem. Phys. Lipids* **2002**; 115(1-2): 39–61.
- Bird JL, Simpson R, Vllasaliu D, Goddard AD. Neurotensin receptor 1 facilitates intracellular and transepithelial delivery of macromolecules. *Eur J Pharm Biopharm* **2017**; 119: 300–9.
- Bortner CD, Cidlowski JA. A necessary role for cell shrinkage in apoptosis. *Biochem. Pharmacol.* **1998**; 56(12): 1549–59.
- Bourquin J, Milosevic A, Hauser D, Lehner R, Blank F, Petri-Fink A, et al. Biodistribution, Clearance, and Long-Term Fate of Clinically Relevant Nanomaterials. *Adv. Mater.* **2018**; 30(19): e1704307.
- Boya P, Kroemer G. Lysosomal membrane permeabilization in cell death. *Oncogene* **2008**; 27(50): 6434–51.
- Brown CM, Petersen NO. Free clathrin triskelions are required for the stability of clathrin-associated adaptor protein (AP-2) coated pit nucleation sites. *Biochem Cell Biol* **1999**; 77(5): 439–48.

- Brunetti J, Falciani C, Lelli B, Minervini A, Ravenni N, Depau L, et al. Neurotensin branched peptide as a tumor-targeting agent for human bladder cancer. *Biomed Res Int* **2015**; 2015: 173507.
- Buchner M, García Calavia P, Muhr V, Kröninger A, Baeumner AJ, Hirsch T, et al. Photosensitizer functionalised luminescent upconverting nanoparticles for efficient photodynamic therapy of breast cancer cells. *Photochem Photobiol Sci* **2019**; 18(1): 98–109.
- Buford MC, Hamilton RF, Holian A. A comparison of dispersing media for various engineered carbon nanoparticles. *Part. Fibre Toxicol.* **2007**; 4: 6.
- Cai R, Chen C. The Crown and the Scepter: Roles of the Protein Corona in Nanomedicine. *Adv. Mater.* **2019**; 31(45): e1805740.
- Carter D, Ho J. Structure of Serum Albumin. *Adv. Protein Chem.* **1994**(45): 153–76.
- Casals E, Pfaller T, Duschl A, Oostingh GJ, Puntès V. Time evolution of the nanoparticle protein corona. *ACS Nano* **2010**; 4(7): 3623–32.
- Chandran P, Riviere JE, Monteiro-Riviere NA. Surface chemistry of gold nanoparticles determines the biocorona composition impacting cellular uptake, toxicity and gene expression profiles in human endothelial cells. *Nanotoxicology* **2017**; 11(4): 507–19.
- Chang J-S, Chang KLB, Hwang D-F, Kong Z-L. In vitro cytotoxicity of silica nanoparticles at high concentrations strongly depends on the metabolic activity type of the cell line. *Environ. Sci. Technol.* **2007**; 41(6): 2064–8.
- Chen F, Zhang S, Bu W, Chen Y, Xiao Q, Liu J, et al. A uniform sub-50 nm-sized magnetic/upconversion fluorescent bimodal imaging agent capable of generating singlet oxygen by using a 980 nm laser. *Chemistry* **2012**; 18(23): 7082–90.
- Chen G, Jaskula-Sztul R, Esquibel CR, Lou I, Zheng Q, Dammalapati A, et al. Neuroendocrine Tumor-Targeted Upconversion Nanoparticle-Based Micelles for Simultaneous NIR-Controlled Combination Chemotherapy and Photodynamic Therapy, and Fluorescence Imaging. *Adv. Funct. Mater.* **2017**; 27(8).
- Chen G, Qiu H, Prasad PN, Chen X. Upconversion nanoparticles: design, nanochemistry, and applications in theranostics. *Chem Rev* **2014**; 114(10): 5161–214.

- Chen J, Fan T, Xie Z, Zeng Q, Xue P, Zheng T, et al. Advances in nanomaterials for photodynamic therapy applications: Status and challenges. *Biomaterials* **2020**; 237: 119827.
- Cheng X, Tian X, Wu A, Li J, Tian J, Chong Y, et al. Protein Corona Influences Cellular Uptake of Gold Nanoparticles by Phagocytic and Nonphagocytic Cells in a Size-Dependent Manner. *ACS Appl Mater Interfaces* **2015**; 7(37): 20568–75.
- Cho EC, Zhang Q, Xia Y. The effect of sedimentation and diffusion on cellular uptake of gold nanoparticles. *Nat Nanotechnol* **2011**; 6(6): 385–91.
- Chow EK-H, Ho D. Cancer nanomedicine: from drug delivery to imaging. *Sci Transl Med* **2013**; 5(216): 216rv4.
- Christou N, Blondy S, David V, Verdier M, Lalloué F, Jauberteau M-O, et al. Neurotensin pathway in digestive cancers and clinical applications: an overview. *Cell Death Dis* **2020**; 11(12): 1027.
- Cohen JM, Teeguarden JG, Demokritou P. An integrated approach for the in vitro dosimetry of engineered nanomaterials. *Part Fibre Toxicol* **2014**; 11: 20.
- Condon ND, Heddleston JM, Chew T-L, Luo L, McPherson PS, Ioannou MS, et al. Macropinosome formation by tent pole ruffling in macrophages. *J Cell Biol* **2018**; 217(11): 3873–85.
- Cullis PR, Hope MJ, Tilcock CP. Lipid polymorphism and the roles of lipids in membranes. *Chem. Phys. Lipids* **1986**; 40(2-4): 127–44.
- DaCosta MV, Doughan S, Han Y, Krull UJ. Lanthanide upconversion nanoparticles and applications in bioassays and bioimaging: a review. *Anal Chim Acta* **2014**; 832: 1–33.
- Debayle M, Balloul E, Dembele F, Xu X, Hanafi M, Ribot F, et al. Zwitterionic polymer ligands: an ideal surface coating to totally suppress protein-nanoparticle corona formation? *Biomaterials* **2019**; 219: 119357.
- Déciga-Alcaraz A, Delgado-Buenrostro NL, Ispanixtlahuatl-Meráz O, Freyre-Fonseca V, Flores-Flores JO, Ganem-Rondero A, et al. Irreversible disruption of the cytoskeleton as induced by non-cytotoxic exposure to titanium dioxide nanoparticles in lung epithelial cells. *Chem Biol Interact* **2020a**; 323: 109063.

- Déciga-Alcaraz A, Medina-Reyes EI, Delgado-Buenrostro NL, Rodríguez-Ibarra C, Ganem-Rondero A, Vázquez-Zapién GJ, et al. Toxicity of engineered nanomaterials with different physicochemical properties and the role of protein corona on cellular uptake and intrinsic ROS production. *Toxicology* **2020b**; 442: 152545.
- DeLoid GM, Cohen JM, Pyrgiotakis G, Demokritou P. Preparation, characterization, and in vitro dosimetry of dispersed, engineered nanomaterials. *Nat. Protoc.* **2017**; 12(2): 355–71.
- Demartis S, Obinu A, Gavini E, Giunchedi P, Rassu G. Nanotechnology-based rose Bengal: A broad-spectrum biomedical tool. *Dyes Pigm.* **2021a**; 188: 109236.
- Demartis S, Rassu G, Murgia S, Casula L, Giunchedi P, Gavini E. Improving Dermal Delivery of Rose Bengal by Deformable Lipid Nanovesicles for Topical Treatment of Melanoma. *Mol. Pharm.* **2021b**; 18(11): 4046–57.
- Diao S, Hong G, Antaris AL, Blackburn JL, Cheng K, Cheng Z, et al. Biological imaging without autofluorescence in the second near-infrared region. *Nano Res.* **2015**; 8(9): 3027–34.
- Ding Y, Wu F, Zhang Y, Liu X, Jong EMLD de, Gregorkiewicz T, et al. Interplay between Static and Dynamic Energy Transfer in Biofunctional Upconversion Nanoplatfoms. *J Phys Chem Lett* **2015**; 6(13): 2518–23.
- Dong A, Ye X, Chen J, Kang Y, Gordon T, Kikkawa JM, et al. A generalized ligand-exchange strategy enabling sequential surface functionalization of colloidal nanocrystals. *J Am Chem Soc* **2011**; 133(4): 998–1006.
- Dougherty TJ, Gomer CJ, Henderson BW, Jori G, Kessel D, Korbelik M, et al. Photodynamic therapy. *J Natl Cancer Inst* **1998**; 90(12): 889–905.
- Doughty MJ. Rose bengal staining as an assessment of ocular surface damage and recovery in dry eye disease-a review. *Contact Lens Anterior Eye* **2013**; 36(6): 272–80.
- Downes GB, Gautam N. The G protein subunit gene families. *Genomics* **1999**; 62(3): 544–52.
- Du B, Yu M, Zheng J. Transport and interactions of nanoparticles in the kidneys. *Nat Rev Mater* **2018**; 3(10): 358–74.

- Dukhno O, Przybilla F, Muhr V, Buchner M, Hirsch T, Mély Y. Time-dependent luminescence loss for individual upconversion nanoparticles upon dilution in aqueous solution. *Nanoscale* **2018**; 10(34): 15904–10.
- Ehrlich M, Boll W, van Oijen A, Hariharan R, Chandran K, Nibert ML, et al. Endocytosis by random initiation and stabilization of clathrin-coated pits. *Cell* **2004**; 118(5): 591–605.
- Eruslanov E, Kusmartsev S. Identification of ROS using oxidized DCFDA and flow-cytometry. *Methods Mol Biol* **2010**; 594: 57–72.
- Estebanez N, González-Béjar M, Pérez-Prieto J. Polysulfonate Cappings on Upconversion Nanoparticles Prevent Their Disintegration in Water and Provide Superior Stability in a Highly Acidic Medium. *ACS Omega* **2019**; 4(2): 3012–9.
- Fan W, Bu W, Shi J. On The Latest Three-Stage Development of Nanomedicines based on Upconversion Nanoparticles. *Adv. Mater.* **2016**; 28(21): 3987–4011.
- Faria M, Björnmalm M, Thurecht KJ, Kent SJ, Parton RG, Kavallaris M, et al. Minimum information reporting in bio-nano experimental literature. *Nat Nanotechnol* **2018**; 13(9): 777–85.
- Fedoryshin LL, Tavares AJ, Petryayeva E, Doughan S, Krull UJ. Near-infrared-triggered anticancer drug release from upconverting nanoparticles. *ACS Appl Mater Interfaces* **2014**; 6(16): 13600–6.
- Feenstra RP, Tseng SC. Comparison of Fluorescein and Rose Bengal Staining. *Ophthalmology* **1992a**; 99(4): 605–17.
- Feenstra RP, Tseng SC. What is actually stained by rose bengal? *Arch. Ophthalmol.* **1992b**; 110(7): 984–93.
- Feliu N, Sun X, Alvarez Puebla RA, Parak WJ. Quantitative Particle-Cell Interaction: Some Basic Physicochemical Pitfalls. *Langmuir* **2017**; 33(27): 6639–46.
- Feng Q, Liu Y, Huang J, Chen K, Huang J, Xiao K. Uptake, distribution, clearance, and toxicity of iron oxide nanoparticles with different sizes and coatings. *Sci Rep* **2018**; 8(1): 2082.

- Fichter KM, Flajolet M, Greengard P, Vu TQ. Kinetics of G-protein-coupled receptor endosomal trafficking pathways revealed by single quantum dots. *Proc Natl Acad Sci U S A* **2010**; 107(43): 18658–63.
- Fleischer CC, Payne CK. Nanoparticle-cell interactions: molecular structure of the protein corona and cellular outcomes. *Acc Chem Res* **2014**; 47(8): 2651–9.
- Fleming GR, Knight AWE, Morris JM, Morrison RJS, Robinson GW. Picosecond fluorescence studies of xanthene dyes. *J. Am. Chem. Soc.* **1977**; 99(13): 4306–11.
- Forest V, Pourchez J. The nanoparticle protein corona: The myth of average. *Nano Today* **2016**; 11(6): 700–3.
- Foroozandeh P, Aziz AA, Mahmoudi M. Effect of Cell Age on Uptake and Toxicity of Nanoparticles: The Overlooked Factor at the Nanobio Interface. *ACS Appl Mater Interfaces* **2019**; 11(43): 39672–87.
- Freedman NJ, Lefkowitz RJ. Desensitization of G protein-coupled receptors. *Recent Prog Horm Res* **1996**; 51: 319-51; discussion 352-3.
- Furuta S, Kisara K, Sakurada S, Sakurada T, Sasaki Y, Suzuki K. Structure-antinociceptive activity studies with neurotensin. *Br J Pharmacol* **1984**; 83(1): 43–8.
- Gainer CF, Utzinger U, Romanowski M. Scanning two-photon microscopy with upconverting lanthanide nanoparticles via Richardson-Lucy deconvolution. *J Biomed Opt* **2012**; 17(7): 76003.
- Gao J, Li R, Wang F, Liu X, Zhang J, Hu L, et al. Determining the Cytotoxicity of Rare Earth Element Nanoparticles in Macrophages and the Involvement of Membrane Damage. *Environ Sci Technol* **2017**; 51(23): 13938–48.
- García-Garayoa E, Allemann-Tannahill L, Bläuenstein P, Willmann M, Carrel-Rémy N, Tourwé D, et al. In vitro and in vivo evaluation of new radiolabeled neurotensin(8–13) analogues with high affinity for NT1 receptors. *Nucl. Med. Biol.* **2001**; 28(1): 75–84.
- García-Hevia L, Valiente R, Martín-Rodríguez R, Renero-Lecuna C, González J, Rodríguez-Fernández L, et al. Nano-ZnO leads to tubulin microtubule assembly and actin bundling, triggering cytoskeletal catastrophe and cell necrosis. *Nanoscale* **2016**; 8(21): 10963–73.

- Germain M, Caputo F, Metcalfe S, Tosi G, Spring K, Åslund AKO, et al. Delivering the power of nanomedicine to patients today. *J Control Release* **2020**; 326: 164–71.
- Giaever I, Keese CR. Monitoring fibroblast behavior in tissue culture with an applied electric field. *Proc. Natl. Acad. Sci. U.S.A.* **1984**; 81(12): 3761–4.
- Giaever I, Keese CR. Micromotion of mammalian cells measured electrically. *Proc Natl Acad Sci U S A* **1991**; 88(17): 7896–900.
- Gnach A, Lipinski T, Bednarkiewicz A, Rybka J, Capobianco JA. Upconverting nanoparticles: assessing the toxicity. *Chem. Soc. Rev.* **2015**; 44(6): 1561–84.
- Gonzalez L, Santis Puzzon M de, Ricci R, Aureli F, Guarguaglini G, Cubadda F, et al. Amorphous silica nanoparticles alter microtubule dynamics and cell migration. *Nanotoxicology* **2015**; 9(6): 729–36.
- Gonzalez-Mariscal L, Contreras RG, Bolívar JJ, Ponce A, Chávez De Ramirez B, Cereijido M. Role of calcium in tight junction formation between epithelial cells. *Am J Physiol* **1990**; 259(6 Pt 1): C978-86.
- Götz C. Expanding the Scope of Impedance Spectroscopy for the Analysis of Adherent Cells: Electrode Material, Electrode Design, and Data Analysis, 2018.
- Guillot C, Lecuit T. Mechanics of epithelial tissue homeostasis and morphogenesis. *Science* **2013**; 340(6137): 1185–9.
- Guller AE, Generalova AN, Petersen EV, Nechaev AV, Trusova IA, Landyshev NN, et al. Cytotoxicity and non-specific cellular uptake of bare and surface-modified upconversion nanoparticles in human skin cells. *Nano Res.* **2015**; 8(5): 1546–62.
- Haase M, Schäfer H. Upconverting nanoparticles. *Angew. Chem. Int. Ed.* **2011**; 50(26): 5808–29.
- Hadjidemetriou M, Kostarelos K. Nanomedicine: Evolution of the nanoparticle corona. *Nat Nanotechnol* **2017**; 12(4): 288–90.
- He M, Pang X, Liu X, Jiang B, He Y, Snaith H, et al. Monodisperse Dual-Functional Upconversion Nanoparticles Enabled Near-Infrared Organolead Halide Perovskite Solar Cells. *Angew. Chem. Int. Ed.* **2016**; 55(13): 4280–4.

- Hemmer E, Yamano T, Kishimoto H, Venkatachalam N, Hyodo H, Soga K. Cytotoxic aspects of gadolinium oxide nanostructures for up-conversion and NIR bioimaging. *Acta Biomater* **2013**; 9(1): 4734–43.
- Hild W, Pollinger K, Caporale A, Cabrele C, Keller M, Pluym N, et al. G protein-coupled receptors function as logic gates for nanoparticle binding and cell uptake. *Proc Natl Acad Sci U S A* **2010**; 107(23): 10667–72.
- Himmelstoß, Hirsch T. A critical comparison of lanthanide based upconversion nanoparticles to fluorescent proteins, semiconductor quantum dots, and carbon dots for use in optical sensing and imaging. *Methods Appl Fluoresc* **2019**; 7(2): 22002.
- Hinze C, Boucrot E. Endocytosis in proliferating, quiescent and terminally differentiated cells. *J. Cell Sci.* **2018**; 131(23).
- Homann C., L. Krukewitt, F. Frenzel, B. Grauel, C. Würth, U. Resch-Genger, et al. NaYF₄:Yb,Er/NaYF₄ Core/Shell Nanocrystals with High Upconversion Luminescence Quantum Yield. *Angew. Chem. Int. Ed.* **2018**; 57(28): 8765–9.
- Horwitz AR, Parsons JT. Cell migration--movin' on. *Science* **1999**; 286(5442): 1102–3.
- Hu X, Li D, Mu L. Biotransformation of graphene oxide nanosheets in blood plasma affects their interactions with cells. *Environ. Sci.: Nano* **2017**; 4(7): 1569–78.
- Huang P, Zheng W, Zhou S, Tu D, Chen Z, Zhu H, et al. Lanthanide-doped LiLuF₄ upconversion nanoprobe for the detection of disease biomarkers. *Angew. Chem. Int. Ed.* **2014**; 53(5): 1252–7.
- Hübner H, Schellhorn T, Gienger M, Schaab C, Kaundl J, Leeb L, et al. Structure-guided development of heterodimer-selective GPCR ligands. *Nat. Commun.* **2016**; 7: 12298.
- Iavicoli I, Calabrese EJ, Nascarella MA. Exposure to nanoparticles and hormesis. *Dose-Response* **2010**; 8(4): 501–17.
- Ingen-Housz-Oro S, Pham-Ledard A, Brice P, Lebrun-Vignes B, Zehou O, Reitter D, et al. Immediate hypersensitivity reaction to pegylated liposomal doxorubicin: management and outcome in four patients. *Eur J Dermatol* **2017**; 27(3): 271–4.

- Insel PA, Sriram K, Gorr MW, Wiley SZ, Michkov A, Salmerón C, et al. GPCRomics: An Approach to Discover GPCR Drug Targets. *Trends Pharmacol Sci* **2019**; 40(6): 378–87.
- Israelachvili JN, Mitchell DJ, Ninham BW. Theory of self-assembly of hydrocarbon amphiphiles into micelles and bilayers. *J. Chem. Soc., Faraday Trans. 2* **1976**; 72: 1525.
- Iyer BR, Mahalakshmi R. Hydrophobic Characteristic Is Energetically Preferred for Cysteine in a Model Membrane Protein. *Biophys J* **2019**; 117(1): 25–35.
- J. C. Mathai, S. Tristram-Nagle, J. F. Nagle, M. L. Zeidel. Structural determinants of water permeability through the lipid membrane. *J Gen Physiol* **2008**; 131(1): 69–76.
- Jaiswal JK, Andrews NW, Simon SM. Membrane proximal lysosomes are the major vesicles responsible for calcium-dependent exocytosis in nonsecretory cells. *J Cell Biol* **2002**; 159(4): 625–35.
- Jeevanandam J, Barhoum A, Chan YS, Dufresne A, Danquah MK. Review on nanoparticles and nanostructured materials: history, sources, toxicity and regulations. *Beilstein J Nanotechnol* **2018**; 9: 1050–74.
- Jeong J, Kim S-H, Lee S, Lee D-K, Han Y, Jeon S, et al. Differential Contribution of Constituent Metal Ions to the Cytotoxic Effects of Fast-Dissolving Metal-Oxide Nanoparticles. *Front Pharmacol* **2018**; 9: 15.
- Ji T, Xu X, Wang X, Zhou Q, Ding W, Chen B, et al. Point of care upconversion nanoparticles-based lateral flow assay quantifying myoglobin in clinical human blood samples. *Sens Actuator B Chem* **2019**; 282: 309–16.
- Jiang X, Röcker C, Hafner M, Brandholt S, Dörlich RM, Nienhaus GU. Endo- and exocytosis of zwitterionic quantum dot nanoparticles by live HeLa cells. *ACS Nano* **2010**; 4(11): 6787–97.
- Jiao Z-H, Li M, Feng Y-X, Shi J-C, Zhang J, Shao B. Hormesis effects of silver nanoparticles at non-cytotoxic doses to human hepatoma cells. *PLoS One* **2014**; 9(7): e102564.
- Jimenez-Vargas NN, Gong J, Wisdom MJ, Jensen DD, Latorre R, Hegron A, et al. Endosomal signaling of delta opioid receptors is an endogenous mechanism and therapeutic target for relief from inflammatory pain. *Proc Natl Acad Sci U S A* **2020**; 117(26): 15281–92.

- Kang Y, Nack LM, Liu Y, Qi B, Huang Y, Liu Z, et al. Quantitative considerations about the size dependence of cellular entry and excretion of colloidal nanoparticles for different cell types. *ChemTexts* **2022**; 8(1): 9.
- Keller M, Kuhn KK, Einsiedel J, Hübner H, Biselli S, Mollereau C, et al. Mimicking of Arginine by Functionalized N(ω)-Carbamoylated Arginine As a New Broadly Applicable Approach to Labeled Bioactive Peptides: High Affinity Angiotensin, Neuropeptide Y, Neuropeptide FF, and Neurotensin Receptor Ligands As Examples. *J Med Chem* **2016**; 59(5): 1925–45.
- Keller M, Mahuroof SA, Hong Yee V, Carpenter J, Schindler L, Littmann T, et al. Fluorescence Labeling of Neurotensin(8-13) via Arginine Residues Gives Molecular Tools with High Receptor Affinity. *ACS Med Chem Lett* **2020**; 11(1): 16–22.
- Kelly PM, Åberg C, Polo E, O'Connell A, Cookman J, Fallon J, et al. Mapping protein binding sites on the biomolecular corona of nanoparticles. *Nat. Nanotechnol.* **2015**; 10(5): 472–9.
- Kembuan C, Oliveira H, Graf C. Effect of different silica coatings on the toxicity of upconversion nanoparticles on RAW 264.7 macrophage cells. *Beilstein J. Nanotechnol.* **2021**; 12: 35–48.
- Kettler K, Veltman K, van de Meent D, van Wezel A, Hendriks AJ. Cellular uptake of nanoparticles as determined by particle properties, experimental conditions, and cell type. *Environ Toxicol Chem* **2014**; 33(3): 481–92.
- Khammanit R, Chantakru S, Kitiyanant Y, Saikhun J. Effect of serum starvation and chemical inhibitors on cell cycle synchronization of canine dermal fibroblasts. *Theriogenology* **2008**; 70(1): 27–34.
- Kim I-Y, Joachim E, Choi H, Kim K. Toxicity of silica nanoparticles depends on size, dose, and cell type. *Nanomedicine* **2015**; 11(6): 1407–16.
- Kim J, Kwon JH, Jang J, Lee H, Kim S, Hahn YK, et al. Rapid and background-free detection of avian influenza virus in opaque sample using NIR-to-NIR upconversion nanoparticle-based lateral flow immunoassay platform. *Biosens Bioelectron* **2018**; 112: 209–15.
- Kim JA, Åberg C, Salvati A, Dawson KA. Role of cell cycle on the cellular uptake and dilution of nanoparticles in a cell population. *Nat. Nanotechnol.* **2011**; 7(1): 62–8.

- Kim T-H, Kim M, Park H-S, Shin US, Gong M-S, Kim H-W. Size-dependent cellular toxicity of silver nanoparticles. *J Biomed Mater Res A* **2012**; 100(4): 1033–43.
- Klose C, Surma MA, Simons K. Organellar lipidomics--background and perspectives. *Curr Opin Cell Biol* **2013**; 25(4): 406–13.
- Koivula T, Koivusalo M. Partial purification and properties of a phenobarbital-induced aldehyde dehydrogenase of rat liver. *Biochim Biophys Acta* **1975**; 410(1): 1–11.
- Kooijman EE, Carter KM, van Laar EG, Chupin V, Burger KNJ, Kruijff B de. What makes the bioactive lipids phosphatidic acid and lysophosphatidic acid so special? *Biochemistry* **2005**; 44(51): 17007–15.
- Kooijman EE, Tieleman DP, Testerink C, Munnik T, Rijkers DTS, Burger KNJ, et al. An electrostatic/hydrogen bond switch as the basis for the specific interaction of phosphatidic acid with proteins. *J Biol Chem* **2007**; 282(15): 11356–64.
- Kopac T. Protein corona, understanding the nanoparticle-protein interactions and future perspectives: A critical review. *Int J Biol Macromol* **2021**; 169: 290–301.
- Lahtinen S, Lyytikäinen A, Pääkkilä H, Hömppi E, Perälä N, Lastusaari M, et al. Disintegration of Hexagonal NaYF₄:Yb³⁺,Er³⁺ Upconverting Nanoparticles in Aqueous Media: The Role of Fluoride in Solubility Equilibrium. *J. Phys. Chem. C* **2017**; 121(1): 656–65.
- Lammers T, Ferrari M. The success of nanomedicine. *Nano Today* **2020**; 31.
- Lara S, Alnasser F, Polo E, Garry D, Lo Giudice MC, Hristov DR, et al. Identification of Receptor Binding to the Biomolecular Corona of Nanoparticles. *ACS Nano* **2017**; 11(2): 1884–93.
- Latreille P-L, Le Goas M, Salimi S, Robert J, Crescenzo G de, Boffito DC, et al. Scratching the Surface of the Protein Corona: Challenging Measurements and Controversies. *ACS Nano* **2022**.
- Laurent S, Burtea C, Thirifays C, Häfeli UO, Mahmoudi M. Crucial ignored parameters on nanotoxicology: the importance of toxicity assay modifications and "cell vision". *PLoS One* **2012**; 7(1): e29997.
- Lavington S, Watts A. Lipid nanoparticle technologies for the study of G protein-coupled receptors in lipid environments. *Biophys Rev* **2020**.

- Lee C, Xu EZ, Liu Y, Teitelboim A, Yao K, Fernandez-Bravo A, et al. Giant nonlinear optical responses from photon-avalanching nanoparticles. *Nature* **2021**; 589(7841): 230–5.
- Lesniak A, Fenaroli F, Monopoli MP, Åberg C, Dawson KA, Salvati A. Effects of the presence or absence of a protein corona on silica nanoparticle uptake and impact on cells. *ACS Nano* **2012**; 6(7): 5845–57.
- Li H, Wang X, Huang D, Chen G. Recent advances of lanthanide-doped upconversion nanoparticles for biological applications. *Nanotechnology* **2020**; 31(7): 72001.
- Li R, Ji Z, Chang CH, Dunphy DR, Cai X, Meng H, et al. Surface interactions with compartmentalized cellular phosphates explain rare earth oxide nanoparticle hazard and provide opportunities for safer design. *ACS Nano* **2014**; 8(2): 1771–83.
- Li R, Ji Z, Dong J, Chang CH, Wang X, Sun B, et al. Enhancing the imaging and biosafety of upconversion nanoparticles through phosphonate coating. *ACS Nano* **2015**; 9(3): 3293–306.
- Li Y, Sun L, Jin M, Du Z, Liu X, Guo C, et al. Size-dependent cytotoxicity of amorphous silica nanoparticles in human hepatoma HepG2 cells. *Toxicol In Vitro* **2011**; 25(7): 1343–52.
- Li Z, Sun L, Zhang Y, Dove AP, O'Reilly RK, Chen G. Shape Effect of Glyco-Nanoparticles on Macrophage Cellular Uptake and Immune Response. *ACS Macro Lett* **2016**; 5(9): 1059–64.
- Li Z, Zhang Y, Jiang S. Multicolor Core/Shell-Structured Upconversion Fluorescent Nanoparticles. *Adv. Mater.* **2008**; 20(24): 4765–9.
- Liang G, Wang H, Shi H, Wang H, Zhu M, Jing A, et al. Recent progress in the development of upconversion nanomaterials in bioimaging and disease treatment. *J Nanobiotechnology* **2020**; 18(1): 154.
- Lieb S, Michaelis S, Plank N, Bernhardt G, Buschauer A, Wegener J. Label-free analysis of GPCR-stimulation: The critical impact of cell adhesion. *Pharmacol Res* **2016**; 108: 65–74.
- Lin C-AJ, Sperling RA, Li JK, Yang T-Y, Li P-Y, Zanella M, et al. Design of an amphiphilic polymer for nanoparticle coating and functionalization. *Small* **2008**; 4(3): 334–41.
- Lin XP, Mintern JD, Gleeson PA. Macropinocytosis in Different Cell Types: Similarities and Differences. *Membranes (Basel)* **2020**; 10(8).

- Lisjak D, Plohl O, Vidmar J, Majaron B, Ponikvar-Svet M. Dissolution Mechanism of Upconverting AYF₄:Yb,Tm (A = Na or K) Nanoparticles in Aqueous Media. *Langmuir* **2016**; 32(32): 8222–9.
- Lisjak D, Vozlič M, Kostiv U, Horák D, Majaron B, Kralj S, et al. NaYF₄-based upconverting nanoparticles with optimized phosphonate coatings for chemical stability and viability of human endothelial cells. *Methods Appl. Fluoresc.* **2021**; 10(1).
- Liu B, Chen Y, Li C, He F, Hou Z, Huang S, et al. Poly(Acrylic Acid) Modification of Nd³⁺ - Sensitized Upconversion Nanophosphors for Highly Efficient UCL Imaging and pH-Responsive Drug Delivery. *Adv. Funct. Mater.* **2015**; 25(29): 4717–29.
- Liu F, Ma D, Chen W, Chen X, Qian Y, Zhao Y, et al. Gold Nanoparticles Suppressed Proliferation, Migration, and Invasion in Papillary Thyroid Carcinoma Cells via Downregulation of CCT3. *J Nanomater* **2019**; 2019: 1–12.
- Liu N, Tang M. Toxic effects and involved molecular pathways of nanoparticles on cells and subcellular organelles. *J Appl Toxicol* **2020**; 40(1): 16–36.
- Ludvíková L, Friš P, Heger D, Šebej P, Wirz J, Klán P. Photochemistry of rose bengal in water and acetonitrile: a comprehensive kinetic analysis. *Phys Chem Chem Phys* **2016**; 18(24): 16266–73.
- Lukic S, Wegener J. Impedimetric Monitoring of Cell-Based Assays. *eLS* **2015**: 1–8.
- Mahmoudi M. The need for robust characterization of nanomaterials for nanomedicine applications. *Nat. Commun.* **2021**; 12(1): 5246.
- Mahmoudi M, Saeedi-Eslami SN, Shokrgozar MA, Azadmanesh K, Hassanlou M, Kalhor HR, et al. Cell "vision": complementary factor of protein corona in nanotoxicology. *Nanoscale* **2012**; 4(17): 5461–8.
- Maiorano G, Sabella S, Sorce B, Brunetti V, Malvindi MA, Cingolani R, et al. Effects of cell culture media on the dynamic formation of protein-nanoparticle complexes and influence on the cellular response. *ACS Nano* **2010**; 4(12): 7481–91.
- Mandl GA, Cooper DR, Hirsch T, Seuntjens J, Capobianco JA. Perspective: lanthanide-doped upconverting nanoparticles. *Methods Appl Fluoresc* **2019**; 7(1): 12004.

- Manuja A, Kumar B, Kumar R, Chhabra D, Ghosh M, Manuja M, et al. Metal/metal oxide nanoparticles: Toxicity concerns associated with their physical state and remediation for biomedical applications. *Toxicol Rep* **2021**; 8: 1970–8.
- Marano F, Hussain S, Rodrigues-Lima F, Baeza-Squiban A, Boland S. Nanoparticles: molecular targets and cell signalling. *Arch Toxicol* **2011**; 85(7): 733–41.
- Marichal L, Giraudon-Colas G, Cousin F, Thill A, Labarre J, Boulard Y, et al. Protein-Nanoparticle Interactions: What Are the Protein-Corona Thickness and Organization? *Langmuir* **2019**; 35(33): 10831–7.
- Märkl S, Schroter A, Hirsch T. Small and Bright Water-Protected Upconversion Nanoparticles with Long-Time Stability in Complex, Aqueous Media by Phospholipid Membrane Coating. *Nano Lett* **2020**; 20(12): 8620–5.
- Martin MM. Hydrogen bond effects on radiationless electronic transitions in xanthene dyes. *Chem Phys Lett* **1975**; 35(1): 105–11.
- Martiskainen I, Talha SM, Vuorenperä K, Salminen T, Juntunen E, Chattopadhyay S, et al. Upconverting nanoparticle reporter-based highly sensitive rapid lateral flow immunoassay for hepatitis B virus surface antigen. *Anal Bioanal Chem* **2021**; 413(4): 967–78.
- Matteis V de, Cascione M, Toma CC, Leporatti S. Morphomechanical and organelle perturbation induced by silver nanoparticle exposure. *J Nanopart Res* **2018**; 20(10).
- May ER, Kopelevich DI, Narang A. Coarse-grained molecular dynamics simulations of phase transitions in mixed lipid systems containing LPA, DOPA, and DOPE lipids. *Biophys J* **2008**; 94(3): 878–90.
- McMahon HT, Boucrot E. Membrane curvature at a glance. *J Cell Sci* **2015**; 128(6): 1065–70.
- Meijer, V. S. Talens, M. F. Hilbers, R. E. Kieltyka, A. M. Brouwer, M. M. Natile, et al. NIR-Light-Driven Generation of Reactive Oxygen Species Using Ru(II)-Decorated Lipid-Encapsulated Upconverting Nanoparticles. *Langmuir* **2019**; 35(37): 12079–90.
- Mendez-Gonzalez D, Torres Vera V, Zabala Gutierrez I, Gerke C, Cascales C, Rubio-Retama J, et al. Upconverting Nanoparticles in Aqueous Media: Not a Dead-End Road. Avoiding Degradation by Using Hydrophobic Polymer Shells. *Small* **2022**; 18(8): e2105652.

- Milani S, Bombelli FB, Pitek AS, Dawson KA, Rädler J. Reversible versus irreversible binding of transferrin to polystyrene nanoparticles: soft and hard corona. *ACS Nano* **2012**; 6(3): 2532–41.
- Mironava T, Hadjiargyrou M, Simon M, Jurukovski V, Rafailovich MH. Gold nanoparticles cellular toxicity and recovery: effect of size, concentration and exposure time. *Nanotoxicology* **2010**; 4(1): 120–37.
- Misra SK, Dybowska A, Berhanu D, Luoma SN, Valsami-Jones E. The complexity of nanoparticle dissolution and its importance in nanotoxicological studies. *Sci Total Environ* **2012**; 438: 225–32.
- Moan J, Berg K. The photodegradation of porphyrins in cells can be used to estimate the lifetime of singlet oxygen. *Photochem Photobiol* **1991**; 53(4): 549–53.
- Mohamed M, Abu Lila AS, Shimizu T, Alaaeldin E, Hussein A, Sarhan HA, et al. PEGylated liposomes: immunological responses. *Sci Technol Adv Mater* **2019**; 20(1): 710–24.
- Mouritsen OG. Lipids, curvature, and nano-medicine. *Eur J Lipid Sci Technol* **2011**; 113(10): 1174–87.
- Muhr V, Würth C, Kraft M, Buchner M, Baeumner AJ, Resch-Genger U, et al. Particle-Size-Dependent Förster Resonance Energy Transfer from Upconversion Nanoparticles to Organic Dyes. *Anal. Chem.* **2017**; 89(9): 4868–74.
- Nagarajan R. Molecular Packing Parameter and Surfactant Self-Assembly: The Neglected Role of the Surfactant Tail. *Langmuir* **2002**; 18(1): 31–8.
- Navarro V, Martin S, Mazella J. Internalization-dependent regulation of HT29 cell proliferation by neurotensin. *Peptides* **2006**; 27(10): 2502–7.
- Nehls S, Nöding H, Karsch S, Ries F, Janshoff A. Stiffness of MDCK II Cells Depends on Confluency and Cell Size. *Biophys J* **2019**; 116(11): 2204–11.
- Niedergang F, Grinstein S. How to build a phagosome: new concepts for an old process. *Curr Opin Cell Biol* **2018**; 50: 57–63.

- Nomikou N, Fowley C, Byrne NM, McCaughan B, McHale AP, Callan JF. Microbubble-sonosensitizer conjugates as therapeutics in sonodynamic therapy. *Chem Commun (Camb)* **2012**; 48(67): 8332–4.
- Oliveira H, Bednarkiewicz A, Falk A, Fröhlich E, Lisjak D, Prina-Mello A, et al. Critical Considerations on the Clinical Translation of Upconversion Nanoparticles (UCNPs): Recommendations from the European Upconversion Network (COST Action CM1403). *Adv Healthc Mater* **2019**; 8(1): e1801233.
- Ouyang Q, Zhou J, Yang W, Cui H, Xu M, Yi L. Oncogenic role of neurotensin and neurotensin receptors in various cancers. *Clin Exp Pharmacol Physiol* **2017**; 44(8): 841–6.
- P. A. Rojas-Gutierrez, C. DeWolf, J. A. Capobianco. Formation of a Supported Lipid Bilayer on Faceted $\text{LiYF}_4:\text{Yb}^{3+}/\text{Er}^{3+}$ Upconversion Nanoparticles. *Part. Part. Syst. Charact.* **2016**; 33(12): 865–70.
- P. A. Rojas-Gutierrez, D. Bekah, J. Seuntjens, C. DeWolf, J. A. Capobianco. Cellular Uptake, Cytotoxicity and Trafficking of Supported Lipid-Bilayer-Coated Lanthanide Upconverting Nanoparticles in Alveolar Lung Cancer Cells. *ACS Appl. Bio Mater.* **2019**; 2(10): 4527–36.
- Paine PL, Moore LC, Horowitz SB. Nuclear envelope permeability. *Nature* **1975**; 254(5496): 109–14.
- Palm W. Metabolic functions of macropinocytosis. *Philos Trans R Soc Lond , B, Biol Sci* **2019**; 374(1765): 20180285.
- Panet E, Mashriki T, Lahmi R, Jacob A, Ozer E, Vecsler M, et al. The interface of nanoparticles with proliferating mammalian cells. *Nat. Nanotechnol.* **2017**; 12(7): 598–600.
- Park J, An K, Hwang Y, Park J-G, Noh H-J, Kim J-Y, et al. Ultra-large-scale syntheses of monodisperse nanocrystals. *Nat Mater* **2004**; 3(12): 891–5.
- Park K. The beginning of the end of the nanomedicine hype. *J Control Release* **2019**; 305: 221–2.
- Park YI, Lee KT, Suh YD, Hyeon T. Upconverting nanoparticles: a versatile platform for wide-field two-photon microscopy and multi-modal in vivo imaging. *Chem Soc Rev* **2015**; 44(6): 1302–17.

- Parsons JT, Horwitz AR, Schwartz MA. Cell adhesion: integrating cytoskeletal dynamics and cellular tension. *Nat Rev Mol Cell Biol* **2010**; 11(9): 633–43.
- Partikel K, Korte R, Mulac D, Humpf H-U, Langer K. Serum type and concentration both affect the protein-corona composition of PLGA nanoparticles. *Beilstein J Nanotechnol* **2019**; 10: 1002–15.
- Patra JK, Das G, Fraceto LF, Campos EVR, Del Rodriguez-Torres MP, Acosta-Torres LS, et al. Nano based drug delivery systems: recent developments and future prospects. *J Nanobiotechnology* **2018**; 16(1): 71.
- Pelaz B, Alexiou C, Alvarez-Puebla RA, Alves F, Andrews AM, Ashraf S, et al. Diverse Applications of Nanomedicine. *ACS Nano* **2017**; 11(3): 2313–81.
- Peng X, Huang B, Pu R, Liu H, Zhang T, Widengren J, et al. Fast upconversion super-resolution microscopy with 10 μ s per pixel dwell times. *Nanoscale* **2019**; 11(4): 1563–9.
- Pereira PCdS, Costa PFdA, Pellosi DS, Calori IR, Vilsinski BH, Estevão BM, et al. Photophysical properties and interaction studies of Rose Bengal derivatives with biomimetic systems based in micellar aqueous solutions. *J Mol Liq* **2017**; 230: 674–85.
- Peters MF, Scott CW. Evaluating cellular impedance assays for detection of GPCR pleiotropic signaling and functional selectivity. *J Biomol Screen* **2009**; 14(3): 246–55.
- Pichaandi J, Boyer J-C, Delaney KR, van Veggel FCJM. Two-Photon Upconversion Laser (Scanning and Wide-Field) Microscopy Using Ln^{3+} -Doped NaYF_4 Upconverting Nanocrystals: A Critical Evaluation of their Performance and Potential in Bioimaging. *J. Phys. Chem. C* **2011**; 115(39): 19054–64.
- Pierce KL, Lefkowitz RJ. Classical and new roles of beta-arrestins in the regulation of G-protein-coupled receptors. *Nat Rev Neurosci* **2001**; 2(10): 727–33.
- Plohl O, Kraft M, Kovač J, Belec B, Ponikvar-Svet M, Würth C, et al. Optically Detected Degradation of $\text{NaYF}_4\text{:Yb,Tm}$ -Based Upconversion Nanoparticles in Phosphate Buffered Saline Solution. *Langmuir* **2017a**; 33(2): 553–60.

- Plohl O, Kralj S, Majaron B, Fröhlich E, Ponikvar-Svet M, Makovec D, et al. Amphiphilic coatings for the protection of upconverting nanoparticles against dissolution in aqueous media. *Dalton Trans.* **2017b**; 46(21): 6975–84.
- Pollard TD, Borisy GG. Cellular Motility Driven by Assembly and Disassembly of Actin Filaments. *Cell* **2003**; 112(4): 453–65.
- Pombo García K, Zarschler K, Barbaro L, Barreto JA, O'Malley W, Spiccia L, et al. Zwitterionic-coated "stealth" nanoparticles for biomedical applications: recent advances in countering biomolecular corona formation and uptake by the mononuclear phagocyte system. *Small* **2014**; 10(13): 2516–29.
- Porter GC, Duncan WJ, Jude A, Abdelmoneim D, Easingwood RA, Coates DE. Endocytosed silver nanoparticles degrade in lysosomes to form secondary nanoparticle structures during expression of autophagy genes in osteogenic cells. *Nanomedicine* **2021**; 33: 102355.
- Qiu H, Tan M, Ohulchanskyy TY, Lovell JF, Chen G. Recent Progress in Upconversion Photodynamic Therapy. *Nanomaterials (Basel)* **2018**; 8(5).
- Qiu S, Pellino G, Fiorentino F, Rasheed S, Darzi A, Tekkis P, et al. A Review of the Role of Neurotensin and Its Receptors in Colorectal Cancer. *Gastroenterol Res Pract* **2017**; 2017: 6456257.
- Rafique R, Baek SH, Park CY, Chang S-J, Gul AR, Ha S, et al. Morphological evolution of upconversion nanoparticles and their biomedical signal generation. *Sci Rep* **2018**; 8(1): 17101.
- Rampado R, Crotti S, Caliceti P, Pucciarelli S, Agostini M. Recent Advances in Understanding the Protein Corona of Nanoparticles and in the Formulation of "Stealthy" Nanomaterials. *Front Bioeng Biotechnol* **2020**; 8: 166.
- Rankovic Z, Brust TF, Bohn LM. Biased agonism: An emerging paradigm in GPCR drug discovery. *Bioorg Med Chem Lett* **2016**; 26(2): 241–50.
- Rauch J, Kolch W, Laurent S, Mahmoudi M. Big signals from small particles: regulation of cell signaling pathways by nanoparticles. *Chem Rev* **2013**; 113(5): 3391–406.

- Rauch J, Kolch W, Mahmoudi M. Cell type-specific activation of AKT and ERK signaling pathways by small negatively-charged magnetic nanoparticles. *Sci Rep* **2012**; 2: 868.
- Rees P, Wills JW, Brown MR, Barnes CM, Summers HD. The origin of heterogeneous nanoparticle uptake by cells. *Nat. Commun.* **2019**; 10(1): 2341.
- Reiss B, Wegener J. Impedance analysis of different cell monolayers grown on gold-film electrodes. *Annu Int Conf IEEE Eng Med Biol Soc* **2015**; 2015: 7079–82.
- Rennick JJ, Johnston APR, Parton RG. Key principles and methods for studying the endocytosis of biological and nanoparticle therapeutics. *Nat. Nanotechnol.* **2021**; 16(3): 266–76.
- Rewatkar PV, Parton RG, Parekh HS, Parat M-O. Are caveolae a cellular entry route for non-viral therapeutic delivery systems? *Adv Drug Deliv Rev* **2015**; 91: 92–108.
- Rim KT, Koo KH, Park JS. Toxicological evaluations of rare earths and their health impacts to workers: a literature review. *Saf Health Work* **2013**; 4(1): 12–26.
- Rinkel T, Nordmann J, Raj AN, Haase M. Ostwald-ripening and particle size focussing of sub-10 nm NaYF₄ upconversion nanocrystals. *Nanoscale* **2014**; 6(23): 14523–30.
- Rock KL, Kono H. The inflammatory response to cell death. *Annu. Rev. Pathol.* **2008**; 3: 99–126.
- Rodríguez-Hernández AG, Vazquez-Duhalt R, Huerta-Saquero A. Nanoparticle-plasma Membrane Interactions: Thermodynamics, Toxicity and Cellular Response. *Curr Med Chem* **2020**; 27(20): 3330–45.
- Rojas-Gutierrez PA, Bekah D, Seuntjens J, DeWolf C, Capobianco JA. Cellular Uptake, Cytotoxicity and Trafficking of Supported Lipid-Bilayer-Coated Lanthanide Upconverting Nanoparticles in Alveolar Lung Cancer Cells. *ACS Appl. Bio Mater.* **2019**; 2(10): 4527–36.
- Rojas-Gutierrez PA, DeWolf C, Capobianco JA. Formation of a Supported Lipid Bilayer on Faceted LiYF₄:Tm³⁺/Yb³⁺ Upconversion Nanoparticles. *Part. Part. Syst. Charact.* **2016**; 33(12): 865–70.
- Rosenbaum DM, Rasmussen SGF, Kobilka BK. The structure and function of G-protein-coupled receptors. *Nature* **2009**; 459(7245): 356–63.
- S. Wilhelm. Perspectives for Upconverting Nanoparticles. *ACS Nano* **2017**; 11(11): 10644–53.

- Saha K, Rahimi M, Yazdani M, Kim ST, Moyano DF, Hou S, et al. Regulation of Macrophage Recognition through the Interplay of Nanoparticle Surface Functionality and Protein Corona. *ACS Nano* **2016**; 10(4): 4421–30.
- Sakhtianchi R, Minchin RF, Lee K-B, Alkilany AM, Serpooshan V, Mahmoudi M. Exocytosis of nanoparticles from cells: role in cellular retention and toxicity. *Adv Colloid Interface Sci* **2013**; 201-202: 18–29.
- Saleh MI, Rühle B, Wang S, Radnik J, You Y, Resch-Genger U. Assessing the protective effects of different surface coatings on NaYF₄:Yb³⁺, Er³⁺ upconverting nanoparticles in buffer and DMEM. *Sci. Rep.* **2020**; 10(1): 19318.
- Salvati A, Pitek AS, Monopoli MP, Prapainop K, Bombelli FB, Hristov DR, et al. Transferrin-functionalized nanoparticles lose their targeting capabilities when a biomolecule corona adsorbs on the surface. *Nat Nanotechnol* **2013**; 8(2): 137–43.
- Saw PE, Xu X, Zhang M, Cao S, Farokhzad OC, Wu J. Nanostructure Engineering by Simple Tuning of Lipid Combinations. *Angew. Chem. Int. Ed.* **2020**; 59(15): 6249–52.
- Schrand AM, Rahman MF, Hussain SM, Schlager JJ, Smith DA, Syed AF. Metal-based nanoparticles and their toxicity assessment. *Wiley Interdiscip Rev Nanomed Nanobiotechnol* **2010**; 2(5): 544–68.
- Schroter A, Märkl S, Weitzel N, Hirsch T. Upconversion Nanocrystals with High Lanthanide Content: Luminescence Loss by Energy Migration versus Luminescence Enhancement by Increased NIR Absorption. *Adv. Funct. Mater.* **2022**: 2113065.
- Scott CW, Peters MF. Label-free whole-cell assays: expanding the scope of GPCR screening. *Drug Discov Today* **2010**; 15(17-18): 704–16.
- Seiffert JM, Baradez M-O, Nischwitz V, Lekishvili T, Goenaga-Infante H, Marshall D. Dynamic monitoring of metal oxide nanoparticle toxicity by label free impedance sensing. *Chem. Res. Toxicol.* **2012**; 25(1): 140–52.
- Shang L, Nienhaus K, Nienhaus GU. Engineered nanoparticles interacting with cells: size matters. *J Nanobiotechnology* **2014**; 12: 5.

- Sharma A, Kontodimas K, Bosmann M. Nanomedicine: A Diagnostic and Therapeutic Approach to COVID-19. *Front Med* **2021**; 8: 648005.
- Shi J, Kantoff PW, Wooster R, Farokhzad OC. Cancer nanomedicine: progress, challenges and opportunities. *Nat Rev Cancer* **2017**; 17(1): 20–37.
- Snijder B, Sacher R, Rämö P, Damm E-M, Liberali P, Pelkmans L. Population context determines cell-to-cell variability in endocytosis and virus infection. *Nature* **2009**; 461(7263): 520–3.
- Sood A, Salih S, Roh D, Lacharme-Lora L, Parry M, Hardiman B, et al. Signalling of DNA damage and cytokines across cell barriers exposed to nanoparticles depends on barrier thickness. *Nat Nanotechnol* **2011**; 6(12): 824–33.
- Sousa de Almeida M, Susnik E, Drasler B, Taladriz-Blanco P, Petri-Fink A, Rothen-Rutishauser B. Understanding nanoparticle endocytosis to improve targeting strategies in nanomedicine. *Chem. Soc. Rev.* **2021**; 50(9): 5397–434.
- Sperber M, Hupf C, Lemberger M-M, Goricnik B, Hinterreiter N, Lukic S, et al. Monitoring the Impact of Nanomaterials on Animal Cells by Impedance Analysis: A Noninvasive, Label-Free, and Multimodal Approach. *Springer International Publishing*, 2016.
- Spinnler K, Krüchten L von, Konieczny A, Schindler L, Bernhardt G, Keller M. An Alkyne-functionalized Arginine for Solid-Phase Synthesis Enabling "Bioorthogonal" Peptide Conjugation. *ACS Med Chem Lett* **2020**; 11(3): 334–9.
- Stebbing A. Hormesis — The stimulation of growth by low levels of inhibitors. *Sci Total Environ* **1982**; 22(3): 213–34.
- Stolwijk JA, Skiba M, Kade C, Bernhardt G, Buschauer A, Hübner H, et al. Increasing the throughput of label-free cell assays to study the activation of G-protein-coupled receptors by using a serial agonist exposure protocol. *Integr Biol* **2019**.
- Studer AM, Limbach LK, van Duc L, Krumeich F, Athanassiou EK, Gerber LC, et al. Nanoparticle cytotoxicity depends on intracellular solubility: comparison of stabilized copper metal and degradable copper oxide nanoparticles. *Toxicol Lett* **2010**; 197(3): 169–74.

- Su G, Zhou X, Zhou H, Li Y, Zhang X, Liu Y, et al. Size-Dependent Facilitation of Cancer Cell Targeting by Proteins Adsorbed on Nanoparticles. *ACS Appl Mater Interfaces* **2016**; 8(44): 30037–47.
- Summers HD, Rees P, Holton MD, Brown MR, Chappell SC, Smith PJ, et al. Statistical analysis of nanoparticle dosing in a dynamic cellular system. *Nat. Nanotechnol.* **2011**; 6(3): 170–4.
- Sun D, Zhou S, Gao W. What Went Wrong with Anticancer Nanomedicine Design and How to Make It Right. *ACS Nano* **2020**; 14(10): 12281–90.
- Suyver JF, Grimm J, van Veen MK, Biner D, Krämer KW, Güdel HU. Upconversion spectroscopy and properties of NaYF₄ doped with Er³⁺, TM³⁺ and/or Yb³⁺. *Journal of Luminescence* **2006**; 117(1): 1–12.
- Tan MC, Al-Baroudi L, Riman RE. Surfactant effects on efficiency enhancement of infrared-to-visible upconversion emissions of NaYF₄:Yb-Er. *ACS Appl Mater Interfaces* **2011**; 3(10): 3910–5.
- Tanaka M, Fujimoto K, Yumura S. Regulation of the Total Cell Surface Area in Dividing Dictyostelium Cells. *Front Cell Dev Biol* **2020**; 8: 238.
- Taulet N, Delorme-Walker VD, DerMardirossian C. Reactive oxygen species regulate protrusion efficiency by controlling actin dynamics. *PLoS One* **2012**; 7(8): e41342.
- Teeguarden JG, Hinderliter PM, Orr G, Thrall BD, Pounds JG. Particokinetics In Vitro: Dosimetry Considerations for In Vitro Nanoparticle Toxicology Assessments. *Toxicol Sci* **2007**; 97(2): 614.
- Tenzer S, Docter D, Kuharev J, Musyanovych A, Fetz V, Hecht R, et al. Rapid formation of plasma protein corona critically affects nanoparticle pathophysiology. *Nat Nanotechnol* **2013**; 8(10): 772–81.
- Tian J, Zeng X, Xie X, Han S, Liew O-W, Chen Y-T, et al. Intracellular Adenosine Triphosphate Deprivation through Lanthanide-Doped Nanoparticles. *J Am Chem Soc* **2015**; 137(20): 6550–8.

- Tong L, Lu E, Pichaandi J, Cao P, Nitz M, Winnik MA. Quantification of Surface Ligands on NaYF₄ Nanoparticles by Three Independent Analytical Techniques. *Chem. Mater.* **2015**; 27(13): 4899–910.
- Tonigold M, Simon J, Estupiñán D, Kokkinopoulou M, Reinholz J, Kintzel U, et al. Pre-adsorption of antibodies enables targeting of nanocarriers despite a biomolecular corona. *Nat Nanotechnol* **2018**; 13(9): 862–9.
- Torresan MF, Wolosiuk A. Critical Aspects on the Chemical Stability of NaYF₄-Based Upconverting Nanoparticles for Biomedical Applications. *ACS Appl. Bio Mater.* **2021**; 4(2): 1191–210.
- Turner JT, James-Kracke MR, Camden JM. Regulation of the neurotensin receptor and intracellular calcium mobilization in HT29 cells. *J Pharmacol Exp Ther* **1990**; 253(3): 1049–56.
- Umair M, Javed I, Rehman M, Madni A, Javeed A, Ghafoor A, et al. Nanotoxicity of Inert Materials: The Case of Gold, Silver and Iron. *J Pharm Pharm Sci* **2016**; 19(2): 161–80.
- Unfried K, Albrecht C, Klotz L-O, Mikecz A von, Grether-Beck S, Schins RP. Cellular responses to nanoparticles: Target structures and mechanisms. *Nanotoxicology* **2007**; 1(1): 52–71.
- Utembe W, Potgieter K, Stefaniak AB, Gulumian M. Dissolution and biodurability: Important parameters needed for risk assessment of nanomaterials. *Part Fibre Toxicol* **2015**; 12: 11.
- V. Muhr, S. Wilhelm, T. Hirsch, O. S. Wolfbeis. Upconversion nanoparticles: from hydrophobic to hydrophilic surfaces. *Acc Chem Res* **2014**; 47(12): 3481–93.
- Valenzeno DP, Trudgen J, Hutzenbuhler A, Milne M. Singlet oxygen involvement in photohemolysis sensitized by merocyanine-540 and rose bengal. *Photochem Photobiol* **1987**; 46(6): 985–90.
- Venkatakrishnan AJ, Deupi X, Lebon G, Tate CG, Schertler GF, Babu MM. Molecular signatures of G-protein-coupled receptors. *Nature* **2013**; 494(7436): 185–94.
- Vozlič M, Černič T, Gyergyek S, Majaron B, Ponikvar-Svet M, Kostiv U, et al. Formation of phosphonate coatings for improved chemical stability of upconverting nanoparticles under physiological conditions. *Dalton Trans.* **2021**; 50(19): 6588–97.

- Vuong NQ, Goegan P, Mohottalage S, Breznan D, Ariganello M, Williams A, et al. Proteomic changes in human lung epithelial cells (A549) in response to carbon black and titanium dioxide exposures. *J Proteomics* **2016**; 149: 53–63.
- Walczyk D, Bombelli FB, Monopoli MP, Lynch I, Dawson KA. What the cell "sees" in bionanoscience. *J Am Chem Soc* **2010**; 132(16): 5761–8.
- Wang C, Cheng L, Liu Z. Upconversion nanoparticles for photodynamic therapy and other cancer therapeutics. *Theranostics* **2013**; 3(5): 317–30.
- Wang C, He M, Chen B, Hu B. Study on cytotoxicity, cellular uptake and elimination of rare-earth-doped upconversion nanoparticles in human hepatocellular carcinoma cells. *Ecotoxicol. Environ. Saf.* **2020**; 203: 110951.
- Wang C, Tao H, Cheng L, Liu Z. Near-infrared light induced in vivo photodynamic therapy of cancer based on upconversion nanoparticles. *Biomaterials* **2011**; 32(26): 6145–54.
- Wang F, Gómez-Sintes R, Boya P. Lysosomal membrane permeabilization and cell death. *Traffic* **2018**; 19(12): 918–31.
- Wang M, Petersen NO. Characterization of phospholipid-encapsulated gold nanoparticles: a versatile platform to study drug delivery and cellular uptake mechanisms. *Can. J. Chem.* **2015**; 93(2): 265–71.
- Wegener J, Keese CR, Giaever I. Electric cell-substrate impedance sensing (ECIS) as a noninvasive means to monitor the kinetics of cell spreading to artificial surfaces. *Exp Cell Res* **2000**; 259(1): 158–66.
- Wegener J, Zink S, Rösen P, Galla H. Use of electrochemical impedance measurements to monitor beta-adrenergic stimulation of bovine aortic endothelial cells. *Pflugers Arch* **1999**; 437(6): 925–34.
- Weissleder R. A clearer vision for in vivo imaging. *Nat Biotechnol* **2001**; 19(4): 316–7.
- Weissleder R, Kelly K, Sun EY, Shtatland T, Josephson L. Cell-specific targeting of nanoparticles by multivalent attachment of small molecules. *Nat Biotechnol* **2005**; 23(11): 1418–23.
- Wen S, Zhou J, Zheng K, Bednarkiewicz A, Liu X, Jin D. Advances in highly doped upconversion nanoparticles. *Nat. Commun.* **2018**; 9(1): 2415.

- White JF, Noinaj N, Shibata Y, Love J, Kloss B, Xu F, et al. Structure of the agonist-bound neurotensin receptor. *Nature* **2012**; 490(7421): 508–13.
- Wiesholler LM, Hirsch T. Strategies for the design of bright upconversion nanoparticles for bioanalytical applications. *Optical Materials* **2018**; 80: 253–64.
- Wilhelm S, Kaiser M, Würth C, Heiland J, Carrillo-Carrion C, Muhr V, et al. Water dispersible upconverting nanoparticles: effects of surface modification on their luminescence and colloidal stability. *Nanoscale* **2015**; 7(4): 1403–10.
- Wilhelm S, Tavares AJ, Dai Q, Ohta S, Audet J, Dvorak HF, et al. Analysis of nanoparticle delivery to tumours. *Nat Rev Mater* **2016**; 1(5).
- Woods AS, Ferré S. Amazing stability of the arginine-phosphate electrostatic interaction. *J Proteome Res* **2005**; 4(4): 1397–402.
- Wu Z, Martinez-Fong D, Trédaniel J, Forgez P. Neurotensin and its high affinity receptor 1 as a potential pharmacological target in cancer therapy. *Front endocrinol* **2012**; 3: 184.
- Wysokińska E, Cichos J, Kowalczyk A, Karbowski M, Strzdała L, Bednarkiewicz A, et al. Toxicity Mechanism of Low Doses of NaGdF₄:Yb³⁺,Er³⁺ Upconverting Nanoparticles in Activated Macrophage Cell Lines. *Biomolecules* **2019**; 9(1).
- Xia T, Kovochich M, Liong M, Mädler L, Gilbert B, Shi H, et al. Comparison of the mechanism of toxicity of zinc oxide and cerium oxide nanoparticles based on dissolution and oxidative stress properties. *ACS Nano* **2008**; 2(10): 2121–34.
- Yang FY, Huang YG, Tu YP. Divalent cation and lipid-protein interactions of biomembranes. *Biosci Rep* **1993**; 13(3): 143–57.
- Yang W, Wang L, Mettenbrink EM, DeAngelis PL, Wilhelm S. Nanoparticle Toxicology. *Annu. Rev. Pharmacol. Toxicol.* **2021**; 61: 269–89.
- Yang Y. Upconversion nanophosphors for use in bioimaging, therapy, drug delivery and bioassays. *Microchim Acta* **2014**; 181(3-4): 263–94.
- Yang Z, Loh KY, Chu Y-T, Feng R, Satyavolu NSR, Xiong M, et al. Optical Control of Metal Ion Probes in Cells and Zebrafish Using Highly Selective DNAzymes Conjugated to Upconversion Nanoparticles. *J Am Chem Soc* **2018**; 140(50): 17656–65.

- Yazdimamaghani M, Barber ZB, Hadipour Moghaddam SP, Ghandehari H. Influence of Silica Nanoparticle Density and Flow Conditions on Sedimentation, Cell Uptake, and Cytotoxicity. *Mol Pharm* **2018**; 15(6): 2372–83.
- Yin W, Li Z, Jin M, Yin Y-L, Waal PW de, Pal K, et al. A complex structure of arrestin-2 bound to a G protein-coupled receptor. *Cell Res* **2019**; 29(12): 971–83.
- Yu M, Li F, Chen Z, Hu H, Zhan C, Yang H, et al. Laser scanning up-conversion luminescence microscopy for imaging cells labeled with rare-earth nanophosphors. *Anal Chem* **2009**; 81(3): 930–5.
- Yu Q, Rodriguez EM, Naccache R, Forgione P, Lamoureux G, Sanz-Rodriguez F, et al. Chemical modification of temoporfin--a second generation photosensitizer activated using upconverting nanoparticles for singlet oxygen generation. *Chem Comm* **2014**; 50(81): 12150–3.
- Zarschler K, Prapainop K, Mahon E, Rocks L, Bramini M, Kelly PM, et al. Diagnostic nanoparticle targeting of the EGF-receptor in complex biological conditions using single-domain antibodies. *Nanoscale* **2014**; 6(11): 6046–56.
- Zegarlińska J, Piaścik M, Sikorski AF, Czogalla A. Phosphatidic acid - a simple phospholipid with multiple faces. *Acta Biochim Pol* **2018**; 65(2): 163–71.
- Zhang C, Yan L, Wang X, Zhu S, Chen C, Gu Z, et al. Progress, challenges, and future of nanomedicine. *Nano Today* **2020a**; 35: 101008.
- Zhang L, He R, Gu H-C. Oleic acid coating on the monodisperse magnetite nanoparticles. *Appl Surf Sci* **2006**; 253(5): 2611–7.
- Zhang X-D, Di Wu, Shen X, Liu P-X, Yang N, Zhao B, et al. Size-dependent in vivo toxicity of PEG-coated gold nanoparticles. *Int J Nanomedicine* **2011**; 6: 2071–81.
- Zhang Y, Wiesholler LM, Rabie H, Jiang P, Lai J, Hirsch T, et al. Remote Control of Neural Stem Cell Fate Using NIR-Responsive Photoswitching Upconversion Nanoparticle Constructs. *ACS Appl Mater Interfaces* **2020b**; 12(36): 40031–41.
- Zhu S, Tian R, Antaris AL, Chen X, Dai H. Near-Infrared-II Molecular Dyes for Cancer Imaging and Surgery. *Adv. Mater.* **2019**; 31(24): e1900321.

Zinkl M, Wegener J. Using animal cells as sensors for xenobiotics: monitoring phenotypic changes by multimodal impedance assays. *Curr Opin Environ Sci* **2019**; 10: 30–7.

11 Appendix

11.1 Supporting Figures and Tables

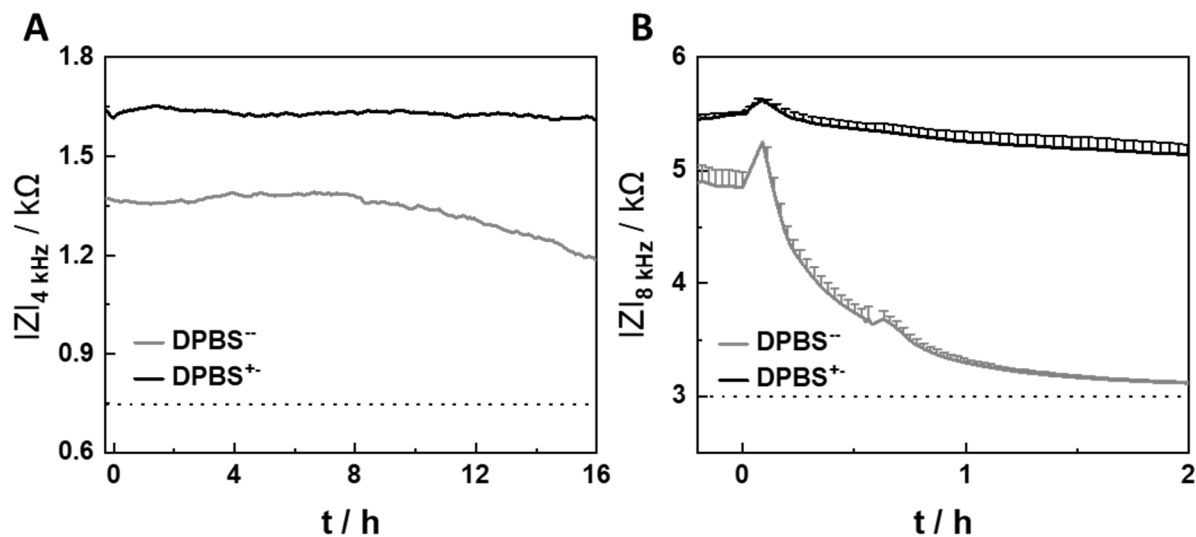


Figure A 1. Impedance time course (A) at 4 kHz of NRK cells on an 8W10E array ($N = 1$) and (B) at 8 kHz of HT-29 cells on a 96W1E⁺ array (mean \pm SEM, $N = 3$) at 37 °C in DPBS⁻ and DPBS⁺ (DPBS⁻, 180 μM CaCl_2). Cell medium was exchanged with buffers at time point 0 h. Dashed lines represent the values of a cell-free electrode.

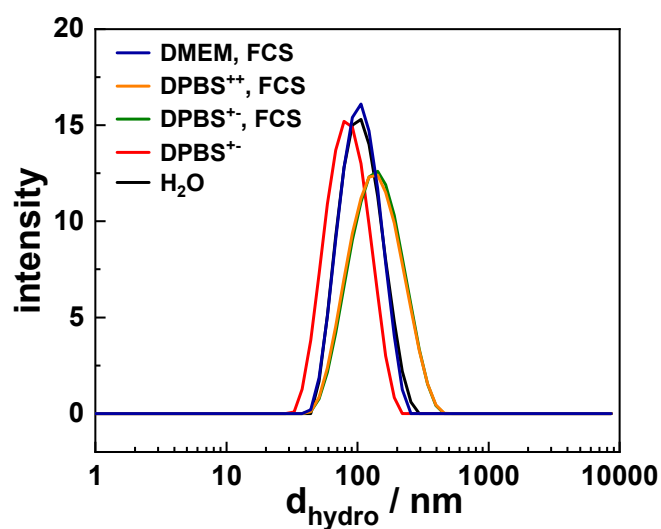


Figure A 2. Representative intensity weighted hydrodynamic diameter distribution (d_{hydro}) of 12 nm UCNPs@PLM at rt in H₂O, DPBS⁺, DPBS⁺ (5% FCS), DPBS⁺⁺ (5% FCS) and DMEM (5% FCS).

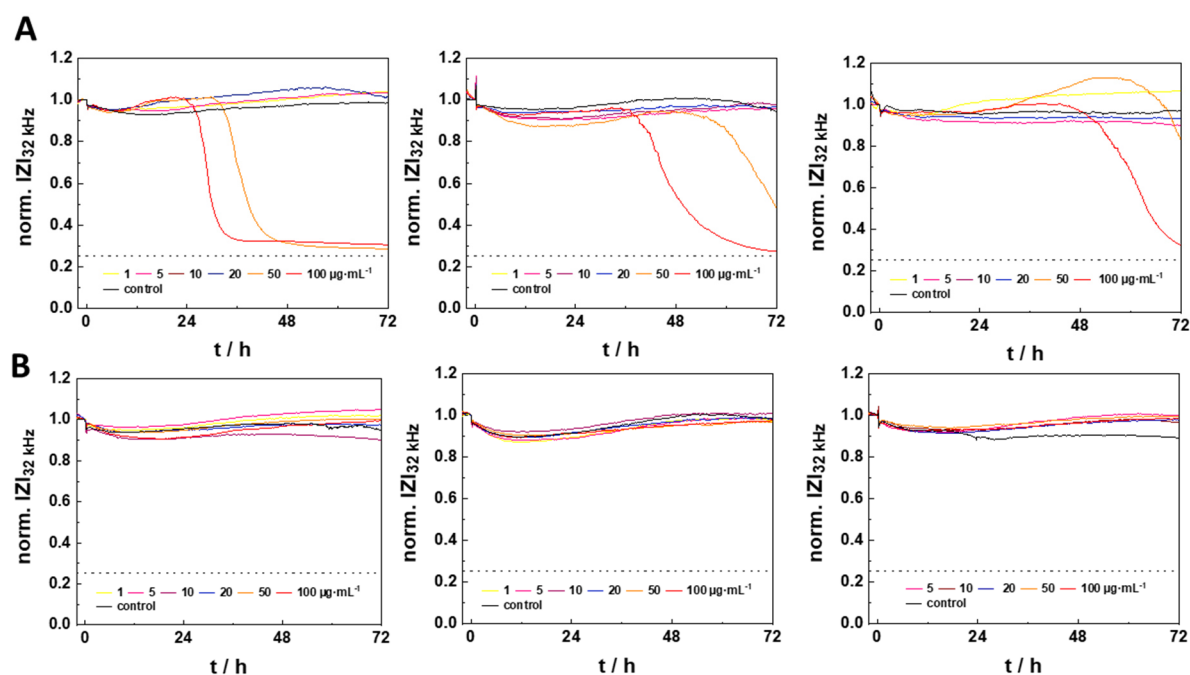


Figure A 3. Averaged and normalized impedance time courses of NRK cells at 32 kHz, exposed to 33 nm (A) UCNPs@AP and (B) UCNPs@PLM (1 - 100 µg·mL⁻¹, DPBS, 5% FCS, 1 mg·mL⁻¹ glucose) at time point 0 h at 37 °C. Three representative measurements with cells from rising passage number (subculture 24 – 27, left to right). Dotted lines represent cell-free impedance level. Average baseline impedance magnitude was (1.08 ± 0.01) kΩ before compound addition (N = 24).

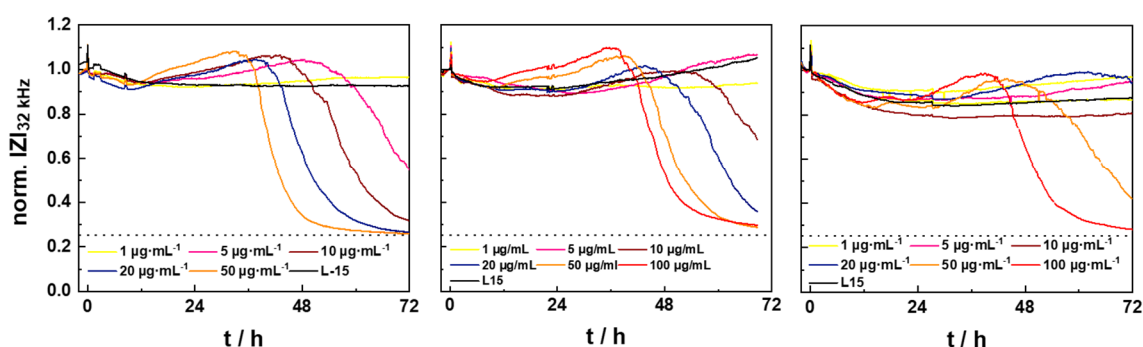


Figure A 4. Averaged and normalized impedance time courses of NRK cells at 32 kHz, exposed to 33 nm UCNPs@AP (1 – 100 µg·mL⁻¹, L-15, 5% FCS) at time point 0 h at 37 °C. Three representative measurements with cells from rising passage number (subculture 24 – 27, left to right). Dotted lines represent cell-free impedance level. Average baseline impedance magnitude was (1.08 ± 0.01) kΩ before addition (N = 16).

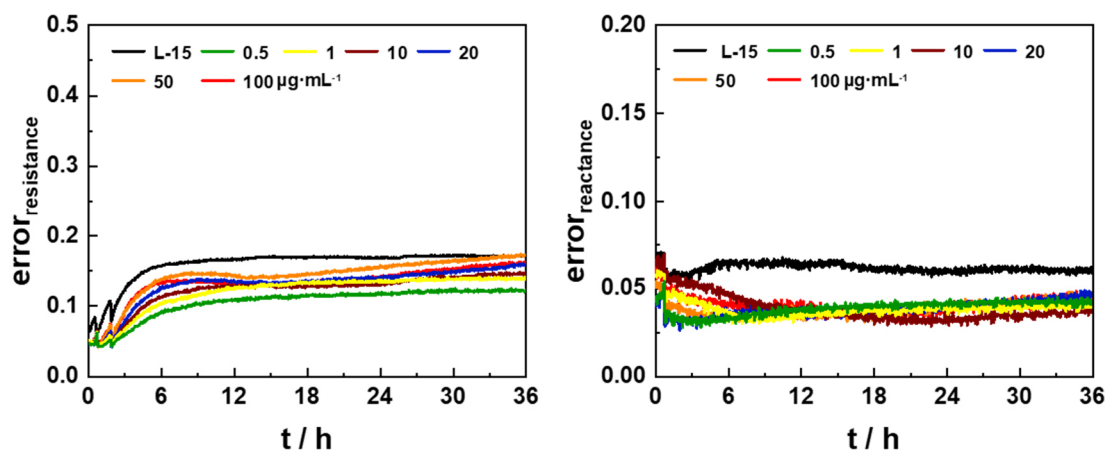


Figure A 5. Error of resistance and error of reactance of the fit.

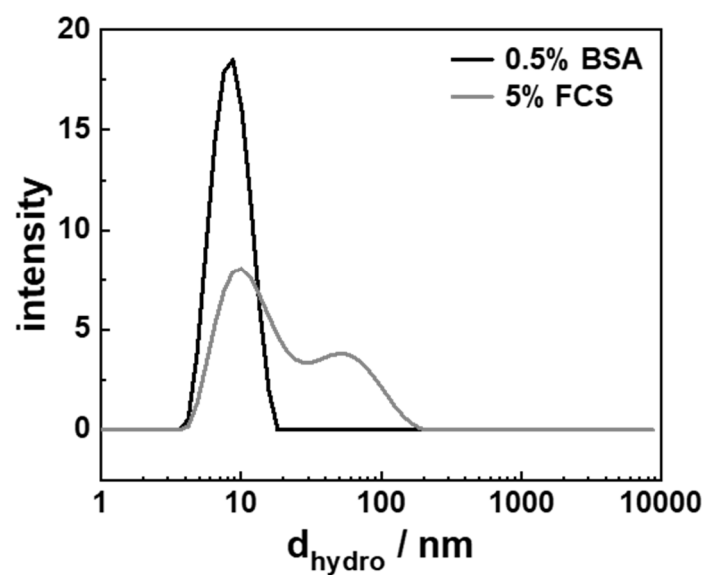


Figure A 6. Hydrodynamic diameter distribution of BSA (0.5%) and FCS (5%) at rt in DPBS⁺.

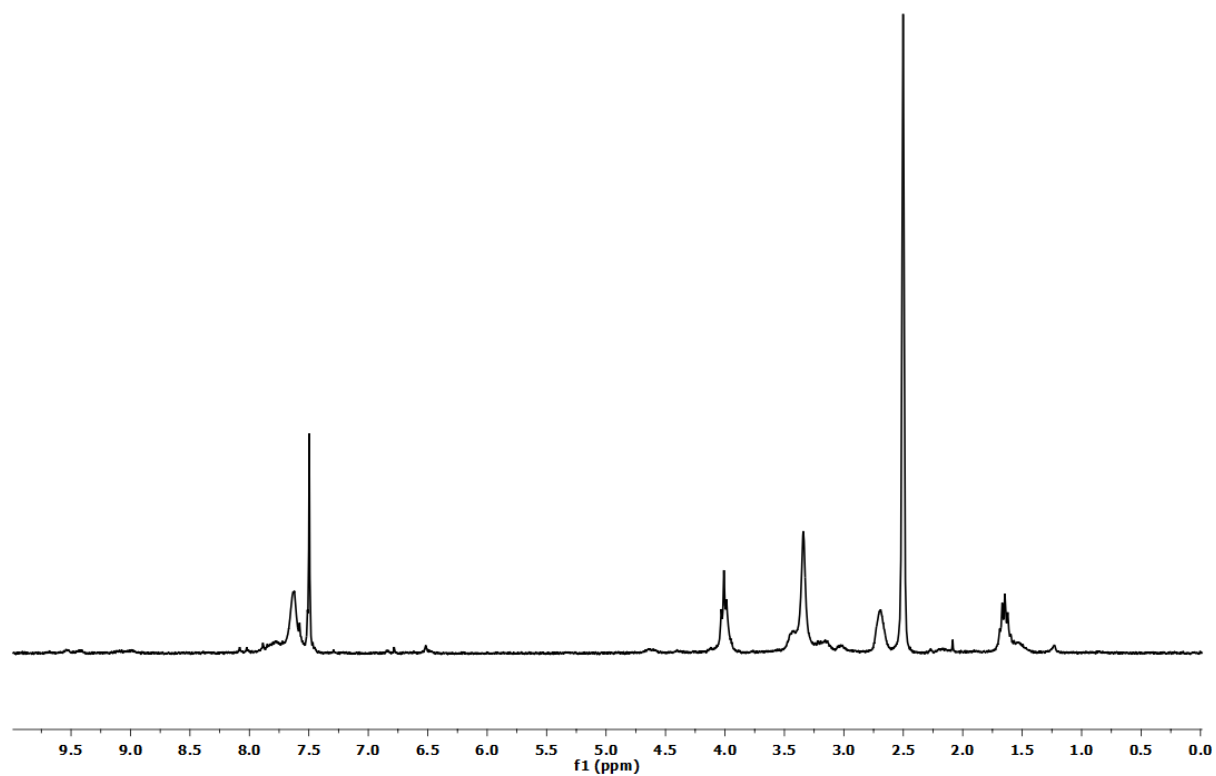


Figure A 7. ^1H NMR (300 MHz, DMSO-d_6) of aminated rose bengal.

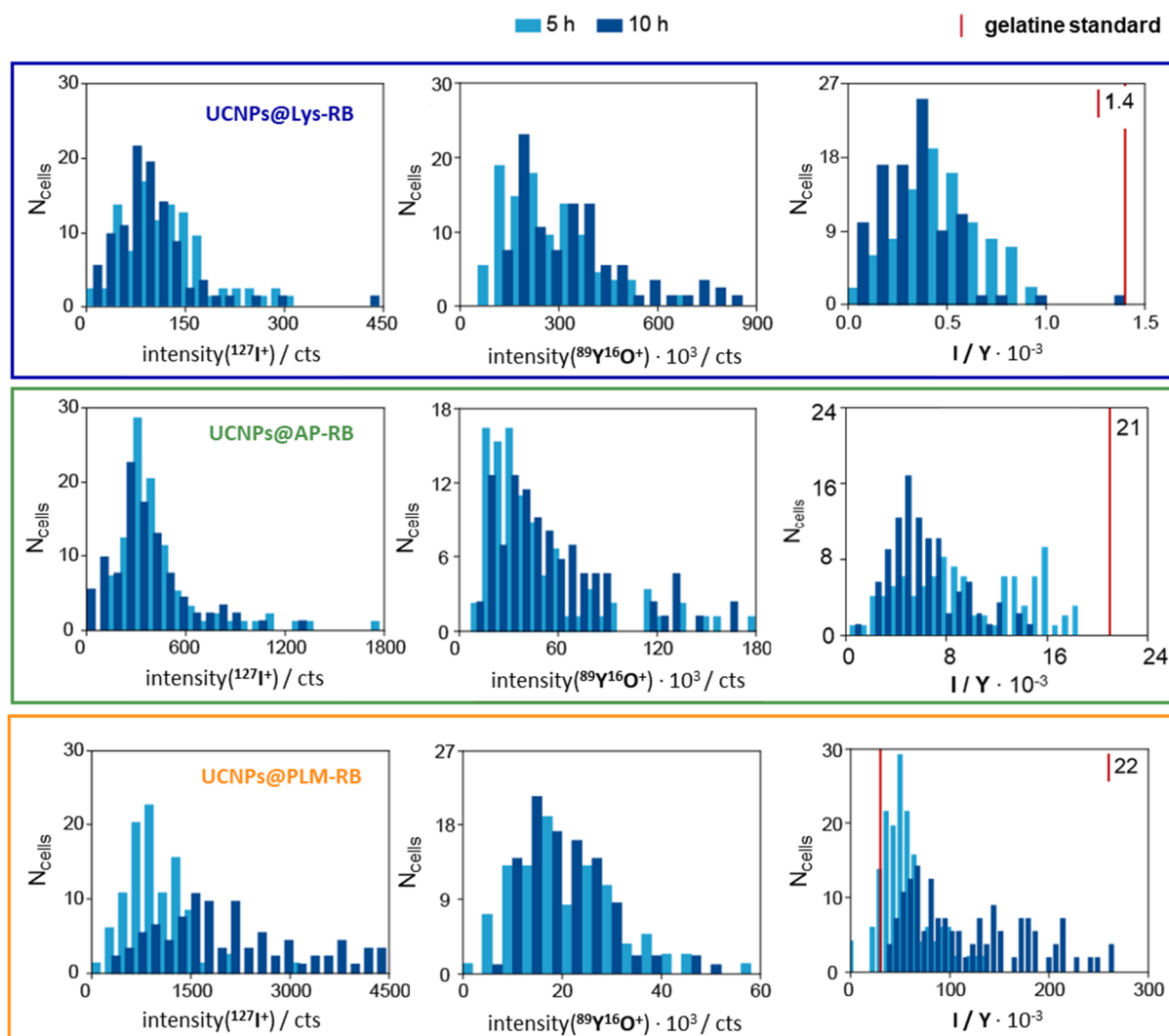


Figure A 8. Distributions of the cellular iodine content ($\text{intensity}({}^{127}\text{I}^+)$), yttrium content ($\text{intensity}({}^{89}\text{Y}^{16}\text{O}^+)$), and the corresponding I/Y ratio of 100 individual NRK cells determined *via* LA-ICP-MS after incubation with 24 nm UCNPs@Lys-RB ($50 \mu\text{g}\cdot\text{mL}^{-1}$, DMEM, 1% DMSO), UCNPs@AP-RB, or UCNPs@PLM-RB (each $50 \mu\text{g}\cdot\text{mL}^{-1}$, DMEM, 5% FCS) at 37°C for 5 h or 10 h. Cell-free determined I/Y ratios of the UCNPs in gelatine are shown as red line.

Table A 1. Hydrodynamic diameters (d_{hydro} , mean \pm SD, N =3) and zeta potential (ζ , mean \pm SD, N =3) of 12 nm as well as 33 nm UCNPs@AP and UCNPs@PLM at rt in H₂O and in the media for cell experiments L-15 (5% FCS, 100 $\mu\text{g}\cdot\text{mL}^{-1}$ pen and strep), DPBS (5% FCS, 1 $\text{mg}\cdot\text{mL}^{-1}$ glucose), cell culture medium DMEM (5% FCS, 1 mM L-glutamine, 100 $\mu\text{g}\cdot\text{mL}^{-1}$ pen and strep).

	UCNPs@AP 12 nm	UCNPs@PLM 12 nm	UCNPs@AP 33 nm	UCNPs@PLM 33 nm
$d_{\text{hydro}}(\text{H}_2\text{O}) / \text{nm}$	22.60 \pm 0.08 (Pdl = 0.09 \pm 0.01)	60.8 \pm 0.1 (Pdl = 0.16 \pm 0.01)	56.0 \pm 0.6 (Pdl = 0.12 \pm 0.02)	125 \pm 2 (Pdl = 0.19 \pm 0.01)
ζ / mV	-29 \pm 2	-41 \pm 3	-19.3 \pm 0.3	-63 \pm 3
$d_{\text{hydro}}(\text{L-15}) / \text{nm}$	50.1 \pm 0.5 (Pdl = 0.27 \pm 0.01)	140 \pm 1 (Pdl = 0.17 \pm 0.01)	97 \pm 1 (Pdl = 0.30 \pm 0.01)	
$d_{\text{hydro}}(\text{DPBS}) / \text{nm}$			93 \pm 2 (Pdl = 0.26 \pm 0.01)	148 \pm 4 (Pdl = 0.19 \pm 0.02)
$d_{\text{hydro}}(\text{DMEM}) / \text{nm}$		119 \pm 2 (Pdl = 0.11 \pm 0.01)		180 \pm 6 (Pdl = 0.12 \pm 0.02)

11.2 List of Materials

Chemicals

<i>Acros Organics</i> (Geel, Belgium)	hexane (95%)
<i>Alfa Aesar GmbH</i> (Karlsruhe, Germany)	1-octadecene (90%), oleic acid (90%)
<i>Avanti Polar Lipids Inc.</i> (Alabaster, USA)	1,2-dioleoyl-sn-glycero-3-phosphate (sodium salt) (DOPA), 1,2-dioleoyl-sn-glycero-3-phosphoethanolamine (DOPE)
<i>Bernd Kraft GmbH</i> (Duisburg, Germany)	multielement standard (10,000 ppb Y ³⁺ , Yb ³⁺ , Er ³⁺ , Tm ³⁺ , Gd ³⁺)
<i>Carl Roth GmbH</i> (Karlsruhe, Germany)	albumin
<i>Fisher Chemical</i> (Schwerte, Germany)	chloroform (99.98 %), diethyl ether, DMF (99.9%), methanol (99.99%)
<i>Gibco by Thermo Fisher</i> (Waltham, USA)	fetal bovine serum (FBS)
<i>Invitrogen AG</i> (Carlsbad, USA)	2',7'-dichlorodihydrofluorescein-diacetate (H ₂ DCFDA)
<i>Invivogen GmbH</i> (San Diego, USA)	hygromycin B gold
<i>Life Technologies GmbH</i> (Carlsbad, USA)	Leibovitz L-15 medium, PrestoBlue® reagent
<i>Dr. Keller's working group</i> (University of Regensburg, Germany)	alkyne-NT(8-13), methyl-ether-PEG3-NHS ester, N(Me)-Leu-NT(8-13), SR142948, [³ H]27
<i>Merck KGaA</i> (Darmstadt, Germany)	KCl (99.5%), KH ₂ PO ₄ (99.5%), Na ₂ HPO ₄ (99.5%), sodium hydroxide
<i>Perkin Elmer Inc.</i> (Waltham, USA)	liquid scintillator optiphase supermix, multi element standard (pureplus), Rh standard (pureplus),

<i>Selleckchem GmbH</i> (Houston, USA)	dynasore
<i>Serva Electrophoresis GmbH</i> (Heidelberg, Germany)	bacitracin
<i>Sigma Aldrich GmbH</i> (Steinheim, Germany)	azido-PEG3-NHS ester, 3-bromopropylamine, cholesterol (99%), CuSO ₄ , DPBS ⁻ , DPBS ⁺⁺ , DMSO-d ₆ , dodecylamine, D ₂ O, 1-ethyl-3-(3-dimethylaminopropyl)carbodiimide (EDC), EDTA in DPBS ⁻ , erbium(III) chloride, D-glucose, DMEM high glucose, DMEM/HAM12, L-glutamine, guanidinium chloride, 2-[4-(2-hydroxyethyl)piperazin-1-yl]ethanesulfonic acid (HEPES, 99.5%), hexahydrate (99.99%), lysine, 2-morpholin-4-ium-4-ylethanesulfonate (MES, 99.5%), Na-oleate (82%), N-hydroxysuccinimide (NHS), NOBF ₄ (95%), penicillin/streptomycin, phosphotungstic acid, poly(acrylic acid) (PAA), poly(isobutyl maleic anhydride) (6,000 g·mol ⁻¹ 98%), rose bengal, RPMI1640, sodium ascorbate, sucrose, tert-butyl hydroperoxide tris(hydroxymethyl)aminomethane (Tris, 99.8%), thulium(III) chloride, trypsin - EDTA
<i>Treibacher Industrie AG</i> (Althofen, Austria)	ytterbium(III) chloride hexahydrate (99.999%) and yttrium(III) chloride hexahydrate (99.99%)
<i>VWR International GmbH</i> (Fontenay-sous-Bois cedex, France)	cyclohexane (100%), 67% w/v HNO ₃ (ultrapure), NaCl

All other reagents and organic solvents were of the highest grade available. Unless otherwise noted, all chemicals were used as received without any further purification. All aqueous solutions were prepared with double distilled water.

Non-sterile Consumables

<i>Carl Roth GmbH</i> (Karlruhe, Germany)	Rotilabo filter (PES, 0.22 µm)
<i>Sigma Aldrich GmbH</i> (Steinheim, Germany)	Ultra centrifugal filter (NMWK 3 k)
<i>Spectrum Laboratories</i> (Rancho Dominguez, USA)	dialysis membrane tube (MWCO 12 – 14 kDa)
<i>Plano GmbH</i> (Wetzlar, Germany)	copper grids (coated with carbon, 400 mesh)

Sterile Consumables for Cell Experiments

<i>Applied Biophysics Inc.</i> (Troy, USA)	8W1E ECIS array, 8W10E ECIS array, 96W1E+ ECIS array
<i>Cellvis</i> (Mountain View, USA)	8 well chambered cover glass
<i>Corning Inc.</i> (Corning, USA)	96W white (clear bottom)
<i>Greiner Bio-One GmbH</i> (Frickenhausen, Germany)	96W white (F-bottom, high binding), 96W black (µclear, high binding), 96W cell culture (F-bottom), 24W cell culture
<i>Ibidi GmbH</i> (Gräfelfing, Germany)	µ-dish with glass bottom
<i>Perkin Elmer Inc.</i> (Waltham, USA)	permanent seal for microplates
<i>Sarstedt Inc.</i> (Nümbrecht, Germany)	Filtropur S 0.2, µ-dish

12 Curriculum Vitae

Name: Susanne Märkl
Geburtsdatum: 3. Oktober 1994

AUSBILDUNG

- 12/18 – 10/22 **Promotion**, Analytische Chemie, Universität Regensburg
unter der Leitung von Prof. Dr. Joachim Wegener
“Colloidally Dispersed Upconversion Nanoparticles: How the Surface Composition Affects Brightness, Stability and Toxicity in Cellular Applications”
- 10/16 - 09/18 **Master of Science**, Chemie, Universität Regensburg
Schwerpunkte: Analytische Chemie, Organische Chemie, Biochemie
Masterarbeit: *“Small Upconversion Nanoparticles with Lipid Bilayer Functionalization for Bioassays”*
- 10/13 - 09/16 **Bachelor of Science**, Chemie, Universität Regensburg
- 09/05 - 07/13 **Allgemeine Hochschulreife**, Gymnasium der Ursulinen Straubing

WISSENSCHAFTLICHE ARBEIT

- 10/21 - 11/21 **Forschungsaufenthalt** im Rahmen der Promotion
Universität Straßburg
- 08/16 - 12 /16 **Studentische Hilfskraft**
Analytische und Organische Chemie, TUM Campus Straubing
- 06/16 - 07/15 **Studentische Hilfskraft**
09/15 - 10/15 Analytische Chemie, Universität Regensburg

FORTBILDUNGEN

BWL für Ingenieure

Strategische Partnerschaft Sensorik e.V., 2021

Optochemische Sensorik

ASCOS, Bertinoro, 2019

Qualitätsmanagement in der Analytischen Chemie

Universität Regensburg, 2018

Methoden und Probleme in der industriellen Analytik

GDCh Frühjahrsschule in Essen, 2017

AUSZEICHNUNGEN UND STIPENDIEN

01/22 - 03/22

Promotionsabschlusstipendium

bayrisches Programm zur Realisierung der Chancengleichheit für Frauen in Forschung und Lehre

10/21 - 11/21

Mobilitätstipendium nach Frankreich Procope

französische Botschaft in Deutschland

04/18

Best Poster Award

Konferenz UPCON, Valencia

07/17

Bester Bachelorabschluss in Analytischer Chemie

GDCh

KONFERENZEN UND SEMINARE

04/21

Konferenz UPCON, virtuell

Poster: *Surface Engineering of Small Upconversion Nanoparticles to Enhance the Brightness in Aqueous Media*

09/20

Interdisziplinäres Doktorandenseminar „Online-Analytik im Wandel“, virtuell

Vortrag: *Surface Engineering of Small Upconversion Nanoparticles to Enhance the Brightness in Aqueous Media*

04/18

Konferenz UPCON, Valencia

Poster: *Synthesis and Surface Engineering of Biocompatible Upconversion Nanoparticles for Theranostic Applications*

PUBLIKATIONEN

Schroter A., **Märkl S.**, Hirsch T. **2022**. Upconversion Nanocrystals with High Lanthanide Content: Luminescence Loss by Energy Migration versus Luminescence Enhancement by Increased NIR Absorption. *Adv. Funct. Mat.*

Schwanzer, P., Schillinger M., Mieslinger J., Walter S., Hagen G., **Märkl S.**, Haft G., Dietrich M., Moos R., Gaderer M., Rabl H.-P. **2021**. A Synthetic Ash-Loading Method for Gasoline Particulate Filters with Active Oil Injection. *SAE Int. J. Engines*. 14(4): 493-505.

Wunderlich, L., Hausler P., **Märkl S.**, Bierl R., Hirsch T. **2021**. Nanoparticle Determination in Water by LED-Excited Surface Plasmon Resonance Imaging. *Chemosensors*. 9(7):175.

Märkl S., Schroter A., Hirsch T. **2020**. Small and Bright Water-Protected Upconversion Nanoparticles with Long-Time Stability in Complex, Aqueous Media by Phospholipid Membrane Coating. *Nano Letters*. 20(12): 8620-8625.

Hirmer A., **Märkl S.**, Schroter A., Hirsch T. **2020**. Surface engineering of small and bright upconversion nanoparticles providing chemical and colloidal stability in biological media. Proc. SPIE 11467, *Nanoengineering: Fabrication, Properties, Optics, Thin Films, and Devices XVII*, 114670X.

Hofmann C., Kaiser B., **Maerkl S.**, Duerkop A., Baeumner A. J. **2020**. Cationic liposomes for generic signal amplification strategies in bioassays. *Anal Bioanal Chem*. 412(12): 3383–3393.

Himmelstoß S. F., Wiesholler L. M., Buchner M., Muhr V., **Märkl S.**, Baeumner A. J., Hirsch T. **2017**. 980 nm and 808 nm excitable upconversion nanoparticles for the detection of enzyme related reactions. *Proc. of SPIE*. 10077: 100770L1-100770L6.

Eidesstattliche Erklärung

Ich erkläre hiermit an Eides statt, dass ich die vorliegende Arbeit ohne unzulässige Hilfe Dritter und ohne Benutzung anderer als der angegebenen Hilfsmittel angefertigt habe. Die aus anderen Quellen direkt oder indirekt übernommenen Daten und Konzepte sind unter Angabe des Literaturzitats gekennzeichnet.

Weitere Personen waren an der inhaltlich-materiellen Herstellung der vorliegenden Arbeit nicht beteiligt. Insbesondere habe ich hierfür nicht die entgeltliche Hilfe eines Promotionsberaters oder anderer Personen in Anspruch genommen. Niemand hat von mir weder unmittelbar noch mittelbar geldwerte Leistungen für Arbeiten erhalten, die im Zusammenhang mit dem Inhalt der vorgelegten Dissertation stehen.

Die Arbeit wurde bisher weder im In- noch im Ausland in gleicher oder ähnlicher Form einer anderen Prüfungsbehörde vorgelegt.

Ich versichere an Eides statt, dass ich nach bestem Wissen die reine Wahrheit gesagt und nichts verschwiegen habe.

Vor Aufnahme der obigen Versicherung an Eides statt wurde ich über die Bedeutung der eidesstattlichen Versicherung und die strafrechtlichen Folgen einer unrichtigen oder unvollständigen eidesstattlichen Versicherung belehrt.

Ort, Datum, Unterschrift